# The role of microbial rhodopsins in the evolution and adaptation of a marine diatom

Longji Deng

100189430

A thesis submitted for the degree of Doctor of Philosophy

University of East Anglia, Norwich, UK

School of Environmental Sciences

September 2024

# Abstract

Microbial rhodopsins have been identified in bacteria, archaea, viruses, and eukaryotic phytoplankton, but their in-vivo function in the latter group has largely remained elusive. The discovery of two variants (FR1/FR2) of xanthorhodopsin in 2008, as part of the *Fragilariopsis cylindrus* genome project, initiated focused research to explore the role of these proton-pumping and retinal-binding membrane proteins in key oceanic primary producers. This thesis is one such project, aimed at uncovering how microbial rhodopsins in the polar diatom *Fragilariopsis cylindrus* contribute to the success of these primary producers, particularly in polar regions like the Southern Ocean.

Using a combination of bioinformatics, molecular biology, and physiological experiments, this thesis reveals how rhodopsins in *F. cylindrus* enhance diatom growth, especially in the iron-limited Southern Ocean, a high-nutrient, low-chlorophyll (HNLC) region. The findings indicate that the xanthorhodopsin variant FR1 acts as a light-driven proton pump with significant activity in cold, iron-limited environments, typical of the Southern Ocean. This suggests that microbial rhodopsins provide an additional energy acquisition pathway, supplementing photosynthesis when iron is scarce.

Furthermore, a genetically modified *Thalassiosira pseudonana* strain expressing FR1 exhibited enhanced growth and photosynthetic efficiency under iron-limited conditions, highlighting the adaptive advantage provided by these microbial rhodopsins. The expression of FR1 in the heterotrophic diatom *Nitzschia putrida* further demonstrated that, even in the absence of photosynthetic electron transport, FR1 can function as an alternative “photosystem,” allowing heterotrophic organisms to harness light for proton generation, supporting ATP synthesis or aiding in nutrient acquisition for growth.

# Contents

# Contents of figures and tables

# Preface

This statement confirms that the work contained in this thesis was conceived, planned, conducted, interpreted, and written by Longji Deng. Apart from the experiments mentioned below, all the results were completed and analysed by Longj Deng, including the lab work and bioinformatic analysis. Prof. Thomas Mock, my primary supervisor, was involved throughout all stages of this PhD, including reviewing the five chapters contained within this thesis. Involvement of other members of the Mock lab and collaborators is outlined below.

Chapter 2 lays the foundation by investigating the structural and functional characteristics of two rhodopsin variants, FR1 and FR2, identified in the polar diatom *Fragilariopsis cylindrus*. Some of the data presented in this chapter were contributed by my co-authors on articles where I am the second author, including physiological characterisation responses of diatom rhodopsin FR1 and FR2 were provided by Jan Strauss during his job at German Maritime Centre and Shiqiang Gao from the Department of Neurophysiology, Institute of Physiology, University of Würzburg; The RT-qPCR results and part of the fluorescence microscope images were provided by Jan Strauss during his PhD in Thomas Mock's lab.

Chapter 3 details the builds on this foundation by examining the phenotypic effects of rhodopsin expression in the model diatom *Thalassiosira pseudonana*. Plasmids used in setting up the transformation were provided by Jan Strauss. Rapid light curve experiments data were collected with the help of Sayanya Acharya when she was a Master student working in Thomas Mock's lab guided by me. Cell slicing and immunogold labelling were carried out with the help of Prof. Junrong Liang and her PhD student Lu Huang from Xiamen University.

Chapter 4 starts with setting up a transformation protocol for heterotrophic diatoms *Nitzschia putrida* and then expands the scope of rhodopsin research to help the heterotrophic diatom *N. putrida* to regain the ability to use light by rhodopsin. Ryoma Kamikawa and his students Yasuhiro Tanizawa and Yasukazu Nakamura contributed to providing the highest gene expression data. Amanda Hopes, during her post-doc in Thomas Mock's lab, gave advice on Golden-Gate cloning. She also provides the plasmids containing domesticated eGFP and nourseothricin resistance gene. Golden-gate vector backbones were provided by Vladimir Nekrasov and Oleg Raitskin from the repository at the Sainsbury Laboratory. Cell slicing and immunogold labelling were carried out with the help of Prof. Junrong Liang and her PhD student Lu Huang from Xiamen University. Lulu Wang, Yixuan Li, and Shunan Fu, PhD students in Thomas Mock's lab, helped cultivate the algae.

# Abbreviations

AOX - Alternative oxidase

ATP - Adenosine triphosphate

ATPse - Adenosine triphosphatase

BCMO - Beta-carotene monooxygenase

BR - Bacteriorhodopsin

BSA - Bovine serum albumin

CCM - Carbon concentrating mechanism

cDNA - Complementary DNA

CO2 – Carbon dioxide

Cred - Canthaxanthin biosynthesis gene marker

Ct - Cycle threshold

Cyt b6/f - Cytochrome b6/f complex

DAPI - 4',6-diamidino-2-phenylindole

DAQ – Data acquisition

DMSO - Dimethyl sulfoxide

DNA - Deoxyribonucleic acid

DPSS - Diode-pumped solid-state

EDTA - Ethylenediaminetetraacetic acid

eGFP - Enhanced green fluorescent protein

EPS - Extracellular polysaccharides

ER - Endoplasmic reticulum

ETR - Electron transport rate

ETRmax - Maximum electron transport rate

FACS - Fluorescence-activated cell sorting

fcp - Fucoxanthin chlorophyll a/c-binding protein

Fe - Iron

$Fe^{2+}$ - Ferrous iron

$Fe^{3+}$ - Ferric iron

FLDA - Flavodoxin

FR - Fragilariopsis cylindrus rhodopsin

FSC/SSC - Forward scatter/side scatter

FTN - Ferritin

Fv/Fm - Maximum quantum yield of photosystem II

gDNA - Genomic DNA

GFP - Green fluorescent protein

HNLC - High nutrient low chlorophyll

HOT – the Hawaii Ocean Time-series

HR – Halorhodopsin

Ik - Light saturation point

IPTG - Isopropyl β-D-1-thiogalactopyranoside

ISIPs - Iron starvation-induced proteins

I-TASSER - Iterative Threading ASSembly Refinement

JGI – Joint Genome Institute

$K^+$ - Potassium ion

kDa - Kilodalton

L0/L1/L2 - Level 0/1/2

LB - Luria-Bertani broth

Lys - Lysine

MATOU - Marine Atlas of Tara Ocean Unigenes

ML - Maximum likelihood

MSA - Multiple sequence alignment

$Na^+$ - Sodium ion

NADH - Nicotinamide adenine dinucleotide hydride

NADPH - Nicotinamide adenine dinucleotide phosphate

NAT - Nourseothricin acetyltransferase/Nourseothricin Resistance Protein

NCBI – National Center for Biotechnology Information

NCMA - National Center for Marine Algae and Microbiota

NiR - Nitrite reductase

NMG - N-methyl-D-glucamine

NpRHO - Nitzschia putrida rhodopsin knock-in strain

NpWT - Nitzschia putrida wild type strain

NR - Nitrate reductase

NRAMPs - Natural resistance-associated macrophage proteins

OD - Optical density

OGA - Ocean gene atlas

PAM - Pulse amplitude modulation

PAR - Photosynthetically active radiation

PBS - Phosphate-buffered saline

PC – Plastocyanin

PCR - Polymerase chain reaction

PETE - Plastocyanin

PETF – Ferredoxin

PMF - Proton motive force

POC - Particulate Organic Carbon

PQ - Plastoquinone

PR - Proteorhodopsin

PSI - Photosystem I

PSII - Photosystem II

PSU - Practical salinity units

qPCR - Quantitative polymerase chain reaction

RHO - Rhodopsin-expressing strain

RLC – Rapid light curve

ROS - Reactive oxygen species

RT-PCR - Reverse transcription polymerase chain reaction

RT-qPCR - Quantitative real-time polymerase chain reaction

RT-qPCR - Real-time quantitative PCR

SDM - Site-directed mutagenesis

SOC – Super optimal broth

SR I/II - Sensory rhodopsin I/II

TEM - Transmission electron microscopy

TEVC - Two-electrode voltage clamp

TpRHO - Thalassiosira pseudonana rhodopsin knock-in strain

TpWT - Thalassiosira pseudonana wild type strain

WT - Wild type

α - Initial slope of rapid light curve

# Acknowledgements

First of all, I would like to express my sincere gratitude to my parents **Zhaohui Jin (靳朝晖)** and **Dr. Yunfeng Deng (邓云锋)** for supreme support and heavenly love. They did their best to provide me with the opportunity and financial support to continue my Ph.D. study. I would also thank my Godparents, **Yu Liu (刘煜)** and **Yuchu Ma (马玉初)**, for their tremendous support throughout this journey.

I am deeply grateful to my supervisors, **Prof. Thomas Mock** and **Prof. Cock van Oosterhout**, for their continuous support, guidance, and patience throughout my PhD journey. From a rookie who couldn't do anything to today's graduation, their invaluable advice and insights have significantly shaped the direction and success of this research.

My heartfelt thanks go to my colleagues and collaborators, **Prof. Ryoma Kamikawa (神川龍馬)**, **Prof. Yunyun Zhuang (庄昀筠)**, **Prof. Jifeng Qi (齐继峰)**, Prof. Guangce Wang (王广策), **Dr. Jan Strauss**, **Dr. Shan Gao (高山)**, Dr. Nigel Belshaw, Dr. Amanda Hopes, Dr. Krisztina Sarkozi, Dr. Reuben Gilbertson, Dr. Monica Pichler, **Dr. Xuewei Mao (毛雪微)**, Dr. Yuanxu Dong (董原旭), Dr. Chuanchuan Cao (曹川川), Dr. Lulu Wang (王璐璐), William Boulton, Yixuan Li (李奕璇), Johanna Winder, Shunan Fu (傅书南), for their constant assistance, fruitful discussions, and the motivation they provided throughout this project.

Due to Covid-19, I found myself too busy and unable to travel back home for many reasons, missing many important family events during my PhD. I deeply regret not being able to attend or care for my family members who were sick, and I offer great thanks to those who helped my parents during that difficult time. My grandfather, **Yuanding Jin (靳元鼎)**, was gravely ill and passed away, and my grandmother, **Qin Han (韩琴)**, was paralysed. I am regretful that I cannot be with them at the hard time.They brought me up and gave me a lot of love. This thesis is a gift for them as

well.

I must also thank my friends for helping me through such a difficult and lonely time: **Zihan Wang (王子涵)**, Zijian Chen (陈梓健), Lixuan Zhao, Yang Xiao (肖扬), Liyan Deng (邓立言), Arash Shi, Leo Zack, Ke Zhang (张轲), Jingchen Wang, Yunze Zhu (竺昀泽), Keyu Lu (卢科宇), Zixi Guo. Special thanks to **Shunkai Yang (杨舜凯)** who helped me and discussed many questions with me at the beginning of my Ph.D. journey.

Before starting my Ph.D. travel, I had the opportunity to take my first steps into the molecular biology field at the Ocean University of China and The Institute of Oceanology, Chinese Academy of Sciences. I would like to thank Prof. Yunyun Zhuang (庄昀筠) and her student Yu Zang (臧瑜), Prof. Guangce Wang (王广策), and Dr. Xiujun Xie (解修俊) for their hands-on guidance and support. Without their help, my journey at the beginning would have been much harder.

In October 2023, I had the chance to visit Xiamen University for a month. I am incredibly grateful to **Prof. Junrong Liang (梁君荣)** and her student **Dr. Lu Huang (黄璐)** for welcoming me into their lab and help hand-to-hand with the immunogold labelling for my project.

In the end, I would like to thank my lovely cat, Sakurakouji Luna. His coming brings a lot of joy not only to me but also to my friends, helping with the lonely journey during the Covid.

# Chapter 1

# Introduction

## Introduction to marine photosynthesis and iron limitation

### Phytoplankton and marine primary production

The evolutionary history of photosynthetic organisms traces back to approximately 3.8 billion years ago. It was around 200 million years ago that these organisms began to significantly shape the structure of marine ecosystems (Cardona, 2018; Hull, 2017). The oceans, covering more than 70% of the Earth's surface, are not only the cradle of life but also contribute nearly as much to global primary productivity as terrestrial environments (Field et al., 1998). This significant contribution is largely due to phytoplankton, the principal primary producers in the euphotic zone where sunlight penetrates the ocean.

These tiny organisms, despite constituting only about 1% of total global plant biomass, contribute to over 40% of the world's total primary productivity (Falkowski, 1994; Field et al., 1998). This disproportionate impact highlights their crucial role in marine ecosystems and global biogeochemical cycles. They convert inorganic materials into organic matter through photosynthesis, driving the flow of energy through the marine food web and influencing the health of the entire planet (Basu & Mackey, 2018).

In the global carbon cycle, phytoplankton function as biological carbon pumps. They transform atmospheric $CO_2$ into particulate organic carbon, which can be sequestered deep in the ocean when these organisms die and their remains sink to the seafloor (Claustre et al., 2021). A significant portion of this exported carbon is facilitated by diatoms as their silicate shell makes them sink faster. Faster sinking reduces the time POC spends in the upper ocean where decomposition occurs, significantly increasing

the amount of carbon transported to, and sequestered in, the deep ocean. (Basu & Mackey, 2018; Claustre et al., 2021). This process is critical for regulating the Earth's climate, as it temporarily removes $CO_2$ from the atmosphere and helps mitigate the impacts of climate change (Hofmann & Schellnhuber, 2009).

The productivity of phytoplankton not only supports the vast array of marine life but also plays a pivotal role in global food security. Regions with higher primary productivity, driven by phytoplankton, often support larger fisheries, which are crucial for feeding the global population (Bunt, 1973). Therefore, understanding the dynamics of phytoplankton productivity is essential for managing marine resources and developing sustainable strategies to cope with environmental changes.

Given their central role in ecological and climate frameworks, studying phytoplankton is crucial for advancing our understanding of marine biology and addressing broader environmental challenges. This makes research into specific adaptations and functions, such as how rhodopsin influences phytoplankton's response to environmental variables like light and nutrient availability, particularly relevant. Such studies not only enhance our understanding of ecological and evolutionary processes but also have implications for biotechnology and climate change mitigation.

## Sources and ecological effects of iron in the ocean

### Sources and forms of iron in the ocean

The biogeochemical cycling of iron in marine ecosystems exhibits pronounced spatial and temporal heterogeneity, primarily dictated by a multitude of abiotic and biotic factors. As depicted in Figure 1.1, in the euphotic zone—where solar irradiance facilitates photosynthetic activities—iron predominantly originates from terrestrial runoff, atmospheric deposition both dry and wet, upwelled deep oceanic waters, hydrothermal vent emissions, anthropogenic inputs, and the thawing of polar glaciers (Hutchins & Boyd, 2016; Tagliabue et al., 2017).

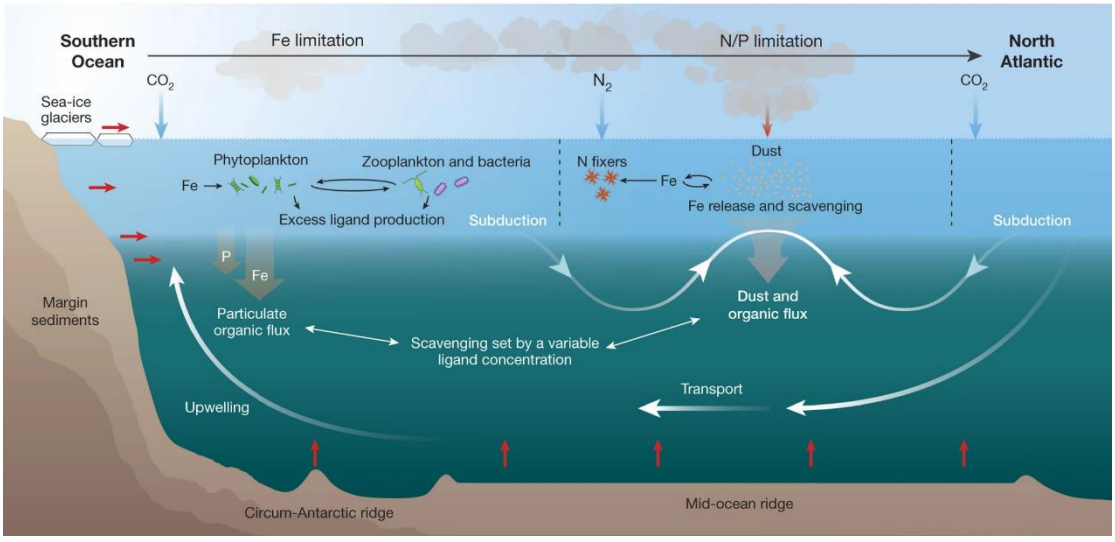


**Figure 1.1 The integral role of iron in ocean biogeochemistry a present model (Tagliabue et al., 2017).**

The pivotal role of iron cannot be overstated in the ocean; it acts as a crucial limiting micronutrient for phytoplankton, whose capacity for primary production is often limited by the availability of this trace element. Rapid assimilation of iron by phytoplankton, coupled with its adsorption onto biogenic particles, precipitates a marked depletion of iron in the euphotic zone, constraining biomass productivity (Bruland et al., 1994). Beyond this sunlit zone, iron concentrations increase towards the mesopelagic and bathypelagic layers. This gradient is established as iron-containing particulates undergo remineralisation, releasing iron back into the water during their descent through the water column (Bressac et al., 2019).

In littoral zones, fluvial systems dominate iron transport, with riverine discharge

acting as a substantial vector for iron transport to marine basins (Klunder et al., 2012; Wetz et al., 2006). Contrarily, in pelagic realms far from terrestrial influence, aeolian processes predominate, with dust from arid regions serving as a significant source of iron, further augmented by anthropogenic emissions which can modify the natural iron inputs (Mahowald et al., 2005).

Iron in marine environments exists in various forms, including dissolved inorganic states, dissolved organic complexes, colloidal materials, and mineral particles (Kappler et al., 2021). Predominantly, dissolved Fe(III) exists as organic complexes, accounting for 99.9% of dissolved iron in seawater (Rue & Bruland, 1995). Common organic carriers of iron include siderophores, ferroporphyrins, extracellular polysaccharides (EPS), and humic substances (Albelda-Berenguer et al., 2019; Feng et al., 2019; Hunter et al., 2011; Yamashita et al., 2020). Among them, siderophores are particularly noteworthy. They are high-affinity, specific biological chelators with small molecular weights and thermodynamic stability constants ranging from $10^{25}$ to $10^{50}$ $M^{-1}$, demonstrating exceptional chelating strength (Kraemer, 2004). In iron-deficient environments, genes related to siderophores in bacteria and fungi are highly expressed, leading to the secretion of siderophores that enhance the affinity for environmental iron (Winkelmann, 1992) (Winkelmann, 1992; (Boukhalfa & Crumbliss, 2002). These siderophores are taken up by cells via efficient transport systems, and iron is subsequently released at specific locations and times to satisfy cellular iron requirements (Boukhalfa & Crumbliss, 2002; Winkelmann, 1992).

Marine siderophores are primarily synthesised by various marine bacteria (Hider & Kong, 2010), and although their production is species-specific, bacteria do not selectively absorb siderophores from different sources (Stintzi et al., 2000). At present, more than 200 marine siderophores have been isolated and identified from the marine environment, mainly divided into hydroxamates, catecholates, and carboxylates, essential for iron chelation (Kramer et al., 2020; Zhang et al., 2022).

Another major organic complex is porphyrin, which includes chlorophyll and its degradation products, such as ferroheme and vitamin B12, a potential iron ligand (Gledhill & Buck, 2012). Recent studies have also revealed that humic substances and extracellular polysaccharides participate in iron chelation, with stability constants similar to those of natural organic ligands (Gledhill & Buck, 2012).

**Ecological effects of iron**

Iron is an essential element for nearly all organisms, playing a critical role in various cellular processes and maintaining normal cellular functions (Gledhill & Buck, 2012). In marine environments, iron is a major factor influencing plankton population dynamics and driving global biogeochemical cycles and climate change (Figure 1.2) (Hutchins & Boyd, 2016; Jiang et al., 2024; Martin et al., 1994). Recent studies highlight iron's significant role in mitigating the greenhouse effect and promoting the carbon cycle, effectively contributing to the Earth's cooling (Martin, 1990).

Approximately 3 billion years ago, photosynthetic oxygen-producing organisms emerged on Earth. The oxygen released by photosynthesis increases both atmospheric oxygen and dissolved oxygen in seawater. This rise in oxygen levels facilitated the

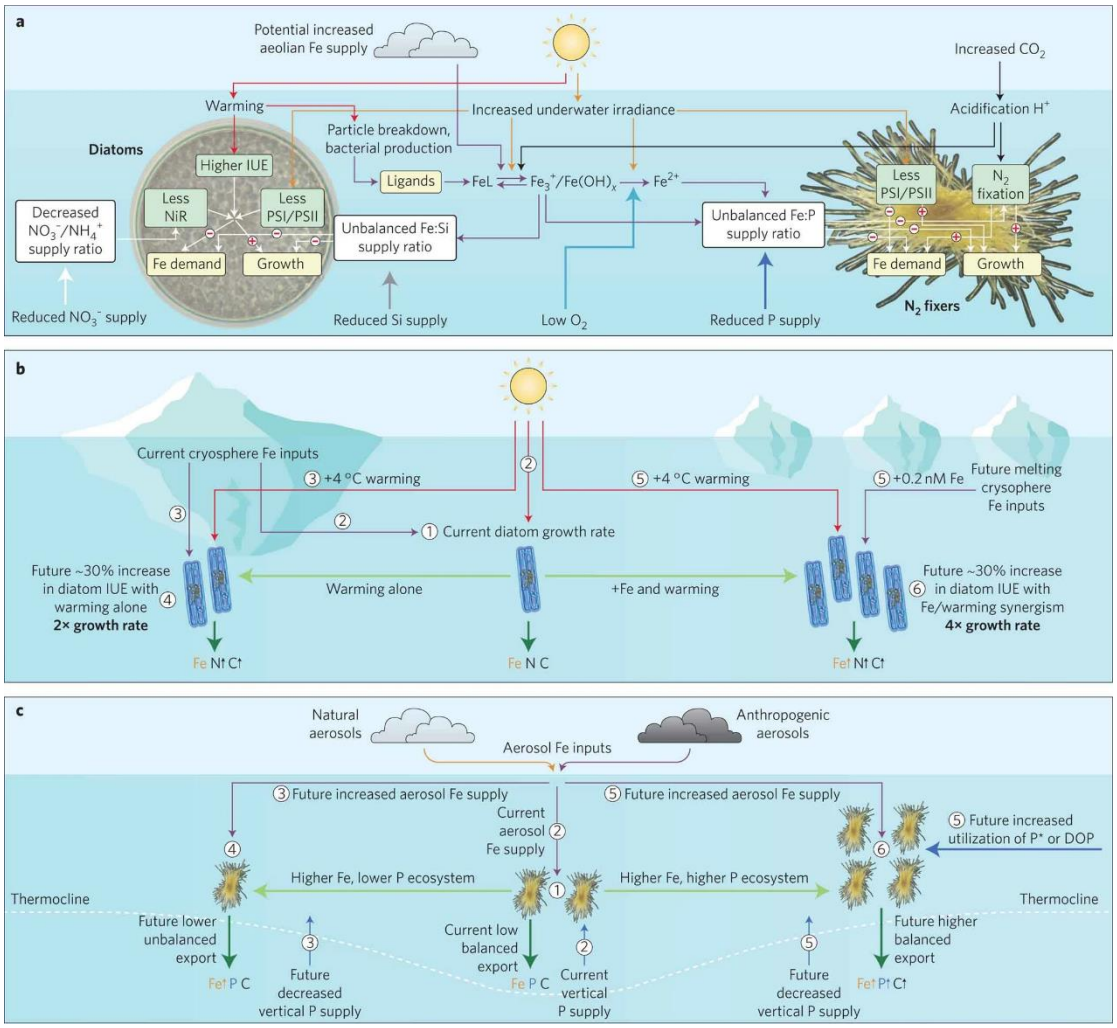


**Figure 1.2 Global change and the interactive effects of Fe on Southern Ocean diatoms and subtropical N2-fixing *Trichodesmium* (Hutchins & Boyd, 2016). a) Schematic of warming, increased irradiance, acidification, deoxygenation, reduced nutrient supply ($NO_3^-$, Si, $PO_4^{3-}$), and aeolian Fe inputs affecting diatom and Trichodesmium physiology. Arrows denote positive (+) or negative (–) impacts on growth and Fe demand from nutrient imbalances (Fe:Si, Fe:P). b) Diatom response to warming and Fe. c) Diazotroph adaptation to Fe/P supply.**

conversion of the unstable $Fe^{2+}$ ion to the more stable Fe3+ ion in seawater (Anbar & Knoll, 2002). Unlike $Fe^{2+}$, $Fe^{3+}$ has extremely low solubility, forming insoluble iron oxides that settle on the seafloor. This process significantly reduced the concentration of soluble iron in seawater(Anbar & Knoll, 2002).

As biological evolution progressed, photosynthetic organisms' demand for iron grew. However, the concentration of dissolved iron in the ocean ranges from 0.02 to 1.0 nM,

barely sufficient to meet the minimum iron requirements of phytoplankton, which is typically around 0.3 nM (Moore & Braucher, 2008; Rijkenberg et al., 2014; Wells et al., 1995). This concentration is below the iron needed to sustain maximum growth rates, usually around 1.0 nM (Sunda & Huntsman, 1997; Wells et al., 1995) (Wells et al., 1995; Huntsman and Sunda, 1997). Thus, increasing the concentration of iron ions in the ocean is crucial for the growth and reproduction of phytoplankton.

Approximately 30% of the surface ocean, known as high nutrient low chlorophyll (HNLC) regions, have abundant nutrients but low biomass (Moore et al., 2013). The persistence of these nutrients despite favourable light conditions remained a significant puzzle until Martin and Fitzwater (1988) discovered very low dissolved iron concentrations in HNLC waters. They proposed that iron deficiency limits phytoplankton growth in these regions through limiting the uptake of macronutrients such as nitrate and silicate (Martin & Fitzwater, 1988; Martin et al., 1989). Subsequent experiments confirmed that adding iron to seawater from HNLC regions stimulates nitrate consumption and therefore significantly increases phytoplankton growth and biomass accumulation (Martin & Fitzwater, 1988).

There are three main HNLC regions in the oceans (Figure 1.3b): the Southern Ocean, parts of the equatorial Pacific, and parts of the subarctic Pacific (Boyd et al., 2007; de Baar et al., 2005), where low iron availability constrains diatom blooms despite abundant macronutrients. This iron limitation extends beyond HNLC zones: phytoplankton in tropical/subtropical upwelling regions also experience periodic iron scarcity (Firme et al., 2003; Hutchins & Bruland, 1998). Crucially, when iron is supplied (e.g., via natural deposition or experiments), diatoms rapidly bloom—demonstrating their physiological potential is unlocked by iron repletion (Boyd et al., 2007; Martin et al., 1994). Collectively, these dynamics explain why iron limits 30-40% of global phytoplankton primary productivity (Moore et al., 2001).

The "Iron Hypothesis" mentioned by Martin has greatly advanced the study of iron

and phytoplankton physiological ecology (Martin, 1990). Given the abundance of iron on land and the relatively small amount required by marine phytoplankton, scientists have proposed the "iron fertilisation" strategy in the oceans, bringing broader attention to the impact of iron limitation. This involves artificially adding iron to HNLC regions to promote phytoplankton growth, consume atmospheric carbon dioxide, mitigate the greenhouse effect, and cool the Earth. Several large-scale *in-situ* iron fertilisation experiments in HNLC regions have successfully induced diatom-dominated phytoplankton blooms (Buesseler et al., 2005; Lemaitre et al., 2016; Smetacek et al., 2012). These blooms are accompanied by decreased surface seawater CO2 concentrations and increased deposition of particulate organic carbon into the deep sea (Buesseler et al., 2005; Lemaitre et al., 2016; Smetacek et al., 2012). During these processes, diatoms have demonstrated strong adaptability to both iron limitation and iron input. Investigating the complex physiological mechanisms behind this adaptability has become a prominent research topic in phytoplankton physiological ecology. Enhanced comprehension of these processes is essential for elucidating the past, present, and future states of marine ecosystems. Particularly, it allows for a refined understanding of how climatic variability and anthropogenic influences might shift the paradigms of iron availability and, thus, the global carbon cycle.

## Introduction of diatom

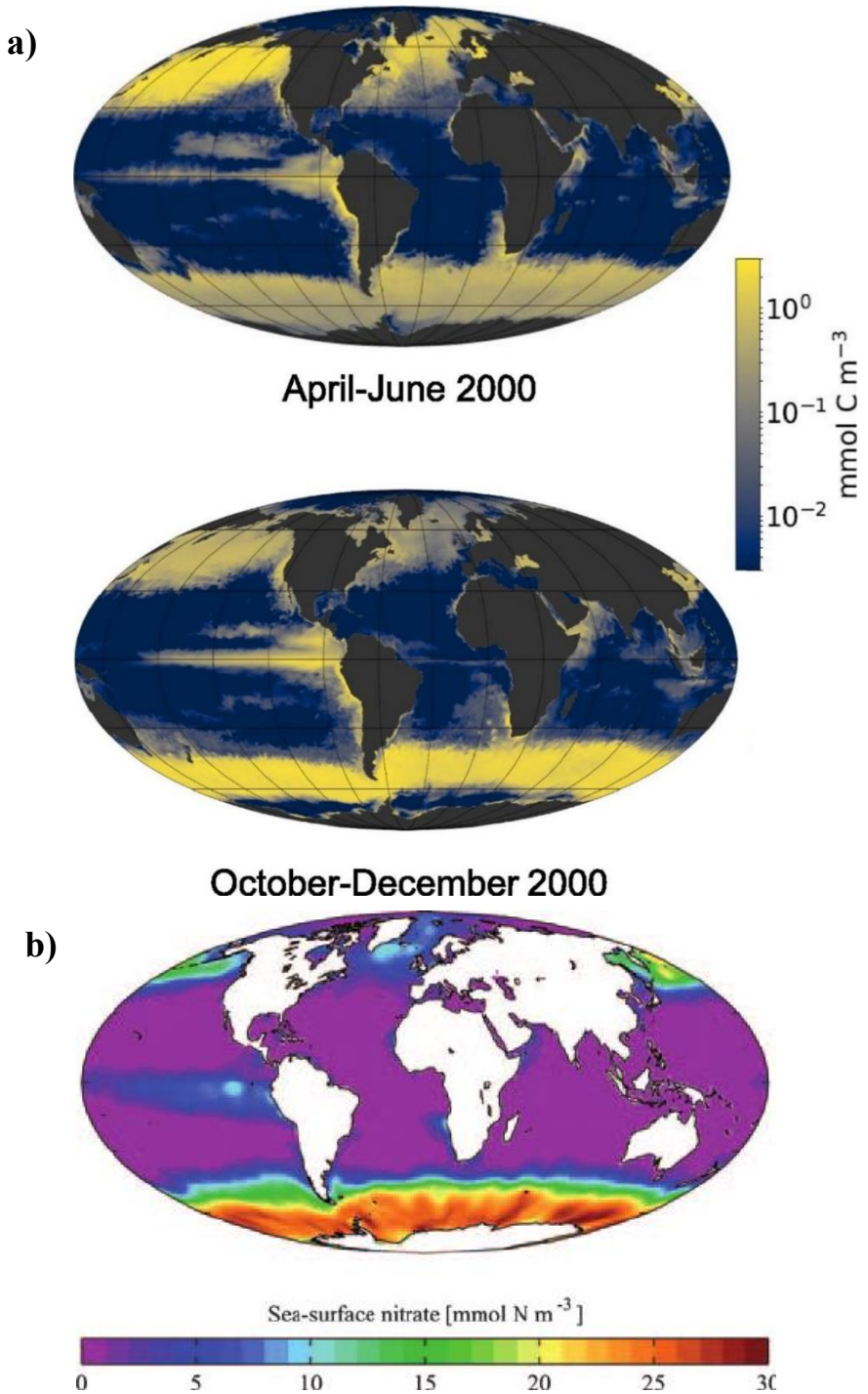


**Figure 1.3 a) Global distribution of surface ocean diatom biomass (log scale, mmol C $m^{-3}$) during (a) April-June and (b) October-December 2000 (Falciatore et al., 2019). Simulated using the MIT Darwin Model. (b) Map of High Nutrient–Low Chlorophyll (HNLC) regions around the world. Measurement in map is of nitrate, with the scale as a gradient of colour pictured on the bottom (Mock & Thomas, 2008)**

Diatoms are a diverse class of photosynthetic, autotrophic single-celled algae that are extensively distributed across a variety of habitats, ranging from oceans, lakes, and rivers to moist soils (Petersen, 1928) and subterranean environments (Falasco et al., 2014; Falciatore et al., 2019) In the global oceans, they dominate phytoplankton communities across diverse biogeochemical provinces, with their highest concentrations occurring in nutrient-rich high-latitude and upwelling regions (Marañón et al., 2013) (Figure 1.3). They represent the most diverse phytoplankton class in the contemporary ocean, with an estimated 100,000 species globally (Malviya et al., 2016; Mann & Vanormelingen, 2013).

The origin of diatoms could be traced back to a significant symbiotic event approximately 1.5 billion years ago, when a heterotrophic eukaryotic cell captured the green alga and red alga (Figure 1.4), an event that profoundly shaped their

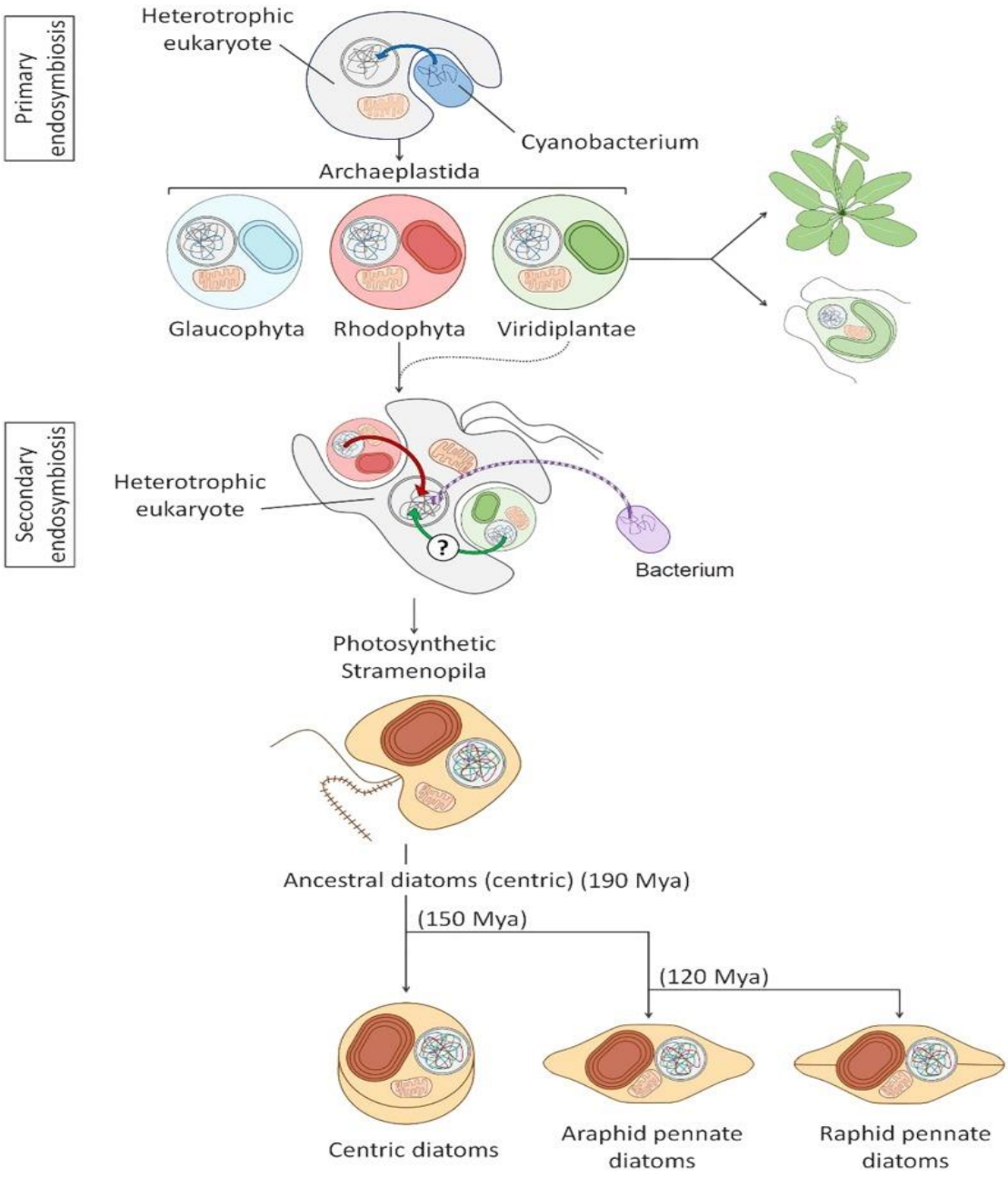


**Figure 1.4 Diagram of diatom evolution through primary and secondary endosymbiosis (Falciatore et al., 2019).**

evolutionary trajectory (Falciatore et al., 2019; Falkowski et al., 2004). This endosymbiotic relationship gave rise to the complex plastids that are a hallmark of diatoms today, eventually diversifying into an extensive array of forms now categorized into two primary morphological classes: the centric diatoms (Coscinodiscophyceae), the pennate without raphe (Fragilariophyceae), and pennate with a raphe (Bacillariophyceae) (Fu et al., 2022). Approximately 100 million years

ago, diatoms quickly rose to prominence in marine environments due to their unique evolutionary status and distinctive adaptation mechanisms (Armbrust, 2009). Throughout their evolutionary history, diatoms have continuously adapted to new ecological niches, making them one of the most successful phytoplankton in the ocean. Their ability to efficiently harness solar energy for photosynthesis, coupled with their specialised siliceous cell walls and nutrient uptake strategies have enabled them to thrive in diverse marine settings and dominate the phytoplankton community (Behrenfeld et al., 2021; Litchman et al., 2007).

Diatoms primarily reproduce asexually, dividing into two cells where the original silicified cell walls split to form one larger and one smaller daughter cell (Figure 1.5a). After several cycles of such divisions, the size of the daughter cells becomes significantly smaller than the original parent cell. At this point, diatoms switch to sexual reproduction to restore the size of the original mother cell (Figure 1.5b) (Poulíčková et al., 2019). In environments with limited resources, diatoms can enter a

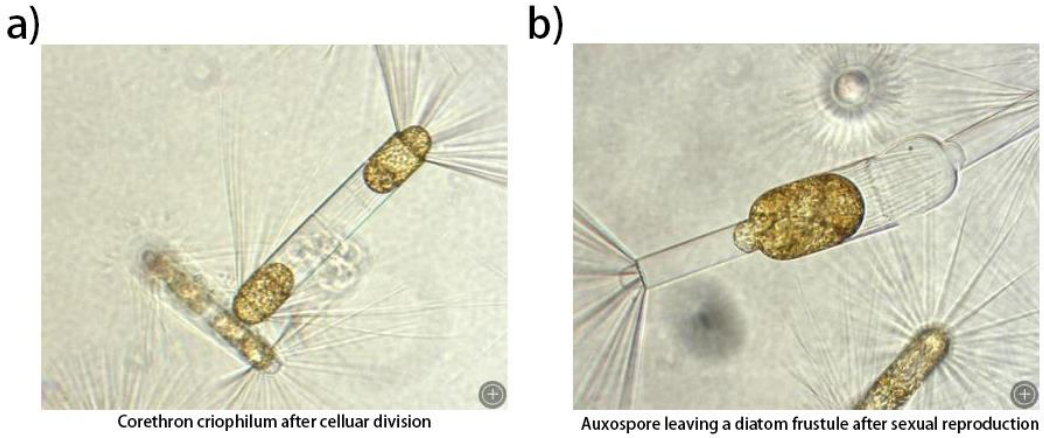


**Figure 1.5 Images demonstrate the (a) asexual reproduction and (b) sexual reproduction of diatom *Corethron criophilum* from Southern Ocean (Vernet, 2009). Images were taken by an optical microscope.**

dormant state, forming resting spores or cells that can survive even thousands of years of adverse conditions (Sanyal et al., 2022; Sugie & Kuma, 2008; Wang et al., 2024). When environmental conditions become favourable again, these dormant spores or

cells can germinate,  reverting to active vegetative cells (Davis & Hildebrand, 2008). This adaptive strategy allows diatoms to efficiently manage their life cycles in response to fluctuating environmental conditions, ensuring their survival and continued success in diverse habitats.

Diatoms exhibit a remarkable size range, spanning almost nine orders of magnitude, from a few micrometres to several millimetres in cell diameter (Litchman et al., 2009). Most diatoms are planktonic, floating freely in the water column, while others are benthic, adhering to various substrates (Fu et al., 2022). As one of the most abundant and ecologically significant groups in marine environments, diatoms play a crucial role in the global carbon cycle. They convert inorganic carbon into organic carbon through photosynthesis, a process powered by solar energy. (Sethi et al., 2020).  Diatoms are responsible for more than 20% of the global primary productivity and up to 40% of the marine primary productivity, significantly influencing the biogeochemical dynamics of the world's oceans (Granum et al., 2005; Roberts et al., 2007). They contribute approximately half of the organic carbon to the oceanic carbon pool, an essential process for the regulation of atmospheric CO2 and global climate (Jin et al., 2006; Smetacek, 1999).

Furthermore, diatoms are central to the production of biogenic silica, utilising silicic acid from their environment to construct their characteristic siliceous cell walls. This not only provides them with structural integrity but also facilitates their role in the silica cycle, which is crucial for maintaining marine ecosystem function (Yool & Tyrrell, 2003). Critically, their dense silicate shells enhance carbon export efficiency via the ballast effect – accelerating particle sinking rates and reducing organic carbon remineralization in surface waters (Armstrong et al., 2001; Tréguer et al., 2018). Diatoms also participate actively in the broader geochemical cycles of phosphorus, and nitrogen (Paytan & McLaughlin, 2007; Zehr & Ward, 2002) . The ecological importance of diatoms extends beyond all these geochemical cycling as they are a

fundamental component of the marine food web, serving as a primary food source for marine zooplankton and forming a significant part of the diet for many fish and shellfish species (Russo et al., 2018). Considering that diatom cells are rich in fatty acids, proteins, amino acids, and various bioactive substances (Li et al., 2014), making them valuable as aquaculture feed, pharmaceutical resources, and bioenergy materials (Bhattacharjya et al., 2024; Savio et al., 2020; Sharma et al., 2021). Thus, diatoms hold significant fisheries and economic value and play a pivotal role in the biogeochemical cycling of elements and energy transfer globally, which is essential in mitigating climate change (Fu et al., 2022) .

Overall, by understanding the broad ecological roles and evolutionary history of diatoms, we can better appreciate their significance in marine ecosystems and their potential applications in addressing environmental and economic challenges. This expanded understanding also sets the stage for exploring specific physiological and biochemical mechanisms within diatoms, which may hold the key to unlocking new technologies and strategies for environmental sustainability.

**Photosynthetic processes**

Photosynthesis stands as one of the most crucial biochemical processes on Earth, fundamentally defined as the light-driven synthesis of ATP and reducing power (NADPH) required for carbon fixation. This process transforms solar energy into chemical energy, thus fuelling a vast array of life forms.

This process, primarily oxygenic in nature, harnesses solar energy to synthesise glucose and oxygen, indispensable for marine and terrestrial ecosystems. By using water as an electron donor, photosynthesis not only sustains individual organisms but also supports complex ecological networks (Fleming & Grondelle, 1994).

In contrast, photoheterotrophy describes a metabolic strategy where organisms use light to generate ATP but cannot fix $CO_2$, instead requiring organic carbon sources for

biosynthesis (Béjà et al., 2000).

The initiation of light reactions occurs when photons are harvested by the photosynthetic apparatus within the thylakoid membranes of chloroplasts. Specialised molecules such as chlorophylls and accessory pigments like carotenes and phycobilins absorb the photons (Simkin et al., 2022). The absorbed energy is then transferred to reaction centres containing P680 and P700 chlorophyll molecules. This excitation triggers a cascade of electron transfers crucial for subsequent biochemical reactions. The organisation of these reactions into photosystem I (PSI) and photosystem II (PSII), exemplifies the Z-scheme, which efficiently converts light energy into chemical energy stored as adenosine triphosphate (ATP) and nicotinamide adenine dinucleotide phosphate (NADPH) (Johnson, 2016) (Figure 1.6). In PSII, photon energy excites P680, which oxidises water into oxygen, protons, and electrons. Plastoquinone (PQ) and the cytochrome b6/f complex (Cyt) transfer these electrons to plastocyanin (PC), the direct electron donor to PSI. PQ also transfers protons from the stromal side of the thylakoid to the lumen (Arnon, 1971; Zehr & Kudela, 2009).

In PSI, P700 is excited either by resonance energy transfer through photosynthetic antenna pigments or direct photon energy. P700 then draws electrons from plastocyanin and passes them to ferredoxin, a strong reductant that reduces NADP+ to NADPH on the stromal side of the thylakoid(Brettel, 1997). The breakdown of water and proton transport by PQ creates a higher proton concentration in the thylakoid

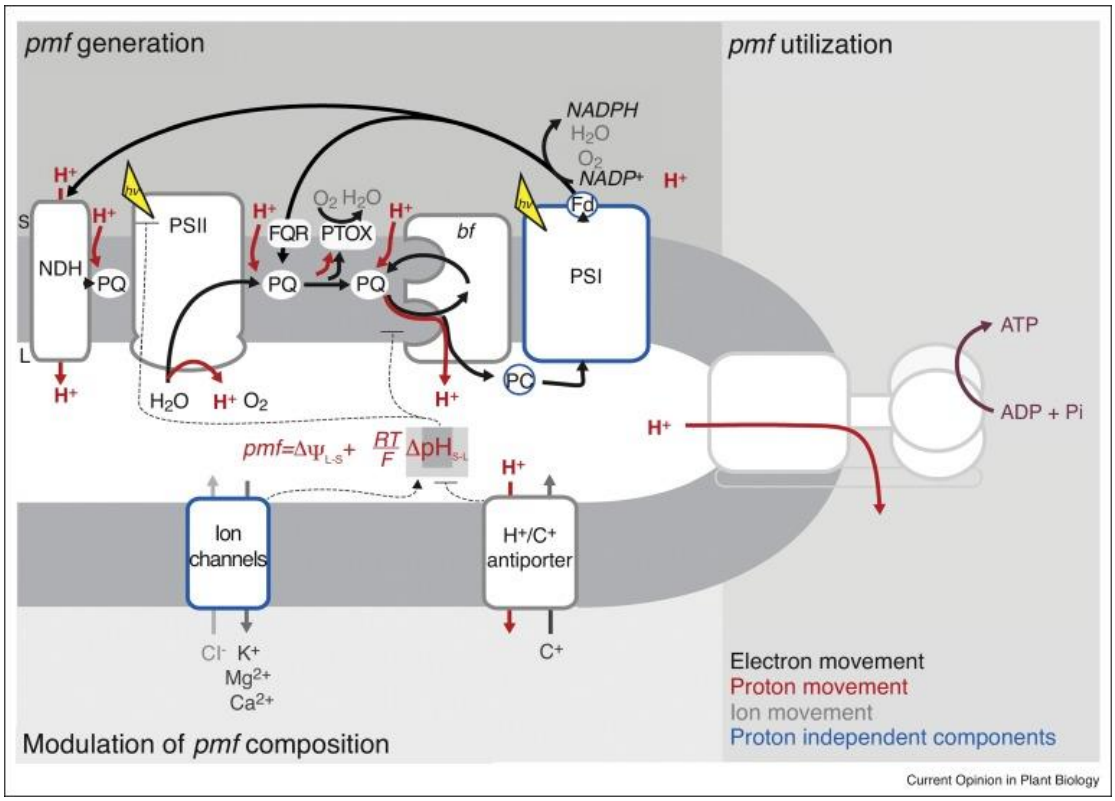


**Figure 1.6 The process of photosynthesis and PMF production. (Armbruster et al., 2017)**

lumen than in the stroma, inducing a proton motive force (PMF) (Armbruster et al., 2017). This PMF drives protons through ATP synthase to synthesize ATP outside the thylakoid membrane as part of cellular respiration (Figure 1.6).

In summary, photosynthesis provides essential energy (ATP) and reductants (NADPH) for autotrophic carbon fixation. Cellular respiration subsequently utilises these products to maintain metabolic functions. Photoheterotrophs supplement this process by using light-derived ATP to metabolise organic carbon. Limitations in photosynthesis directly constrain primary production and ecosystem function.

**The use of iron by diatoms**

Diatoms are significantly affected by iron availability in the ocean. Large-scale in-situ iron fertilisation experiments in High Nutrient, Low Chlorophyll (HNLC) regions have demonstrated that introducing iron can rapidly induce phytoplankton blooms with a shift in the phytoplankton community composition from cyanobacteria and dinoflagellates to diatoms (Martin & Fitzwater, 1988; Martin et al., 1989). This shift suggests that diatoms possess unique physiological mechanisms allowing them to efficiently utilise environmental iron, a trait they have developed through long-term evolution adaptation to low-iron conditions. Consequently, the relationship between diatoms and iron has become a prominent research focus in phytoplankton evolution.

Iron is an essential metal element for most organisms due to its property to oxidise and reduce easily. In various metalloproteins, iron exists as heme or iron-sulfur clusters and participates in numerous metabolic pathways (Galaris et al., 2019). It is the most abundant metal element in the photosynthetic system, particularly crucial for oxygen-producing photosynthetic organisms: there are twelve and three iron complexes or proteins in the two photosynthetic reaction centres PSI and PSII, respectively (Figure 1.7) (Raven, 1990). Meanwhile, the cytochrome (Cyt) *b6f* complex contains five iron ions and the chloroplast electron transport chain protein, ferredoxin, contains two iron ions (Raven, 1990).

Therefore, under the iron limitation, the photosynthetic system of phytoplankton is the first to be influenced, shown by reduced synthesis of photosynthetic pigments and pigment-binding proteins, decreased chlorophyll content, damage to photosystem reaction centres, and reduced photosynthetic electron transport efficiency (Behrenfeld & Milligan, 2013). Consequently, the limitation of the light reaction caused by iron limitation will further restrict the carbon fixation process. Compared to iron-sufficient cells, the carbon fixation rate of iron-limited diatom cells can decrease by 14-fold

(Allen et al., 2008).

Besides, iron also plays a key role in nutrient metabolism (Figure 1.8). As for nitrogen

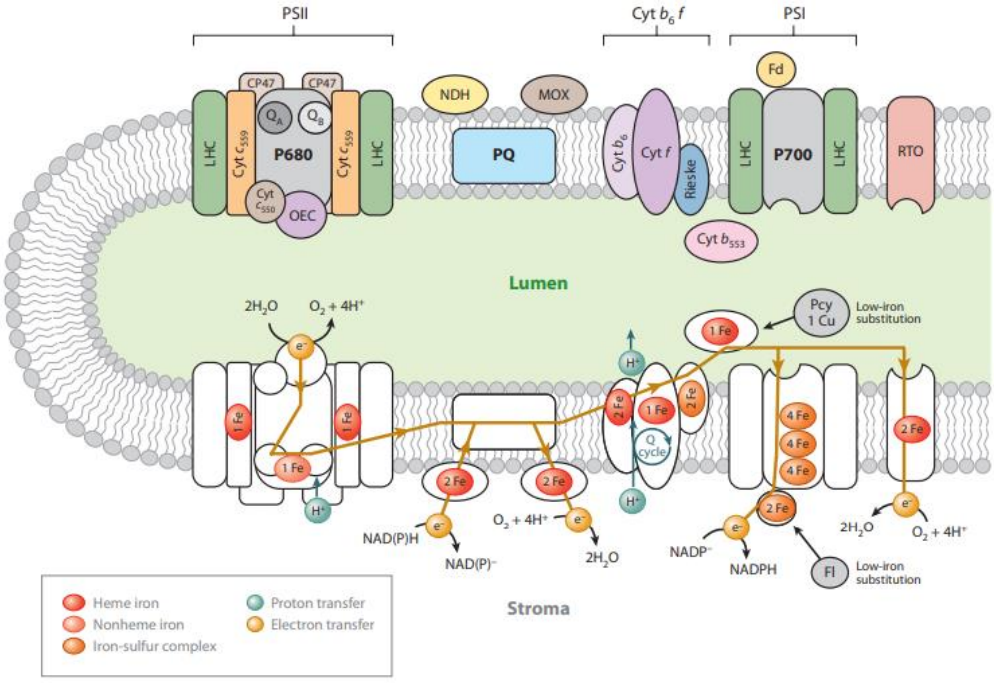


**Figure 1.7 Diatom Thylakoid membrane architecture, iron requirements, and primary electron/proton transport pathways in photosynthesis (Behrenfeld & Milligan, 2013).**

assimilation, nitrate reductase (NR) and nitrite reductase (NiR) are required to assimilate the nitrate and nitrite into ammonium in diatom and phytoplankton, which contain one iron atom and 5-6 iron atoms, respectively (Milligan & Harrison, 2000; Raven, 1990). Under iron deficiency, the enzyme activity of NiR in diatoms can decrease by as much as 50 times, severely inhibiting the assimilation of NO2 (Milligan & Harrison, 2000). Under iron-limited conditions, cells grow faster with $NO_3^-$ than $NH_4^+$, contrary to theoretical calculations that cell $NO_3^-$ should require more iron than those on $NH_4^+$ (Raven, 1988). This difference may arise from iron limitation severely influencing photosynthesis, resulting in insufficient energy for growth and masking nitrogen source differences caused by nitrogen sources (Maldonado & Price, 1996; Price et al., 1991). This suggests that the photosystem is the most severely impacted component under iron-limited conditions, even though

nitrogen assimilation is also affected, leading to the influences on cell growth.

Additionally, iron plays a critical role in the nitrogen fixation process, essential for converting atmospheric nitrogen into biologically available ammonium. The enzyme nitrogenase complex, which catalyses this conversion, is the most iron-rich enzyme (Whittaker et al., 2011). It comprises two iron-containing proteins, each having a 4Fe-4S cluster and a larger dimeric MoFe protein that contains 30 iron atoms, bringing the total to 38 iron atoms in each complex (Whittaker et al., 2011). Nitrogen fixation is also energy intensive, requiring substantial amounts of ATP and NADPH (Kustka et al., 2003). These energy molecules are largely provided by photosynthesis, which is heavily dependent on iron, thus linking the demand for iron in photosynthesis and

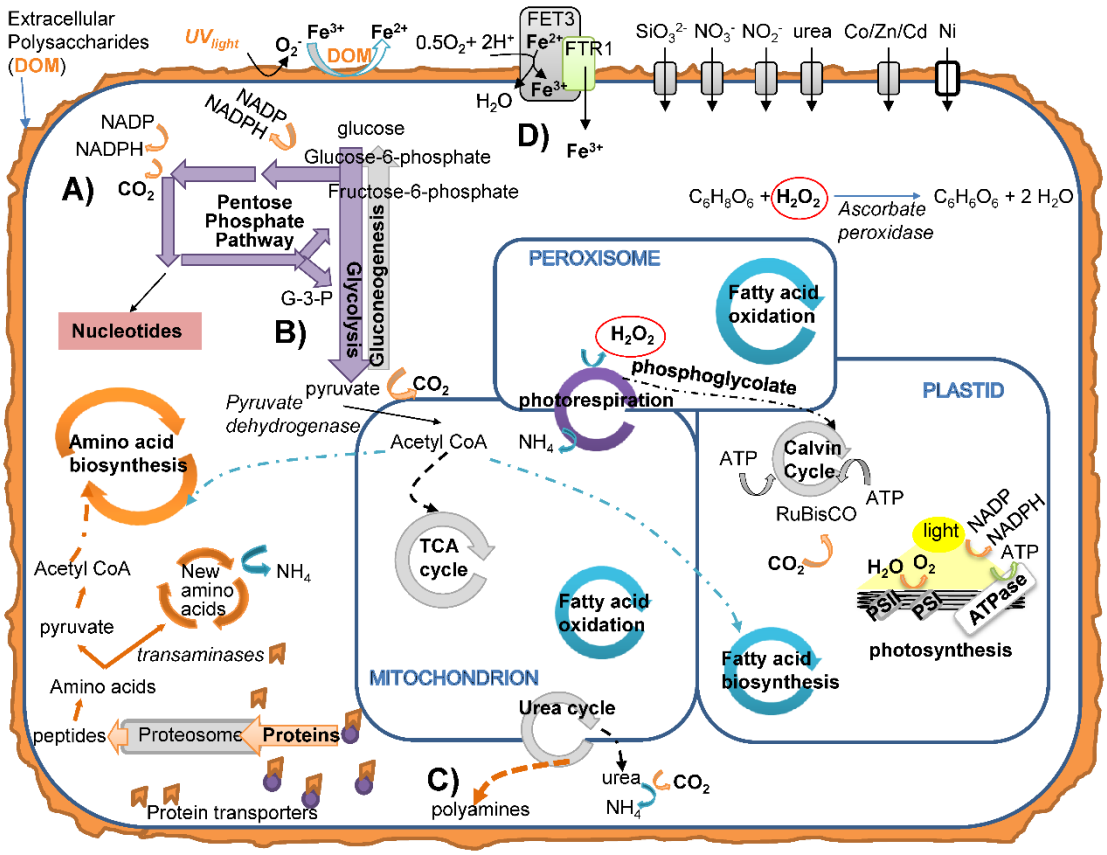


**Figure 1.8 Diatom cell biochemistry under Fe-limitation conditions.** Black and grey pathways and proteins represent those active during Fe-limitation, while white proteins indicate significantly down-regulated proteins. Coloured pathways highlight those that were significantly up-regulated in Fe-limited cells compared to Fe-replete cells (Nunn et al., 2013).

nitrogen fixation. Thus, in many marine environments, even if iron availability does not directly limit the growth rate of nitrogen-fixing organisms, it can still influence the overall nitrogen fixation rate. This reduces the supply of newly fixed nitrogen (primarily bioavailable ammonium, $NH_4^+$), ultimately limiting the availability of inorganic nitrogen substrates (nitrate, $NO_3^-$ and ammonium, $NH_4^+$) for phytoplankton communities (Capone et al., 2005; Moore et al., 2009; Zehr & Ward, 2002).

Iron also has a close relationship with silicon metabolisms in diatom cells. Research by Mock et al. (2008) shows that a quarter of the genes upregulated in *Thalassiosira pseudonana* under silicon limitation are also induced by iron limitation, suggesting co-regulation of these nutrient pathways. Critically, under iron-deficient conditions, diatoms exhibit significant shifts in elemental stoichiometry, characterized by decreased cellular iron quotas and increased silicon assimilation efficiency. This results in a higher Si : Fe ratio (2000:1) in Fe-limited zones where the ratio is only about 200:1 in replete conditions, and enhanced biogenic silica production per cell (Pichevin et al., 2014). Field and laboratory experiments confirm that iron limitation reduces diatom growth rates but simultaneously upregulates silicification genes, leading to morphological variations and higher Si : C and Si : N ratios (Meyerink et al., 2017). Although definitive evidence of a relationship between genes involved in iron and silicon metabolism is still lacking, the complexity of their interaction suggests a positive correlation between these pathways (Mock et al., 2008).

Iron is critical for properly functioning mitochondrial respiration through its role in key components such as alternative oxidase (AOX). It helps maintain redox balance, supports photosynthetic activity, and mitigates oxidative stress (Murik et al., 2019). Iron limitation leads to increased reactive oxygen species (ROS) and reduced efficiency in photosynthetic and respiratory processes, it also reduces the expression of genes associated with mitochondrial respiration, thereby inhibiting the activity of the respiratory electron transport chain in diatom *P. tricornutum* (Allen et al., 2008;

Murik et al., 2019). These results demonstrate the interconnectedness of iron availability, mitochondrial function, and overall cellular health in diatoms. Additionally, in cells, iron is involved in several other important processes, including the synthesis of vitamins and fatty acids. These roles indicate that iron plays a crucial role in maintaining cellular health and functionality (Wolfe-Simon et al., 2005).

Overall, iron, as an essential element, is involved in many physiological processes, such as photosynthesis, respiration, nitrogen assimilation, nitrogen fixation, and silicon metabolisms, making it an important metal element for diatoms. As the main phytoplankton widely distributed in HNLC regions, diatoms have unique adaptation mechanisms to low-iron environments.

Diatoms often adapt to low light and various nutrient limitations by reducing their cell size (Sunda & Huntsman, 1997). A reduction in cell volume is particularly advantageous for cells living in a low Fe environment because it not only reduces sinking rates but also reduces cellular requirements for N, C, and Fe (Muggli et al., 1996). Smaller cells possess a higher surface-area-to-volume ratio, which maximises the exchange rate on the membrane. In iron-deficient regions, species with smaller cell volumes often dominate(Sunda & Huntsman, 1997). Research has shown that the cell volume of some microalgae can decrease by 20-46% under such conditions (Muggli et al., 1996). These findings suggest that smaller cells have a competitive advantage in securing iron (Marchetti & Harrison, 2007; Sunda & Huntsman, 1997). However, the structure of cell walls in some cells may limit this change, allowing a small number of larger cells to persist in iron-limited regions over the long term. Interestingly, certain diatoms, such as *Proboscia inermis* and *Eucampia antarctica*, respond to iron limitation by increasing their size rather than becoming more heavily silicified (Meyerink et al., 2017). This adaptation strategy may be related to factors like nutrient storage and robust periodic vertical migration capabilities, indicating that large cell volumes can also adapt to environments with low iron availability

(Smetacek et al., 2004).

Another strategy that diatoms have developed is adjusting the relative content of photosystem complexes. Under iron limitation, diatom tends to downregulate the PSI concentration (Strzepek et al., 2019). The oceanic diatoms have five times lower photosystem I and up to seven times lower Cyt *b6f* complex concentrations than coastal diatoms, such as *Thalassiosira oceanica*, a diatom that thrives in long-term iron-limited region, has evolved to maintain its PSII:PSI ratio at around 10:1 while also reducing the concentration of the Cyt *b6f* complex (Figure 1.9) (Strzepek & Harrison, 2004). This adjustment allows *T. oceanica* to significantly reduce its iron requirement while maintaining an efficient photosynthetic rate, making *T. oceanica* grow better than coastal diatoms under iron-deficient conditions. Besides, researchers compared the transcriptomes and proteomes of *Pseudo-nitzschia granii* and

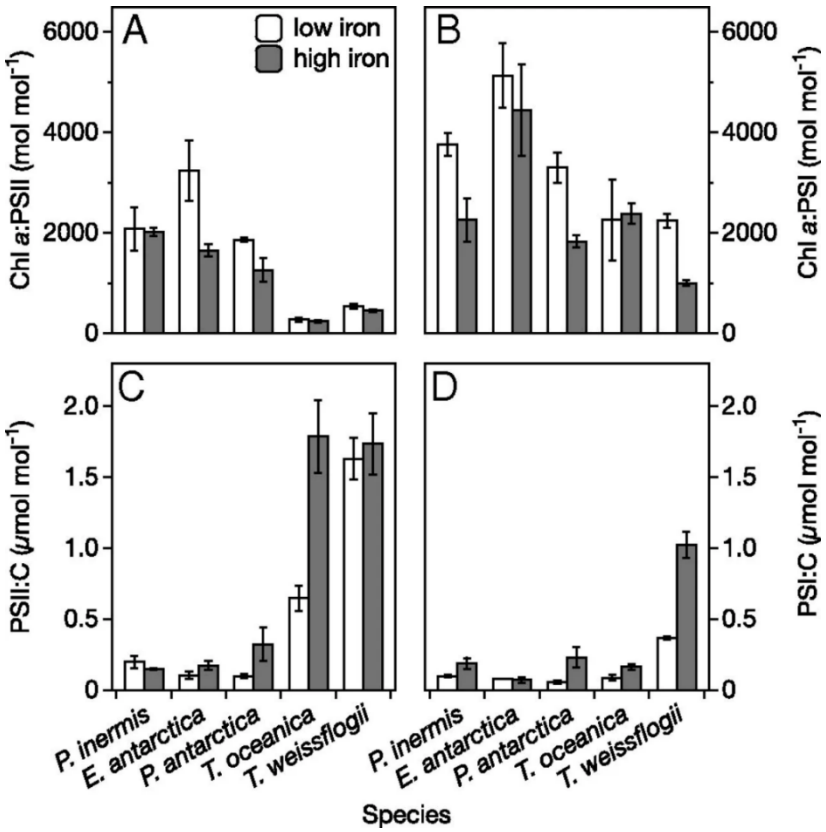


**Figure 1.9 Ratios of cellular chlorophyll a (Chl a) to PSII (A), cellular Chl a to PSI (B), PSII to cellular carbon (C), and PSI to cellular carbon (D) across different iron conditions and species.** Iron repletion shown in dark bar and iron limitation shown in white bar (Strzepek et al., 2019).

*Fragilariopsis cylindrus* from the Southern Ocean (Cohen, Gong, et al., 2018). Their findings revealed similar phenomena, indicating that diatoms inhabiting long-term iron-limited environments adapt by restructuring their photosystems.

Another important mechanism of diatoms respond to iron limitation is replacing iron-rich essential proteins with functional similar proteins that do not require iron as a cofactor or substituting iron-containing proteins with others that incorporate more readily available redox-active trace metals (Gao et al., 2021). Such as iron-free flavodoxin (FLDA), which replaces iron-rich ferredoxin (PETF) for a similar function in the chloroplast electron transport chain (Sétif, 2001). Another effective substitution strategy diatoms under iron limitation use is replacing iron-rich Cyt *c6* protein with copper-containing protein plastocyanin (PETE). Plastocyanin and cytochrome c6 perform similar roles in electron transport within the chloroplast, facilitating the transfer of electrons between the Cyt *b6f* and PSI. However, plastocyanin uses copper as its central metal cofactor instead of iron to reduce the iron demand (Peers & Price, 2006).

Diatoms' ability to dominate in HNLC regions is also supported by their effective mechanisms for iron storage and regulation of intracellular iron concentrations. Currently, two methods of iron storage have been discovered in diatoms: storing iron in a mineralised form within ferritin (FTN) and storing it in vacuoles (Theil, 1987). The FTN can store up to 4,500 insoluble oxidised iron to release $Fe^{2+}$ when the cell needs it (Liu & Theil, 2005). Marine diatoms living in long-term iron-deficient conditions will upregulate ferritin expression in iron-rich environments to increase iron storage. Once iron deficiency occurs, diatoms use the iron stored in ferritin to sustain cell growth and reproduction (Cohen, Mann, et al., 2018; Marchetti et al., 2009). Additionally, the function of ferritin in diatoms is not only to store long-term iron but also to play a crucial role in rapidly buffering intracellular free iron. This capability is vital for photosynthetic organisms, as it helps to prevent the potential

toxicity of free iron while ensuring an immediate supply of iron for essential metabolic processes (Pfaffen et al., 2015). Additionally, recent research suggests that iron starvation-induced proteins (ISIPs) may also function in intracellular iron storage (Behnke & LaRoche, 2020; Kazamia et al., 2018). The expression of ISIPs are significantly upregulated under iron-deficient conditions (Allen et al., 2008).

A proposed alternative mechanism for long-term iron storage is the vacuole. The process of loading and releasing iron into and from vacuoles was first identified in yeast and is mediated by natural resistance-associated macrophage proteins (NRAMPs) in Arabidopsis (Curie et al., 2000; Lanquar et al., 2005). In synchrotron X-ray fluorescence elemental mapping experiments, intracellular iron pockets indicative of storage characteristics were identified in *T. pseudonana* and *T. weissflogii* (Nuester et al., 2012). These studies suggest that vacuoles may play a significant role in iron storage and regulation, further illustrating the complex mechanisms diatoms employ to cope with iron limitation.

Overall, iron is an essential nutrient for diatom growth and plays a critical role in various metabolic processes. Although iron is limited in most diatoms' living regions, substantial evidence suggests that diatoms, as a group, can successfully compete for iron and often dominate phytoplankton blooms stimulated by iron. Studies show that diatoms employ various strategies to acquire different forms of iron in the ocean. These strategies collectively give diatoms a significant survival and competitive advantage in iron-limited environments, explaining their dominance in HNLC regions. Through these complex and efficient iron acquisition and utilisation mechanisms, diatoms can not only cope with environmental iron limitations but also maintain their crucial role in the phytoplankton ecosystem.

## Rhodopsin

### Introduction

Rhodopsins are a diverse group of light-absorbing pigment proteins integral to various organisms' membranes with about 26 kDA (Oesterhelt & Stoeckenius, 1973). Rhodopsins consist of seven transmembrane α-helices, which form the structural framework necessary for their function in light detection and energy conversion (Pechkova et al., 2014).

These proteins covalently bind to a chromophore called retinal through a protonated Schiff base linked to a lysine residue (Lys) located on the G helix (Bayley et al., 1981). This binding is crucial for the protein's ability to perform its light-related functions. As an unsaturated aldehyde, retinal plays a key role as it can absorb specific wavelengths of light, which initiates the photochemical reaction necessary for rhodopsins function. When photons are absorbed, retinal undergoes isomerisation, triggering a series of conformational changes in the opsin protein, ultimately leading

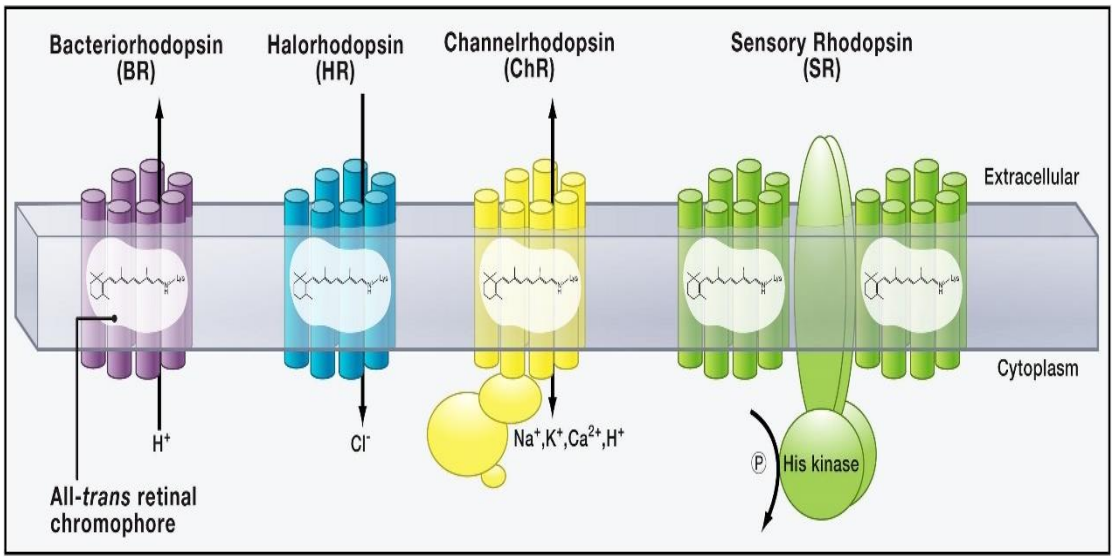


**Figure 1.10 Four different type I microbial rhodopsins (Zhang et al., 2011). This schematic illustrates four major subtypes of Type I (microbial) rhodopsins, each embedded in the cell membrane and containing a covalently bound all-trans retinal chromophore (shown in the center of each protein). These rhodopsins use light energy to drive various physiological functions.**

to ion transport or the transmission of optical signals (Man et al., 2003).

| Name / Term | Definition / Function | When and Why to Use This Term |
|---|---|---|
| **Rhodopsin** | General term for light-sensitive membrane proteins with seven α-helices and a retinal chromophore. | Use when referring broadly to all retinal-binding, light-sensitive proteins, without distinguishing between types. |
| **Microbial Rhodopsin** | Type I rhodopsins found in prokaryotes and some eukaryotes, involved in light-driven ion transport or signal transduction. | Use when discussing the evolutionary or ecological role of light-driven energy systems in marine microbes or phytoplankton and before determining the FR1/FR2 classification. |
| **Type I Rhodopsin** | Also called microbial rhodopsin; includes bacteriorhodopsin, halorhodopsin, channelrhodopsin, sensory rhodopsin, proteorhodopsin, etc. | Use in comparative structural/functional discussions between Type I and Type II rhodopsins. |
| **Type II Rhodopsin** | Rhodopsins found in animals (e.g., vertebrate visual pigments); G-protein-coupled receptors (GPCRs). | Use only for contrast with Type I rhodopsins, especially when explaining classification and evolutionary divergence. |
| **Bacteriorhodopsin (BR)** | Classic light-driven proton pump from Halobacterium salinarum; creates a proton gradient for ATP synthesis. | Use when comparing with FR1/FR2 proton pump activity or discussing model systems for microbial rhodopsin function. |
| **Halorhodopsin (HR)** | Chloride pump from halophilic archaea. | Mention when describing diversity of microbial rhodopsin ion transport modes. |
| **Sensory Rhodopsin (SR)** | Rhodopsins coupled with transducers to mediate light-based behavior changes. | Use when discussing rhodopsins with non-ion-pumping signaling functions, especially in prokaryotes. |
| **Channelrhodopsin (ChR)** | Light-gated cation channels found in algae; allow passive ion flow (e.g., $H^+$, $Na^+$, $K^+$, $Ca^{2+}$). | Mention as contrast to active pumps; useful in optogenetics, also for function comparison with diatom rhodopsins. |
| **Proteorhodopsin (PR)** | Marine bacterial proton pump; absorbs blue or green light; ecologically widespread. | Use when discussing marine microbial light-utilizing mechanisms in bacteria or comparison to algal rhodopsins. |
| **Proton-pump rhodopsins** | General term for rhodopsins with the ability to undergo light-driven proton transmembrane. | Used to explain their energy conversion mechanism and before determining the FR1/FR2 classification (refer to FR1/FR2). |
| **Xanthorhodopsin (XR)** | Proton-pumping rhodopsin with a carotenoid antenna (e.g., salinixanthin) that enhances light capture. First discovered in *Salinibacter ruber*. | Use when referring to rhodopsins with dual chromophores and enhanced light-harvesting ability; crucial term in the context of FR1/FR2 characterisation. |
| **FR1 / FR2** | Diatom xanthorhodopsin variants found in *Fragilariopsis cylindrus*; light-driven proton pumps. | Use throughout the thesis when discussing your core research targets; preferred for experiments and functional studies involving engineered diatoms. |
| **Diatom Rhodopsin** | General term for rhodopsins found in diatoms; may include xanthorhodopsin and other yet-to-be-classified variants. | Use when referring to the diversity or presence of rhodopsins in diatoms in a general or evolutionary context. |
| **Microbial Rhodopsin FR1** | Specific proton-pumping diatom xanthorhodopsin variant characterised in this study. | Use when highlighting specific findings and physiological implications of FR1 expression in *T. pseudonana* or *N. putrida*. |
| **Eukaryotic Microbial Rhodopsin** | Microbial rhodopsins found in eukaryotic phytoplankton, such as diatoms and dinoflagellates. | Use when distinguishing from bacterial/archaeal rhodopsins and highlighting rhodopsin function in eukaryotic photosynthetic lineages. |

**Table 1.1 Overview of rhodopsin types mentioned in this thesis and their recommended usage context.**

They are typically divided into two categories: Type I and Type II (Table 1.1). Type I

rhodopsins were initially identified in the halophilic archaea *Halobacterium salinarum*. Four different rhodopsins were found in *H. salinarum* including bacteriorhodopsin (BR as proton pump) and halorhodopsin (HR as chloride pump), along with two types of sensory rhodopsins (SR I and SR II) (Grigorieff et al., 1996; Hoff et al., 1997) (Figure 1.10). On the other hand, Type II rhodopsins, also known as animal-type rhodopsins, are common in higher eukaryotes. These include the visual pigments found in the eyes of animals, specifically in the rod and cone cells of humans, and are also present in the pineal gland and thalamus of some lower vertebrates (Spudich et al., 2000).

Among the diverse types of functional rhodopsins, proton pump rhodopsins are particularly notable. These proteins create a proton gradient across cellular membranes, a process that is crucial for several biological metabolisms, including the production of ATP, the energy currency of the cell, which supports numerous metabolic activities (Höhner et al., 2016).

Besides the BR proton pump, recent studies have unveiled significant findings about rhodopsins, particularly the discovery of a gene encoding a protein similar to bacteriorhodopsin in marine microbial DNA, later named proteorhodopsin (PR). This protein, identified by Béjà et al. (2000), shares about 30% homology with bacteriorhodopsin and is predominantly found in α-Proteobacteria, γ-Proteobacteria, and Bacteroidetes (Béjà et al., 2000; de la Torre et al., 2003). Further research has categorised PR into two types based on their light absorption properties: blue-light-absorbing and green-light-absorbing PR, each having distinct ecological roles (Wang et al., 2003). PR exhibits high genetic mobility and is prevalent in diverse aquatic environments, from freshwater to marine settings. PR has been detected in locations such as the Pacific's Hawaiian HOT station, the Red Sea, and the Mediterranean (Béjà et al., 2001; Sabehi et al., 2003). Moreover, recent findings highlight the presence of PR or BR-like rhodopsin in various eukaryotic species, including diatoms,

dinoflagellates, and cryptomonads, where it directly converts light energy into chemical energy, supplying essential energy for cellular functions (Marchetti et al., 2015; Slamovits et al., 2011).

Another homologous rhodopsin, xanthorhodopsin, is an intriguing retinal protein-carotenoid complex identified in the extreme halophile *Salinibacter ruber* (Balashov et al., 2005). Like bacteriorhodopsin, xanthorhodopsin functions as a light-driven proton pump; however, it is uniquely characterised by the presence of a carotenoid antenna, specifically salinixanthin, which plays a critical role in enhancing its photochemical efficiency (Balashov et al., 2005). This complex enhances light absorption and energy transfer efficiencies, significantly broadening the operational wavelength spectrum for more effective proton transport across cell membranes (Lanyi & Balashov, 2008). The unique architecture of xanthorhodopsin allows for a high degree of interaction between salinixanthin and retinal, facilitating efficient energy transfer, which is critical for its function in the highly saline environments where *S. ruber* thrives (Balashov et al., 2005). Recent studies found that the xanthorhodopsin family is not only in the bacteria and archaea but also widely distributed across diverse marine algae, including dinoflagellates, haptophytes, and diatoms (Lin et al., 2010; Marchetti et al., 2012; Mock et al., 2017; Slamovits et al., 2011; Strauss et al., 2023). In summary, microbial rhodopsins are prevalent across a wide range of organisms, and their light-driven proton pump mechanisms have significant potential impacts on marine ecosystems. However, accurately estimating the contribution of microbial rhodopsins to these ecosystems is challenging. Consequently, further research is essential to explore various aspects of microbial rhodopsins, including their ecological roles and functional mechanisms.

**The role of microbial rhodopsins in the marine ecosystem**

When marine microbial rhodopsins were first discovered, it was hypothesised that they might support a photoheterotrophic lifestyle or represent an unrecognised form of

marine photoautotroph (Béjà et al., 2000). Both possibilities suggest an unrecognized phototrophic pathway that could significantly impact global carbon and energy fluxes in marine ecosystems. Rhodopsins have numerous potential roles in growth strategies and energy acquisition for various microbial groups (Martinez et al., 2007). By acting as outward cation pumps or inward anion pumps, rhodopsins convert light energy into a proton motive force, synthesising ATP via ATP synthase, providing essential energy for cellular processes (Matsuno-Yagi & Mukohata, 1977; Yoshizawa et al., 2012).

In addition to ATP production, the transmembrane ion gradients generated by proton pumps can drive flagellar rotation or facilitate active ion transport through secondary transport systems (Walter et al., 2007). While the overall contribution of proton pump rhodopsins to energy dynamics in marine ecosystems remains difficult to quantify, many studies suggest they enhance organisms growth, improve starvation survival rates, adjust intercellular pH homeostasis, and increase inorganic carbon fixation (Gómez-Consarnau et al., 2010; Gómez-Consarnau et al., 2007; Lin, 2023; Yoshizawa et al., 2022). These findings suggest that rhodopsins represent an alternative light-driven energy acquisition mechanism, supplementing the long-held assumption that chlorophyll-based photosynthesis is the dominant or exclusive gateway for light energy in marine ecosystems. Thus, this kind of microbial rhodopsin is considered to play an important role in carbon fixation which has important implications for the marine plankton community and the carbon cycle (Giovannoni et al., 2005; Sabehi et al., 2003).

In marine eukaryotic phytoplankton, which has a high demand for iron in photosynthesis, although the detailed mechanisms of how rhodopsins help them thrive have still not been resolved, rhodopsins are suggested to provide an alternative pathway for light energy absorption that does not require trace metal elements such as iron (Raven, 2009). Thus, under low iron conditions, when photosynthesis and ATP production are limited, eukaryotic rhodopsins might supplement or replace the proton

motive force typically generated by ATPase hydrolysis (Slamovits et al., 2011). Although this pathway has not yet been confirmed, some researchers propose that proton-pump rhodopsins might also interact with iron transport or carbon concentrating mechanisms (CCM) (Strauss et al., 2023; Yoshizawa et al., 2022).

Despite these advantages, rhodopsins, compared to chlorophyll-based systems, typically possess a much smaller antenna structure. In chlorophyll-based systems, these antenna complexes significantly increase the effective absorption cross-section of each photosynthetic reaction centre, allowing a single reaction centre to utilise energy from many absorbed photons (Lokstein et al., 2021). In contrast, rhodopsin is a structurally simple light-harvesting protein, composed of a single polypeptide and one retinal chromophore, and typically lacks accessory light-harvesting pigments (Bryant & Frigaard, 2006). As a result, the light-harvesting capacity of rhodopsin is effectively limited to capturing a single photon per molecule. At the level of a single cell or photochemical unit, its photon capture efficiency might be much lower than that of chlorophyll systems. A further limitation of rhodopsin is its narrow absorption spectrum. The absorption wavelengths of most retinal chromophores are concentrated in the blue-green region, typically not exceeding 600 nm (Karasuyama et al., 2018; Lanyi & Balashov, 2008). In contrast, chlorophyll systems can absorb both blue and red light effectively and, with the help of accessory pigments such as chlorophyll b, carotenoids, and phycobilins, extend absorption across the full visible spectrum (Mirkovic et al., 2017). Therefore, the spectral coverage of the chlorophyll system is broader than that of rhodopsin.

These limitations of rhodopsins raise critical questions about their actual contributions to light energy acquisition, especially in complex eukaryotic systems. However, despite growing interest, our understanding of rhodopsins in eukaryotic phytoplankton remains limited. For instance, Guo et al. (2014) found that the expression of rhodopsins in marine dinoflagellates increased under nutrient starvation and light

conditions, leading to higher survival rates than those cultivated without light—similarly, Shi et al. Shi et al. (2015) observed that the expression of rhodopsin genes in the dinoflagellate *Prorocentrum donghaiense* was higher under light conditions than in the dark, indicating a light-dependent regulation of these genes, providing a potential function that similar natural environments such as the surface ocean, the rhodopsin could compensate for the light-harvesting process in case the cells are impaired due to stress conditions such as iron limitation.

As for rhodopsins in diatoms, Marchetti et al. (2012) used comparative metatranscriptome analyses to study gene expression related to iron limitation in diatoms and other eukaryotic plankton from the northeastern Pacific Ocean. Their results showed differential expression of PR genes in diatoms under iron-rich and iron-limited conditions. Additionally, Marchetti et al. (2015) found that rhodopsin gene and protein expressions significantly increased in the marine diatom *Pseudo-nitzschia granii* under iron-limited conditions. These findings suggest that proton-pump rhodopsins in diatoms might produce ATP under iron limitation, indicating a potential adaptive mechanism.

In 2017, genome sequencing of *Fragilariopsis cylindrus* revealed the presence of a bacteria-like rhodopsin, a gene not found in *P. tricornutum* and *Thalassiosira pseudonana* (Mock et al., 2017). According to the research, the *F. cylindrus* rhodopsin (FR) clusters closely with PR in the phylogenetic tree, suggesting it functions as a proton pump. However, like other eukaryotic rhodopsins, the detailed mechanism of diatom rhodopsins remains unclear (Strauss et al., 2023).

Overall, microbial rhodopsins facilitate solar energy conversion and photosensitive transduction in various prokaryotic and eukaryotic microorganisms. They perform multiple functions, including acting as photoreceptors, photo-switches for gene expression, photo-activators, light-driven ion pumps, and light-activated ion channels. Among these, proton pump rhodopsins are particularly significant as they absorb light

and drive the movement of protons across membranes, creating an outward proton gradient that generates a proton motive force for ATP synthesis. Given their crucial role in light energy fixation and energy synthesis, understanding the specific functions of rhodopsins in different phytoplankton is essential. Studying rhodopsins in diatoms could provide valuable insights into the mechanisms behind diatom adaptation to specific environmental conditions.

**Aim of thesis**

To date, little is known about rhodopsins in eukaryotes, especially in diatoms. The recently discovered rhodopsin in the diatom *Fragilariopsis cylindrus* presents an ideal subject for studying its mechanism (Strauss, 2012). Therefore, this thesis aims to use the rhodopsin from *F. cylindrus* to investigate the functional role of rhodopsins in diatoms, focusing on their contribution to energy metabolism and adaptation under nutrient-limited, especially iron-deficient, marine environments. By integrating bioinformatic analyses, molecular biology techniques, and physiological experiments, the research seeks to uncover how rhodopsins, particularly those found in *Fragilariopsis cylindrus* and *Thalassiosira pseudonana*, enhance diatom fitness, growth, and survival.

This thesis aims to clarify the function of microbial rhodopsins in diatoms by utilising several species that do not naturally encode rhodopsin genes, thereby providing an appropriate genetic background for functional characterisation. By employing gene editing techniques, I have knocked in FR derived from *F. cylindrus* into these diatoms, enabling heterologous expression of the FR. I have then investigated the physiological responses of these diatoms under both iron-sufficient and iron-limited conditions. Furthermore, I have employed subcellular-localisation techniques to obtain high-resolution protein localisation images using transmission electron microscope combined with immunogold labelling  Finally, to clarify the specific physiological *in-vivo* functions of rhodopsins independent of photosynthesis in eukaryotes, I have

conducted heterologous expression experiments in the heterotrophic diatom *Nitzschia putrida*, focusing on light-driven proton pumping activity and growth performance under nutrient-limited conditions.

## Outline of PhD thesis

The work presented in this thesis is divided into three major parts:

**Chapter 2, Characterisation of diatom rhodopsins genes:** This part investigates rhodopsin genes in diatoms, with a special emphasis on FR from *Fragilariopsis cylindrus*. This chapter presents how *in silico* structural simulations and multiple sequence alignments have been performed to investigate the evolutionary conservation and potential functional properties of FR-type rhodopsins. In addition, physiological assays have been conducted to examine rhodopsin gene expression levels under various environmental conditions and to evaluate their putative physiological effects. This integrated approach lays the groundwork for understanding the role of rhodopsins in diatom physiology, particularly under environmental stress such as iron limitation.

**Chapter 3**, **Characterisation of diatom microbial rhodopsins and testing the biological role of a selected variant *in vivo*:** This part involves the characterisation and analysis of *T. pseudonana* strains that have been genetically modified to express rhodopsin. The experiments assess these strains' physiological and growth responses under various conditions, particularly focusing on the effects of iron sufficiency and limitation.

**Chapter 4**, **Testing the role of microbial rhodopsins in a heterotrophic eukaryote that possesses a non-photosynthetic plastid:** This part aims to establish a reliable transformation protocol for *Nitzschia putrida*, a newly sequenced heterotrophic diatom. Following successful transformation, an exogenous rhodopsin was introduced

to enable the cells to use light as an additional energy source alongside their native heterotrophic (osmotrophic) metabolism. The success and functionality of the transformation are assessed through a series of molecular and physiological experiments.

Together, these three parts provide insights into the role of rhodopsins in diatom growth and adaptation, contributing to a broader understanding of their functions under different environmental conditions and metabolic modes.

In the final part **chapter 5**, I conclude with a summary of the major findings of the project and a general discussion of all results. Additionally, I outline future research perspectives, highlighting potential directions and areas for further investigation to advance our understanding of rhodopsin's role in diatom adaptation and evolution.

# Chapter 2

# Characterisation of diatom microbial rhodopsin genes

## Introduction

Microbial rhodopsins were initially discovered only in some bacteria and archaea (Béjà et al., 2000; de la Torre et al., 2003; Ma et al., 2023; Oesterhelt & Stoeckenius, 1971). However, more recently, they have been identified in several marine eukaryotes, including dinoflagellates, haptophytes, and cryptophytes. In 2008, Mock et al. discovered the presence of microbial rhodopsin genes in the diatom *Fragilariopsis cylindrus*, where two divergent microbial rhodopsin gene copies, FR1 and FR2, were found (Mock T, 2008). Since then, microbial rhodopsin genes have also been identified in other diatom genomes, such as *Pseudo-nitzschia subcurvata*, *Chaetoceros cf. sociale*, and *Synedra hyperborea* (Andrew et al., 2023). Earlier studies produced by Jan Straus (2012), conducted *in silico* structural comparisons of FR1 with bacterial rhodopsins (BR) and proteorhodopsins (PR), demonstrating a high degree of homology. This suggests that the microbial rhodopsin in *F. cylindrus* may function as a proton pump. However, the exact mechanism and functional role of microbial rhodopsins in *F. cylindrus* remain unclear. Furthermore, as previously mentioned, research on microbial rhodopsins in eukaryotes, particularly diatoms, is still in its infancy. There is a lack of understanding regarding their prevalence in diatoms, as well as the protein's structure and functional roles in these organisms.

In this chapter, I first performed a comprehensive search and analysis of potential microbial rhodopsins in diatoms using the Tara Ocean database. Following this, I analysed the structure and characteristics of microbial rhodopsins in the diatom *Fragilariopsis cylindrus* to establish a theoretical foundation for future research on their specific mechanisms and functional roles. Part of the results in this chapter were generated and helped by cooperators Jan Strauss and Shiqiang Guo, such as the RT-

qPCR, two-electrode voltage clamp, etc. (mentioned in methods part).

# Methods

### Sequence and structure analysis of microbial rhodopsins from *Fragilariopsis cylindrus*

The DNA and protein sequences of rhodopsin FR1 and FR2 were obtained from the JGI *Fragilariopsis cylindrus* CCMP 1102 database (Protein ID: 271123 and 267528 for FR1 and FR2 separately) (Mock et al., 2017). The secondary structure of the protein was predicted using the I-TASSER server, while the tertiary structure was modelled and predicted using AlphaFold2 and Foldseek.

### Collection and comparison of diatom microbial rhodopsin sequences

Raw data were retrieved from the Ocean Gene Atlas (OGA) platform and the Global Ocean Survey project (Vernette et al., 2022; Villar et al., 2018). The search was conducted using the microbial rhodopsin FR1 protein sequence from *Fragilariopsis cylindrus* within the eukaryotic metagenome (MATOU_metaG) of the Marine Atlas of Tara Ocean Unigenes (MATOU) database, focusing on eukaryotic organisms within the size range of 0.8–2000 µm. Based on the 2850 alignment sequence, the maximum likelihood (ML) tree is constructed with iqtree using parameter ‘iqtree -s sequence.fa -m MFP -bb 1000 -nt 4 -pre sequence.iqtree’. The ML tree is then annotated using iTOL (Letunic & Bork, 2024).

Additionally, representative microbial rhodopsin sequences were also collected from UniProt, Pfam and NCBI databases for further analysis. Sequence conservation and Neighbor-Joining tree were visualised using the Uniprot website (https://www.uniprot.org/blast).

### Two-electrode voltage clamp (TEVC) measurement

To investigate whether of the variants FR1 and FR2 function as proton pumps, we expressed each gene individually in *Xenopus* oocytes and performed electrophysiological characterisation using TEVC measurements.

Photocurrents were observed in some *Xenopus* oocytes expressing wild-type FcR1 when illuminated with a 532 nm diode-pumped solid-state (DPSS) laser. Photocurrents were measured 2 to 3 days after injection using either a 530 nm LED (Thorlabs) or a 532 nm DPSS laser (Changchun New Industries Optoelectronics). Light intensities were measured with a PLUS 2 power and energy meter (LaserPoint Srl). All electrophysiological recordings were conducted at room temperature (20–23°C) using a TEVC amplifier (TURBO TEC-05, npi electronic). Details of the bath solutions used during the measurements are provided in the figure legends. Glass electrodes (1.599 mm diameter, 0.178 mm wall thickness, Hilgenberg) filled with 3 M KCl and having tip resistances between 0.2–1 MΩ were used. Data acquisition was performed using a USB-6221 DAQ device (National Instruments) and WinWCP software (v.5.5.3, University of Strathclyde, UK).

Shiqiang Gao did the TEVC experiments at the University of Würzburg with Jan Strauss when he was Postdoc at University of East Anglia. Their electrophysiological characterisation results were used in this thesis to demonstrate the ion transport activity of FR-type rhodopsins.

**Real-time (RT)-qPCR analysis for microbial rhodopsin expressing level under different growth conditions.**

To investigate the *F. cylindrus* microbial rhodopsin gene expression level under different environmental conditions, a two-step RT-qPCR protocol was applied in this project.

First-step cDNA synthesis was performed using a Superscript II reverse transcriptase kit (Invitrogen, US). A total of 500 ng of RNA was reverse transcribed in a 50 µl

reaction at 42°C for 50 minutes, followed by enzyme inactivation at 70°C for 15 minutes. As a control for potential DNA contamination, RNA samples from each biological replicate were pooled and processed in parallel with using water to replace the reverse transcriptase from the reaction. Primers used to amplify target fragments were listed as follows:

| Primer | Sequence | Size |
|---|---|---|
| FcR_555F | GTTACCGTTCCTCTACATTGTCC | 111 |
| FcR_665R | GTCCACCATTGAACACCCTTA | |

For the qPCR reactions, 5 µl of a 10-fold diluted reverse transcription reaction was mixed with 20 µl of 2× SensiMix SYBR Green NoROX master mix (Bioline, UK). Forward and reverse primers were used at a final concentration of 200 nM. Amplifications were conducted in white 96-well plates using the CFX96 real-time system (Bio-Rad, US), with the following thermocycling conditions: an initial denaturation at 95°C for 10 minutes, followed by 40 cycles of amplification consisting of 15 seconds at 95°C, 15 seconds at 59°C, and 10 seconds at 72°C. To verify the specificity of the amplification, a melting curve analysis was performed from 65°C to 95°C in 0.5°C increments, with a 5-second dwell time at each step.The absolute cDNA quantity in each experimental sample was determined using the equation derived from the logarithmic regression of the standard curve, ensuring accurate quantification of gene expression. The RT-qPCR data presented in this chapter were generated by Jan Strauss during his PhD studentship at University of East Anglia. These results are included here to support the analysis of rhodopsin gene expression under different environmental conditions and to provide a broader context for the physiological characterisation carried out in this PhD thesis.

**Subcellular localisation of FR1 in diatoms *Phaeodactylum tricornutum* and *Thalassiosira pseudonana***

The microbial rhodopsin gene from *Fragilariopsis cylindrus* (FR1/FcR1) was cloned into *Phaeodactylum tricornutum* using the expression vector pPha-T1, and into *Thalassiosira pseudonana* using the pTpFCP-GFP/fcpNat vector. Nuclear transformation in both *P. tricornutum* and *T. pseudonana* was carried out following a previously established protocol (Hopes et al., 2017; Poulsen et al., 2006) , utilising a Biolistic PDS-1000/He particle delivery system (Bio-Rad) equipped with 1,350 psi rupture discs. Transformed *P. tricornutum* cells were selected on a 1.2% agar medium containing 75 µg/ml Zeocin, while *T. pseudonana* transformants were selected using 100 µg/ml nourseothricin.

To confirm GFP expression and analyse cell morphology, wide-field fluorescence microscopy was performed using an Axioplan 2 IE imaging microscope (Zeiss) equipped with a CCD Axiocam camera. Chloroplasts were visualized by their natural red autofluorescence of chlorophyll a/c, excited at 562 ± 20 nm using the Alexa568 filter set.

Plasmid construction, transformation, and the initial microscopy work were performed by Jan Strauss. I contributed to the microscopy analysis.

**Action Spectrum Analysis**

A range of light wavelengths was produced using a PhotoFluor II light source (89 North, US) paired with narrowband interference filters (Edmund Optics, US), each providing a distinct wavelength for the experiment.

**Results and discussion**

**Whole sequences and structure of microbial rhodopsin FR1 and FR2**

Two variants of microbial rhodopsin genes, FR1 and FR2, were identified in the diatom *Fragilariopsis cylindrus*. FR1 consists of four exons interrupted by three introns, with a transcript length of 1119 bp, including a 774 bp coding region. In

contrast, FR2 is composed of five exons and four introns, with a transcript length of 1177 bp, also encoding a 774 bp protein. Although FR1 features an additional 30 amino acids at the N-terminal, including a potential signal peptide cleaved in the mature protein, the nucleotide sequence differences between the two variants account for only 5.44% (Figure 2.1). Notably, their amino acid sequences are identical.

The secondary structures of FR1 and FR2 were predicted using the I-TASSER server (I-TASSER server for protein structure and function prediction (zhanggroup.org) ) (Yang & Zhang, 2015; Zhang et al., 2017; Zheng et al., 2021). Both peptides display a core region of seven α-helices (H1-H7), characteristic of microbial rhodopsin proteins (Figure 2.2). These α-helices are predominantly located in the central and near-terminal regions of the sequences. The length of these helices suggests they play a role in maintaining protein stability. No β-sheet regions were predicted in either protein. Random coils were prevalent, particularly at the N- and C-terminal regions, contributing to the proteins' structural flexibility, which may be important for their dynamic properties.

In addition, full-length alignments of FR1 and FR2 with the characterised microbial rhodopsins, bacteriorhodopsin and proteorhodopsin, revealed conserved residues essential for a green light-absorbing proton pump (Figure 2.3). The characteristic lysine residue (K261) provides the retinal Schiff base linkage, while acidic residues at positions corresponding to proton acceptor (D121) and donor (E132) sites are homologous to K216, D85, and D96 in the archaeal proton-pump microbial rhodopsin bacteriorhodopsin (BR) (Brown et al., 1994; Facciotti et al., 2004; Wang et al., 2013). Furthermore, the presence of L129 indicates that FR1 and FR2 function as green light-absorbing microbial rhodopsin (Man et al., 2003). A retinal binding pocket was also identified by mapping 18 conserved positions from bacteriorhodopsin onto the FR sequences, in line with previous findings (Adamian et al., 2006; Strauss, 2012)

Subsequenty, the 3D structure of FR was predicted (Figure 2.4) utilised AlphaFold 2

and subsequently compared with the structures of several well-characterised microbial rhodopsins (Figure 2.5) utilised Foldseek (Barrio-Hernandez et al., 2023; Jumper et al., 2021; Kim et al., 2024; van Kempen et al., 2024; Varadi et al., 2021; Varadi et al., 2023). The structural alignment reveals that the core regions of FR rhodopsin are highly conserved and show significant similarity to other microbial rhodopsins, including xanthorhodopsin from *Tessaracoccus antarcticus*, bacteriorhodopsin from *Haloarcula marismortui*, and proteorhodopsin from uncultured gamma proteobacterium EBAC31A08. This high degree of structural conservation, particularly in the transmembrane helices, supports the notion that FR rhodopsins likely share functional characteristics with these proton-pumping microbial rhodopsins (Todd et al., 2001). Further phylogenetic analysis focusing on eukaryotic microbial rhodopsins also confirmed that FcR1/2 belongs to the xanthorhodopsin family (Strauss et al., 2023).

In particular, the alignment highlights the previously mentioned conserved regions responsible for the proton transport mechanism, such as the retinal binding pocket and the key residues involved in proton transfer. The presence of these conserved features further indicates that FR rhodopsins may function as light-driven proton pumps, similar to their bacterial homologs. Moreover, the comparison also reveals slight variations in the extracellular loop regions and the N-terminal extension of FR rhodopsins, which may reflect the evolution pathway from bacteria to eukaryote organisms and adaptations to the unique polar environmental conditions faced by influence protein stability and flexibility (Fields et al., 2015; Sikosek & Chan, 2014).

Overall, these structural similarities, combined with the conserved functional motifs, suggest that FR rhodopsins play a critical role in light absorption and energy conversion, contributing to the photophysiology of diatoms, particularly under varying light and nutrient conditions. Further experimental studies are needed to validate the functional role of these structural features in FR rhodopsins.

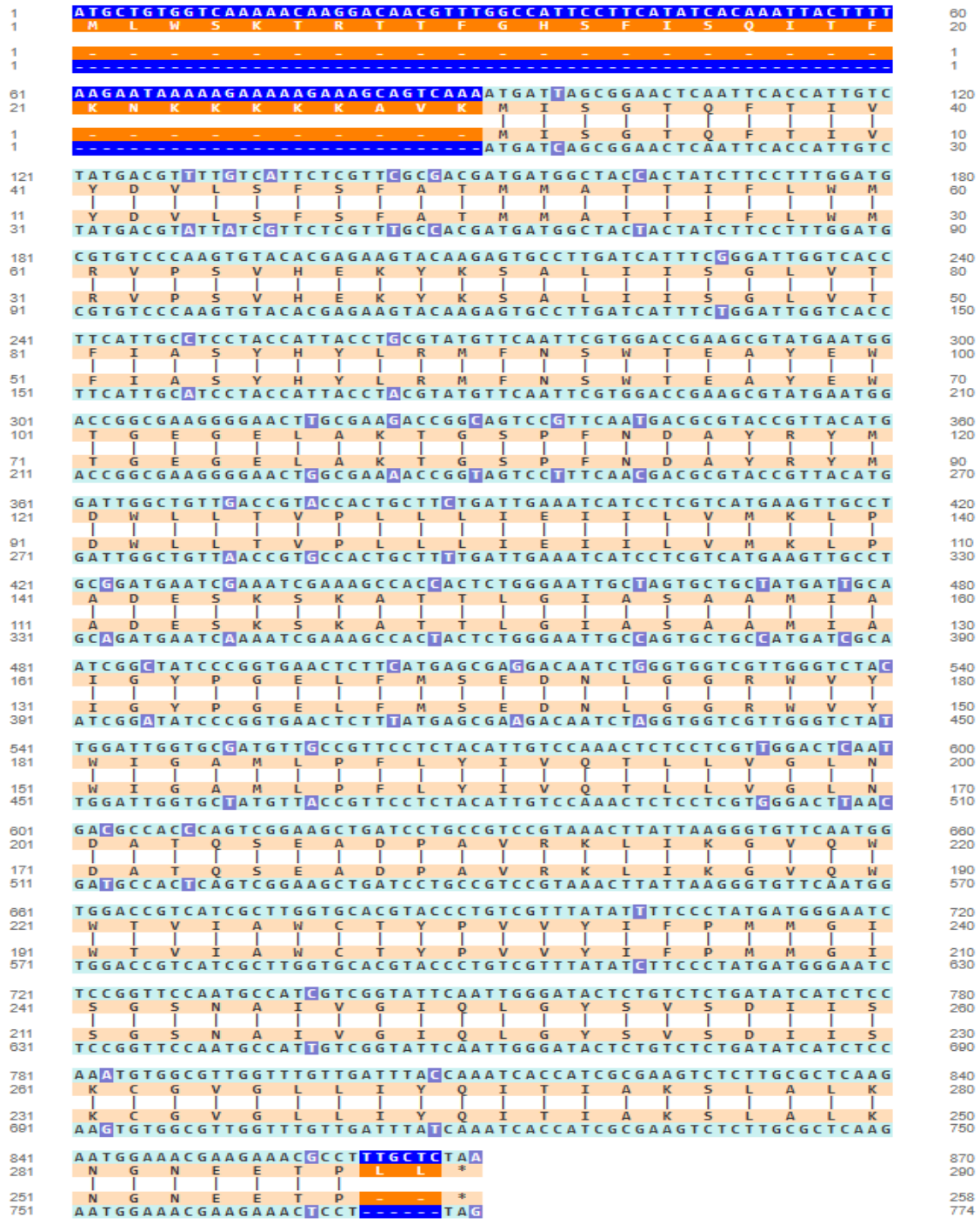

**Figure 2.1 Nucleotide and protein sequence alignment of FR1 and FR2.** Nucleotide sequences are represented by green lines, with FR1 on the top and FR2 on the bottom. Variations between the two sequences are highlighted in light blue. Protein sequences are depicted in yellow lines, with FR1 shown above FR2. Gaps at the first 30 and last two amino acids are marked in deep blue for nucleotides and orange for proteins. https://en.vectorbuilder.com/tool/sequence-alignment.html

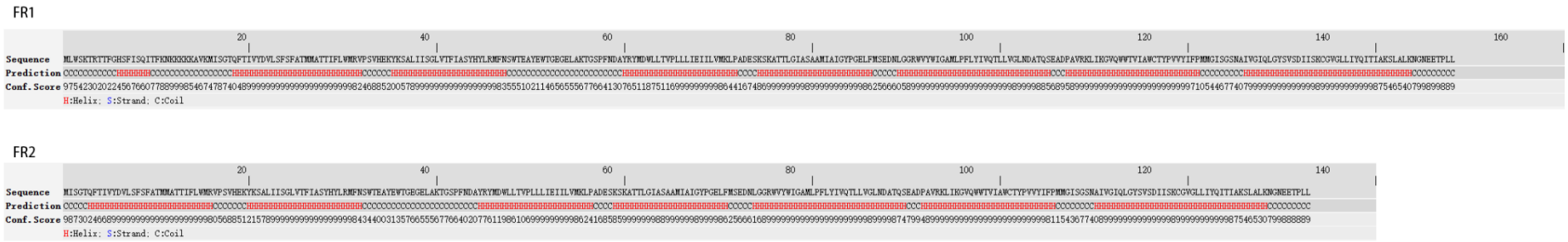


**Figure 2.2 Secondary structure prediction of microbial rhodopsins FR1 and FR2 using the I-TASSER model.** The letters 'H', 'E', and 'C' indicate the α-helix, β-sheet, and coiled coil regions, respectively. Amino acid sequences and confidence scores are also displayed.


**Figure 2.3 Protein sequence alignment of bacteriorhodopsin and proteorhodopsin with FR1 and FR2.** The alignment includes bacteriorhodopsin from *Halobacterium salinarum* (Uniprot: P02945) and proteorhodopsin from *Nonlabens marinus* (Uniprot ID: W8VZ92_9FLAO). Key residues are highlighted with colored circles: proton acceptor D121 and donor E132 are marked in black, Retinal Schiff base K261 in purple, green spectral tuning residue L129 in green, proton channel residue R118H in light blue, and retinal binding pocket residues Y119, W122, V126, L129, A160, U161, G165, W181, A184, M185, F188, W226, Y229, P230, Y233, Y253, and S260 are marked in grey.

## Multiple sequence alignment and conservative analysis

To gain a comprehensive understanding of diatom microbial rhodopsins in the natural environment and their distribution across various organisms, we performed a sequence similarity search based on the FR protein sequences. Microbial rhodopsins sequences were retrieved from the Pfam, NCBI, and UniProt databases, focusing on diatom microbial rhodopsins. A multiple sequence alignment (MSA) was then conducted using these collected sequences. Additionally, homologous sequences from the Tara Ocean metagenomic dataset were used to construct a phylogenetic tree. The

results are shown in Figures 2.6 and 2.7.

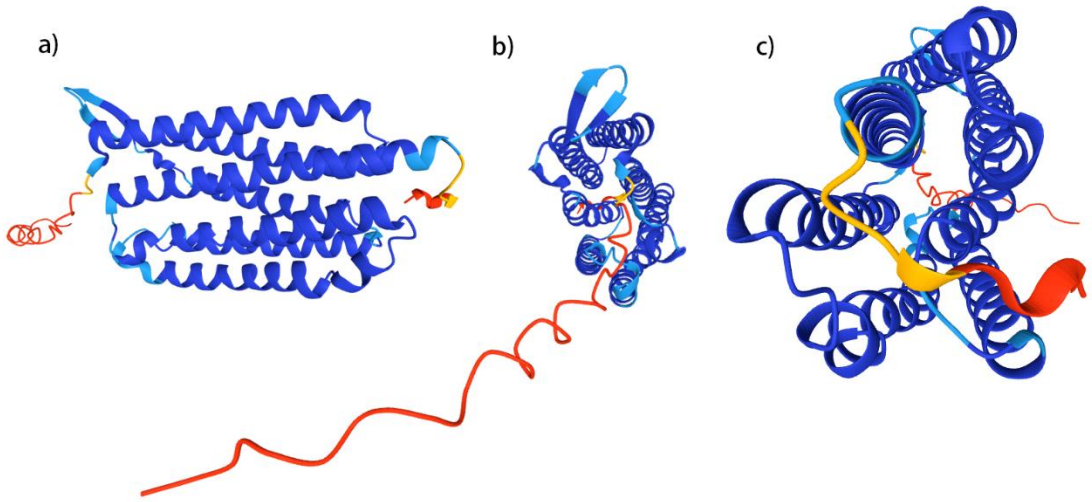


**Figure 2.4 Three-dimensional structural representation of microbial rhodopsin FR1.** Panels (a) through (c) show different views of the 3D structure from various angles.

The MSA results in Figure 2.6 illustrate the high conservation of microbial rhodopsin sequences across various diatom species, particularly within the domain regions associated with the *Archaeal/bacterial/fungal rhodopsin* superfamily (IPR001425). Key functional residues, such as the proton acceptor D121 and donor E132, are highly conserved, indicating that these microbial rhodopsins likely function as proton pumps, similar to FR1. The alignment also highlights the conservation of the L129 residue, which plays a critical role in tuning the microbial rhodopsins for green light absorption. This conservation suggests that a majority of diatom microbial rhodopsins are adapted to absorb green light, a feature possibly linked to the depth-dependent distribution of light in aquatic environments, where green light predominates in surface waters and blue light dominates in deeper layers (Béjà et al., 2001).

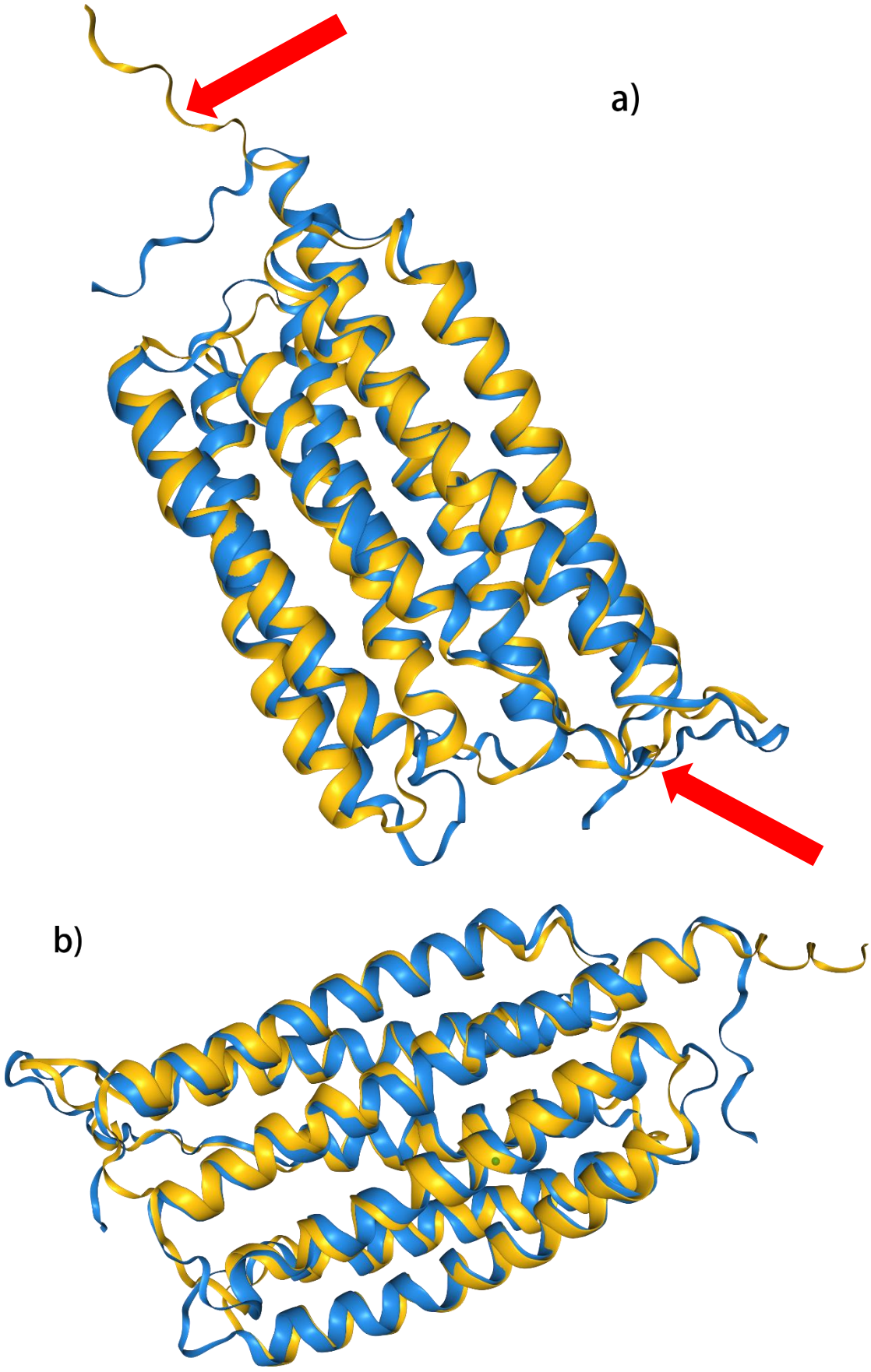
a)
b)

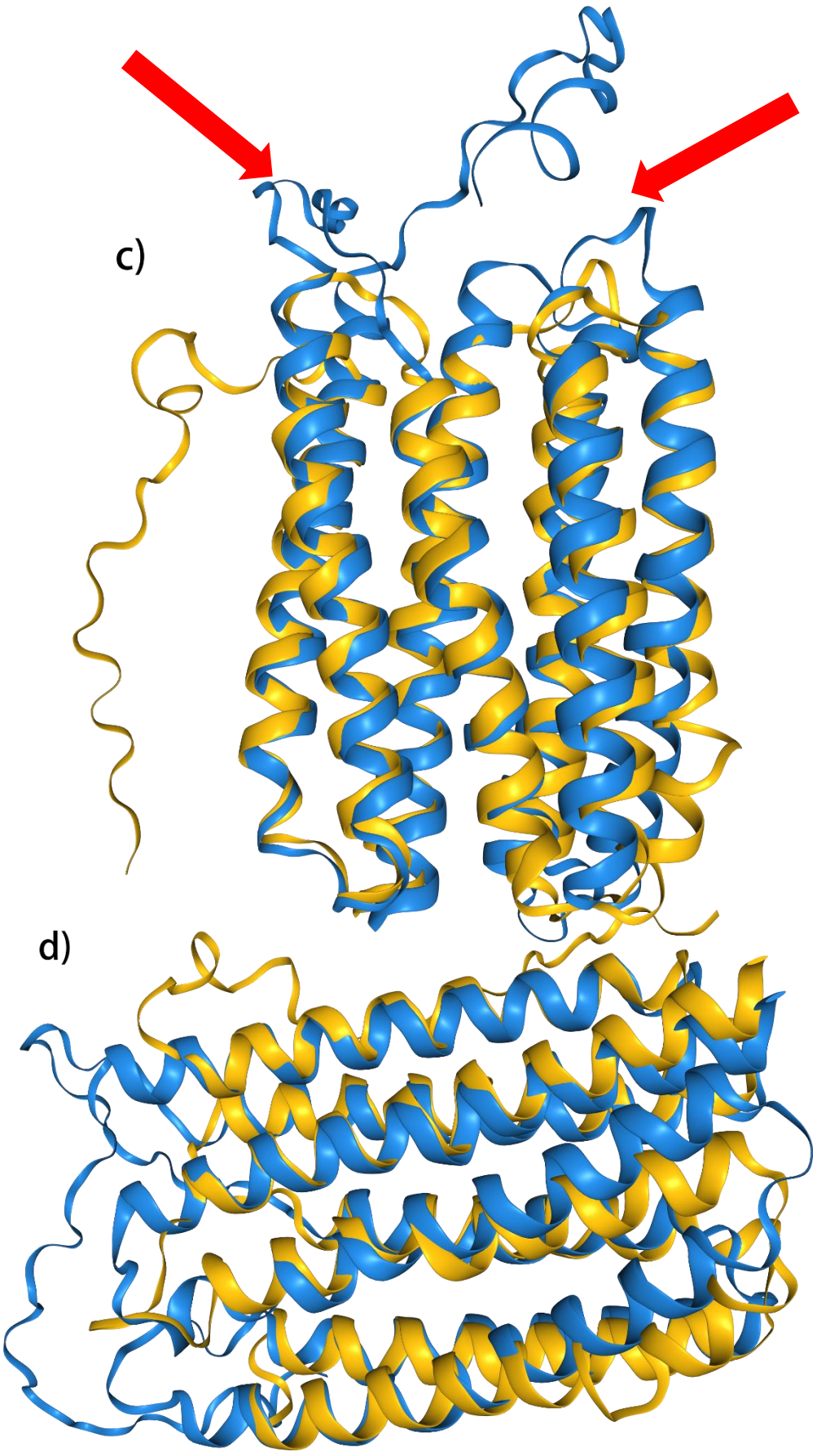
c)
d)

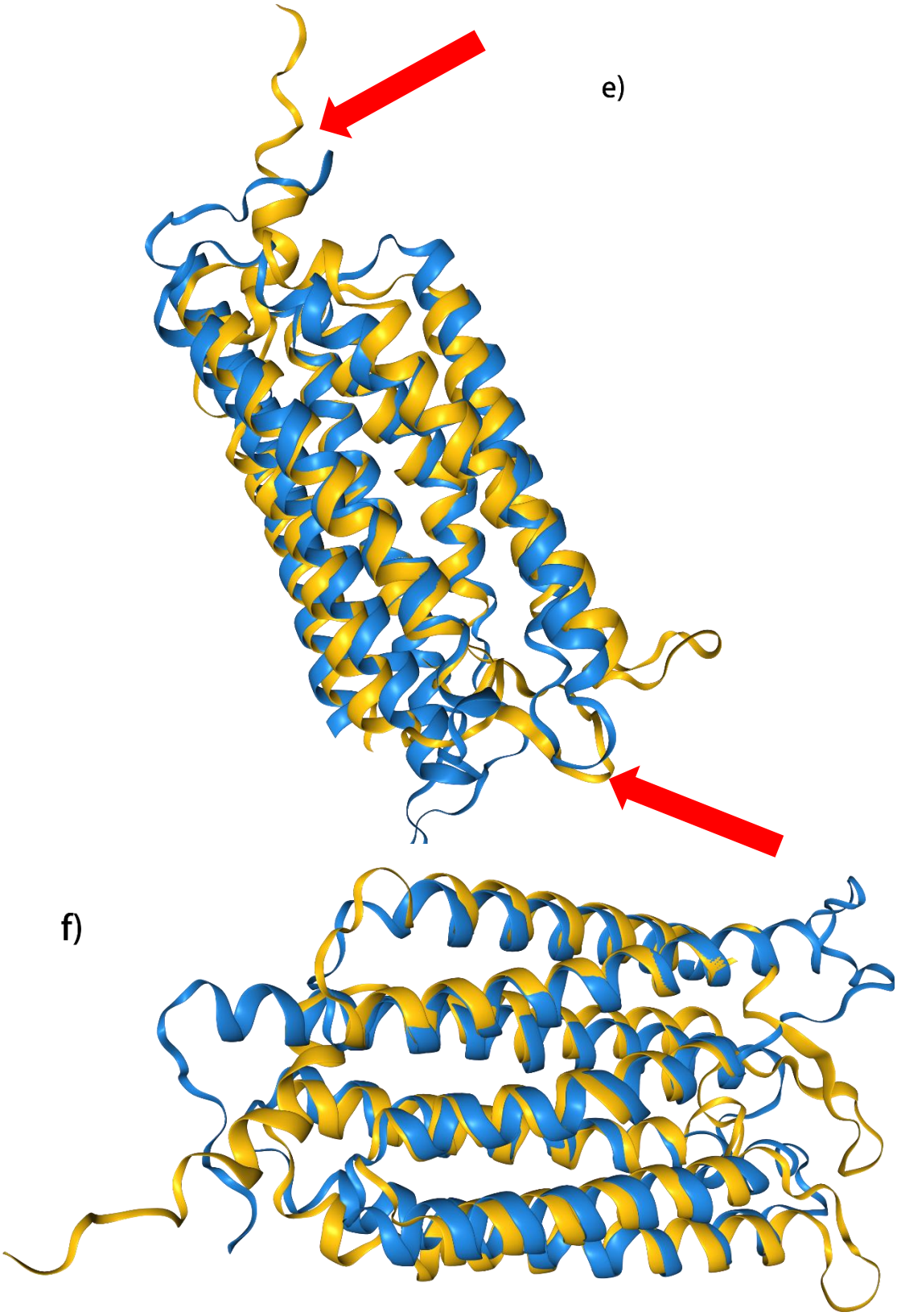


**Figure 2.5 Structural comparison of FR rhodopsin with three proton-pumping rhodopsins.** Panels (a) to (f) display the protein structure comparison of FR1 (blue) to three different proton-pump rhodopsins (yellow). (a) and (b) display comparison to xanthorhodopsin from *Tessaracoccus antarcticus*, (c) and (d) display the comparison to green-light absorbing proteorhodopsin from uncultured gamma proteobacterium EBAC31A08; (e) and (f) display the comparison to bacteriorhodopsin from *Haloarcula marismortui*. Key differences are highlight with red arrows.

Interestingly, some sequences exhibit extended protein lengths compared to FR1, with fewer conserved regions. However, these extended sequences align well with one another, indicating that they may represent a different subfamily or functional variation of microbial rhodopsins in diatoms. The Neighbor-Joining tree (Figure 2.7) further supports these observations. The phylogenetic analysis shows that diatom microbial rhodopsins are grouped into two distinct clusters. One cluster contains highly conserved sequences closely related to FR rhodopsins, while the second cluster exhibits significant divergence from FR, except for the microbial rhodopsin from *Ditylum brightwellii* (ID: UPI0016F67D94), which shares key conserved residues with FR rhodopsins.

The high degree of conservation within the FR-like cluster indicates that these microbial rhodopsins likely share similar functions, potentially as green light-absorbing proton pumps, as suggested by the conserved residues involved in proton transfer (D121, E132, K261). In contrast, the second cluster may represent a more diverse group of microbial rhodopsins with different functions or adaptations. Despite this divergence, the conserved functional residues in Ditylum brightwellii suggest it may still perform similar proton-pumping functions to FR rhodopsins.

This phylogenetic separation implies that while some diatom microbial rhodopsins have retained functional conservation, others have diverged, possibly in response to different environmental pressures or ecological niches. Future studies could focus on the functional characterisation of these divergent microbial rhodopsins to explore potential novel mechanisms of light-driven energy conversion in diatoms. These divergent sequences, while still containing the essential motifs for proton pumping, could represent novel functions or adaptations in diatom microbial rhodopsins that remain to be fully explored. Future research could focus on characterising the functional differences of these extended microbial rhodopsins and their potential roles in diatom physiology, especially under varying light conditions and environmental

stresses.

Consequently, the multiple sequence alignment and phylogenetic analysis revealed that diatom microbial rhodopsins exhibit a complex evolutionary pattern. While some microbial rhodopsins, such as FR1, have retained high conservation of functional residues, suggesting a role as proton-pumping, green light-absorbing proteins, others show signs of diversification. The identification of both conserved and divergent microbial rhodopsins points to potential functional diversification within diatom species, opening avenues for future studies to investigate novel mechanisms of light-driven energy conversion and environmental adaptation in these ecologically important organisms.

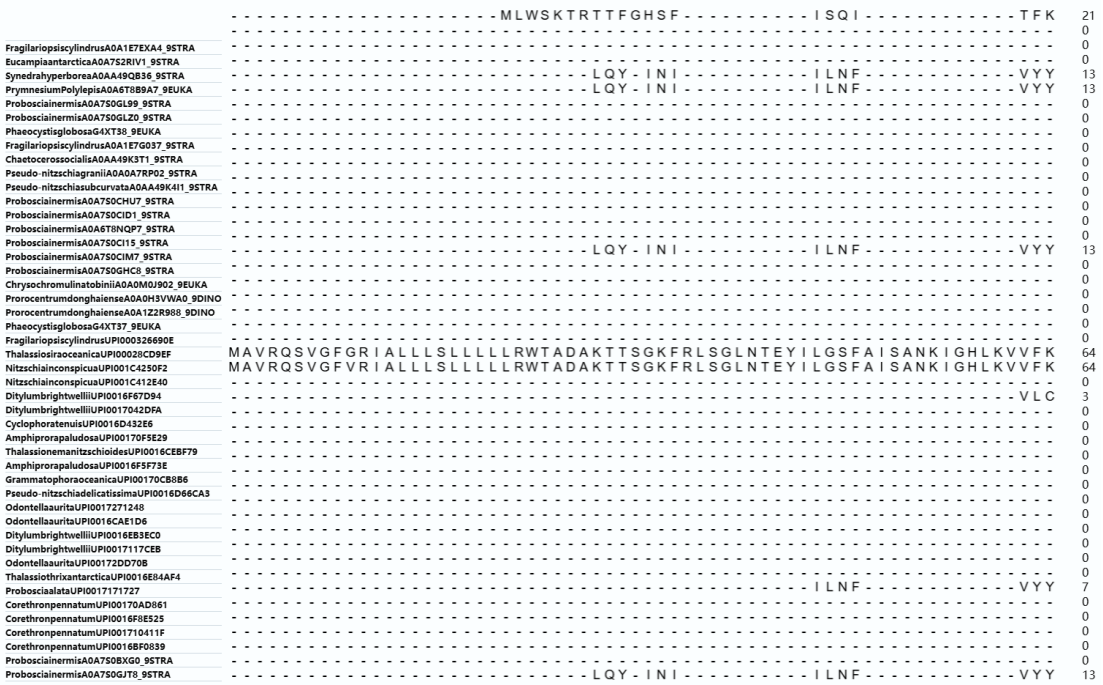
Fragilariopsiscylindrus A0A1E7EXA4 9STRA
Eucampiaantarctica A0A7S2RIV1 9STRA
Synedrahyperboreea A0AA49QB36 9STRA
PrymnesiumPolylepisA0A6T8B9A7 9EUKA
Proboscia inermis A0A7S0GL99 9STRA
Proboscia inermis A0A7S0GLZ0 9STRA
Phaeocystisglobosa G4XT38 9EUKA
Fragilariopsiscylindrus A0A1E7G037 9STRA
Chaetocerossocialis A0AA49K3T1 9STRA
Pseudo-nitzschiagranii A0A0A7RP02 9STRA
Pseudo-nitzschiasubcurvata A0AA49K4I1 9STRA
Proboscia inermis A0A7S0CHU7 9STRA
Proboscia inermis A0A7S0CID1 9STRA
Proboscia inermis A0A6T8NQP7 9STRA
Proboscia inermis A0A7S0CI15 9STRA
Proboscia inermis A0A7S0CIM7 9STRA
Proboscia inermis A0A7S0GHC8 9STRA
Chrysochromulinatobinii A0A0M0J902 9EUKA
Prorocentrumdonghaiense A0A0H3VWA0 9DINO
Prorocentrumdonghaiense A0A1Z2R988 9DINO
Phaeocystisglobosa G4XT37 9EUKA
Fragilariopsiscylindrus UPI000326690E
Thalassiosiraoceanica UPI00028CD9EF
Nitzschiainconspicua UPI001C4250F2
Nitzschiainconspicua UPI001C412E40
Ditylumbrightwellii UPI0016F67D94
Ditylumbrightwellii UPI0017042DFA
Cyclophoratenuis UPI0016D432E6
Amphiproraplaudosa UPI00170F5E29
Thalassionemanitzschioides UPI0016CEBF79
Amphiproraplaudosa UPI0016F5F73E
Grammatophoraoceanica UPI00170CB8B6
Pseudo-nitzschiadelicatissima UPI0016D66CA3
Odontellaauritа UPI0017271248
Odontellaauritа UPI0016CAE1D6
Ditylumbrightwellii UPI0016EB3EC0
Ditylumbrightwellii UPI0017117CEB
Odontellaauritа UPI00172DD70B
Thalassiothrixantarctica UPI0016E84AF4
Prosociaalata UPI0017171727
Corethronpennatum UPI00170AD861
Corethronpennatum UPI0016F8E525
Corethronpennatum UPI001710411F
Corethronpennatum UPI0016BF0839
Proboscia inermis A0A7S0BXG0 9STRA
Proboscia inermis A0A7S0GJT8 9STRA

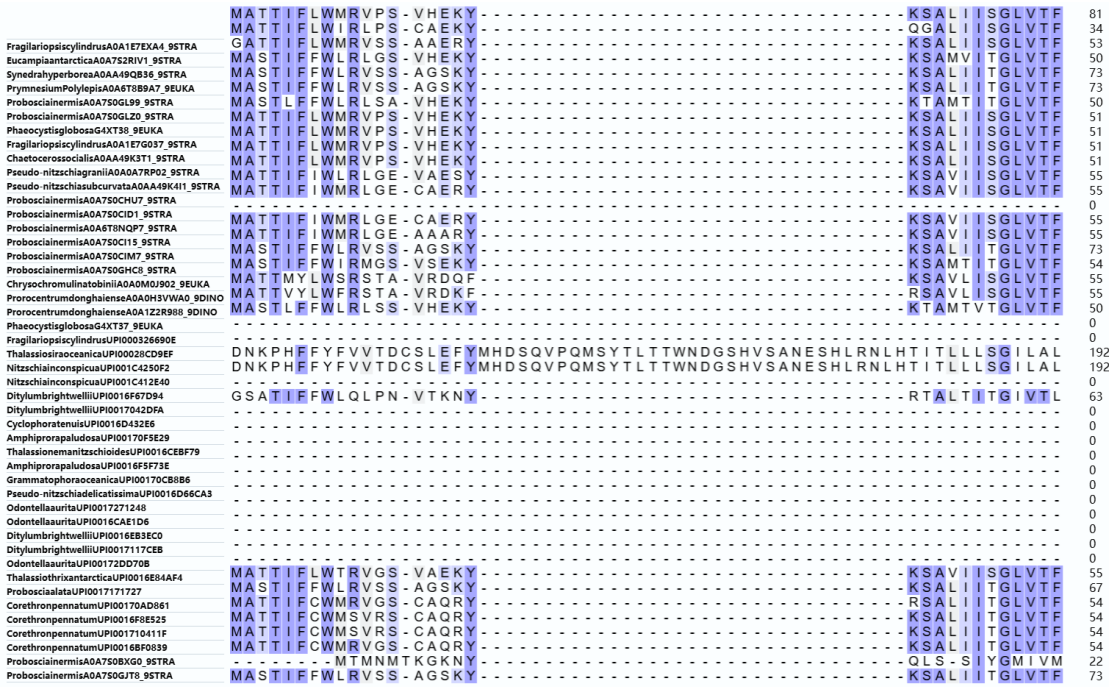
Fragilariopsiscylindrus A0A1E7EXA4 9STRA
Eucampiaantarctica A0A7S2RIV1 9STRA
Synedrahyperborea A0AA49QB36 9STRA
PrymnesiumPolylepis A0A6T8B9A7 9EUKA
Proboscia inermis A0A7S0GL99 9STRA
Proboscia inermis A0A7S0GLZ0 9STRA
Phaeocystisglobosa G4XT38 9EUKA
Fragilariopsiscylindrus A0A1E7G037 9STRA
Chaetocerossocialis A0AA49K3T1 9STRA
Pseudo-nitzschiagranii A0A0A7RP02 9STRA
Pseudo-nitzschiasubcurvata A0AA49K4I1 9STRA
Proboscia inermis A0A7S0CHU7 9STRA
Proboscia inermis A0A7S0CID1 9STRA
Proboscia inermis A0A6T8NQP7 9STRA
Proboscia inermis A0A7S0CI15 9STRA
Proboscia inermis A0A7S0CIM7 9STRA
Proboscia inermis A0A7S0GHC8 9STRA
Chrysochromulina tobiniiA0A0M0J902 9EUKA
Prorocentrum donghaiense A0A0H3VWA0 9DINO
Prorocentrum donghaiense A0A1Z2R988 9DINO
Phaeocystisglobosa G4XT37 9EUKA
Fragilariopsiscylindrus UPI000326690E
Thalassiosiraoceanica UPI00028CD9EF
Nitzschiainconspicua UPI001C4250F2
Nitzschiainconspicua UPI001C412E40
Ditylumbrightwellii UPI0016F67D94
Ditylumbrightwellii UPI0017042DFA
Cyclophoratenuis UPI0016D432E6
Amphiprorapaludosa UPI00170F5E29
Thalassionemanitzschioides UPI0016CEBF79
Amphiprorapaludosa UPI0016F5F73E
Grammatophoraoceanica UPI00170CB8B6
Pseudo-nitzschiadelicatissima UPI0016D66CA3
Odontellaaurita UPI0017271248
Odontellaaurita UPI0016CAE1D6
Ditylumbrightwellii UPI0016EB3EC0
Ditylumbrightwellii UPI0017117CEB
Odontellaaurita UPI00172DD70B
Thalassiothrixantarctica UPI0016E84AF4
Proboscia alata UPI0017171727
Corethronpennatum UPI00170AD861
Corethronpennatum UPI0016F8E525
Corethronpennatum UPI001710411F
Corethronpennatum UPI0016BF0839
Proboscia inermis A0A7S0BXG0 9STRA
Proboscia inermis A0A7S0GJT8 9STRA

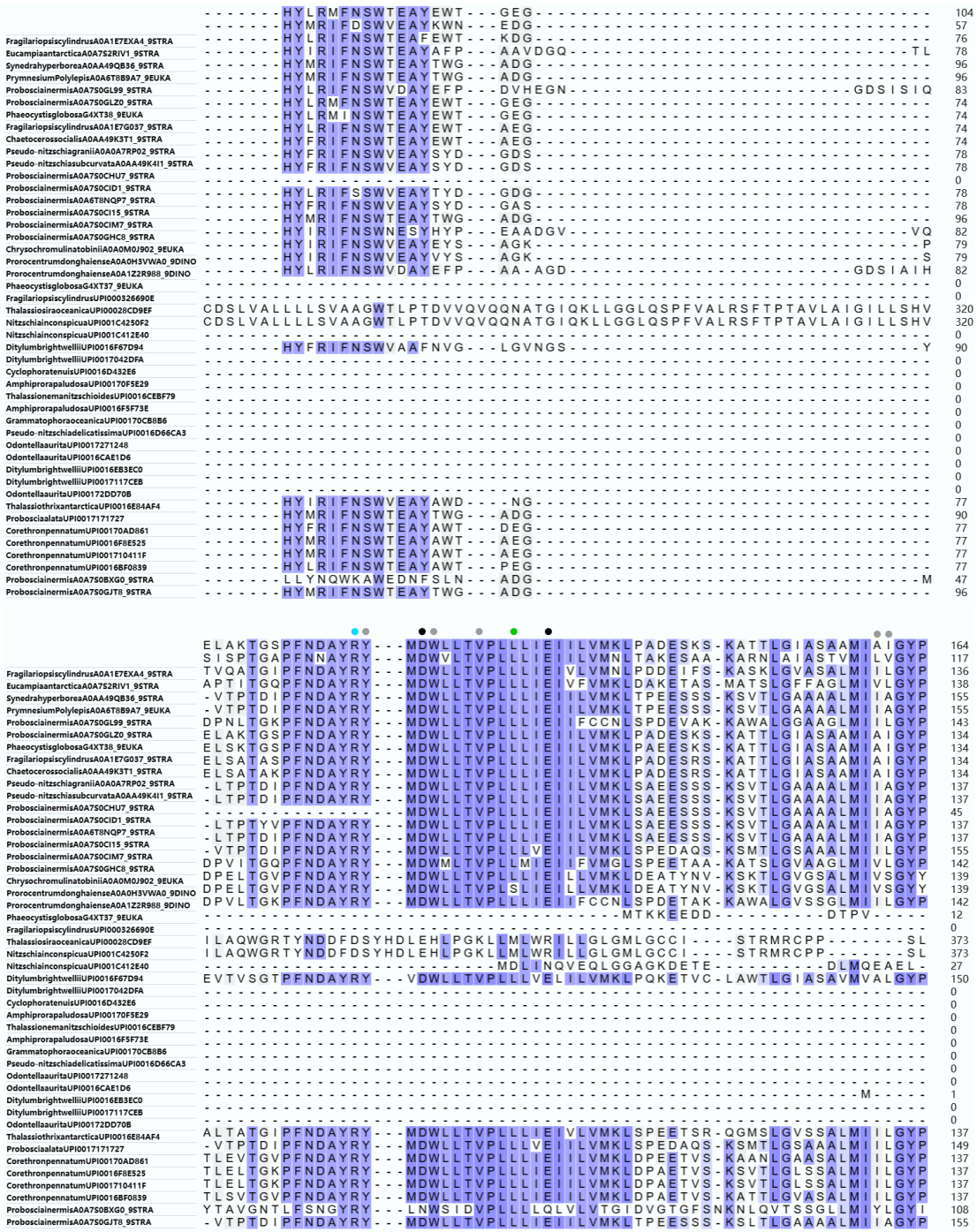

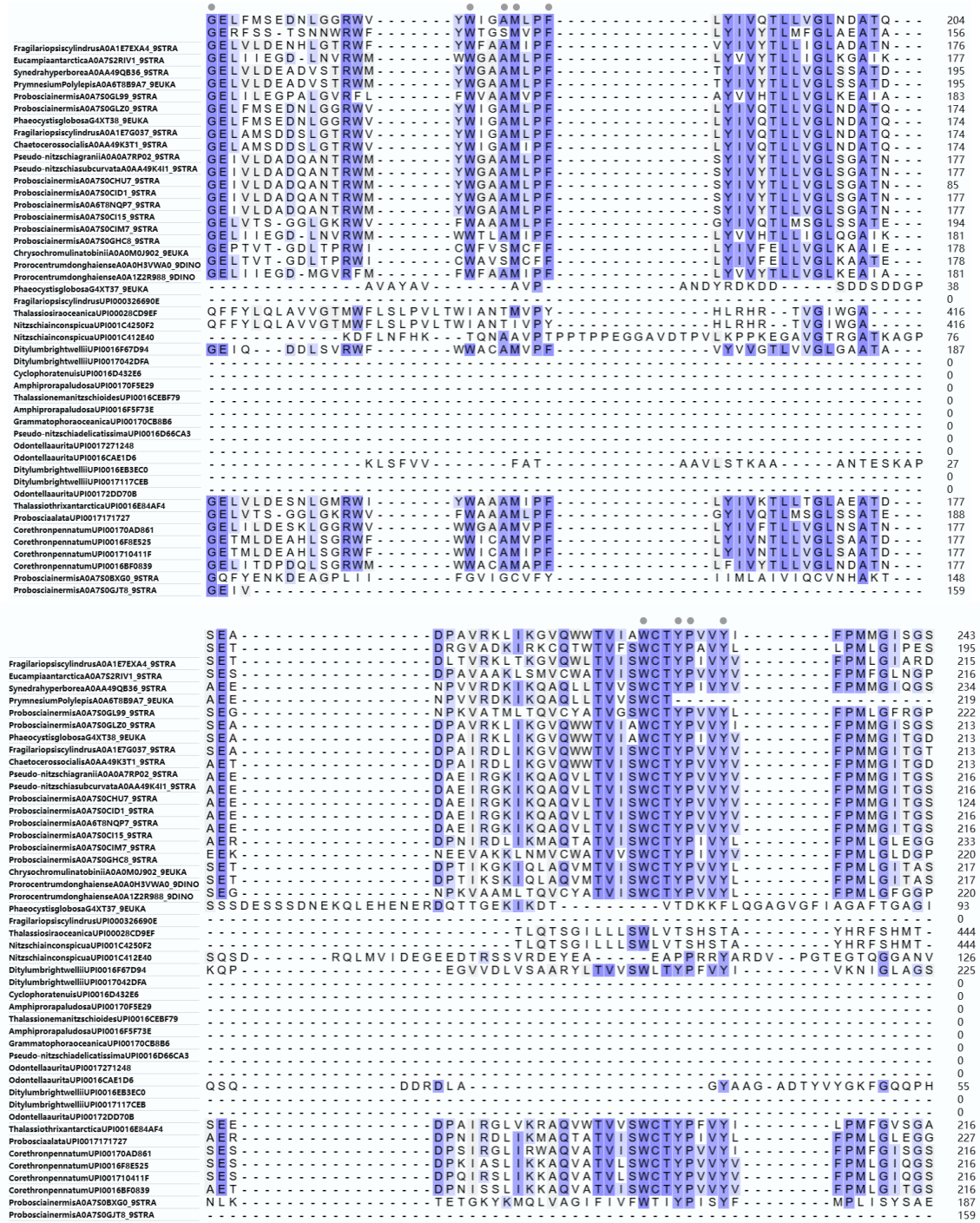
FragilariopsiscylindrusA0A1E7EXA4_9STRA
EucampiaantarcticaA0A7S2RIV1_9STRA
SynedrahyperboreaA0AA49QB36_9STRA
PrymnesiumPolylepisA0A6T8B9A7_9EUKA
ProboscianermisA0A7S0GL99_9STRA
ProboscianermisA0A7S0GLZ0_9STRA
PhaeocystisglobosaG4XT38_9EUKA
FragilariopsiscylindrusA0A1E7G037_9STRA
ChaetocerossocialisA0AA49K3T1_9STRA
Pseudo-nitzschiagraniiA0A0A7RP02_9STRA
Pseudo-nitzschiasubcurvataA0AA49K4I1_9STRA
ProboscianermisA0A7S0CHU7_9STRA
ProboscianermisA0A7S0CID1_9STRA
ProboscianermisA0A6T8NQP7_9STRA
ProboscianermisA0A7S0CI15_9STRA
ProboscianermisA0A7S0CIM7_9STRA
ProboscianermisA0A7S0GHC8_9STRA
Chrysochromulinatobinii A0A0M0J902_9EUKA
ProrocentrumdonghaienseA0A0H3VWA0_9DINO
ProrocentrumdonghaienseA0A1Z2R988_9DINO
PhaeocystisglobosaG4XT37_9EUKA
FragilariopsiscylindrusUPI000326690E
ThalassiosiraoceanicaUPI00028CD9EF
NitzschiainconspicuaUPI001C4250F2
NitzschiainconspicuaUPI001C412E40
DitylumbrightwelliiUPI0016F67D94
DitylumbrightwelliiUPI0017042DFA
CyclophoratenuisUPI0016D432E6
AmphiprorapaludosaUPI00170F5E29
ThalassionemanitzschioidesUPI0016CEBF79
AmphiprorapaludosaUPI0016F5F73E
GrammatophoraoceanicaUPI00170CB8B6
Pseudo-nitzschiadelicatissimaUPI0016D66CA3
OdontellaauritaUPI0017271248
OdontellaauritaUPI0016CAE1D6
DitylumbrightwelliiUPI0016EB3EC0
DitylumbrightwelliiUPI0017117CEB
OdontellaauritaUPI00172DD70B
ThalassiothrixantarcticaUPI0016E84AF4
ProboscialataUPI0017171727
CorethronpennatumUPI00170AD861
CorethronpennatumUPI0016F8E525
CorethronpennatumUPI0017104 11F
CorethronpennatumUPI0016BF0839
ProboscianermisA0A7S0BXG0_9STRA
ProboscianermisA0A7S0GJT8_9STRA

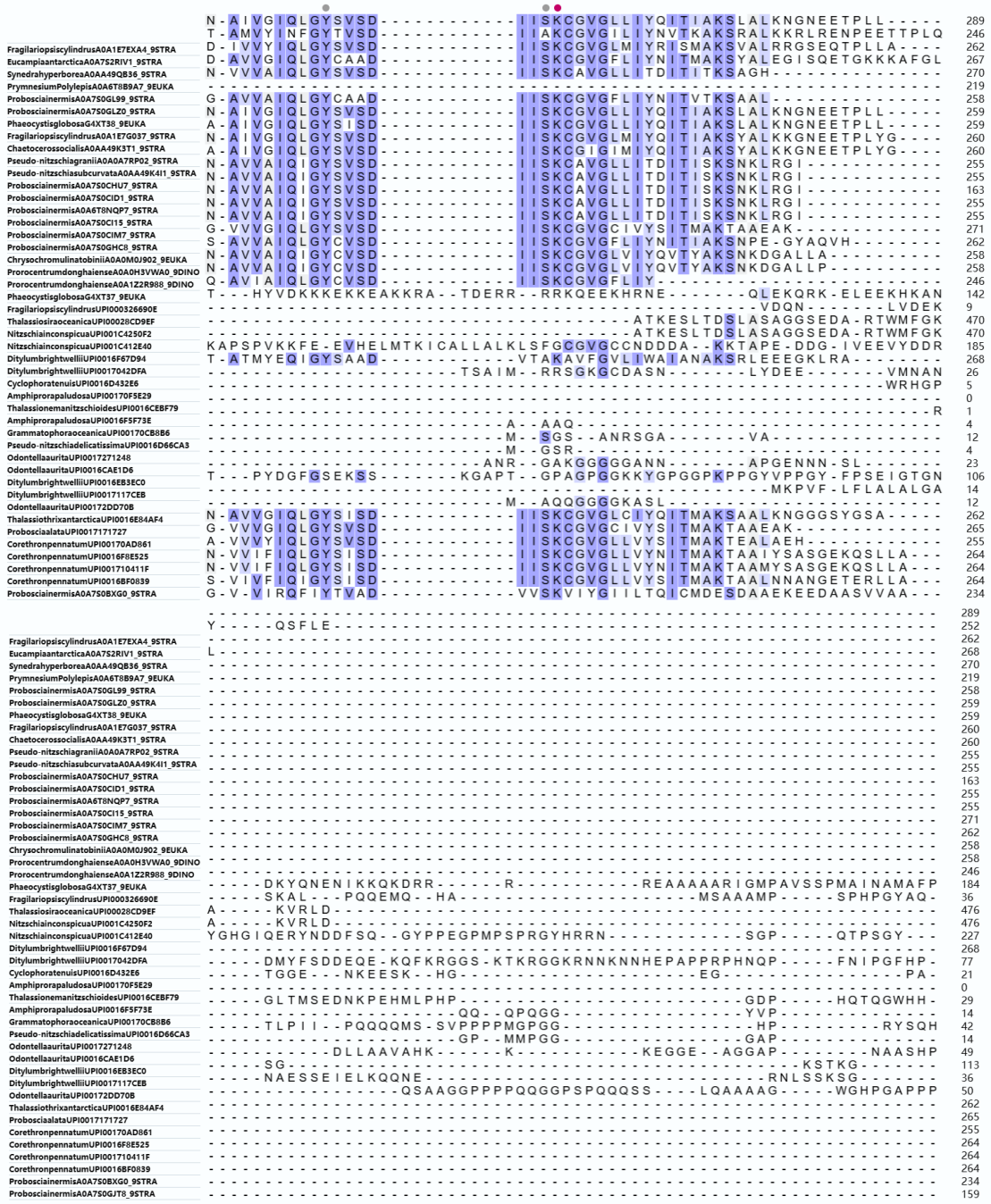
FragilariopsiscylindrusA0A1E7EXA4_9STRA
EucampiaantarcticaA0A7S2RIV1_9STRA
SynedrahyperboreaA0AA49QB36_9STRA
PrymnesiumPolylepisA0A6T8B9A7_9EUKA
ProbosciainermisA0A750GL99_9STRA
ProbosciainermisA0A750GLZ0_9STRA
PhaeocystisglobosaG4XT38_9EUKA
FragilariopsiscylindrusA0A1E7G037_9STRA
ChaetocerossocialisA0AA49K3T1_9STRA
Pseudo-nitzschiagraniiA0A0A7RP02_9STRA
Pseudo-nitzschiasubcurvataA0AA49K4I1_9STRA
ProbosciainermisA0A750CHU7_9STRA
ProbosciainermisA0A750CID1_9STRA
ProbosciainermisA0A6T8NQP7_9STRA
ProbosciainermisA0A750CI15_9STRA
ProbosciainermisA0A750CIM7_9STRA
ProbosciainermisA0A750GHC8_9STRA
ChrysochromulinatobiniiA0A0M0J902_9EUKA
ProrocentrumdonghaienseA0A0H3VWA0_9DINO
ProrocentrumdonghaienseA0A1Z2R988_9DINO
PhaeocystisglobosaG4XT37_9EUKA
FragilariopsiscylindrusUPI000326690E
ThalassiosiraoceanicaUPI00028CD9EF
NitzschiainconspicuaUPI001C4250F2
NitzschiainconspicuaUPI001C412E40
DitylumbrightwelliiUPI0016F67D94
DitylumbrightwelliiUPI0017042DFA
CyclophoratenuisUPI0016D432E6
AmphiprorapaludosaUPI00170F5E29
ThalassionemanitzschioidesUPI0016CEBF79
AmphiprorapaludosaUPI0016F5F73E
GrammatophoraoceanicaUPI00170CB8B6
Pseudo-nitzschiadelicatissimaUPI0016D66CA3
OdontellaauritaUPI0017271248
OdontellaauritaUPI0016CAE1D6
DitylumbrightwelliiUPI0016EB3EC0
DitylumbrightwelliiUPI0017117CEB
OdontellaauritaUPI00172DD70B
ThalassiothrixantarcticaUPI0016E84AF4
ProbosciaalataUPI0017171727
CorethronpennatumUPI00170AD861
CorethronpennatumUPI0016F8E525
CorethronpennatumUPI001710411F
CorethronpennatumUPI0016BF0839
ProbosciainermisA0A750BXG0_9STRA
ProbosciainermisA0A750GJT8_9STRA

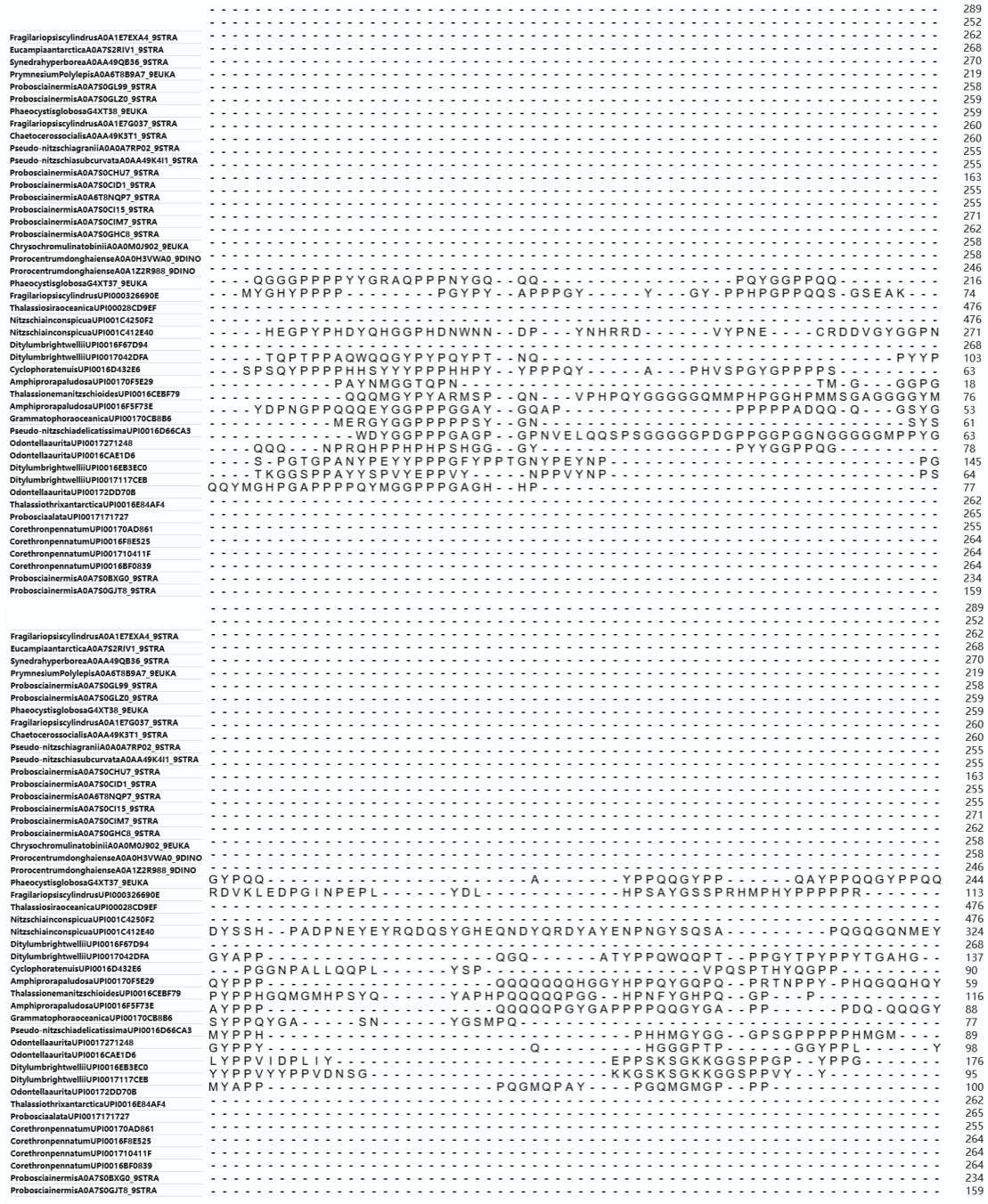
Fragilariopsiscylindrus A0A1E7EXA4 9STRA
Eucampiaantarcticа A0A7S2RIV1 9STRA
Synedrahyperboreа A0AA49QB36 9STRA
PrymnesiumPolylepis A0A6T8B9A7 9EUKA
ProboscіainermisA0A7S0GL99 9STRA
ProboscіainermisA0A7S0GLZ0 9STRA
Phaeocystisglobosa G4XT38 9EUKA
Fragilariopsiscylindrus A0A1E7G037 9STRA
Chaetocerossocialis A0AA49K3T1 9STRA
Pseudo-nitzschiagraniі A0A0A7RP02 9STRA
Pseudo-nitzschiasubcurvata A0AA49K4I1 9STRA
ProboscіainermisA0A7S0CHU7 9STRA
ProboscіainermisA0A7S0CID1 9STRA
ProboscіainermisA0A6T8NQP7 9STRA
ProboscіainermisA0A7S0CI15 9STRA
ProboscіainermisA0A7S0CIM7 9STRA
ProboscіainermisA0A7S0GHC8 9STRA
Chrysochromulinatobiniі A0A0M0J902 9EUKA
Prorocentrumdonghaiense A0A0H3VWA0 9DINO
Prorocentrumdonghaiense A0A1Z2R988 9DINO
Phaeocystisglobosa G4XT37 9EUKA
Fragilariopsiscylindrus UPI000326690E
Thalassiosiraoceanica UPI00028CD9EF
NitzschiainconspicuaUPI001C4250F2
NitzschiainconspicuaUPI001C412E40
DitylumbrightwelliiUPI0016F67D94
DitylumbrightwelliiUPI0017042DFA
CyclophoratenuisUPI0016D432E6
Amphiprorapaludosa UPI00170F5E29
Thalassionemanitzschioides UPI0016CEBF79
Amphiprorapaludosa UPI0016F5F73E
Grammatophoraoceanica UPI00170CB8B6
Pseudo-nitzschiadelicatissima UPI0016D66CA3
OdontellaauritaUPI0017271248
OdontellaauritaUPI0016CAE1D6
DitylumbrightwelliiUPI0016EB3EC0
DitylumbrightwelliiUPI0017117CEB
OdontellaauritaUPI00172DD70B
Thalassiothrixantarctica UPI0016E84AF4
ProboscіaalataUPI0017171727
CorethronpennatumUPI00170AD861
CorethronpennatumUPI0016F8E525
CorethronpennatumUPI001710411F
CorethronpennatumUPI0016BF0839
ProboscіainermisA0A750BXG0 9STRA
ProboscіainermisA0A750GJT8 9STRA

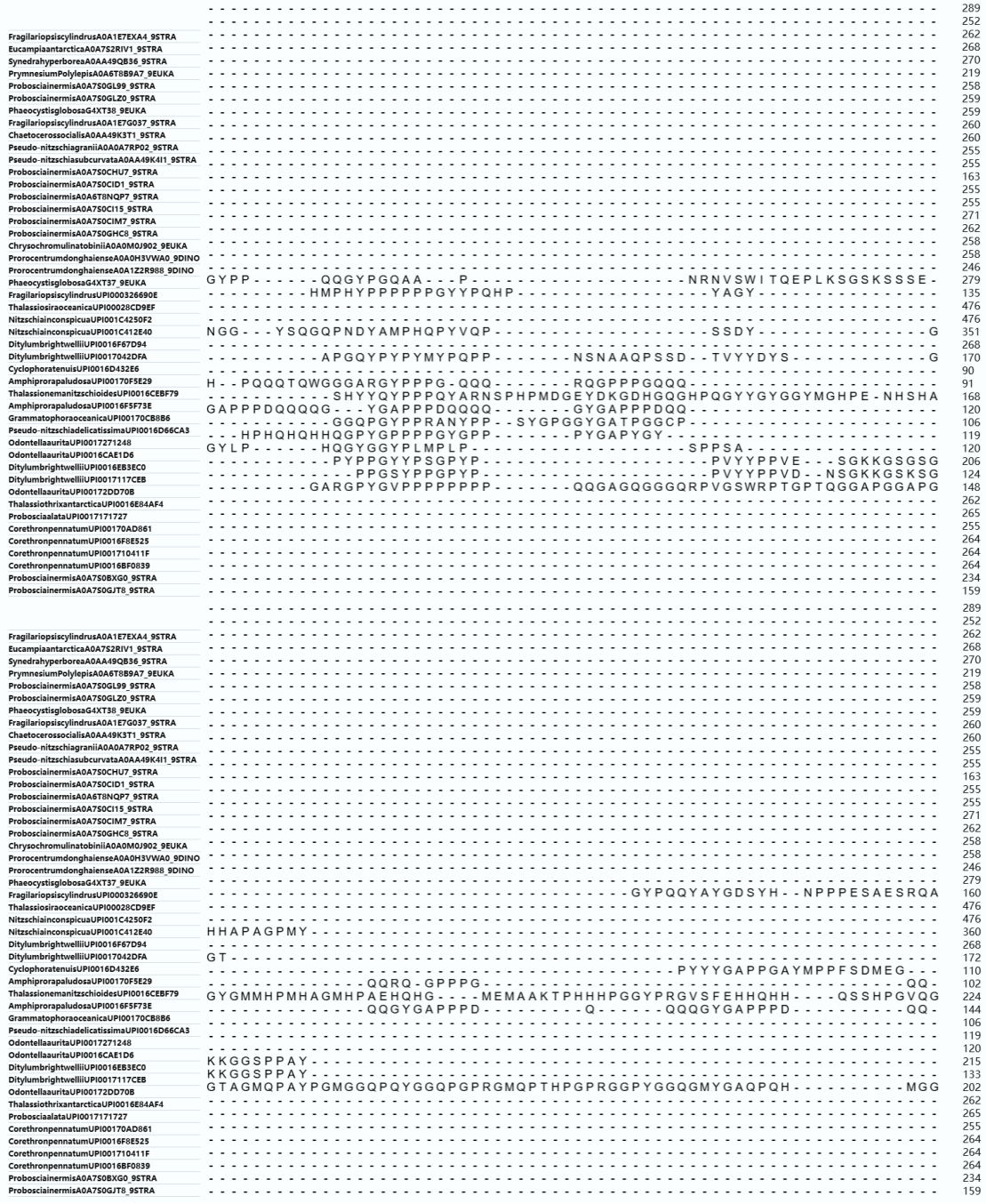
Fragilariopsiscylindrus A0A1E7EXA4_9STRA
Eucampiaantarcticа A0A7S2RIV1_9STRA
Synedrahyperboreа A0AA49QB36_9STRA
PrymnesiumPolylepisA0A6T8B9A7_9EUKA
ProboscіainermisA0A750GL99_9STRA
ProboscіainermisA0A750GLZ0_9STRA
Phaeocystisglobosa G4XT38_9EUKA
Fragilariopsiscylindrus A0A1E7G037_9STRA
Chaetocerossocialis A0AA49K3T1_9STRA
Pseudo-nitzschiagraniiA0A0A7RP02_9STRA
Pseudo-nitzschiasubcurvata A0AA49K4I1_9STRA
ProboscіainermisA0A750CHU7_9STRA
ProboscіainermisA0A750CID1_9STRA
ProboscіainermisA0A6T8NQP7_9STRA
ProboscіainermisA0A750CI15_9STRA
ProboscіainermisA0A750CIM7_9STRA
ProboscіainermisA0A750GHC8_9STRA
ChrysochromulinatobiniiA0A0M0J902_9EUKA
Prorocentrumdonghaiense A0A0H3VWA0_9DINO
Prorocentrumdonghaiense A0A1Z2R988_9DINO
Phaeocystisglobosa G4XT37_9EUKA
Fragilariopsiscylindrus UPI000326690E
Thalassiosiraoceanica UPI00028CD9EF
Nitzschiainconspicua UPI001C4250F2
Nitzschiainconspicua UPI001C412E40
Ditylumbrightwellii UPI0016F67D94
Ditylumbrightwellii UPI0017042DFA
CyclophoratenuisUPI0016D432E6
Amphiprorapaludosa UPI00170F5E29
Thalassionemanitzschioides UPI0016CEBF79
Amphiprorapaludosa UPI0016F5F73E
GrammatophoraoceanicaUPI00170CB8B6
Pseudo-nitzschiadelicatissima UPI0016D66CA3
OdontellaauritaUPI0017271248
OdontellaauritaUPI0016CAE1D6
Ditylumbrightwellii UPI0016EB3EC0
Ditylumbrightwellii UPI0017117CEB
OdontellaauritaUPI00172DD70B
Thalassiothrixantarctica UPI0016E84AF4
ProbosciaalataUPI0017171727
Corethronpennatum UPI00170AD861
Corethronpennatum UPI0016F8E525
Corethronpennatum UPI001710411F
Corethronpennatum UPI0016BF0839
ProboscіainermisA0A750BXG0_9STRA
ProboscіainermisA0A750GJT8_9STRA

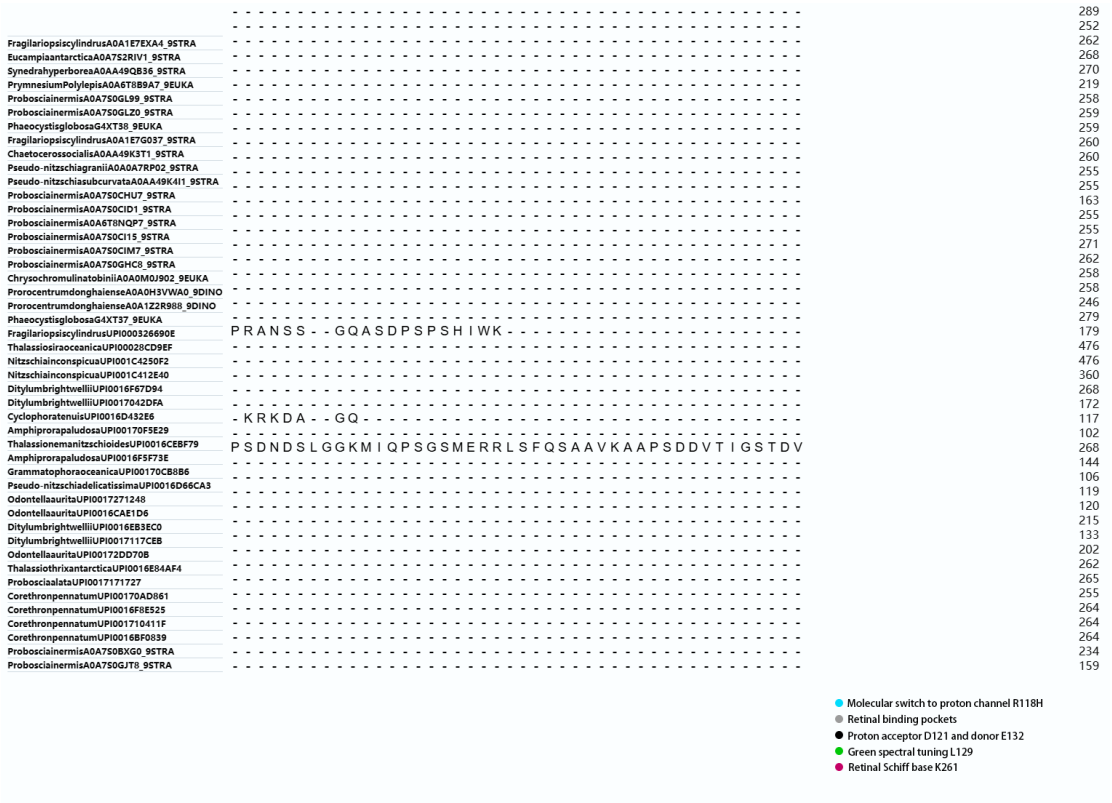

**Figure 2.6 Multiple sequence alignment of diatom microbial rhodopsin protein sequences, using FR1 as the reference sequence.** The left-side labels correspond to species information and protein IDs. The color gradient indicates the degree of conservation, with darker shades representing more conserved amino acid residues.

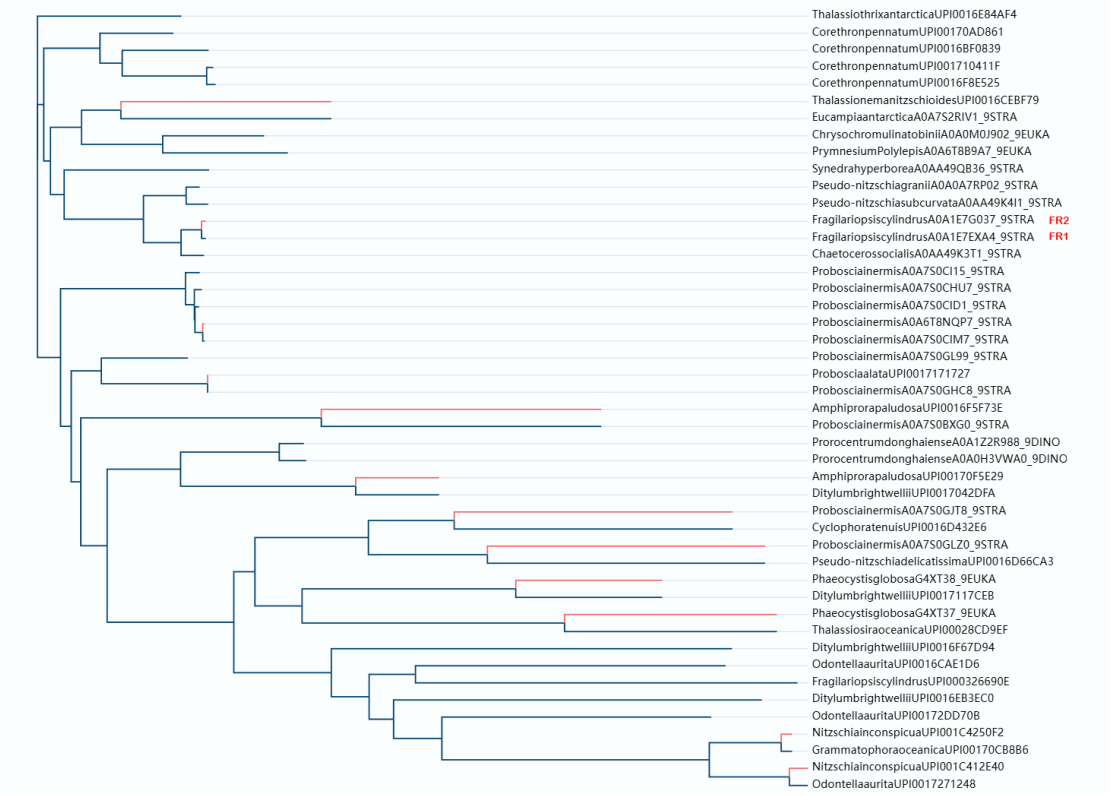


**Figure 2.7 Neighbour-Joining tree showing the taxonomic classification of diatom microbial rhodopsins sequences.** The tree was constructed using diatom microbial rhodopsin protein sequences, with *Fragilariopsis cylindrus* FR1 and FR2 highlighted in red. The tree illustrates the evolutionary relationships between diatom microbial rhodopsins, dividing them into two distinct clusters. Branch lengths represent the evolutionary distance between the sequences.

**Analysis of phylogenetic characteristics**

Based on 2850 homologous of FR1 rhodopsin protein sequences obtained from the Tara Ocean dataset, a Maximum Likelihood (ML) phylogenetic tree was constructed to visualise and compare the evolutionary history and phylogenetic relationships of diatom microbial rhodopsins in the natural marine environment (Figure 2.8). According to the ML tree, the diatom branch (highlighted in red) reveals the evolutionary relationships of diatom microbial rhodopsins within their broader taxonomic context. Diatom microbial rhodopsins form a distinct group closely related to other eukaryotic algae, such as those in the Haptophyta and Pyrrophyta lineages, indicating that microbial rhodopsins in these photosynthetic organisms likely share a common evolutionary origin. This finding is consistent with the observations of Marchetti et al. (2015; 2012). The close phylogenetic relationship among eukaryotic organisms suggests potential functional similarities, particularly in the roles microbial rhodopsins play in light absorption and energy conversion. Additionally, a large number of microbial rhodopsin sequences of unlabelled species have been detected in environmental samples of diatoms, suggesting that the abundance of microbial rhodopsin in eukaryotic algae, especially diatoms, is higher than has been found so far, and there may still be potential species of microbial rhodopsin that have not yet been discovered.

In contrast, the prokaryotic branch, shown in green, displays an evolutionary distance from the eukaryotic microbial rhodopsins. This suggests that although prokaryotic microbial rhodopsins, such as those found in bacteria, perform similar functions (e.g., light-driven proton pumps), their evolutionary history and structural characteristics are significantly different. These differences may stem from the ancient origin of microbial rhodopsins in prokaryotes or their early divergence from the microbial rhodopsins found in eukaryotic organisms by horizontal gene transfer (Marchetti et al., 2015; Strauss et al., 2023).

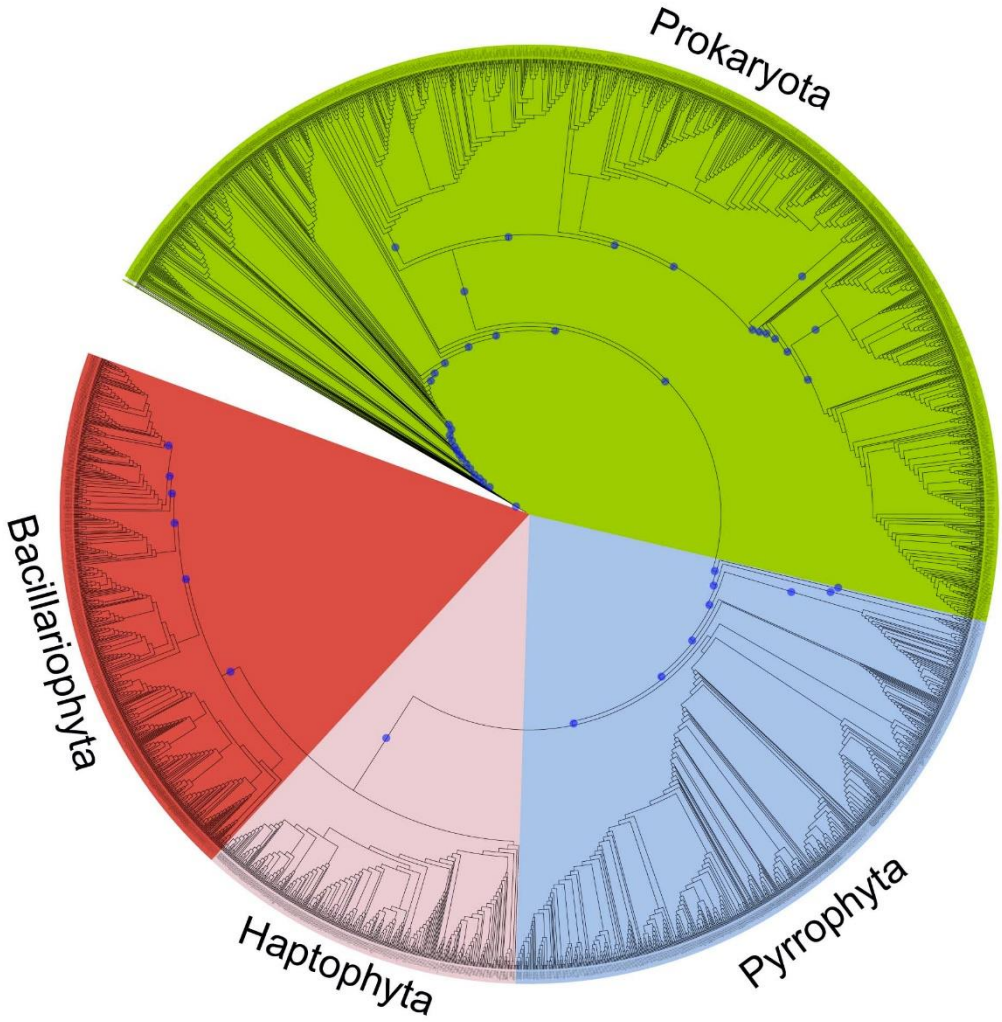


**Figure 2.8 Maximum Likelihood phylogenetic tree based on 2850 homologous FR1 rhodopsin protein sequences from the Tara Ocean dataset.** The tree illustrates the evolutionary relationships between microbial rhodopsins across different taxonomic groups, including Prokaryota (green), Bacillariophyta (diatoms) (red), Haptophyta (pink), and Pyrrhophyta (blue). Bootstraps larger than 60% on main branck are demonstrated as light blue circle (n=2850).

**Physiological characterisation of diatom xanthorhodopsin FR1 and FR2**

As described before (Figure 2.1), FR1 and FR2 microbial rhodopsins share identical amino acid sequences. Despite this, it remains unclear whether these two microbial rhodopsins perform identical functions, particularly in terms of ion specificity and environmental adaptation. To investigate this, we conducted membrane potential experiments and real-time quantitative PCR (qPCR) to shed light on their function as proton pumps and assess their expression under various environmental conditions.

The membrane potential experiments were performed by Shiqiang Gao et al. at the University of Würzburg, Germany. These results are illustrated in Figures 2.9 and 2.10. Initially, we tested the absorption spectrum of FR1, which indicated that its peak activity is within the green light spectrum, around 516 nm (Figure 2.9). This aligns

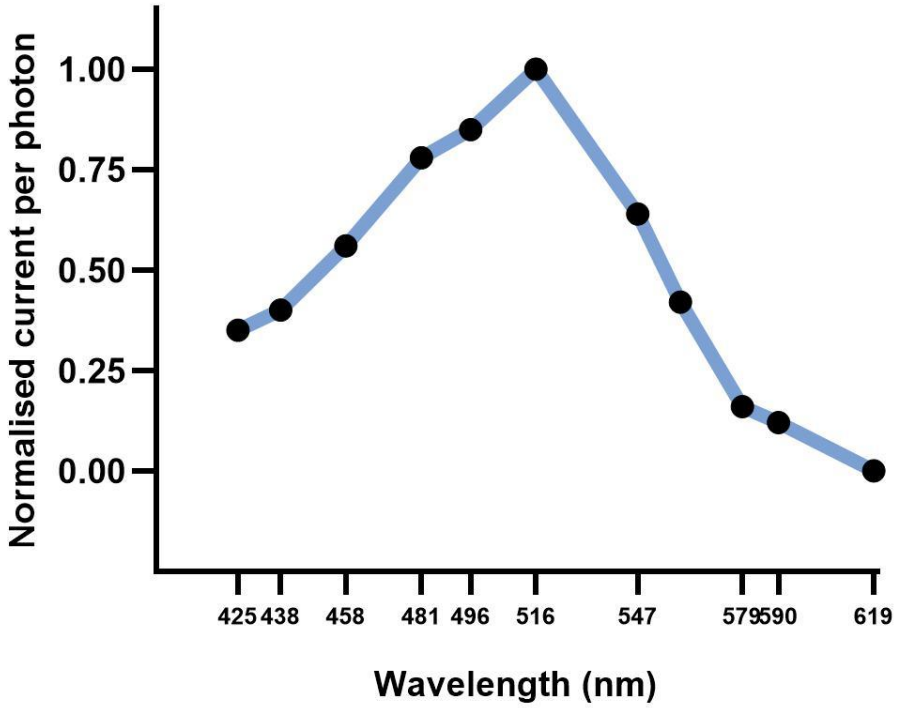


**Figure 2.9 Action spectrum of FR1.** Photocurrents of FcR1 were measured in NMG buffer at pH 7.5 with a membrane potential of −20 mV. Normalised data were obtained from Shiqiang Gao and Jan Strauss et al. (Strauss et al., 2023).

with the typical absorption range of microbial rhodopsins, which often exhibit maximum photocurrent responses in the blue-green light range, supporting its potential role in light-driven proton transport.

Following this, Two-Electrode Voltage Clamp (TEVC) measurements were carried out under green light illumination (530 nm) to explore the ion transport properties of both FR1 and FR2 (Figure 2.10). The results clearly showed that both rhodopsins generated typical ion pump signals, confirming their function as ion transporters. To further determine the ion specificity of FR1, we conducted additional TEVC measurements in various buffer solutions containing different ions, including sodium ($Na^+$), chloride ($Cl^-$), and potassium ($K^+$). Surprisingly, there was no significant variation in the photocurrent intensities across these buffer conditions (Figure 2.10c). This suggests that FR1 functions as a proton-specific pump, consistent with other microbial rhodopsins that act as light-driven proton pumps.

Considering that *Fragilariopsis cylindrus* is a polar diatom that thrives in cold marine environments, we further explored whether FR1 might have evolved cold-adaptive features. To test this hypothesis, we compared the activity of FR1 with that of bacteriorhodopsin (BR), a well-characterised microbial rhodopsin that typically functions at moderate temperatures. Both FR1 and BR were subjected to activity tests at three different temperatures: 10°C, 20°C, and 30°C to simulate ecologically relevant conditions encountered by *Fragilariopsis cylindrus* and *Halobacterium halobium* (Figure 2.11) (Nakayama, 1998). Temperatures below 10°C were not tested due to technical limitations of the oocyte system and signal stability in TEVC measurements. However, the selected range (10–30°C) still effectively captures the differential thermal responses of cold-adapted rhodopsins under ecologically relevant conditions. The results showed a stark difference in temperature sensitivity between FR1 and BR. While BR displayed a significant decline in activity at lower temperatures, FR1 maintained robust photocurrent responses even at 10°C. In fact,

FR1's activity at ten °C was markedly higher than BR's, suggesting that FR1 has undergone evolutionary adaptations to function efficiently in cold environments, such as the polar waters where *F. cylindrus* is found.

These findings prove that FR microbial rhodopsin could work as a proton pump in organisms similar to their homologs bacteriorhodopsin, proteorhodopsin and xanthorhodopsin. In addition, the cold resilience of FR1 highlights its potential role in supporting *F. cylindrus*'s survival in extreme polar conditions, where temperatures are highly variable.

Subsequently, to verify the expression of the FR genes, absolute quantification RT-qPCR for FR gene and relative quantification RT-qPCR for FR1/FR2 were conducted with the assistance of Jan Strauss. *Fragilariopsis cylindrus* was cultivated under various environmental conditions to assess its gene expression response to different stress factors and growth environments. These conditions included polar summer growth conditions (nutrient-replete, +4°C, 35 µmol photons $m^{-2}$ $s^{-1}$), freezing temperatures (−2°C), elevated temperatures (+10°C), elevated carbon dioxide levels (1000 ppm $CO_2$), iron starvation (−Fe), prolonged darkness (1 week), half-saturation with silicate (0.32 µM Si), and exposure to specific light conditions, including red light (550–700 nm) and blue light (480–540 nm). RNA was extracted from these cultures and subsequently used for cDNA synthesis to evaluate the gene expression levels of FR1 and FR2 under these diverse environmental conditions. Results are shown in Figure 2.12. Interestingly, although FR1 and FR2 are 100% identical at the amino acid level, they exhibit differential expression under various environmental conditions. The expression of FR1 is particularly influenced by iron availability, a critical factor in the nutrient-limited waters of the Southern Ocean (Strauss et al., 2023), whereas FR2 have high expression level all the time. The absolute RT-qPCR results also indicate that under the iron limitation, significant increased cDNA of FR gene were obtained (Figure 2.12b). This finding is significant as it demonstrates the

potential of these microbial rhodopsins to contribute to cellular energy metabolism through another phototrophic pathway, especially under conditions where traditional photosynthetic pathways may be limited (Marchetti et al., 2015). Additionally, to the best of our knowledge, this is the first time that two proteins with the same amino acid sequence have been found to have completely different gene expressions. This observation suggests that their regulatory regions may have undergone divergent evolutionary trajectories, potentially due to differences in cis-regulatory elements within their promoter sequences or chromosomal positioning. This phenomenon may represent a case of regulatory sub-functionalisation arising under conditions of functional redundancy—a mechanism previously reported primarily in core genes of animals and plants. For example, the H3F3A and H3F3B genes in animals encode the same H3.3 histone protein despite showing notable nucleotide-level differences across both intron and exon (Muhire et al., 2019). Similarly, in *Lycopersicon esculentum*, the Cab-6A and Cab-6B genes differ by only eight base pairs but encode the same photosynthesis-associated protein (Pichersky et al., 1987).

However, such cases typically occur in highly conserved housekeeping genes and involve only minor DNA sequence differences. In contrast, the FR1 and FR2 gene pair identified in this study not only encodes completely identical protein sequences but also shows substantial divergence at the DNA level and displays distinct regulatory behaviours. Notably, this represents the first known case of such regulatory divergence in microalgae, particularly in rhodopsin-like light-responsive proteins with ecological relevance.

Therefore, the differential expression of FR1 and FR2 provides a rare and illustrative example of how regulatory sequences can evolve independently of protein function, allowing organisms to adapt to complex environmental conditions. This discovery offers a novel perspective on the regulation of light-responsive genes and opens new avenues for exploring the adaptive mechanisms of polar diatoms under iron limitation

and other environmental stresses.

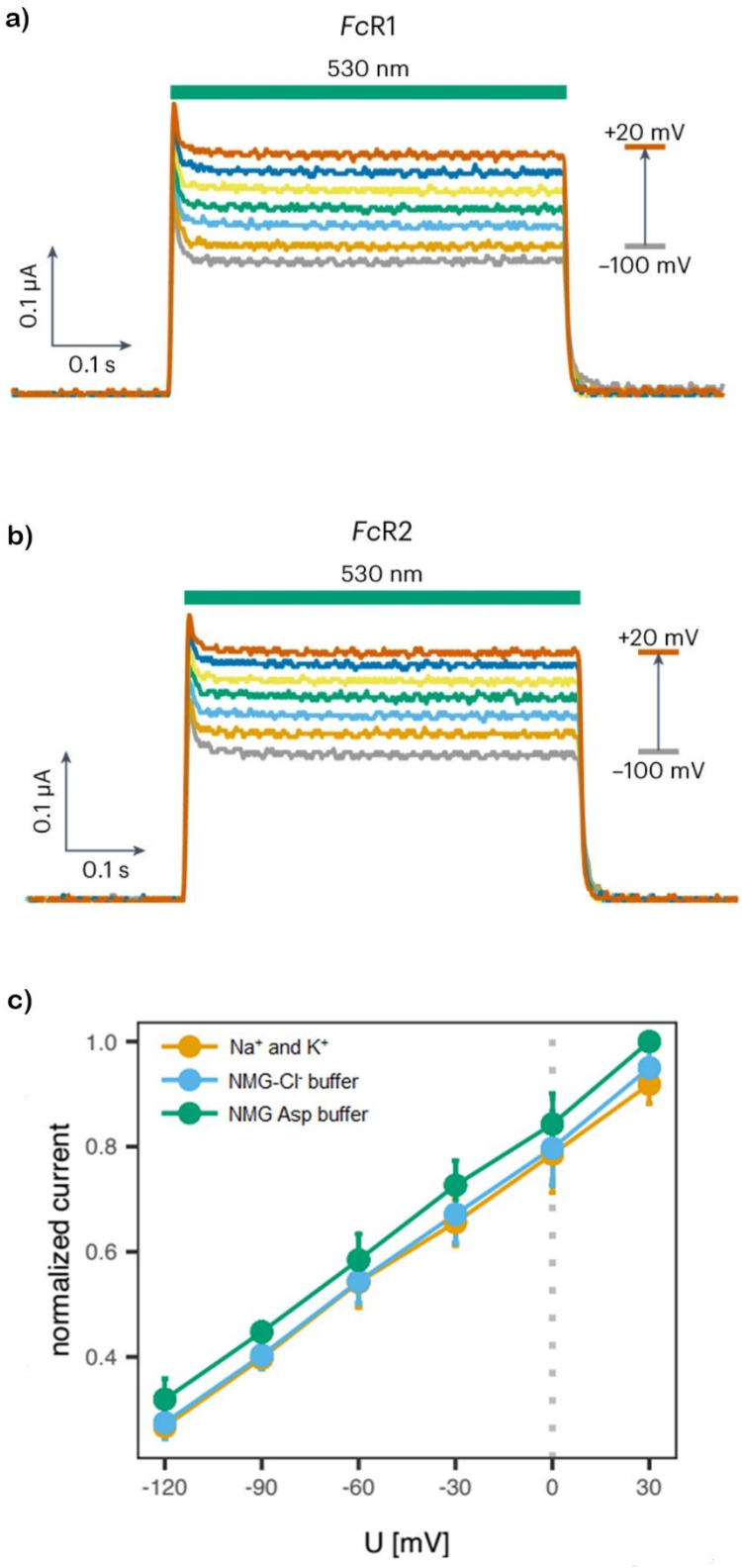


**Figure 2.10 Ion pump characterisation of FR1 and FR2 measured using Two-Electrode Voltage Clamp (TEVC).** Figure(a) and (b) show the photocurrent traces of FR1 and FcR2, respectively, under green light illumination (530 nm). The currents were recorded with membrane potential steps ranging from −100 mV (gray) to +20 mV (orange) in 20 mV increments. Figure (c) displays the normalized photocurrent response of FcR1/2 under three different buffer conditions: $Na^+$ and $K^+$ (yellow), NMG-$Cl^-$ (blue), and NMG-Asp (green). NMG stands for N-Methyl-D-glucamine. Data obtained from Jan Strauss and Shiqiang Gao (Strauss et al., 2023).

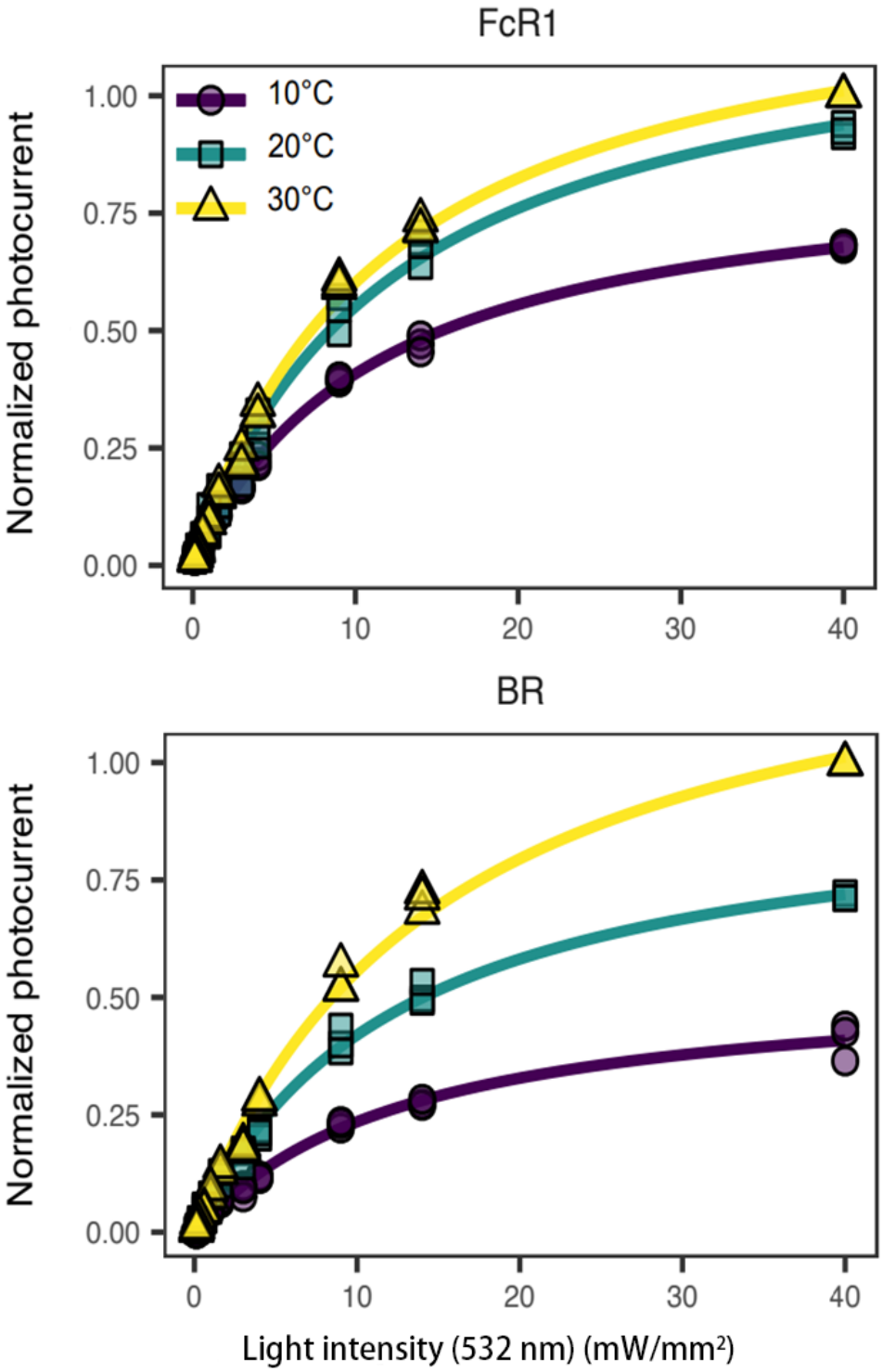


**Figure 2.11 Activity tests of FR1 rhodopsin and bacteriorhodopsin (BR) under different temperatures.** The photocurrent responses were measured at 10°C (purple), 20°C (cyan), and 30°C (yellow) under varying light intensities (532 nm) for FR1 (top panel) and BR (bottom panel). Figure edited from Jan Strauss's data (Strauss et al., 2023).

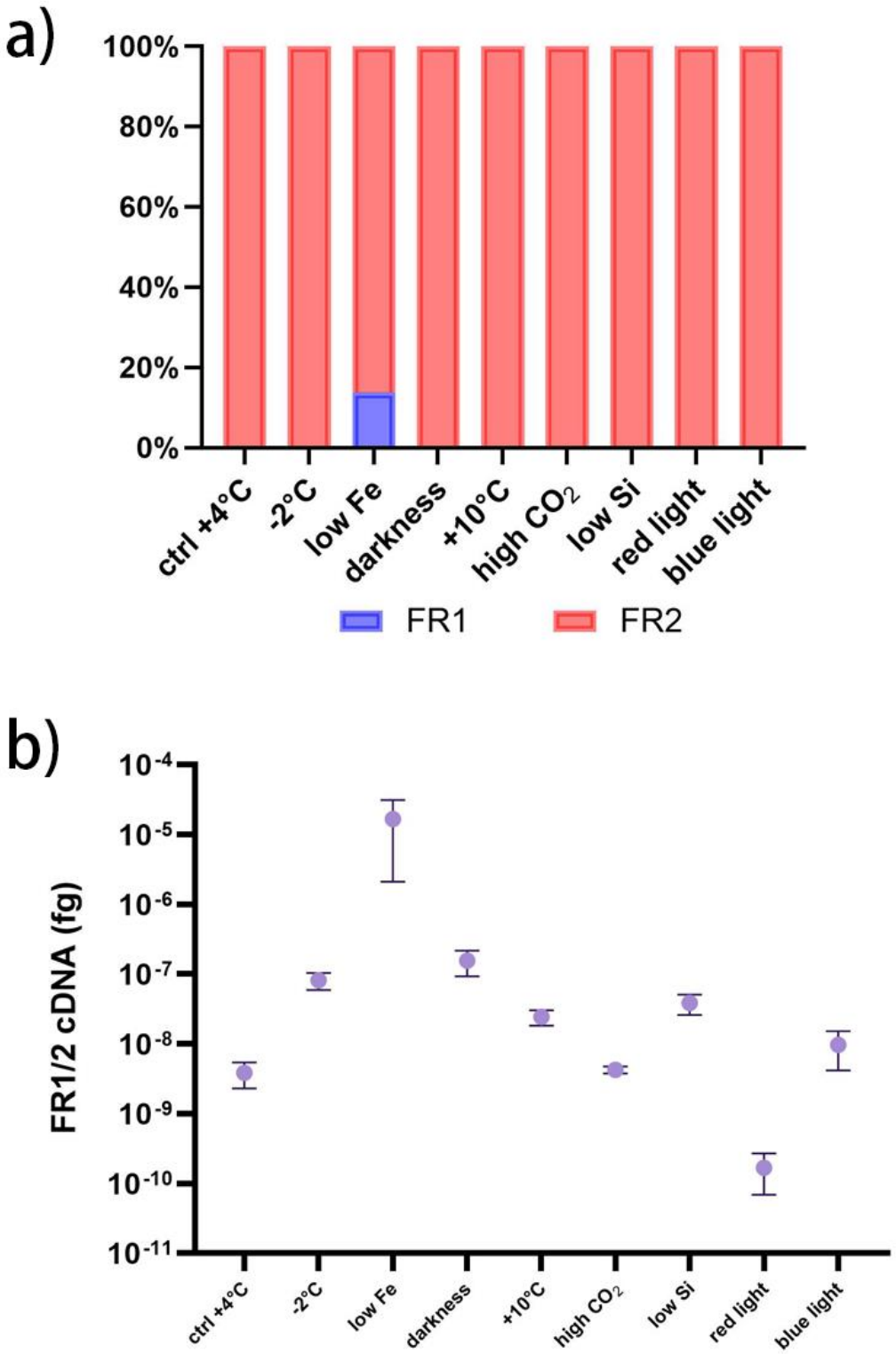


**Figure 2.12 Gene expression levels of two variants FR1 and FR2 under nine different cultivation conditions.** (a) Relative qPCR results depicting the expression of FR1 (blue) and FR2 (red) across various conditions. (b) Absolute qPCR results displaying the total cDNA concentration of FR1 and FR2 combined (FR1+FR2) under the same nine conditions. Values are represented in femtograms (fg) of cDNA. Data obtained from Jan Strauss.

**Subcellular localisation of FR1 in other model diatoms**

Through our investigations, we confirmed that both FR1 and FR2 are proton-pump rhodopsins. Notably, FR1 is specifically expressed under iron-limited conditions, suggesting a potential role in supporting diatom survival in such environments. However, the detailed mechanisms underlying FR1's contribution to diatom adaptation to iron limitation remain unclear. To begin addressing this, we attempted to overexpress FR1 in two model diatoms, *Phaeodactylum tricornutum* and *Thalassiosira pseudonana*, tagging FR1 with a GFP signal at the C-terminal to aid in localising the protein.

Our results demonstrated strong GFP signals in both transformed strains of *P. tricornutum* and *T. pseudonana*, while no GFP signals were detected in the wild-type strains under identical imaging conditions (Figure 2.13). In both transformed strains, the GFP signals co-localized with chlorophyll fluorescence in plastids, suggesting that the subcellular localisation of FR1 is likely within the plastid.

Based on these localisation results, we developed a schematic model to hypothesise the potential roles that FR1 rhodopsins might play in diatoms under iron-limited conditions (Figure 2.14). In **hypothesis 1**, we propose that microbial rhodopsin FR1 localises to the outer plastid membrane, where it could facilitate iron co-transport by generating a proton gradient, thereby aiding in iron uptake under limiting conditions. In **hypothesis 2**, microbial rhodopsin FR1 could localise to the thylakoid membrane, where it may support ATP synthesis during periods of limited photosynthesis, functioning similarly to bacteriorhodopsins in bacteria (Bar-Shalom et al., 2023; Davison et al., 2022). This would enable diatoms to maintain energy production even when photosynthetic activity is compromised by environmental stresses such as iron scarcity.

A more precise understanding of microbial rhodopsin's subcellular localisation is

critical to elucidating its mechanisms and functions. However, due to the limitations of current imaging resolution, we have been unable to confirm the exact membrane on which FR1 is localised—whether it is the chloroplast membrane, the thylakoid membrane, or another plastid membrane. Furthermore, previous work by Jan Strauss suggests that the use of GFP may interfere with microbial rhodopsin expression or function, making fluorescence targeting unreliable for accurately tracking microbial rhodopsin localisation. Therefore, to address these challenges, in the next chapters, I conducted cell-sliced Immunogold labelling using transmission electron microscopy (TEM) to achieve high-resolution subcellular localisation of diatom microbial rhodopsin. This approach will provide the necessary clarity to refine our hypotheses and advance our understanding of the role of microbial rhodopsins in diatom adaptation.

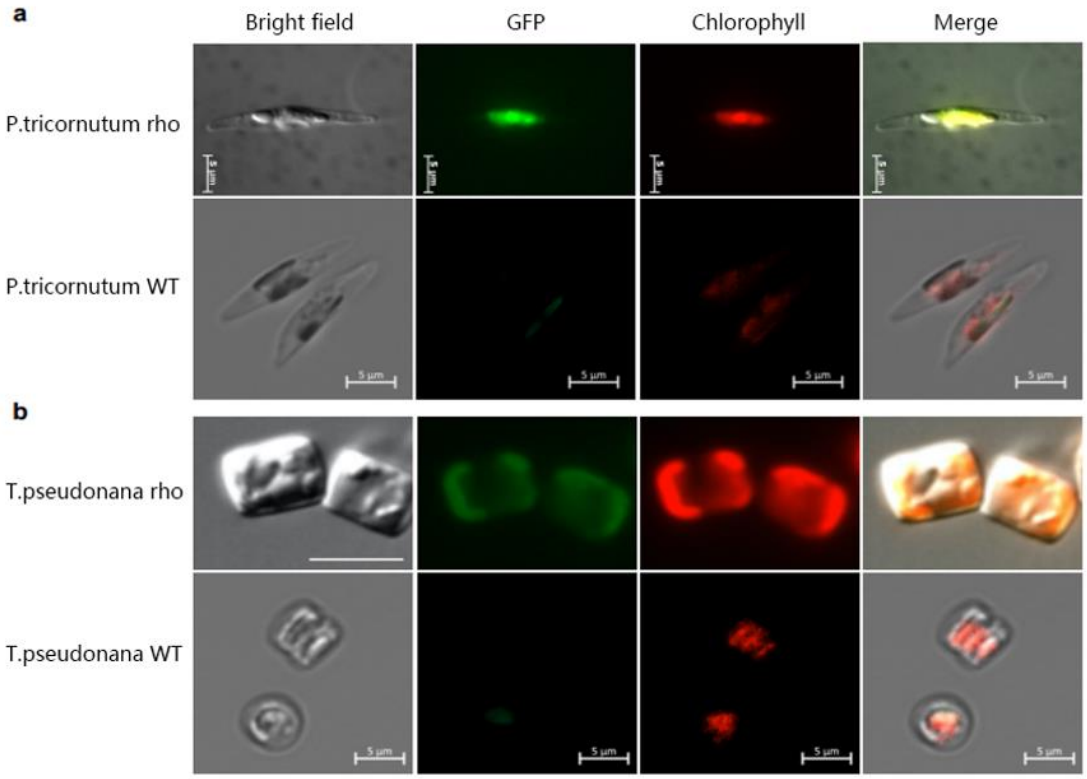


**Figure 2.13 Subcellular localisation of microbial rhodopsin in model diatom *P. tricornutum* and *T. pseudonana*.** (a) Microscope images of rhodopsin knock-in *P. tricornutum* and wild-type *P. tricornutum* strain. Images were shown in four channels for bright field, GFP channel for microbial rhodopsin localisation, Alexa568 channel for chlorophyll, and merged image to visualise co-localisation. (b) Microscope images of rhodopsin knock-in *T. pseudonana* and wild-type *T. pseudonana* strain. Images were shown in four channels for bright field, GFP channel, Alexa568 channel, and merged view. Data were collected by me and Jan Strauss.

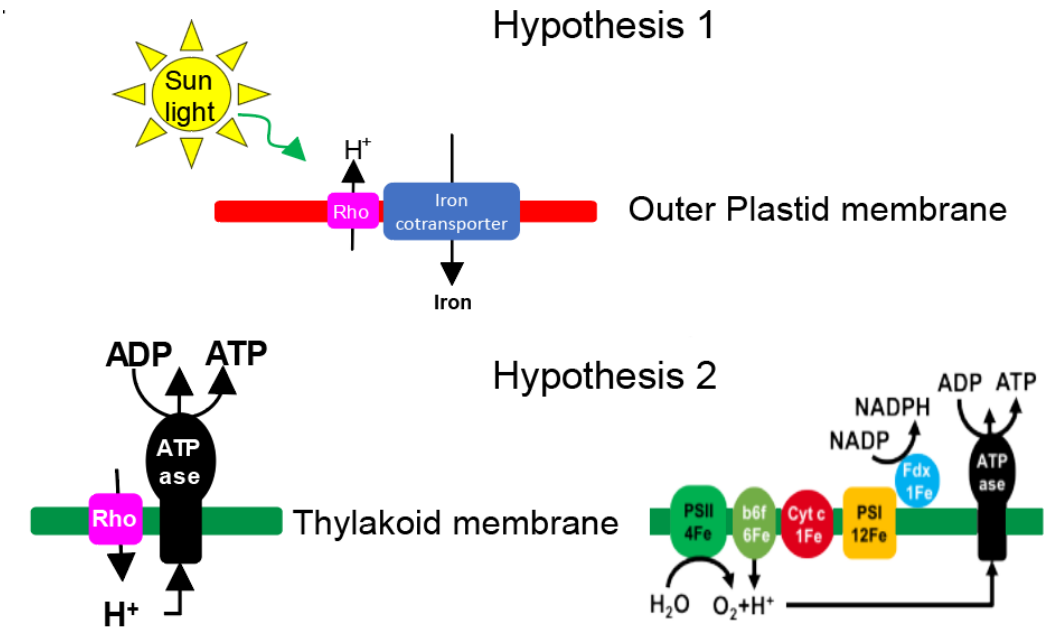


**Figure 2.14 Schematic model for hypothesises of microbial rhodopsin FR1 mechanisms in diatom.** For hypothesis 1, FR1 is localised at the outer plastid membrane and supported by the iron cotransporter. In hypothesis 2, FR1 is localised at the thylakoid membrane and supports the ATP synthesis. Model developed by Jan Strauss (2012).

**Conclusions**

In this chapter, we conducted a comprehensive analysis of the microbial rhodopsin genes FR1 and FR2 in *Fragilariopsis cylindrus*, focusing on their sequences and predicted structures using publicly available databases. We revealed that while both microbial rhodopsins share identical amino acid sequences, their regulatory and functional characteristics differ under various environmental conditions, indicating potential specialisation in their roles.

I also extended our investigation to explore the presence of microbial rhodopsins in other diatom species in natural environments, providing valuable insights into the evolutionary and ecological significance of these proteins. This broader analysis suggests that microbial rhodopsins may play a pivotal role in the ecological success of diatoms, particularly in adapting to varying light conditions and other environmental stresses.

Through membrane potential experiments, we confirmed that both FR1 and FR2 function as proton pumps. FR1 exhibited its peak photocurrent activity under green light (~516 nm), highlighting its potential role in light harvesting and energy conversion. Notably, FR1 showed enhanced performance in colder temperatures, suggesting that it has evolved cold-adaptive features, which may be critical for its function in the polar marine environments where *F. cylindrus* thrives.

Our laboratory experiments further demonstrated that FR1 is highly responsive to environmental changes, particularly under iron-limited conditions. This suggests that FR1 may play a crucial role in supporting diatom growth under the iron-deficient conditions prevalent in polar regions. However, although we investigated that the microbial rhodopsin FR1 is localised at the plastid, the detailed mechanisms by which a proton-pump rhodopsin, like FR1, contributes to diatom survival and adaptation under iron limitation remain elusive. This raises important questions about the

potential interactions between FR1 activity and iron metabolism, which could involve complex regulatory networks yet to be fully explored. To better understand the FR1 functions, we developed a hypothesis of microbial rhodopsin based on its subcellular localisation.

Given these findings, the subsequent chapters will focus on the detailed investigation of FR1's function and its potential mechanism in diatoms, particularly emphasising its role in iron limitation. By narrowing the scope to FR1, we aim to uncover the specifics of this unique adaptation strategy and understand how FR1 contributes to diatom adaptation in challenging polar environments.

# Chapter 3

# Characterisation of diatom microbial rhodopsins and testing the biological role of a selected variant *in vivo*

## Introduction

*Thalassiosira pseudonana* is a centric diatom with ancestry, but mainly found in seawater (Figure 3.1) (Alverson et al., 2011). *T. pseudonana* can tolerate an extensive range of salinity and temperature (Baek et al., 2011). Due to its high growth rate and relatively small genome size, *T. pseudonana* has become a significant model organism in the field of marine biology. It was selected as the first diatom to have its genome fully sequenced and to have an established transformation method (Armbrust et al., 2004). As a result, *T. pseudonana* has served as a central platform for international collaborative research, significantly advancing our understanding of diatom biology and marine ecosystem dynamics. Since the development of molecular tools for *T.*

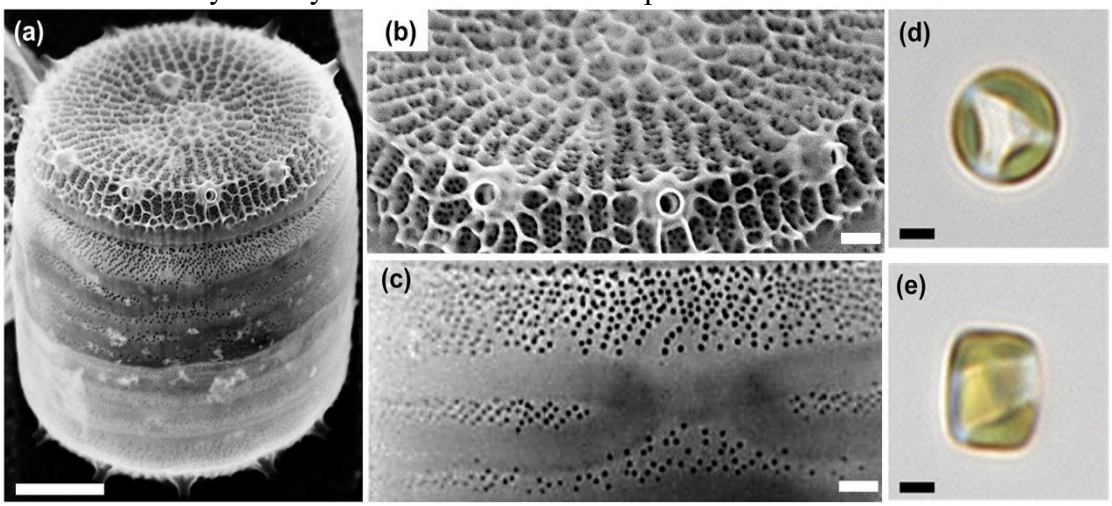


**Figure 3. 1 Cell images of *T. pseudonana* under scanning electron microscopy (a-c, scale bar 1μm).** Bright field microscope image of single cell (d-e, scale bar 2μm). Cited from Poulsen and Kröger (2023).

*pseudonana*, various gene editing methods, including overexpression (Poulsen et al., 2006), RNA silencing (Cook & Hildebrand, 2016; Kirkham et al., 2017), and gene knock-out (Hopes et al., 2016; Trentacoste et al., 2013), have been employed to

investigate specific biological questions. These techniques have matured significantly, making gene editing in *T. pseudonana* a well-established and reliable approach.

Research utilising *T. pseudonana* has provided valuable insights into the genetic and molecular mechanisms underlying diatom biology. The availability of advanced genetic tools has facilitated studies on various topics, from basic cellular processes to complex interactions (Kirkham et al., 2017; Schaum et al., 2018). As a result, *T. pseudonana* continues to be a pivotal organism in marine biological research, driving forward our understanding of diatom physiology, adaptation, and their roles in marine ecosystems. According to the whole genomic sequencing results, there is no microbial rhodopsin gene in *T. pseudonana* (Armbrust et al., 2004), making it an ideal model organism for using a gene editing method to introduce and overexpress a foreign xanthorhodopsin gene FR1 from diatom *Fragilariopsis cylindrus* to investigate its function and potential mechanism in diatom (Strauss et al., 2023).

In this chapter, I analyse the function and mechanisms of xanthorhodopsin FR1 using knock-in and heterologous expression in the model diatom *Thalassiosira pseudonana*. Several advanced methods, including rapid light curve analysis, real-time fluorogenic quantitative PCR, and immunogold staining, were employed to gain a comprehensive understanding of FR1's function and mechanisms.

The primary aim of this chapter is to elucidate the functional mechanisms of FR1 and its role in diatoms' adaptation to iron-limited environments. By integrating these techniques, we can assess the physiological and molecular responses of *T. pseudonana* expressing FR1 under varying iron conditions, thereby providing insights into how FR1 contributes to the diatom's survival and growth in nutrient-limited waters.

This chapter will significantly contribute to our broader understanding of the ecological significance of microbial rhodopsins. Additionally, the findings may have

important applications in biotechnology and marine resource management, potentially leading to new strategies for harnessing microbial rhodopsins for energy production and environmental sustainability.

## Materials and methods

### Growth Media

Iron-free Aquil* medium was prepared according to the National Center for Marine Algae and Microbiota (NCMA) protocol (Sunda et al., 2005). Basic synthetic ocean water was eluted through a column containing Poly(styrene-divinylbenzene) 1% cross-linked ion exchange resin (Alfa Aesar, USA) to remove iron contamination and filter sterilised with 0.2 μm filter unit (Millipore) (Mori et al., 2011). Subsequently, all trace metals were added except iron. Iron-free trace metals were mixed according to the Aquil* protocol (Sunda et al., 2005). The iron stock was prepared separately at a final concentration of 1 mmol $L^{-1}$ $FeCl_3.6H_2O$ with 100 μmol $L^{-1}$ ethylenediaminetetraacetic acid (EDTA), to bind with metal ions to form phytoplankton inaccessible chelates. The all-trans-retinal stock solution was prepared at a concentration of 10 mmol $L^{-1}$ retinal dissolved in 100% DMSO.

### Strains, Culturing and growth rates

The diatom strain of *T. pseudonana* (strain CCMP1335) was obtained from the NCMA. All growth experiments were performed with the diatom strain *Thalassiosira pseudonana* CCMP 1335. All cultures were grown in a 20 ℃ incubator at 38 μmol photons $m^{-2}$ $s^{-1}$ white light and 24-hours daylight (QSL-2101, Biospherical Instruments Inc., USA). Cell cultures were added with a mixed-antibiotic treatment using the following antibiotics according to Strauss (2012) to remove bacterial contamination: ampicillin (50 μg $mL^{-1}$), gentamycin (1 μg $mL^{-1}$), streptomycin (25 μg $mL^{-1}$), chloramphenicol (1 μg $mL^{-1}$), and ciprofloxacin (10 μg $mL^{-1}$). This comprehensive antibiotic regimen ensured the elimination of potential bacterial

contaminants, thereby maintaining the purity and integrity of the diatom cultures for subsequent experiments.

In control treatment and normal cultivation stock, cells were maintained and grown in the iron-enriched Aquil* media (1000 nmol $L^{-1}$ iron). For iron-limitation experiments, cells were transferred into an iron-free Aquil* medium and cultured for five days under iron starvation before the start of the iron-limitation experiments. For the pre-experiment, all diatom cultures were transferred into extremely iron-limited conditions (2.50nM, 1.00nM, 0.25nM, 0.00nM) to simulate the natural western Atlantic Ocean (Rijkenberg et al., 2014). Additionally, considering that the synthesis of microbial rhodopsin in overexpressed strains requires additional retinal, the effect of retinal and DMSO, which work as a solvent of retinal, concentrations on *T. pseudonana* were also tested.

In preparation for the formal experiments, iron-replete stock cultures were initially transferred to an iron-free Aquil* medium and allowed to grow for approximately three days. This step was to deplete any iron stored in cells to ensure iron starvation conditions. After that, all pre-treated, iron-starved diatom cells were inoculated into either iron-replete Aquil* medium as the control group (1000 nmol L-1 iron, 3 μmol $L^{-1}$ retinal) or iron-limited Aquil* media as the treatment group (150nmol L-1 iron, 3 μmol $L^{-1}$ retinal) at an initial concentration of approximately $8\times 10^5$ cells $ml^{-1}$. Lower initial cell densities or prolonged periods of iron starvation may lead to cell mortality and inhibit growth in later cultures under iron limitation. Five replicates each were used for control and treatment groups. To estimate the cell fitness, one-millilitre subsamples were taken from the experiment every 24 hours to measure the cell density for specific growth rate and maximum quantum yield of PSII (Fv/Fm) as an index for cell fitness (Parkhill et al., 2001). The cell density was estimated by a Multisizer 4e Coulter Counter (Beckman, USA). Cell-specific growth rates (μ) were calculated according to the following equation:

$$\mu = (\ln(Nt2) - \ln(Nt1))/\ \Delta t$$

Where $N_{t1}$ and $N_{t2}$ are the cell density (cells $mL^{-1}$) at sampling times $t_1$ and $t_2$, and $\Delta t$ represents the time between the two measurements (Guillard, 1973). Considering differences in the lag time between wildtype (WT) and xanthorhodopsin (RHO) knock-in *T. pseudonana* cell lines, the specific growth rates were calculated from days 4 to 6 for WT and days 3 to 5 for the RHO knock-in cell lines. These days were selected as they represent the exponential growth phase concerning differences in the lag phase between WT and RHO knock-in cell lines.

The maximum quantum yield of PSII (Fv/Fm) was assessed every 24 hours using a Phyto-pulse-amplitude-modulated (PAM) fluorometer (Heinz Walz, Germany). A dark pre-treatment was applied to all samples before measuring. The quantum yields *in vivo* were calculated for each culture using the PhytoWin software with the following equation:

$$Fv/Fm = (Fm - F0)/Fm$$

Where Fm is the maximum fluorescence yield, and F0 is the minimum fluorescence yield (Maxwell & Johnson, 2000).

Student t-test was performed to evaluate the significance of the difference between the growth of the two types. Data were considered statistically significant for p-values $\leq 0.05$.

**Generate microbial rhodopsin knock-in cell lines**

**Bacterial transformation and plasmid preparation**

Plasmids used for generating microbial rhodopsin knock-in cell lines were constructed by Jan Strauss (2012). Vector maps are shown in Figure 3.2. The endogenous fcp promoter and terminator were used in these two plasmids (Poulsen et al., 2006).

Plasmid pTp-FcpNAT contains selective gene nourseothricin (NAT), while the plasmid pTpFcpFR1 contains full-length xanthorhodopsin FR1 sequences. Plasmids were checked by enzyme digestion and sequenced by Eurofins Genomics UK.

To initiate the cloning process, one µl of plasmid stock was introduced into high-efficiency NEB 5-alpha competent E. coli cells, adhering strictly to the transformation protocol provided by New England Biolabs (NEB). Following transformation, aliquots of 20 µl and 40 µl from the transformed cells suspended in SOC medium were evenly spread onto separate Luria-Bertani (LB) agar plates. These plates were fortified with 100 µg/ml ampicillin, ensuring that only cells that had successfully incorporated the plasmid would proliferate. The plates were then incubated at 37°C overnight, facilitating optimal growth and expression of the transformants.

The following day, individual colonies were picked and cultured in a 10 ml LB medium containing 100 µg/ml ampicillin to expand the transformed cell amount. These cultures were incubated overnight under constant shaking. Subsequently, cells were harvested by centrifugation, and plasmids were extracted using the Monarch Plasmid Miniprep Kit (NEB, UK).

To verify the integrity and size of the cloned plasmids, they underwent both single and double restriction enzyme digestions, followed by electrophoresis to visualise full-size linearisation of the plasmids.

Before utilising these plasmids for biolistic transformation, a rigorous precipitation protocol was applied to eliminate any potential residual impurities. This involved adding 1/10 volume of sodium acetate to the DNA solution, followed by pipette thorough mixing. Then, two volumes of chilled 100% ethanol were added. The mixture was left to precipitate overnight at -20°C. The next day, the solution was centrifuged at maximum speed for 15 minutes at 4°C. The supernatant was discarded, and the DNA pellet was washed with 1 ml of 70% ethanol, followed by another round

of centrifugation for 5 minutes at maximum speed and 4°C. After carefully removing the supernatant, the DNA pellet was air-dried and finally resuspended in an appropriate volume of DNase-free water to prepare it for further experiments.

**Heterologous expression of FR1 in *Thalassiosira pseudonana***

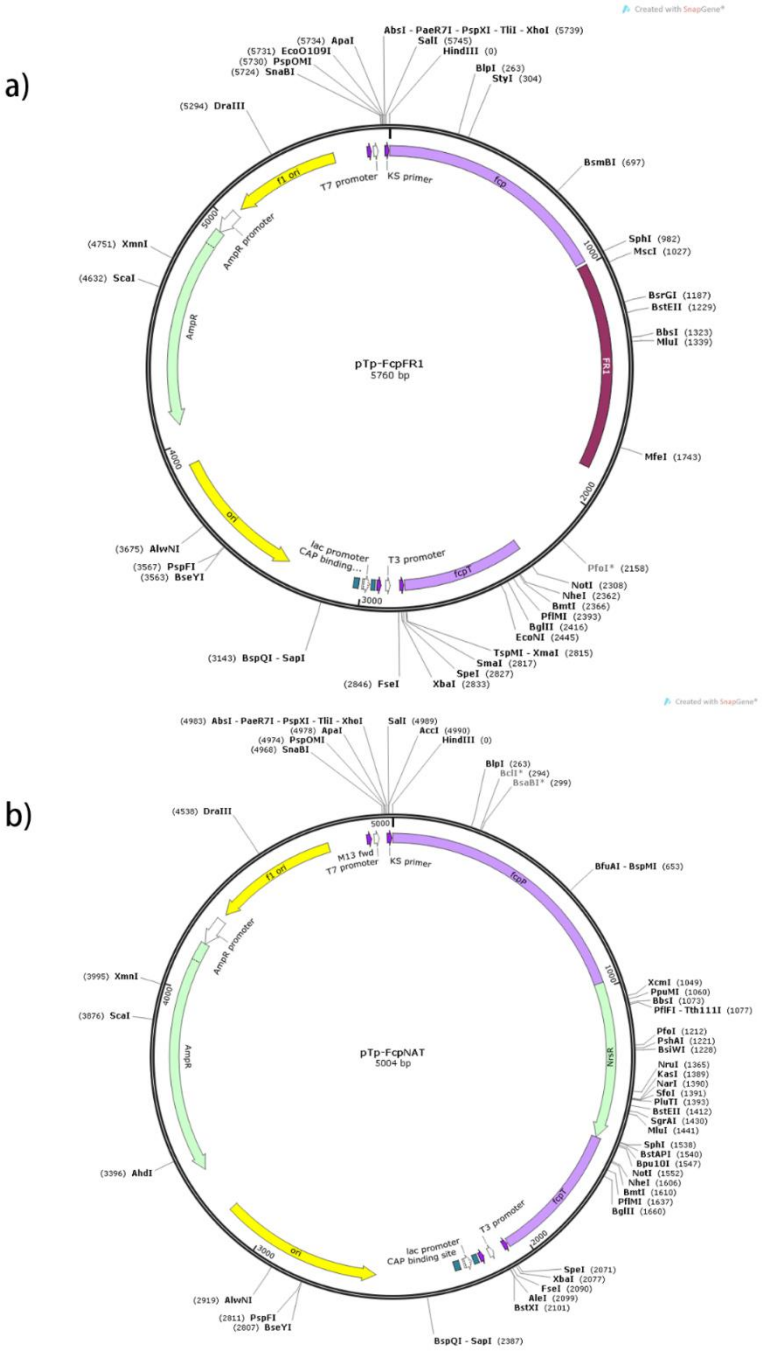


**Figure 3.2 Vector map of pTp-FcpFR1 and pTp-FcpNAT.** Two plasmids were used for a co-transformation to generate FR1 knock-in cell line.

Shooting particles were prepared and coated according to the protocol outlined by Kroth (2007). In this procedure, 50µl (3 mg) of 0.7µm tungsten particles, known as M10, were meticulously coated with 5µg of plasmid DNA. The coating process occurred in a reaction mixture containing calcium chloride and spermidine, which are crucial for facilitating DNA binding to the particles. This preparation yielded enough material for five separate bombardments, with each shot comprising 600 ng of tungsten particles and 1µg of plasmid DNA. A control experiment was included to evaluate the transformation efficacy. In this control, water was used in place of plasmid DNA to prepare the particles. This negative control served as a benchmark to assess the background level of transformation success, thereby enabling a comparative analysis of the transformation efficiency when plasmid DNA was used.

Before the transformation, two concentrations of agar plates, 1.5% and 0.8%, were prepared. The non-selective 1.5% agar plate was used for particle shooting buffer, while 0.8% Aquil* plates supplemented with 100µg/ml NAT were prepared for selecting transformed cells. According to the previous study, NaCl concentration could limit the efficiency of antibiotics (Muto et al., 2013). Therefore, all plates were made as half-salinity Aquil* plates by mixing pre-heated full-salinity Aquil* medium with the same volume of double-concentration agar solution. Additional non-selective 0.8% agar Aquil plates were also prepared to be a positive growth control.

Wild-type *T. pseudonana* cells (5 x $10^7$ cells/ml) were collected using 0.22µm Isopore™ polycarbonate membrane filters (MilliporeSigma) from the exponential growth phase (approximately 8x$10^5$ cells/ml) at room temperature. Filters were placed on a 1.5% agar plate prepared for shooting. Biolistic transformation for generating the FR1 strains followed the protocol of Hopes et al. (2017).

The PDS-1000/He biolistic microparticle delivery system (Bio-Rad) was used to introduce plasmids into the cells based on the manufacturer's instructions. The transformation process uses a rapture disk at 1350 psi, with each shot being executed

in a controlled vacuum environment of 25 mm Hg. To ensure the reproducibility and reliability of results, all bombardments were performed in triplicate, including a negative control where water substituted plasmid DNA to assess baseline transformation efficiency.

After the transformation, the cells were immediately transferred to 15 mL of non-selective, half-salinity Aquil* medium, where they were cultured under continuous white light at an intensity of 38 µmol photons $m^{-2}$ $s^{-1}$ at a stable temperature of 20°C and this cultivation period lasted 24 hours to allow for the recovery and expression of the introduced genes.

The following day, 5 x $10^6$ incubated transformed cells were harvested by centrifugation at 1500rpm. The supernatant was carefully discarded to ensure cell retention. The cell pellet was then resuspended in 100 µL of fresh medium and inoculated onto 0.8% selective agar plates added with 100 µg/ml NAT to select for successfully transformed cells. For comparative analysis and to confirm the viability of the cells post-shooting, 100 µL from the negative control treatment was also spread onto non-selective agar plates, serving as a positive growth control. These plates were then incubated under standard growth conditions. The environment was meticulously maintained to promote the optimal growth of colonies, which were regularly monitored until they became visually apparent. The plates were then cultured under standard growth conditions. The plate lids were lifted every few days to remove condensation and keep air flowing. This environment was meticulously maintained to promote the optimal growth of colonies, which were regularly monitored until they became visually apparent. Following the incubation period, visible colonies were carefully picked from the agar plates using sterile techniques. Each selected colony was then resuspended in 500µl of half-salinity Aquil* medium supplemented with 100 µg/ml NAT. The 12-well plates were maintained under standard laboratory conditions, which include a constant temperature and light exposure, ensuring optimal

growth and development of the diatom colonies. Once the colonies showed robust growth and viability in the 12-well plates, they were transferred to larger flasks containing 25 ml of the same half-salinity selective Aquil* medium for subsequent experiment and storage.

**Screening the transformed cells**

Once cell density from liquid selection and colony cultures reached more than 1x10^6 cells/ml, the genomic DNA (gDNA) was extracted according to Hopes protocol (Hopes et al., 2017). This involved resuspending cell pellets obtained from 5 ml of culture in 10 µl of lysis buffer (10% Triton X-100, 20 mM Tris–HCl pH 8, 10 mM EDTA). To ensure complete cell lysis, this mixture was subjected to a freeze-thaw cycle, starting with incubation at -80°C for 15 minutes, followed by a rapid shift to 95°C for 10 minutes.

For PCR amplification, 2 µl of the lysed sample was used as a template in a 50 µl reaction volume. The PCR reactions were prepared using REDTaq® ReadyMix PCR Reaction Mix™ (Sigma-Aldrich, US). The target genomic region was amplified with specific primers designed for the FR1 sequence:

| Name | Sequence |
|---|---|
| FR271123 F1 | CGTTTGGCCATTCCTTCATATC |
| Rhodopsin screen R | GAACCGGAGATTCCCATCATAG |

PCR amplification was performed with denaturation at 95 °C for 1 min, followed by 35 cycles of 95 °C 30 seconds, 56 °C 30 seconds and 72 °C 1 min; then 72 °C 5 mins. The amplified products were then verified through electrophoresis on a 1% agarose gel, and the bands of interest were sent for sequencing to Eurofins to confirm the specificity and accuracy of the amplification. Positive clones, identified as RHO knock-in mutant cell lines, were thereafter maintained in half-salinity Aquil* medium

supplemented with 100 µg/ml NAT.

**RNA extraction and RT-PCR**

A reverse transcript-PCR (RT-PCR) analysis was conducted to determine the target gene's expression in FR1 knock-in *T. pseudonana* cell lines. Initially, 80 mL of exponential phase cell culture was harvested by centrifugation. These cells were immediately frozen in liquid nitrogen for a rapid freeze-thaw cycle. For cell lysis, 1 ml of Trizol heated to 60°C was added to the cells, and the mixture was shaken using a bead mill (Biospec Products) for 2 minutes at room temperature. Following milling, the mixture was incubated on ice for 1 minute to stabilise the RNA.

Total RNA was subsequently extracted and purified using the Direct-zol RNA Kit and the RNA Clean & Concentrator Kit from Zymo, following the manufacturer's detailed protocols. To ensure the removal of any contaminating genomic DNA, RNase-free DNase treatment was applied at 37°C for 60 minutes before the final RNA clean-up step.

For reverse transcription, 0.2 µg of the purified RNA was used. The reverse transcription was carried out using the SuperScript™ IV First-Strand Synthesis System from Thermo Fisher, strictly according to the provided instructions. This step is crucial for synthesising cDNA from the RNA template.

The RT-PCR amplification was prepared using a 50 µl reaction volume with REDTaq® ReadyMix PCR Reaction Mix™ (Sigma-Aldrich), following the mix's preparation guidelines. Amplification was performed in a PCR cycler (Bio-Rad, USA), performed with denaturation at 95 °C for 1 min, followed by 35 cycles of 95 °C 30 seconds, 56 °C 30 seconds and 72 °C 1 min; then 72 °C 5 mins.

**Rapid light curve measurements**

Since the first discovery of the phenomenon of chlorophyll fluorescence induction in

1931 (Kautsky & Hirsch, 1931), the technology of chlorophyll fluorescence induction kinetics has emerged as a vital tool for studying photosynthetic organism growth and photosynthesis. This technique monitors changes in chlorophyll fluorescence under specific lighting conditions, providing scientists with deep insights into the photosynthetic activity and health status of photosynthetic organisms. In this project, the rapid light curve was used to analyse the photosynthesis efficiency difference between FR1 knock-in strain and wild-type *T. pseudonana*. As previously described, 8 x $10^4$ cells/ml were cultured in iron-limited and iron-repleted conditions and cultured until the exponential phase (approximately 8 x $10^5$). Cell amounts were determined by Multisizer 4e and then diluted into 1ml 7 x $10^5$ cells/ml stock with iron-free media. All the stocks were dark-treated to remove light affection for at least 30 mins. The rapid light curve was measured using a PhytoPAM; each sample was measured from 8 µmol photons m-2 s-1 to 2064 µmol photons m-2 s-1 in a total of 14 steps, with each with the 20s illuminated. Positive sequence and negative sequence were used, and each sequence was repeated three times, which was completed by three biological replicate experiments. The parameters were expressed and calculated by the following equation:

$$Yield = (Fs - Ft)/Fs$$

Where yield represents the effective quantum efficiency, Fs represents the maximal fluorescence during actinic irradiation, and Ft represents the instantaneous fluorescence.

The electron transport rate (ETR) was calculated according to the following equation (Beer et al., 2000):

$$ETR = PAR \times 0.84 \times 0.5 \times \Delta F/Fs$$

Where PAR is the amount of incident light (µmol photons $m^{-2}$ $s^{-1}$), 0.84 is the incident light conversion efficiency in green plants, and 0.5 is two photons necessary to drive

both photosystems.

After obtaining the data from PhytoPAM measurements, ETR is curve-fitted using the following formula, with various parameters derived from Eilers and Peeters (1988):

$$ETR = PAR/(a \times PAR^2 + b \times PAR + c)$$

$$\alpha = \frac{1}{c}$$

$$ETR_{max} = \frac{1}{b + 2\sqrt{a \cdot c}}$$

$$I_k = \frac{c}{b + 2\sqrt{a \cdot c}}$$

The initial slope of the rapid light curve, denoted as α (electrons/photons), is indicative of the quantum efficiency of photosynthesis. This parameter represents how efficiently plants convert light photons into chemical energy during the initial phase of photosynthesis. The maximum electron transport rate, represented as $ETR_{max}$ (μmol electrons/($m^2$·s)), reflects the highest rate at which electrons are transported during photosynthesis under optimal light conditions. Additionally, $I_k$ (μmol photons/($m^2$·s)) defines the transition point in photosynthetically active radiation (PAR) between light-limited and light-saturated conditions, marking the shift from predominantly light-dependent to light-independent reactions in photosynthesis.

**Real-time quantitative polymerase chain reaction (RT-qPCR) for retinal synthetase beta-carotene monooxygenase (BCMO)**

According to the research of Jan Straus (2012), the synthesis of retinal, a vital component of xanthorhodopsin in the diatom *F. cylindrus*, follows a specific biochemical pathway depicted in Figure 3.3

. This pathway involves the enzyme BCMO (beta-carotene monooxygenase), which catalyses the conversion of β-carotene into retinal. Building on this knowledge, our

project extended the investigation to the diatom *Thalassiosira pseudonana*, examining the presence and expression levels of BCMO under both iron-replete and iron-limited conditions. This was conducted in both wild-type and gene knock-in strains using real-time quantitative fluorescence PCR (RT-qPCR).

To verify the identity and function of BCMO and its associated upstream genes in *T. pseudonana*, comparative genomic analysis was performed using NCBI and UniProt BLAST tools. The RT-qPCR experiments were executed following the two-step protocol outlined by Nolan et al. (2006), ensuring accurate quantification of gene expression levels.

First-strand cDNA synthesis was conducted using Superscript IV Reverse Transcriptase (Invitrogen, US). Oligo(dT)20 Primer was used to synthesise the cDNA library. gDNA digestion was conducted as previously described. The reverse transcription was performed with 200 ng of total RNA in a 50µl reaction volume. The reaction conditions were set at 42 °C for 50 minutes, followed by a heat inactivation step at 70 °C for 15 minutes to terminate the enzyme activity. To evaluate potential gDNA contamination, control reactions were set up using water instead of reverse transcriptase, with RNA from each biological replicate. The primers targeting the BCMO gene were specifically designed using the NCBI primer design tool. Criteria set for the primer design included a target amplicon size of 100-150 base pairs, a GC content ranging from 30% to 50%, a primer length between 15 and 30 base pairs, and a melting temperature of 65 degrees Celsius. These specifications are detailed in Table 3.1. The primers were synthesised by Eurofins Genomic, ensuring high quality and specificity for the desired gene sequence.

In addition, the actin gene was selected as the internal reference gene for this experiment due to its stable expression under iron-limited conditions in *T. pseudonana*. The design of the actin gene primers was based on a previous study by Shi et al. (2013), which confirmed the reliability of these primers for accurate

normalisation of gene expression data.

| Name | Sequence (5'-3') | Annealing temp (°C) |
|---|---|---|
| BCMO1 F | GGAGAGGGTGCCAGTCATTC | 6 |
| BCMO1 R | GAAACCATCCTTCGGGTCGT | 60 |
| BCMO2 F | CAGGTGGTGTCAGAGCCAATGT | 63 |
| BCMO2 R | TGACGCAGACTCCCACACAACT | 64 |
| BCMO3 F | GGTACGGATGATGACGTGAAA | 56 |
| BCMO3 R | GCTCATCGTCGTTCTCATAGAC | 57 |
| BCMO4 F | AGGTGGTGTCAGAGCCAATG | 59 |
| BCMO4 R | GGGCCATCAGAAAATGACGC | 59 |
| Actin F | CCGTAGTGAACGCCTATCGTGGC | 64 |
| Actin R | CCATCGTCTCGCTGCGGCTG | 67 |

**Table 3. 1 Primers for amplification of BCMO and reference gene Actin used for RT-qPCR.**

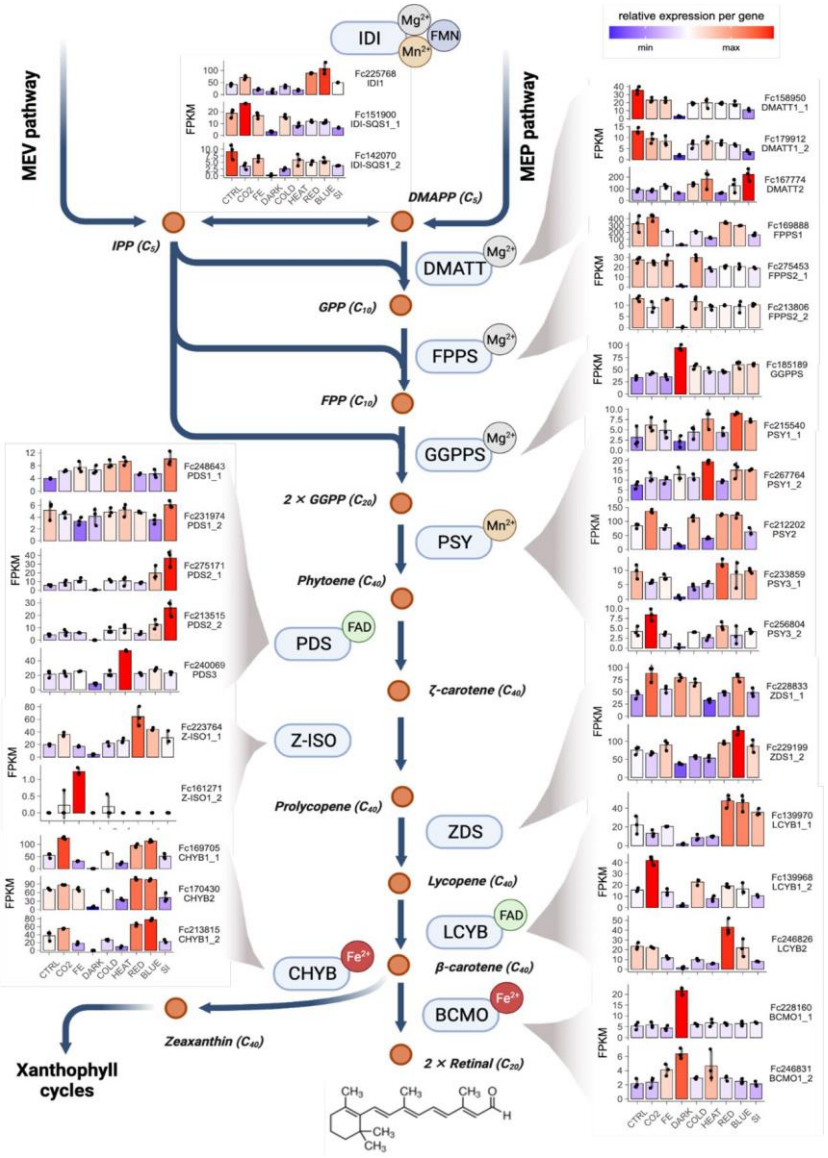


**Figure 3.3 Flow chats from Strauss et al. (2023) detail the genes involved in the putative biosynthetic pathway of all-trans-retinal in *Fragilariopsis cylindrus*.** The pathway illustrates a complex network of enzymes and intermediates critical for retinal production：

BCMO (β-carotene 15,15'-monooxygenase): Converts β-carotene to retinal; CHYB (β-carotene 3-hydroxylase): Hydroxylates β-carotene; DMAPP (dimethylallyl diphosphate) and IPP (isopentenyl diphosphate): Fundamental building blocks in terpenoid synthesis; DMATT (dimethylallyltranstransferase): Catalyzes the transfer of dimethylallyl groups; FAD (flavin adenine dinucleotide) and FMN (flavin mononucleotide): Coenzymes involved in redox reactions; FPP (farnesyl diphosphate) and GGPP (geranylgeranyl diphosphate): Precursors in the biosynthesis of diterpenes and other terpenoids; FPPS (farnesyl diphosphate synthase); GGPPS (geranylgeranyl diphosphate synthase): Enzymes synthesizing farnesyl and geranylgeranyl diphosphate; GPP (geranyl diphosphate): A precursor in monoterpene synthesis; IDI (IPP isomerase): Catalyzes the isomerization between IPP and DMAPP; LCYB (lycopene β-cyclase): Converts lycopene to β-carotene; MEP (Methylerythritol phosphate) and MEV (mevalonic acid): Pathways producing isoprenoid precursors; PDS (phytoene desaturase), PSY (phytoene synthase), ZDS (ζ-carotene desaturase), and Z-ISO (ζ-carotene isomerase): Enzymes involved in carotenoid biosynthesis; FPKM (fragments per kilobase of exon per million mapped fragments): A measure used to estimate gene expression levels.

For the RT-qPCR second strand amplification, 2µL of the 4-fold diluted cDNA from the reverse transcription reaction was used. This was supplemented with ten µL of 2x SYBR® Green Reagents Master Mix (Applied Biosystems, US) to ensure sensitive detection of the PCR products. To this mixture, 0.2µL each of forward and reverse primers was added, with a final concentration of 200nM, to specifically amplify the target sequences. The amplification was carried out in 96-well plates using the StepOne™ Real-Time PCR System (Applied Biosystems, US). The cycling conditions were as follows: an initial denaturation at 95 °C for 10 minutes, followed by 40 cycles of 15 seconds at 95 °C for denaturation and 60 seconds at 60 °C for annealing and extension. To ensure the specificity of the amplification, a melting curve analysis was performed at the end of the cycles. This analysis ranged from 60 °C to 95 °C, with temperature increments of 0.3 °C, which helped identify any primer-dimer formations or non-specific amplification products.

Primer efficiency was checked by generating a standard curve for each primer pair. This curve was constructed using five points derived from 1:2 serial dilutions of the initial reverse transcription reactions, providing a quantitative measure of primer efficiency and reaction dynamics.

Data analysis was conducted using StepOneTM Software v2.3 (Applied Biosystems, US), which automatically determined the cycle thresholds (Ct) for each reaction. The efficiencies of the qPCR reactions were calculated based on the slope of the standard curves. These efficiency calculations are crucial for accurate quantification of gene expression levels, ensuring that the results reflect actual biological variations under different experimental conditions.

$$E = a^{-1/slope} - 1$$

In the qPCR analysis, E represents the PCR efficiency, which varies between 0 (minimum value) and 1 (the theoretical maximum and optimum). The efficiency is

calculated based on the slope of the linear regression of the logarithm of target concentration against the cycle threshold (Ct). For optimal amplification, the efficiency should ideally range between 90% and 110%. This corresponds to a slope between -3.58 and -3.1 on the linear regression plot. In cases where PCR efficiencies have not been empirically determined, a default optimal efficiency (E=1.0) is assumed. This assumption facilitates the calculation and comparison of relative gene expression levels, although actual efficiencies can vary.

**Immunogold labelling under transmission electron microscope (TEM)**

First, 5ml each of *T. pseudonana* wild-type and FR1 knock-in strain cultures were centrifuged at 3000 g for 5 minutes to pellet the cells and discard the supernatant. The cell pellets were then washed once with phosphate-buffered saline (PBS) and resuspended in 1ml of fixative solution by pipette to ensure uniform distribution. After 3 hours of fixation at four °C, the cells were washed three times with PBS. Cells were harvested again using the same method described from PBS and remove the supernatant. The cell pellets were then resuspended in 10µl of PBS to create a high-concentration suspension for further processing. This suspension was added to pre-prepared 1.5% agar blocks. Excess supernatant was absorbed with filter paper before sealing the samples with 1.5% hot agar. Once cooled, the agar was cut into 1.5mm x 1.5mm cubes, making three embedding blocks per sample, which were then fixed overnight at four °C in a fixative solution. Every hundred millilitres fixative solution was prepared according to the following formula: 50 ml 0.2 M PBS, 10 ml 40% paraformaldehyde stock, 32 ml pure water, and 8 ml 2.5% glutaraldehyde.

The following day, the samples were soaked three times in PBS for 15 minutes each to wash out the fixative. Dehydration was achieved through a graded series of pre-chilled ethanol solutions: 30% ethanol for 30 minutes, followed by 50%, 70%, 90%, and finally 100% ethanol, each step lasting 20 minutes, except the last, which lasted 15 minutes.

For resin impregnation, the dehydrated gel blocks were transferred to 15 ml centrifuge tubes. The blocks were first exposed to a 100% ethanol and resin mixture at a 3:1 ratio for 45 minutes, then at a 1:1 ratio for 90 minutes, and finally at a 1:3 ratio for another 90 minutes. The blocks were then moved to new EP tubes, filled with pure LR resin, and left to impregnate overnight. The next day, the LR resin was refreshed, and the blocks soaked for an additional 2 hours.

Post-impregnation, the blocks were transferred to clear PCR tubes, filled with LR resin, and polymerised under UV light at -20°C for 72 to 120 hours until fully hardened. The hardened blocks were then silenced using an EM UC7 ultramicrotome (Leica, Germany) to a 90-100nm thickness and transferred onto nickel grids for antibody labelling.

For antibody concentration selection, 4-6 slices from each sample were tested with different primary and secondary antibodies. The samples underwent colloidal gold labelling and antibody incubation in a humid chamber. The primary antibody was diluted 1:20 with BSA and incubated overnight at 4°C. For the negative control, only the secondary antibody was applied without the primary antibody. After primary antibody application, the samples were rinsed 2 to 3 times in deionised water to remove any residual antibodies. The secondary antibody, containing colloidal gold and diluted in PBS, was then applied and incubated for 3 hours at room temperature in the dark. Following this, the samples were rinsed three times in deionised water, 10 minutes each.

Finally, the samples were fixed with 2.5% glutaraldehyde for 15 minutes, rinsed three times in deionised water to remove any excess fixative, and then subjected to 5 minutes of uranium staining followed by 5 minutes of lead staining to enhance electron microscopy contrast. The prepared samples were observed using an HT-7800 transmission electron microscope (Hitachi, Japan) to assess FR1 subcellular localisation.

## Result

### Transformation, screen, and reverse transcript

Genomic DNA (gDNA) was extracted from the expanded cultures of *T. pseudonana* and was subjected to PCR screening to verify the integration of the target gene into the colonies and the liquid selection cultures. Out of 10 colonies tested, all displayed a positive result for the NAT gene, confirming its successful integration. However, only one colony exhibited a positive response for the FR1 gene primer pair, as documented in Figure 3.4a. This particular colony, *TpRHO*, was subsequently selected for expanded cultivation and continued lineage culture.

After six months of continuous culture, the FR1 gene's presence was screened again in stain *TpRHO*, the results of which are displayed in Figure 3.4b. Following 12 months of continuous cultivation, RNA was extracted from the FR1 knock-in strain, and reverse transcription was carried out as previously described. The resulting cDNA was then analysed via reverse transcription PCR (RT-PCR). The RT-PCR results for the FR1 knock-in strain showed distinct bands, in contrast to the negative control and the wild-type (WT) control groups, which showed no bands, as illustrated in Figure 3.5.

These findings indicate that the FR1 gene was not only successfully expressed in the knock-in strain but also stably inherited across multiple generations. This successful integration and expression of the FR1 gene demonstrate the effectiveness of the gene editing technique and provide a solid foundation for further functional studies and gene expression analysis.

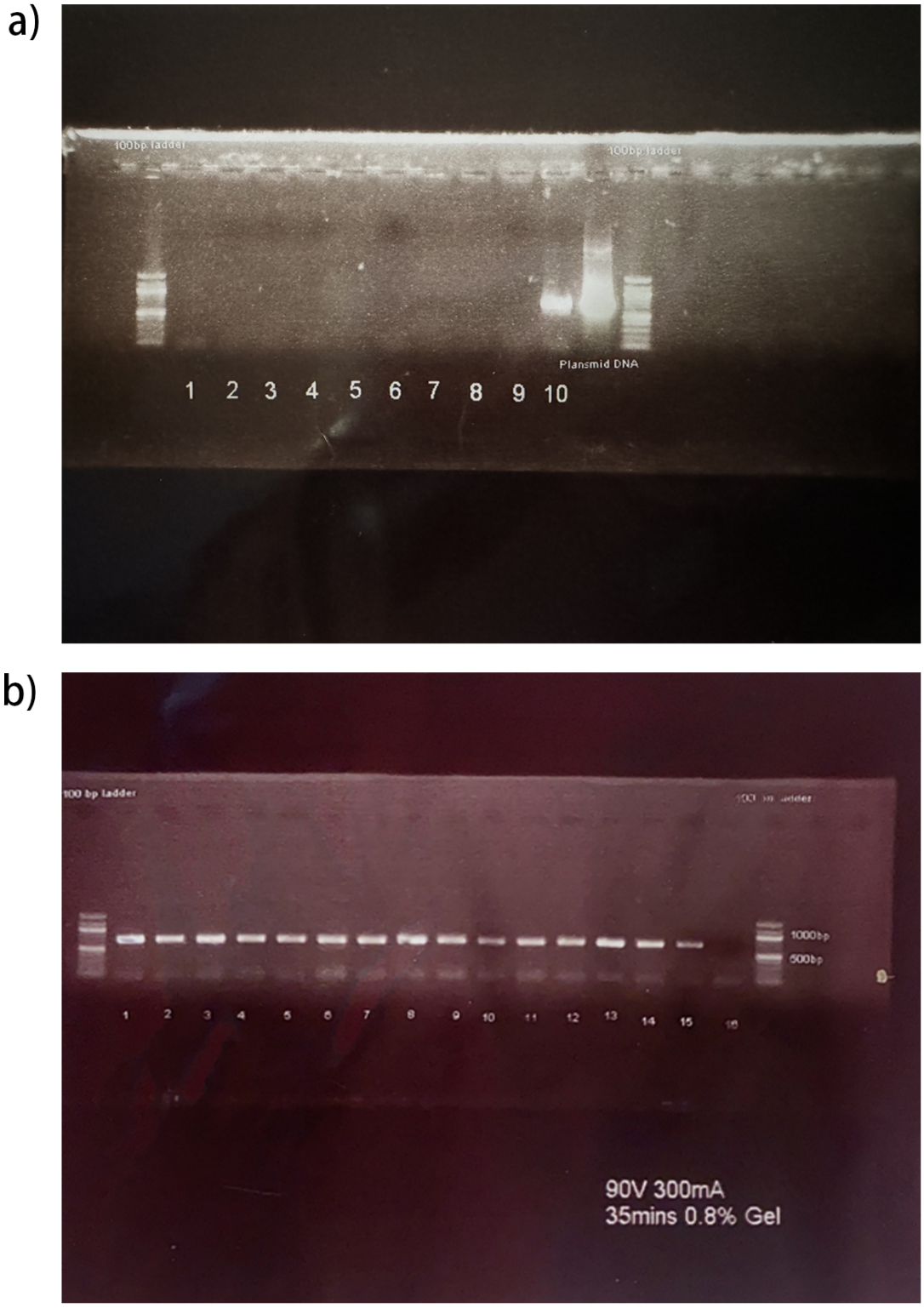


**Figure 3.4 Gel electrophoresis result of transformed *T. pseudonana* screening PCR result.** The marker is 100bp ladder. a) PCR screening of 10 NAT positive strains after biolistic shooting. Line 1 to 10 is ten different colonies, where line 11 is the plasmid DNA positive control and line 13 is the water negative control. Target length is 704bp. b) PCR amplifications of strain No.10 after months continuous cultivation. Line 1 to 15 is the PCR product with rhodopsin primer; line 16 is the negative control reaction (water).

This phase of the research not only confirmed the effectiveness of gene editing techniques but also demonstrated the initial success in integrating the target gene during the screening and cultivation processes, providing a foundation for further functional studies and detailed gene expression analysis.


**Figure 3.5 Gel electrophoresis result of FR1 knock-in *T.pseudonana* RT-PCR results.** The marking is 100bp ladder, line 1 is the *TpRHO* cDNA, line 2 is negative control of reverse transcript reactions, line 4 is negative control of PCR reaction by using water replacing cDNA. Target length 703bp.

**Testing optimal conditions for iron, retinal, and DMSO concentrations in *Thalassiosira pseudonana***

After successfully completing the knock-in experiments, the study aimed to assess the effects of iron limitation on diatoms, specifically examining the growth of the *T. pseudonana* wild type (*TpWT*) and knock-in strain (*TpRHO*) under conditions of extreme iron deficiency (0~2.5nM). The findings, as illustrated in Figure 3.6, indicated that growth of *T. pseudonana* was significantly limited under these conditions. Initially, there was a slight increase in cell density and photosynthetic parameters within the first three to four days, likely due to the utilisation of stored iron reserves. However, as these reserves were exhausted, both *TpWT* and *TpRHO* cells began to die off rapidly, with a corresponding sharp decline in photosynthetic efficiency. No significant differences were observed in the physiological response of both *TpWT* and *TpRHO* strains during these several different extreme iron-limited conditions.

Further experiments were conducted to evaluate the physiological response of *T. pseudonana* under medium iron concentrations (80~150nM), comparing these results with those from cultures grown under fully nutrient-rich conditions (1000nM iron concentration) (Figure 3.7). These studies revealed that while growth was constrained at 80~150nM iron concentrations, which was notably different from that under nutrient-rich conditions, importantly, without resulting in complete cellular mortality.

This data provides crucial insights into the physiological adaptations of *T. pseudonana* under varying iron levels and establishes a foundational understanding for future studies. Consequently, in subsequent experiments, all algal strains were subjected to a 3~4-day period of iron starvation as a pre-treatment to standardise conditions and minimise initial variability. After this phase, the algae were transferred to experimental culture mediums specified in the methods section, only proceeding when the Fv/Fm photosynthetic efficiency metric fell below 0.15, indicating a significant

reduction in photosynthetic capacity and ensuring uniform stress conditions across all test samples. This approach ensures a controlled environment to accurately gauge the impact of gene knock-in on the algae's response to iron stress.

Additionally, considering that FR1 knock-in strain might request extra retinal to synthesise and function xanthorhodopsin, a pre-experiment was carried out to the optimal concentration needed for effective rhodopsin synthesis and functionality in *TpRHO* by testing concentrations ranging from 1μM to 4μM of retinal (Figure 3.8). The findings, as detailed in Figure 3.8, reveal that while the lowest concentration of 1μM supported basic growth, there was a notable enhancement in growth rate at the 2μM and 3μM concentrations ($p<0.05$). This improvement suggests that the FR1 knock-in strain requires a higher concentration of retinal for optimal growth and rhodopsin functionality. Conversely, the highest tested concentration of 4μM had a detrimental effect, resulting in the lowest growth rate and maximum biomass, indicating that excessively high levels of retinal might inhibit cell growth. Based on these observations, a concentration of 3μM retinal was selected for future experiments. This concentration strikes a balance by providing sufficient retinal for enhanced growth and rhodopsin function without the inhibitory effects observed at higher concentrations.

The impact of the retinal solvent DMSO on *Thalassiosira pseudonana* was also assessed to investigate whether it interfered with the growth conditions. According to Figure 3.9, when comparing the growth of the *TpWT* in a control setup without any DMSO to a setup with a 1% concentration of DMSO (equivalent to 10μM retinal solvent), no significant differences were observed. The data indicate that both the maximum cell density and the growth rate were comparable between the two conditions, indicating that low concentration of DMSO does not influence the growth of *T. pseudonana*. Given the preliminary findings and considerations around optimal conditions for testing, the formal experiments were structured to investigate the

physiological effects of xanthorhodopsin on diatoms using specific experimental conditions.

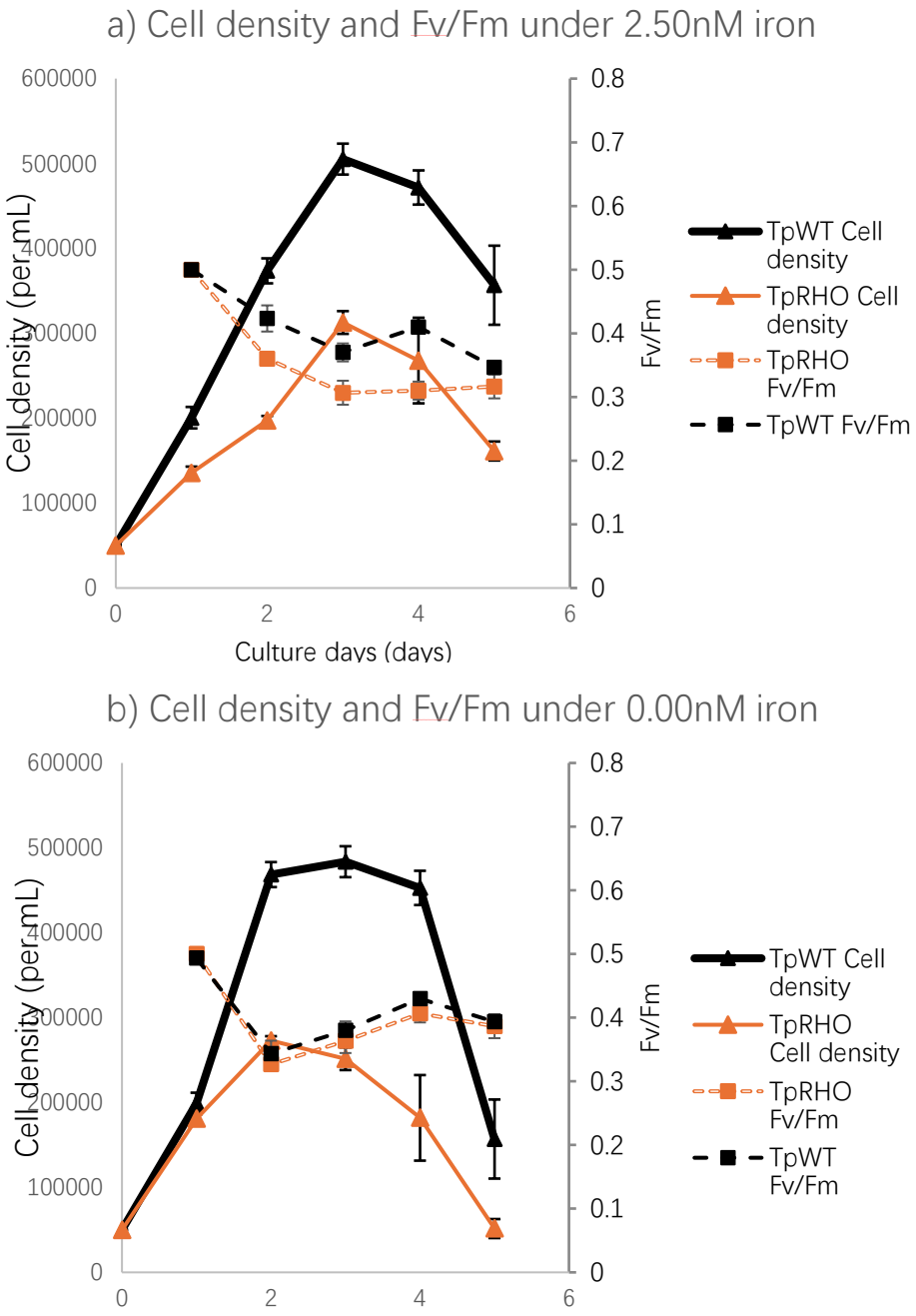


**Figure 3.6 Growth curves of *T. pseudonana* under extreme iron-limited conditions.** The orange lines represent *T. pseudonana* knock-in strain (*TpRHO*), while the black lines depict wildtype strain (*TpWT*). Solid lines indicate cell density, and dashed lines represent Fv/Fm values. The x-axis shows the culture dates. The primary y-axis measures cell density, and the secondary y-axis measures Fv/Fm. Panel (a) displays growth curves at 2.50 nM iron concentration, and panel (b) at 0 nM iron concentration. Each treatments have three replicates; error bars show standard deviation.

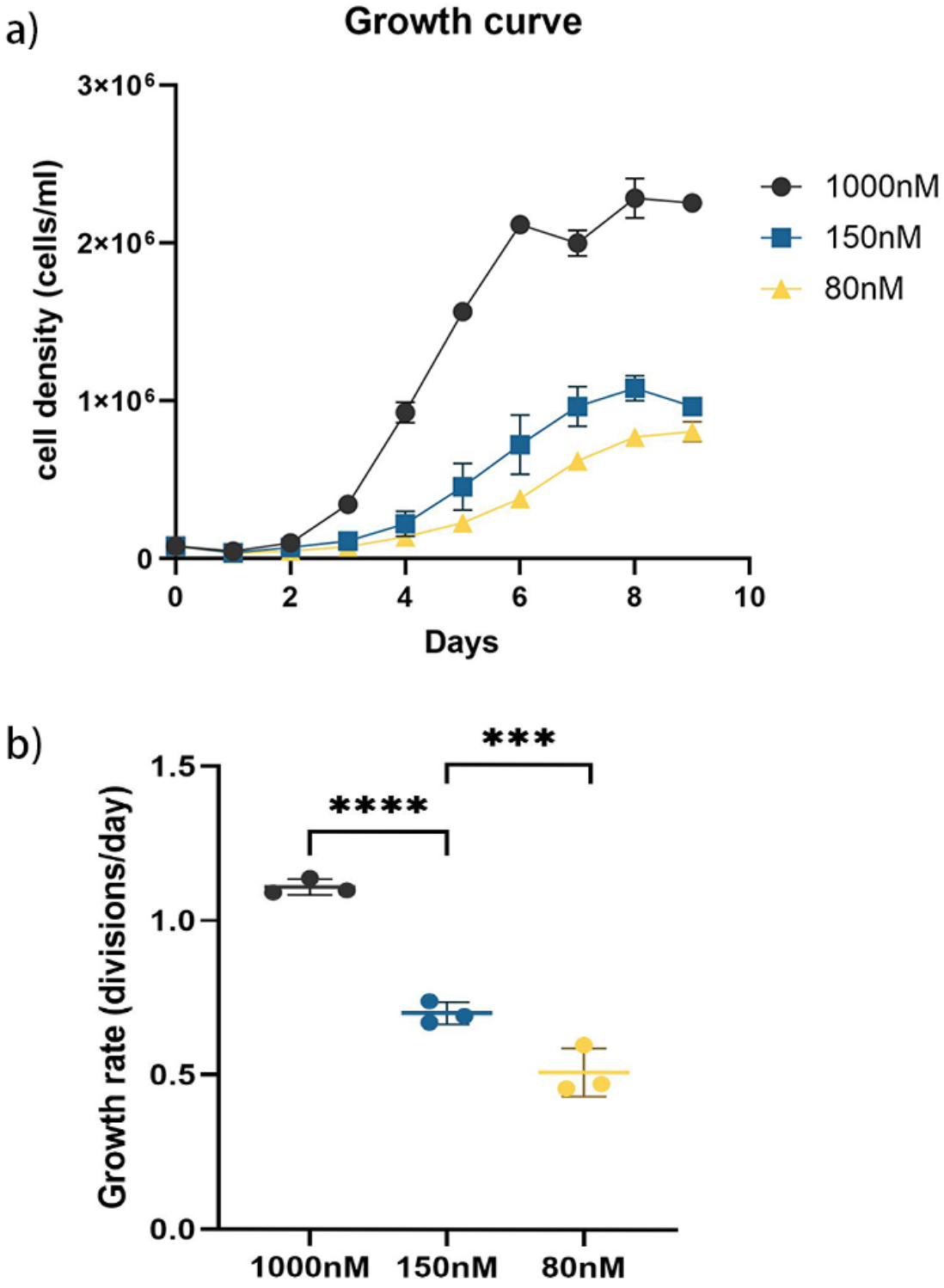


**Figure 3.7 Growth response of *T. pseudonana* wildtype strain (*TpWT*) to different iron concentrations.** a) The growth curve of *TpWT* under varying iron concentrations. The cell density (cells/ml) is plotted against time in days. The symbols represent different iron concentrations: circles for 1000 nM (black), squares for 150 nM (blue), and triangles for 80 nM (yellow). b) **T**he average growth rate (divisions/day) for *TpWT* at the respective iron concentrations. Statistical significance is indicated with asterisks above the comparison lines; '***' and '****' denote p-values less than 0.001 and 0.0001, respectively. Each treatment has three replicates, error bars show standard deviation.

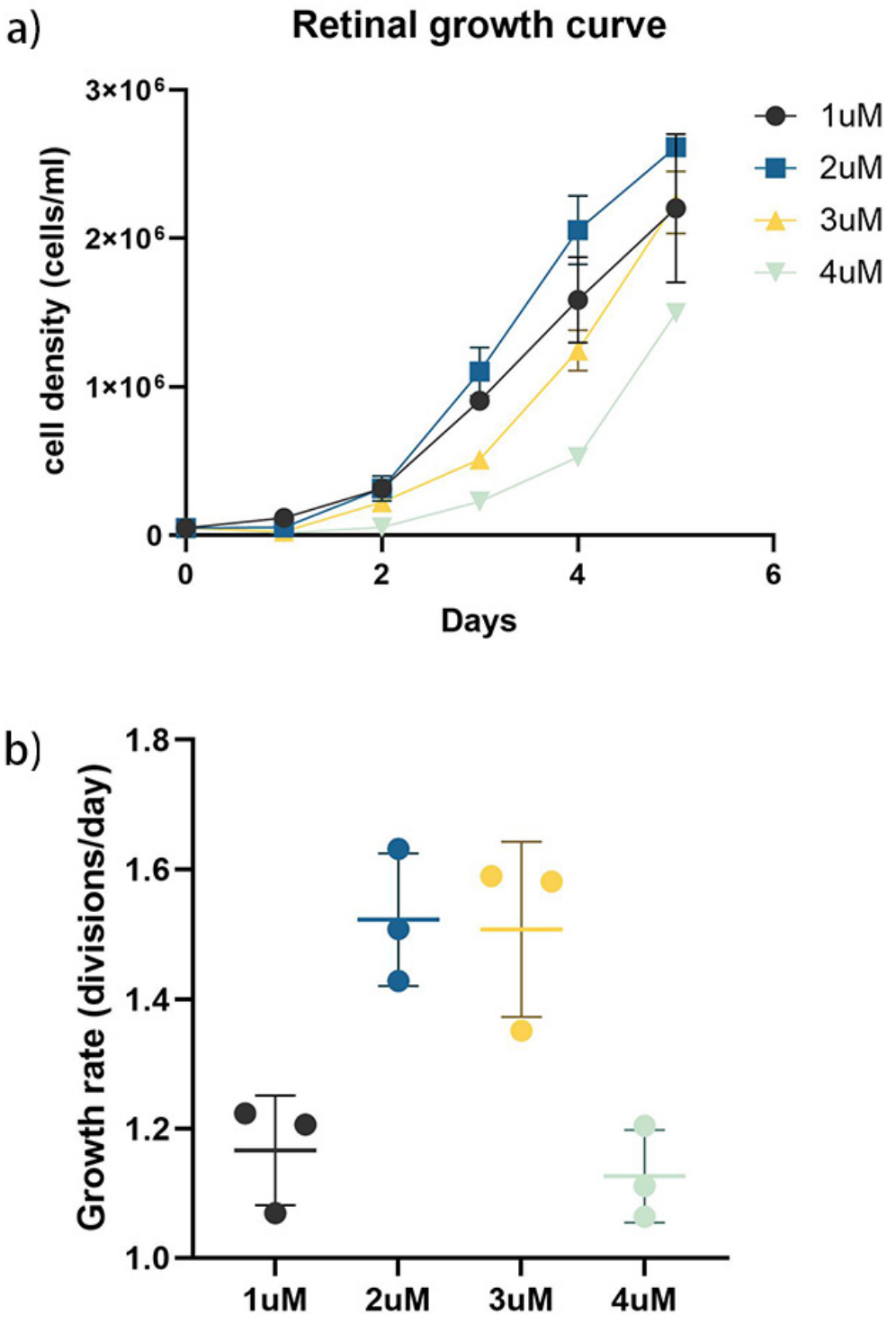


**Figure 3.8 Response of *T. pseudonana* mutant strain (*TpRHO*) to varying retinal concentrations.** a) The growth curve *TpRHO* over a period of six days, plotted against different retinal concentrations, y-axis represent cell density (cells/.ml). Each symbol represents a concentration: circles for 1 µM (black), squares for 2 µM (blue), triangles for 3 µM (yellow), and inverted triangles for 4 µM (green). b) Growth Rate: The average growth rate (divisions/day) of *TpRHO* is plotted for each retinal concentration. Data points are presented with error bars indicating variability within the measurements. Each treatment has three replicates, error bars show standard deviation.

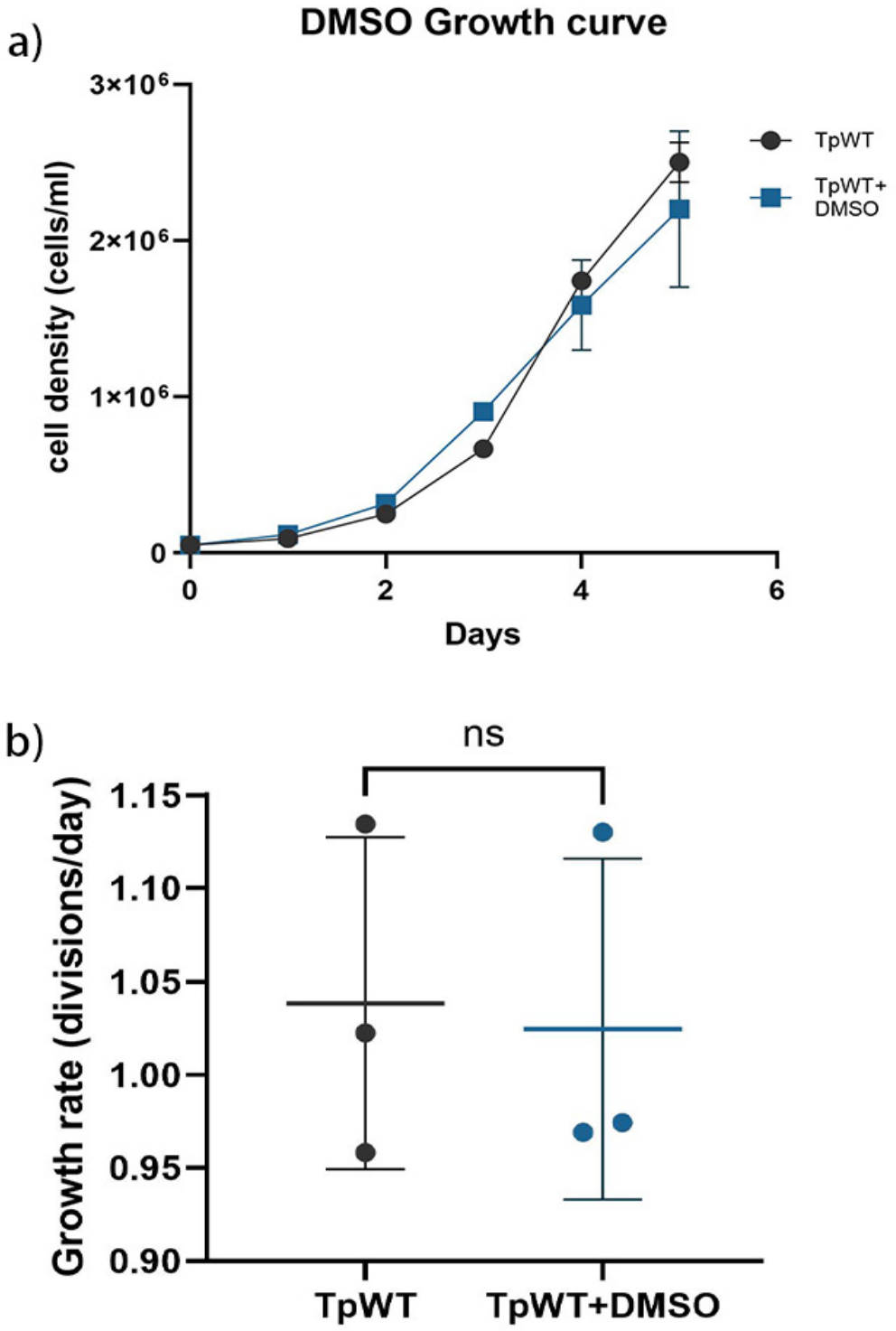


**Figure 3.9 Effect of DMSO on Growth Dynamics of *T. pseudonana* wildtype strain (*TpWT*).** a) The growth curve of *TpWT* with 1% DMSO and control group over a period of six days. The growth curves compare untreated control group (black circles) and cells treated with 1% DMSO (blue squares), which is equivalent to a 10 µM retinal solution. b) Growth rate (divisions/day) for untreated control *TpWT* and DMSO treated group. Statistical insignificance is indicated by "ns" (not significant), showing no substantial difference in growth rates between the two conditions. Each treatment has three replicates, error bars show standard deviation.

**Iron-limitation experiment**

In the conducted experiments to assess the impact of microbial rhodopsin on *Thalassiosira pseudonana*, both the wild type (*TpWT*) and the rhodopsin knock-in strain (*TpRHO*) were subjected to conditions of 150nM iron limitation as well as iron-replete conditions to gauge differences in physiological responses. Under iron-limited conditions (150nM), although both strains showed reduced growth and photosynthetic efficiency, the *TpRHO* strain was able to sustain significantly higher cell densities and exhibited more stable rates of photosynthetic efficiency (Fv/Fm) from the third to the seventh day than *TpWT* (Figure 3.10a). In environments where iron was abundant, *TpRHO* still demonstrated an increased yield and elevated photosynthetic efficiency relative to *TpWT*, especially evident in the period from the fourth to the sixth day (Figure 3.10b), through analysis of growth rates indicated no significant differences between the strains under nutrient-rich condition (Figure 3.10c).

The experimental results underscore the potential of xanthorhodopsin to offer a competitive advantage under conditions of nutrient stress, particularly through mechanisms that could enhance iron utilisation or mitigate the adverse effects of iron deficiency. This capability implies that xanthorhodopsin could also enhance overall cellular performance in environments where iron is abundant, demonstrating its versatile role in diatom physiology. However, the precise mechanisms by which proton-pump rhodopsin supports diatom growth remain unclear. Therefore, to further elucidate the role of microbial rhodopsin in influencing photosynthesis, subsequent experiments focused on assessing various photosynthetic parameters.

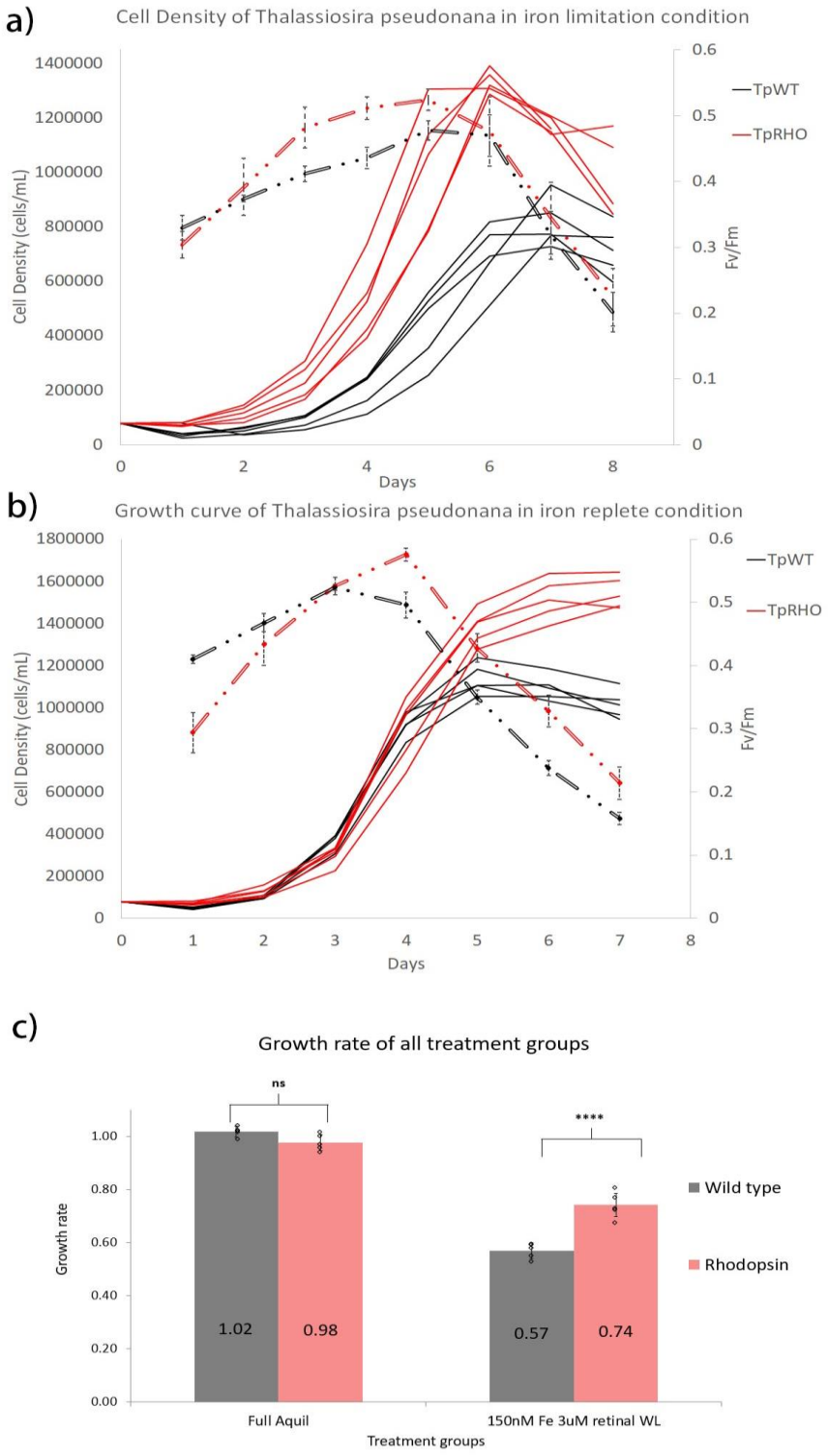


**Figure 3.10 Physiological responses of *T. pseudonana* wildtype strain (*TpWT*) and mutant strain (*TpRHO*) under iron-limited and iron-repleted conditions.** *TpWT* shown in black and *TpRHO* in red (n=5). Solid lines indicate cell density (cells/ml) (n=5), while dashed lines represent the efficiency of photosystem II (Fv/Fm). a) The growth curve of *T .pseudonana* in iron-limited condition. b) The growth curve in iron-repleted condition. c) The growth rates of *TpWT* and *TpRHO* under iron-limited and iron-repleted conditions, with 'ns' indicating no significant differences between the treatments and '****' indicating significant differences ($p<0.001$). Error bars show standard deviation.

**Rapid light curve**

The rapid light curves and their parameters of rhodopsin knock-in and wildtype *T. pseudonana* strains under iron limitation treatments were measured as described, as detailed in Figure 3.11. Four different light wavelengths ranging from blue light to brown light were measured and analysed. Under these conditions, the alpha value, indicative of the initial slope of photosynthetic efficiency, for the rhodopsin strain ranged from 0.16 to 0.21 electrons/photons, while the maximum electron transport rate (ETRmax) varied between 148.6 to 194.4 μmol electrons/($m^2$·s). In contrast, the wildtype strain demonstrated alpha values from 0.12 to 0.14 electrons/photons and ETRmax values from 108.3 to 131 μmol electrons/($m^2$·s). Statistical analysis using the student t-test confirmed that both the alpha and ETRmax values were significantly higher in the rhodopsin mutant strain compared to the wildtype, with p-values of $1.5x10^{-8}$ *and* $3.4x10^{-7}$, separately.

Furthermore, measurements of the maximum quantum yield of photosystem II (Fv/Fm), a critical indicator of potential photosynthetic efficiency in phytoplankton (Zhang et al., 2008), revealed that the rhodopsin strains had Fv/Fm values ranging from 0.560 to 0.596. This was notably higher than the wild-type strains, which ranged from 0.441 to 0.515. The significant difference between the two groups, as supported by a t-test analysis yielding a p-value of 1.43x10-9, indicates a markedly improved photosynthetic potential in the rhodopsin strains (Figure 3.12).

The investigation into the photosynthetic performance of rhodopsin mutant strains of *Thalassiosira pseudonana* demonstrates that these mutants not only maintain higher light use efficiency but also exhibit increased photosynthetic productivity compared to the wild-type strains under conditions of iron limitation. It is important to highlight that those initial experiments lacked a comparative analysis with a control group under iron-replete conditions. Subsequent experiments rectified this by incorporating data from control groups under both iron-limited and iron-replete conditions, as

illustrated in Figure 3.13. These findings confirm that the rhodopsin mutant strains outperform the wild-type in terms of photosynthetic ability across both iron conditions, with detailed parameters presented in Figure 3.14. Results demonstrate that all parameters of the rhodopsin knock-in strain were significantly higher than the wild-type *T. pseudonana*, indicating that the *TpRHO* strain has better photosynthesis efficiency and light utilisation at all iron conditions.

In conclusion, miacrobial rhodopsin significantly enhances diatom photosynthesis not only under iron limitation but also when iron is plentiful, suggesting its broad utility in improving diatom resilience and productivity across varying environmental conditions. Further research is essential to fully unravel the complex role of microbial rhodopsin in diatom physiology and its potential applications in biotechnology.

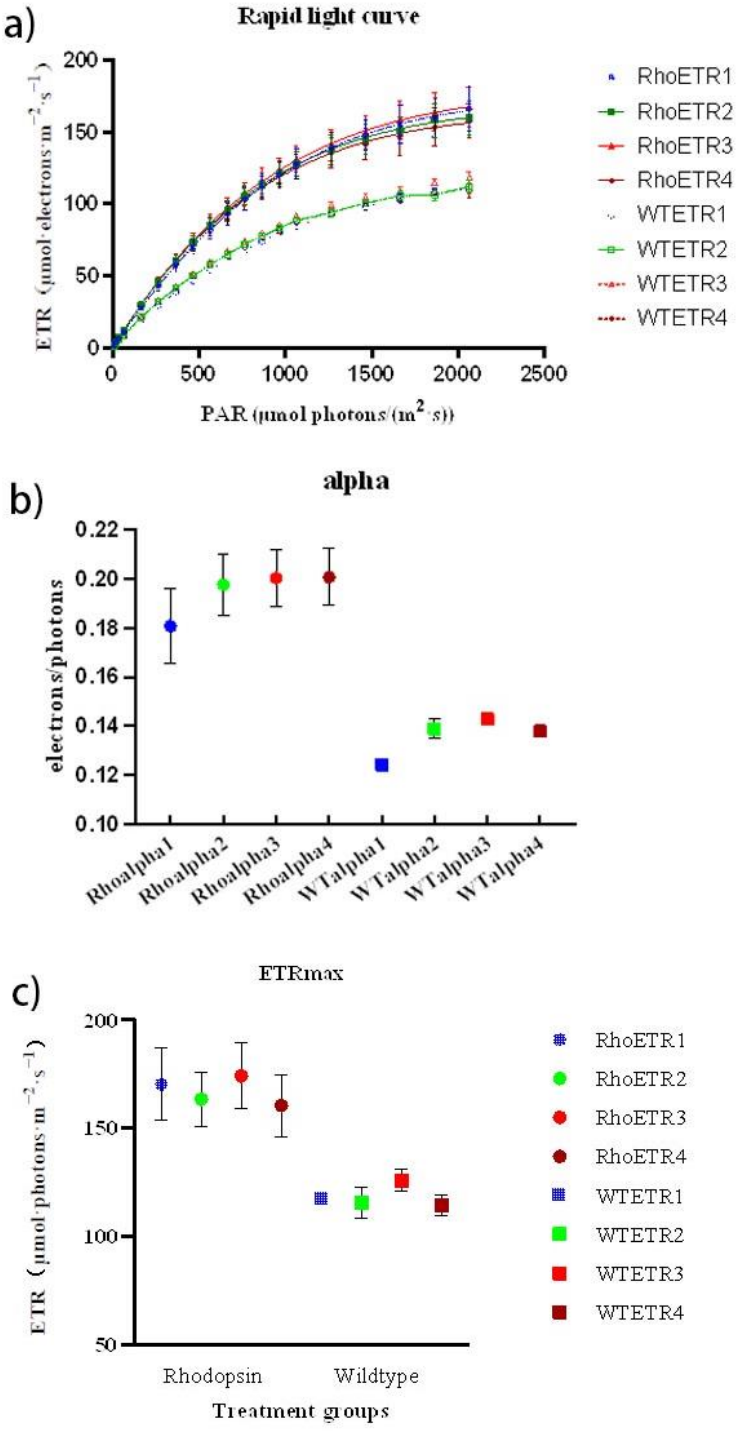


**Figure 3.11 Photosynthesis parameters of *TpRHO* and *TpWT* under iron limitation.** Different colours demonstrate different light channels (blue = 470nm, green = 520nm, red = 645nm, brown = 665 nm). a) Rapid light curve of *TpRHO* (full lines & points, n=3) and *TpWT* (dashed lines & points, n=3) strains. b) Rapid light curve parameter alpha of *TpRHO* (circles, n=3) and *TpWT* (squares, n=3). c) Rapid light curve parameter maximum electron transport rate of *TpRHO* (circles, n=3) and *TpWT* (squares, n=3). Error bars show standard deviation.

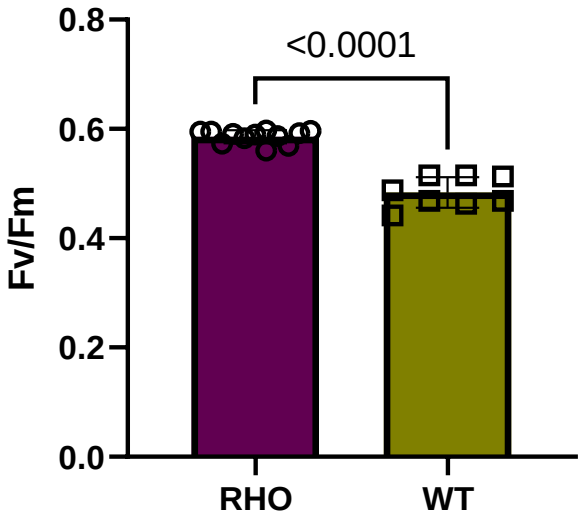


**Figure 3.12 The maximum potential quantum yield of *TpRHO* and *TpWT*.** *TpRHO* shows in purple while *TpWT* shows in yellow. Each group have four replicates. Statistical analysis t-test shows significant difference. Error bars show standard deviation.

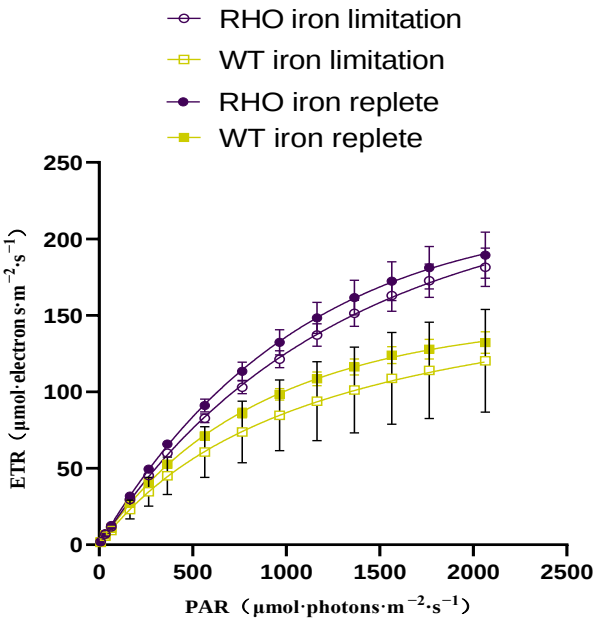


**Figure 3.13 Rapid light curve of different iron concentration treatment *TpWT* and *TpRHO*.** Iron repletion treatment rhodopsin mutant *Thalassiosira pseudonana* (full purple circle, n=4) strains, iron repletion treatment non-rhodopsin wildtype *Thalassiosira pseudonana* (full yellow square, n=4) strains, iron limitation treatment rhodopsin mutant *Thalassiosira pseudonana* (hollow purple circle, n=4) strains, and iron limitation treatment non-rhodopsin wildtype *Thalassiosira pseudonana* (hollow yellow square, n=4) strains. Error bars show standard deviation.

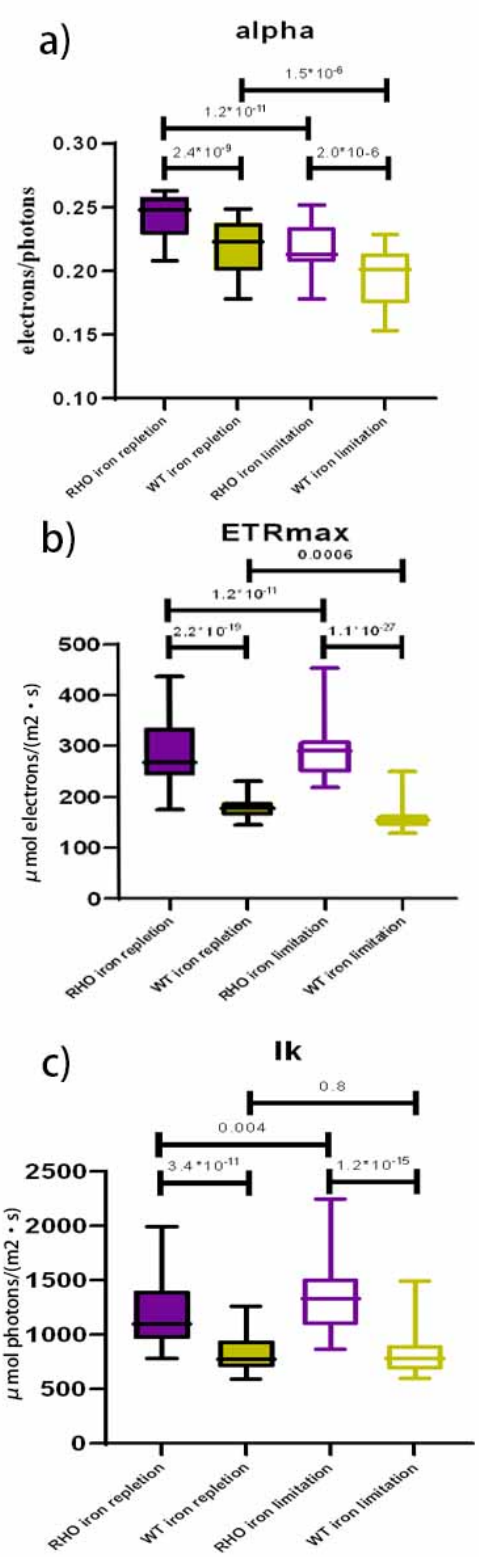


**Figure 3. 14 Rapid light curve parameters of *TpRHO* and *TpWT* under iron repletion and iron limitation.** a) alpha, indication the indicative of the quantum efficiency of photosynthesis., b) ETRmax reflects the highest rate at which electrons are transported during photosynthesis under optimal light conditions, c) Ik, defines the transition point in photosynthetically active radiation (PAR) between light-limited and light-saturated conditions. Each treatment has four replicates. Student t-test is used to measure the statistical significance. P-values are shown in the figure. Error bars show standard deviation.

**qPCRs**

Before embarking on detailed gene expression analysis, a preliminary experiment was carried out to evaluate the performance of four different BCMO primer pairs in comparison with primers for the actin gene, which is commonly used as a reference in such studies. The results from this preliminary test indicated varying levels of efficiency across the different primer sets. Based on these results, the BCMO4 primer set was selected for further testing due to its comparative performance. The decision was supported by the data illustrated in Figure 3.15, which presents the standard curve used to assess primer efficiency.

The calculation of primer efficiency, derived from the fitting equation provided in the methods section, showed that the amplification efficiency of the Actin primers was slightly above the ideal 100%, at 104.87%, while the efficiency for the BCMO primers was 97.19%. These values indicate that both primer sets are within an acceptable range for quantitative PCR, affirming that minor discrepancies in amplification efficiency are unlikely to significantly impact the overall experimental outcomes.

Given the acceptable efficiency and the comparative analysis, the BCMO4 primer pair was subsequently chosen to measure BCMO gene expression levels. This choice ensures that the expression data obtained in subsequent analyses are both accurate and reliable, enabling a thorough investigation into BCMO gene regulation under the study conditions.

The expression level of BCMO was measured for two different iron conditions by ΔΔCt analysis using actin as a reference gene. The result is shown in Figure 3.16. According to the result, the expression levels of BCMO in the wild-type strains under iron-replete (WT iron+) and iron-limited (WT iron-) conditions do not show a statistically significant difference, indicating that BCMO expression in wild-type

strains is relatively stable across varying iron availability. In contrast, the BCMO expression in the rhodopsin mutant strain under iron-replete conditions (RHO iron+) is significantly higher than in all other groups. Its BCMO expression level was 2.96 times that of *TpWT* iron repletion treatment. This elevated expression suggests that the presence of xanthorhodopsin might enhance the gene's activity, or its regulatory mechanisms are different under iron-replete conditions. When comparing the same iron treatment conditions, the rhodopsin mutant strains consistently show higher BCMO expression than their wild-type counterparts. The RHO iron-treatment group shows 1.56 times higher than the same treatment of *TpWT*. This pattern is observed both under iron-replete and iron-limited conditions, but the difference is particularly pronounced under iron-replete conditions. These observations suggest that the xanthorhodopsin mutation could influence BCMO gene regulation or the overall metabolic pathway associated with BCMO.

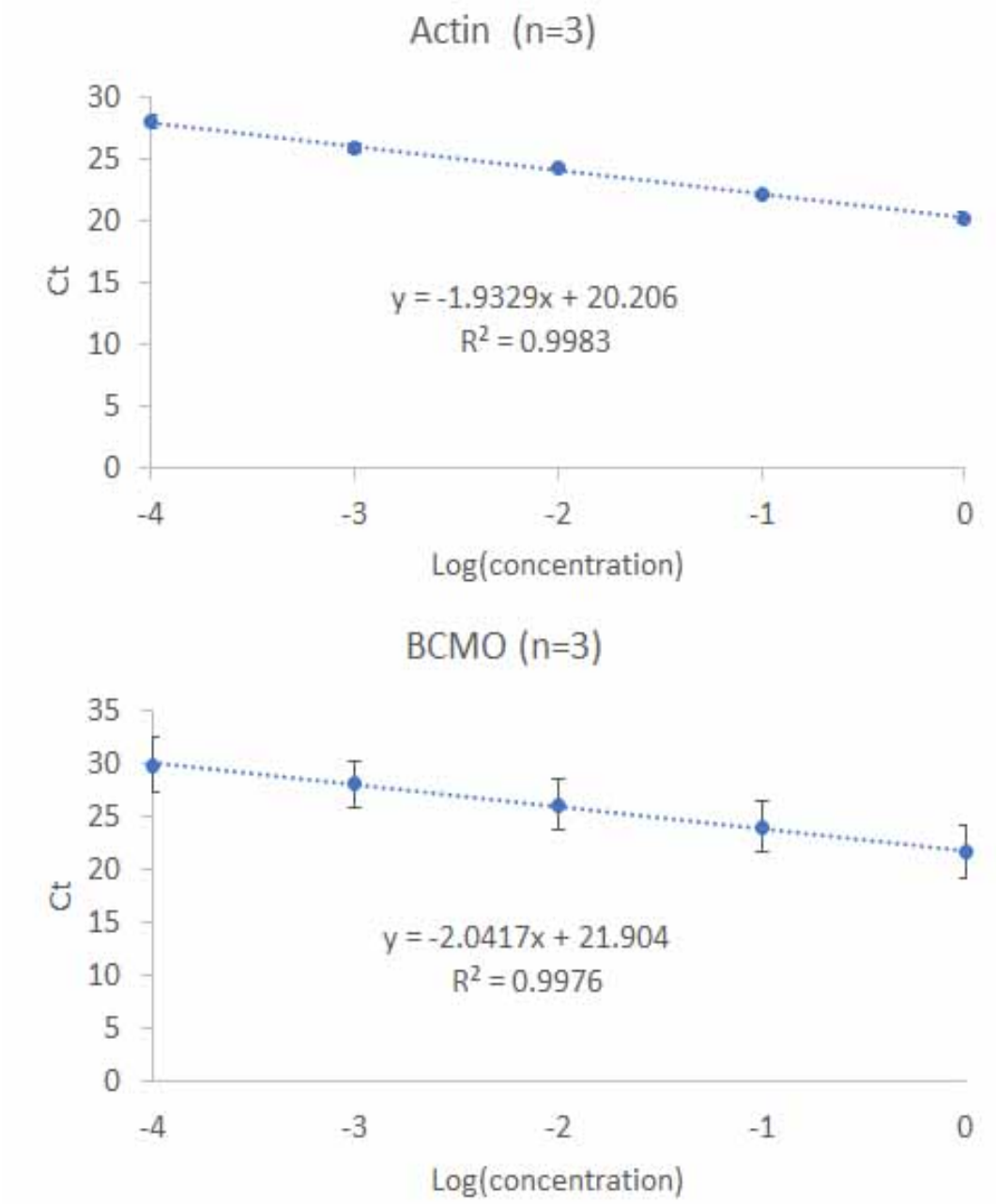


**Figure 3.15 Primer efficiency tests for gene Actin and BCMO.** Upper standard curve shows the cycle threshold (Ct) value of different dilution fold of Actin gene, while lower one shows the Ct value of BCMO gene. Each primer pair has three replicates, error bars show the standard deviation. The fitted lines, equations, and $R^2$ are indicated in the diagram, efficiencies were calculated according to the slope of the fitted lines. Error bars show standard deviation.

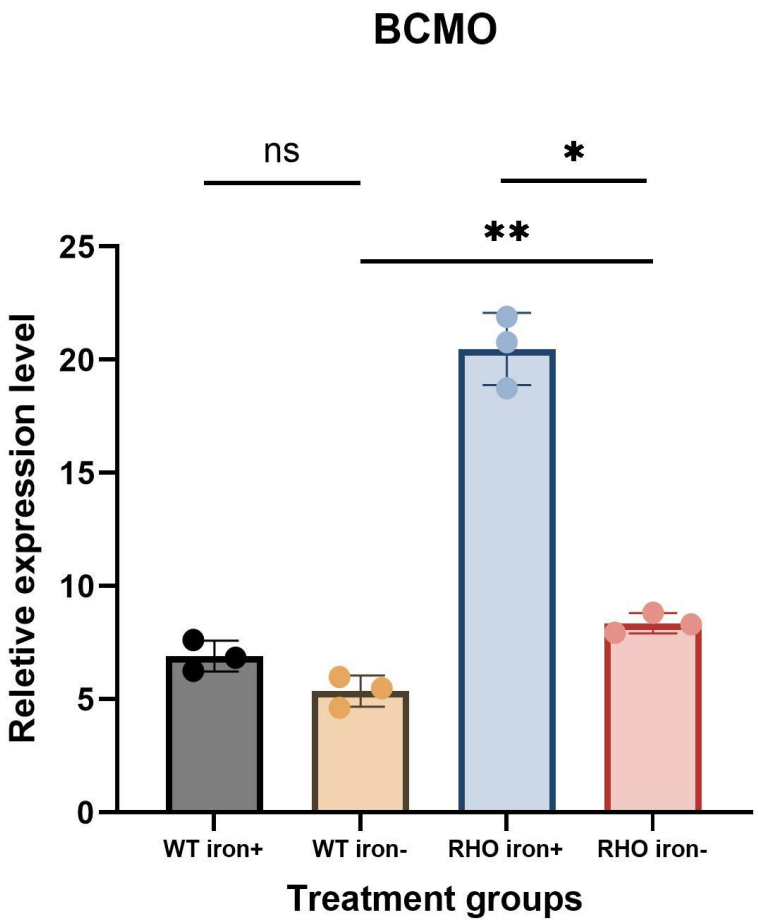


**Figure 3.16 Relative expression level of BCMO of *TpWT* and *TpRHO*.** Each group has three repletes, error bars show standard deviation. Expression levels in wild-type (WT) and rhodopsin-expressing (RHO) strains are compared under iron-repleted (+) and depleted (-) conditions. The expression level of WT under iron repletion is used as the control. Statistical significance is denoted as follows: "ns" indicates no significant difference, "*" for $p < 0.05$, and "**" for $p < 0.01$.

**Immunogold labelling for subcellular localisation**

To obtain a high-resolution localisation of xanthorhodopsin within *Thalassiosira pseudonana* cells, the *TpRHO* strain was processed according to previously described methods, sectioned using an ultramicrotome, and subsequently labelled with antibodies. These antibodies, validated by Jan Strauss via Western Blot, specifically target the extramembrane segment of the microbial rhodopsin FR1. In order to better distinguish the cell structure, Figure 3.17 shows the results of cell structure discrimination based on the original cell section and the results of Wolfe-Simon et al. (2006) as reference. The results, as shown in Figure 3.18, were analysed statistically to determine the potential intracellular localisation of xanthorhodopsin.

The findings indicate that a substantial majority of the xanthorhodopsin labelling, 70.4%, was located within the thylakoids, with 64.8% on the thylakoids themselves and 5.6% on their outer envelope. Additionally, 11.3% of the xanthorhodopsin was localised to vacuoles, while the remainder was localised at unidentified places (Table 3.2). This distribution suggests that xanthorhodopsin predominantly resides on the thylakoid membranes.

| Localisation | Chloroplast | | Vacuole | Unidentified places |
|---|---|---|---|---|
| | Envelope membranes | Lumen including thylakoid membrane | | |
| Number | 4 (5.6%) | 46 (64.8%) | 8 (11.3%) | 13 (18%) |
| Total | 71 TEM images analysed | | | |

**Table 3. 2 Number of antibody signals found in cell images.**

To ensure the specificity of the antibody binding and to validate the markers identified

in the thylakoids as genuine indicators of xanthorhodopsin presence, a negative control was incorporated into the experimental design. This control involved using double-antibody treatments for the *TpWT* and secondary antibody treatments for the *TpRHO*, as presented in Figure 3.19. The purpose was to rule out non-specific binding of the antibodies used in the study. The results from the negative control indicate that no marker targets were observed within the thylakoid regions of the negative control samples, which supports the conclusion that the observed markers within the thylakoids in experimental samples are specific to xanthorhodopsin. The localisation of xanthorhodopsin on the thylakoid membranes supports the hypothesis that microbial rhodopsin plays a critical role in generating a proton gradient across the

thylakoid membrane, thereby assisting in ATP synthesis.

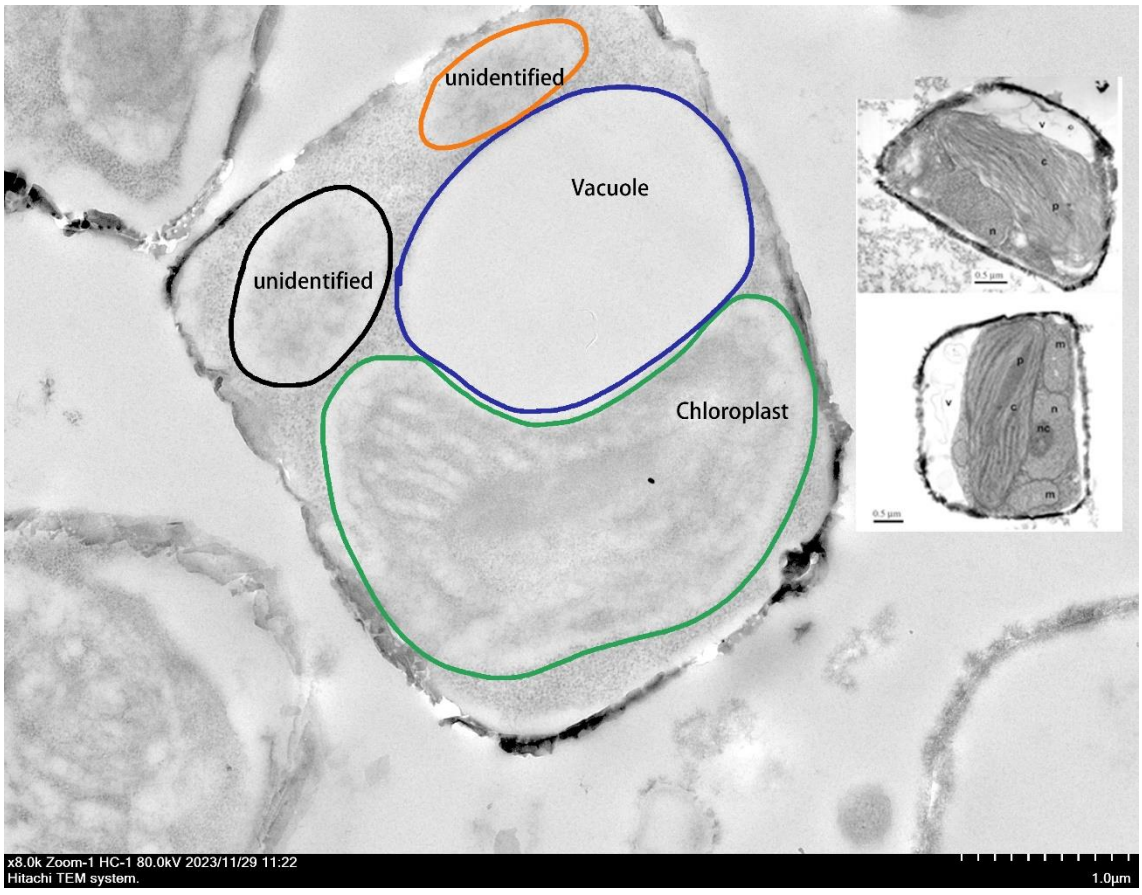


**Figure 3.17 Cell structures of *T. pseudonana* under transmission electron microscope (TEM).** Key organelles are annotated with different colours, where the chloroplast is outlined in green, the vacuole in blue, and two unidentified regions are marked in black and orange. Reference images from Wolfe-Simon et al. (2006) provide a comparison, with the labelled organelles including the chloroplast (c), pyrenoid (p), mitochondrion (m), nucleus (n), nucleolus (nc), and vacuole (v).


a)
Thylakoid membrane
x8.0k Zoom-1 HC-1 80.0kV 2023/11/29 08:26
Hitachi TEM system.
1.0μm

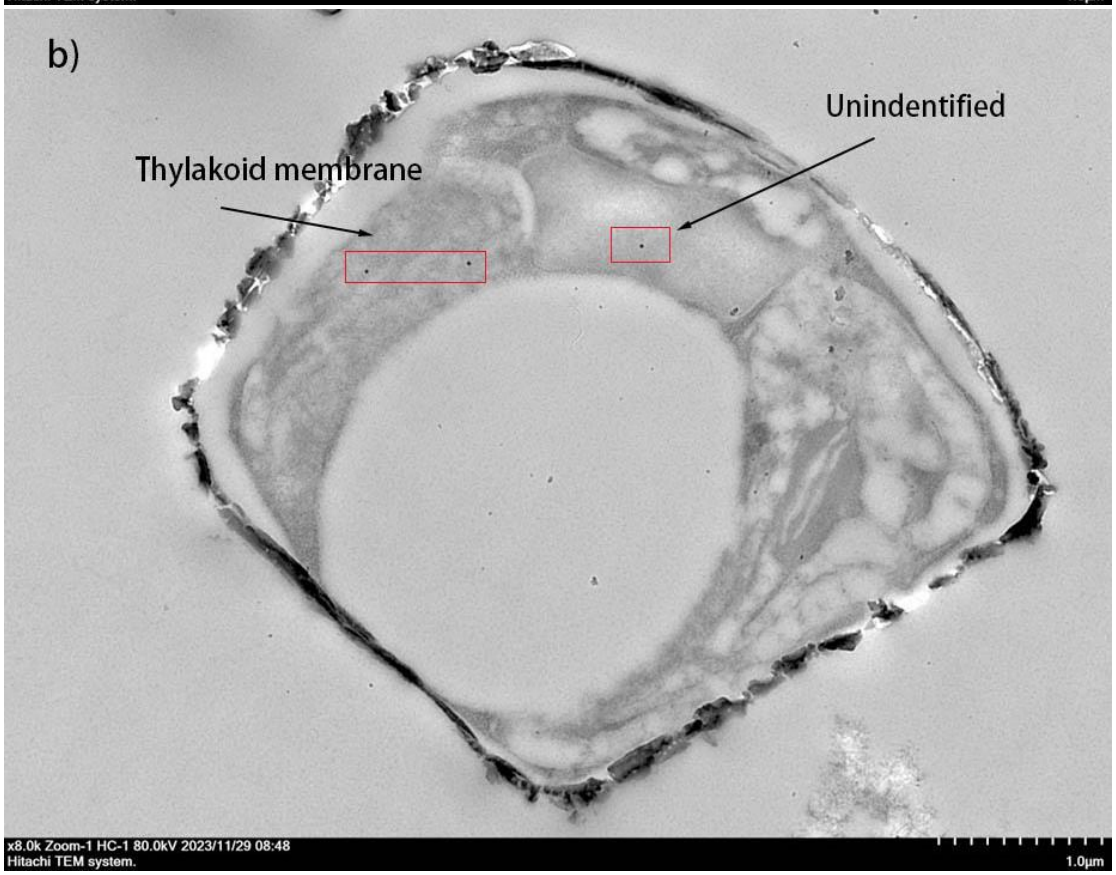
b)
Unindentified
Thylakoid membrane
x8.0k Zoom-1 HC-1 80.0kV 2023/11/29 08:48
Hitachi TEM system.
1.0μm

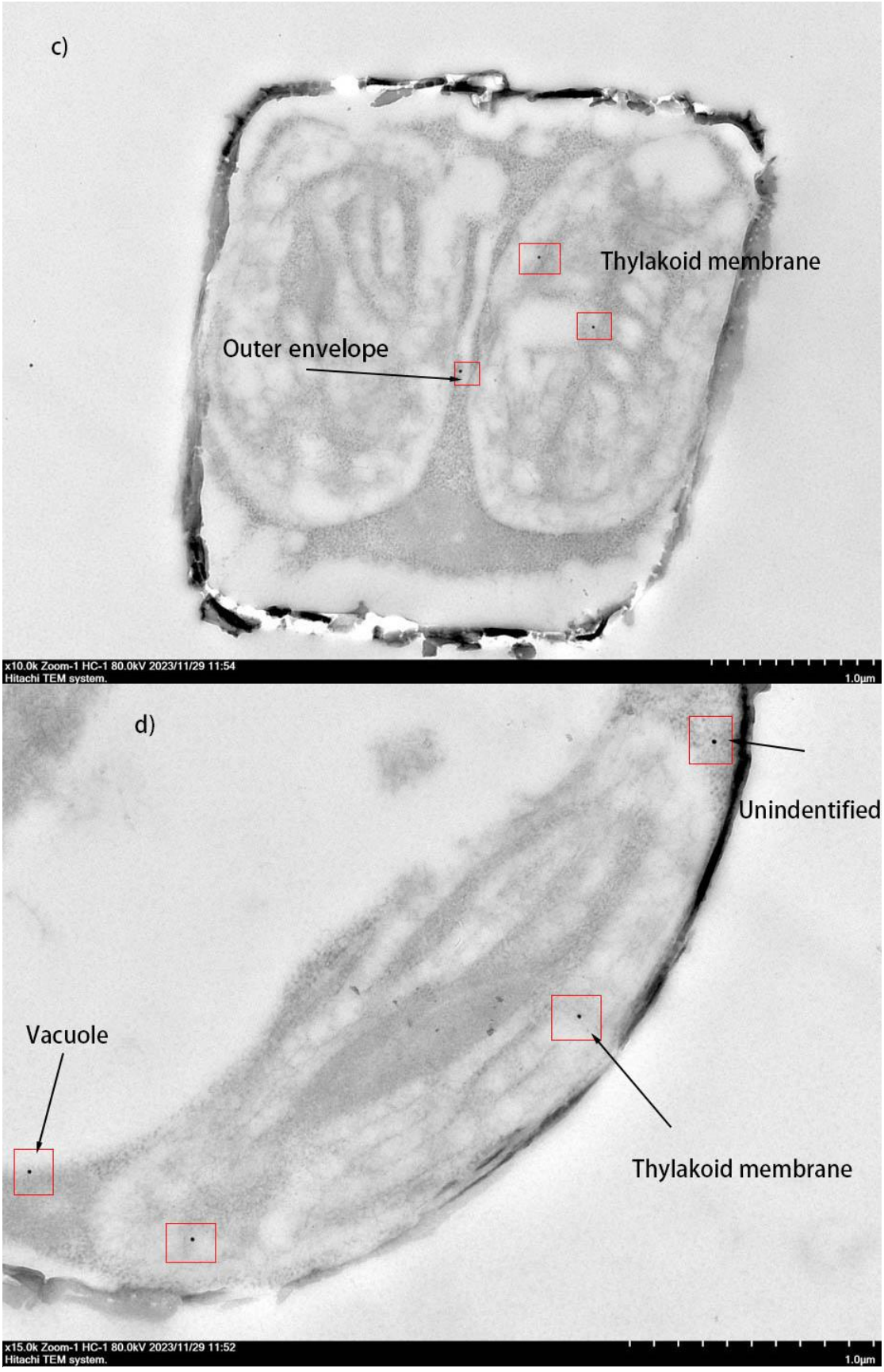


**Figure 3.18 Immunogold staining slicing imaging of *T. pseudonana* rhodopsin knock-in strains using TEM.** Each panel from a-d shows a different cell captured at from 8000x to 15000x magnification. The red boxes highlight specific areas where immunogold labelling points are targeted and visible.

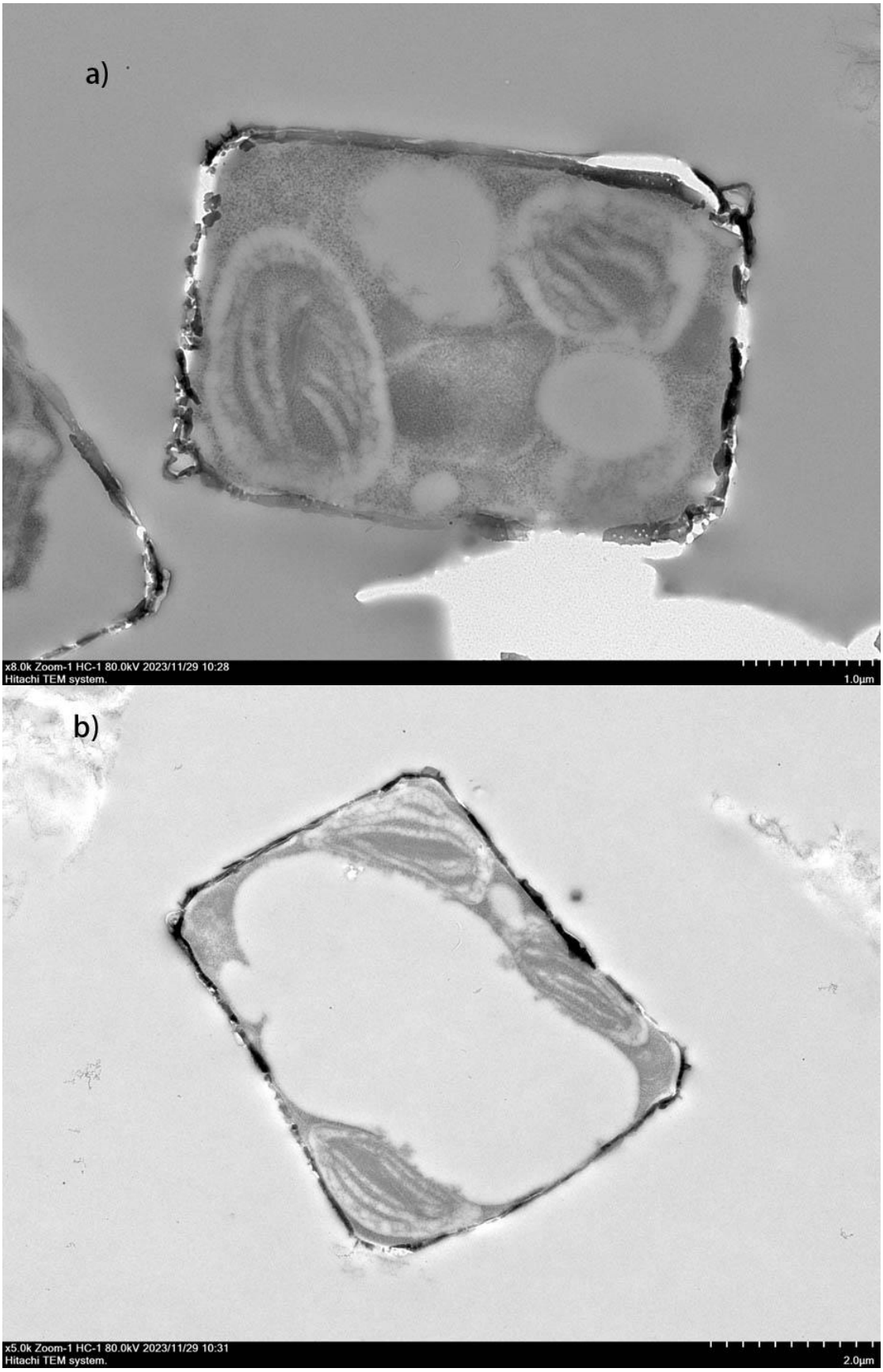


**Figure 3.19 TEM immunogold staining slicing imaging of *T. pseudonana* wild-type (a) and rhodopsin knock-in strain negative control (b).**

**Discussion**

In this research, the construction of a *Thalassiosira pseudonana* strain overexpressing the FR1 gene represents a significant advancement in understanding microbial rhodopsin's role under iron-limited conditions. However, the transformation efficiency in this study was notably lower than expected, achieving only a 10% success rate compared to the 25% to 70% reported in prior research involving the introduction of two transgenes, such as a selection marker and a reporter gene (Falciatore et al., 1999; Ifuku et al., 2015; Moosburner et al., 2020). This discrepancy suggests a unique challenge related to the specific growth conditions of the diatoms before the transformation procedure.

The lower transformation efficiency significantly constrained the number of cell lines available for subsequent functional analyses, limiting this study to a single FR1 overexpressing line. This limitation could impact the generalisability of the findings and highlight the need for further optimisation of the pre-transformation conditions.

Biolistic transformation, while effective, has notable disadvantages, including the potential for complex chromosomal rearrangements, multiple transgene integrations, gene silencing, or altered gene expression, and genetic instability over generations (Gheysen et al., 1987; Meyerink et al., 2017; Nacry et al., 1998; Travella et al., 2005). Additionally, the use of microparticles can cause tissue and cellular damage. Metallic particles entering the target cells can severely damage the nuclear membrane, leading to the exposure of nuclear DNA to cytoplasmic components, thereby inducing DNA breaks and other issues (Godínez-Hernández et al., 2001).

Future studies should aim to generate more FR1 knock-in cell lines to minimise the influence of biolistic transformation's drawbacks. By optimising pre-transformation conditions and employing alternative transformation methods, researchers can improve the efficiency and stability of transgene integration, leading to more robust

and generalisable findings regarding the role of microbial rhodopsin in diatom adaptation and evolution.

Preliminary research results indicate that *Thalassiosira pseudonana* is highly sensitive to iron limitation, requiring substantial iron for growth compared to oceanic diatoms like *P. tricornutum* and *Pseudo-nitzschia* (Cohen, Mann, et al., 2018; Marchetti et al., 2006; Zhao et al., 2018). This makes *T. pseudonana* an excellent species for studying iron limitation. However, the rhodopsin knock-in strains appear to be limited by retinal availability under iron-limited conditions. This limitation can be alleviated by increasing iron concentration or adding extra-retinal (Figure 3.6). The retina is a crucial component in rhodopsin synthesis, and its synthesis enzyme, BCMO, requires iron to work. Therefore, FR1 knock-in strains face a dual limitation under extreme iron restriction (Figure 3.3) (Strauss et al., 2023).

In the initial stages post-knock-in, even under sufficient iron conditions, the FR1 knock-in strains exhibit slight retinal limitation, which is alleviated after 12 months of prolonged cultivation. This suggests an upregulation of internal synthetic pathways over time, eventually making the strains less affected by retinal limitation, which was proved by RT-qPCR results for measuring BCMO expression level. According to the RT-qPCR results, the BCMO expression level was significantly upregulated to meet the demand for extra retinal used for xanthorhodopsin synthesis. Even under the iron limitation, the BCMO expression level in *TpRHO* was still significantly higher than in *TpWT*. However, a decreased trend was observed compared to iron-repleted treatments. Therefore, extra-retinal was added to the culture medium to minimise the influence of retinal lacking. However, adding extra retinal at high concentrations (4μM) was found to limit the growth of diatoms (Figure 3.8). After ruling out the impact of the solvent DMSO on diatoms (Figure 3.9), it appears that the high oxidative of retinal can damage metabolic processes and cellular structures, thereby affecting diatom growth (Dal-Pizzol et al., 2000; Gimeno et al., 2004; Murata &

Kawanishi, 2000).

The physiological experiment has highlighted the pivotal role of xanthorhodopsin in knocked-in *Thalassiosira pseudonana*, particularly under iron-limited conditions. The enhanced performance of FR1 knock-in strains compared to wild-type suggests that xanthorhodopsin contributes significantly to the growth and biomass of diatom species in iron-limited conditions. These findings support previous research indicating that microbial rhodopsin is a novel adaptation strategy for diatoms in iron-limited environments (Marchetti et al., 2015).

Xanthorhodopsins, functioning as light-driven proton pumps, appear to offer a compensatory mechanism during iron limitation. However, the detailed functions were not determined based on these data from physiological experiments. Combined with our hypothesises and recent research, the xanthorhodopsins in diatoms might: (1) localised at the thylakoid membrane, pumping protons from the plastid stroma into the thylakoid lumen to generate the trans-thylakoidal proton gradient and support ATP synthases; (2) localised at the vacuole membrane to support many functions including supporting vacuole ATPase and pyrophosphatase and driving transporters and inorganic ion exchangers. (3) localised in plastid outer membrane, supporting facilitate C fixation by acidifying the intermembrane space or contributing to generating a proton motive force facilitating the uptake of dissolved iron (Andrew et al., 2023; Strauss et al., 2023; Yoshizawa et al., 2023). Both hypotheses could increase the production of ATP under iron-limited growth if iron uptake is suboptimal and contributes to photosynthesis. The significant differences in growth and photosynthetic efficiency between the modified and wild-type strains under varying iron concentrations further underscore the adaptive advantages conferred by xanthorhodopsin expression. This is particularly evident from the rapid light curve analysis, which shows superior performance in FR1-overexpressing strains (Figure 3.13).

Interestingly, the photosynthetic parameters of the *TpRHO* strains under iron-limited conditions are significantly higher than those of the *TpWT* strains under iron-sufficient conditions. Xanthohodopsin not only enhances the light utilisation efficiency of *TpRHO* but also improves the overall electron transport efficiency and the maximum electron transport rate (Figure 3.14). Notably, the *TpRHO* strains exhibit a higher light saturation point, indicating an enhanced capacity to adapt to high-light environments, which is likely due to the presence of more or larger light reaction centres, as posited by Melis(1999). These enhanced reaction centres could potentially boost electron transport and photosynthetic capacity, thus mitigating light-induced damage (Melis, 1999). Furthermore, the connection between microbial rhodopsin and ATP production may also play a crucial role in these physiological improvements. Increased ATP availability, as discussed by Murata et al. (2007), could accelerate the repair rate of light reaction centres, thereby enhancing photosynthetic capacity. However, the production of more light reaction centres, especially under iron limitation, where PSII formation is reduced, still demands significant iron. The potential function of microbial rhodopsin to assist in iron transport or utilisation could be a pivotal mechanism in this context. For example, the action of H-ATPases might facilitate the unbinding of $Fe^{3+}$ within vesicles and its subsequent reduction to $Fe^{2+}$, enhancing iron bioavailability within the cells. Additionally, the involvement of ATP-binding cassette (ABC) superfamily transporters and iron-chelating and reducing proteins such as FBP1 and FRE (Årstøl & Hohmann-Marriott, 2019; Kosman, 2003; Kustka et al., 2007; Sutak et al., 2020). Another possible explanation is that some diatoms, such as *Thalassiosira weissflogii* and *Thalassiosira pseudonana*, have the ability to absorb and store iron when it is abundant (Nuester et al., 2012; Sunda & Huntsman, 1995). This capability allows *TpRHO* to synthesise more photoreactive centres when iron is available, giving it an advantage. After the iron starvation treatment, *TpRHO* still maintained a significantly higher number and size of light reaction centres compared to *TpWT*. It may be beneficial to include a long-term culture of iron-limited *TpRHO* as

a control in future experiments to observe if this has a sustained effect. This additional control could help determine the long-term adaptability and resilience of *TpRHO* under chronic iron limitation and provide further insights into the role of iron storage and utilisation in enhancing photosynthetic capacity and overall growth performance.

Overall, these observations suggest that the role of microbial rhodopsins play in diatom might be multifaceted, producing synergistic effects that enhance various aspects of diatom physiology. To further understand how microbial rhodopsin supports diatoms and other microbes, investigating its high-resolution subcellular localisation could be highly informative.

Therefore, the immunogold labelling was carried out to gain high-resolution imaging of xanthorhodopsin subcellular localisation. According to the results, immunogold labelling has demonstrated that xanthorhodopsin localises to the thylakoid membranes (Figure 3.18). However, the immunogold-labelled cells were severely deformed compared to standard TEM imaging. The structural integrity of the cells was significantly impaired, and the abundance of markers was notably lower. This may be due to the pre-treatment with chemical fixatives (Jiang et al., 2021; Li et al., 2017). Therefore, a new protocol to optimise the chemical fixation process should be developed to achieve a higher abundance of markers. These results prove our previous hypothesis that the xanthorhodopsin is localised at thylakoid membranes and is involved in a unique phototrophic pathway that contributes to ATP synthesis under both iron-limited and iron-replete conditions.

Despite these challenges, the results support our hypothesis that microbial rhodopsin is localised at the thylakoid membranes and involved in a unique phototrophic pathway contributing to ATP synthesis under both iron-limited and iron-replete conditions. This is very similar to the homologous proteins in prokaryotes in diatom, the microbial rhodopsins were localised thylakoid membranes instead of the plasmalemma (Bar-Shalom et al., 2023; Hoffmann et al., 1994). Future work should

focus on refining the fixation process to better preserve cell structure and enhance marker visibility, providing more detailed insights into microbial rhodopsin's role in diatom physiology.

In summary, this research is the first to provide unprecedented insight into understanding the role of microbial rhodopsin under iron-limited conditions through the construction of a *Thalassiosira pseudonana* strain overexpressing the xanthorhodopsin FR1 gene. The physiological experiments demonstrate that xanthorhodopsin enhances growth, biomass, and photosynthesis in diatoms under iron-limited and iron-repleted conditions, indicating that FR1-expressing strains have a significant adaptive advantage over wild-type. To our knowledge, the immunogold labelling results are the first successful confirmation of the subcellular localisation of a diatom’s microbial rhodopsin to the thylakoid membranes, revealing a unique light-harvesting pathway in diatoms that is distinct from photosynthesis. Future studies should aim to unravel the molecular mechanisms underlying these effects, including direct ATP measurement to reveal if the xanthorhodopsin could provide a fitness advantage and RNA-Sequencing to investigate the relevant gene expression level to find out if any iron-connected gene was upregulated or downregulated by xanthorhodopsin. Moreover, although FR1 and FR2 have the same amino acid sequence and proton pump function, their expression conditions are strikingly different. Investigating the relevant properties of FR2 in the future will be a crucial step towards deepening our understanding of microbial rhodopsin in diatoms.

These observations propose a broader ecological and evolutionary significance for microbial rhodopsin in diatoms, which not only enhances our understanding of diatom physiology but also indicates the genetic tools in studying and harnessing the capabilities of these microorganisms for applications in sustainability and biotechnology. By deepening our knowledge of how microbial rhodopsin support diatoms adapt to nutrient limitations, we can better appreciate their role in marine

ecosystems and explore new avenues for utilising their unique properties. This understanding could lead to innovative strategies for leveraging diatoms in environmental management, bioenergy production, and other biotechnological applications.

# Chapter 4

# Testing the role of microbial rhodopsins in a heterotrophic eukaryote that possesses a non-photosynthetic plastid.

## Introduction

Diatoms are among the most species-rich groups of algae and play significant ecological roles as primary producers in aquatic environments. However, the diversity and significance of diatoms extend beyond their role in aquatic photosynthesis. A notable example is the pennate marine diatom *Nitzschia putrida* (ID NIES-4239) (Figure 4.1). Unlike most diatoms that are photosynthetic, *N. putrida* became a non-photosynthetic, heterotrophic diatom during its evolution process, meaning it relies

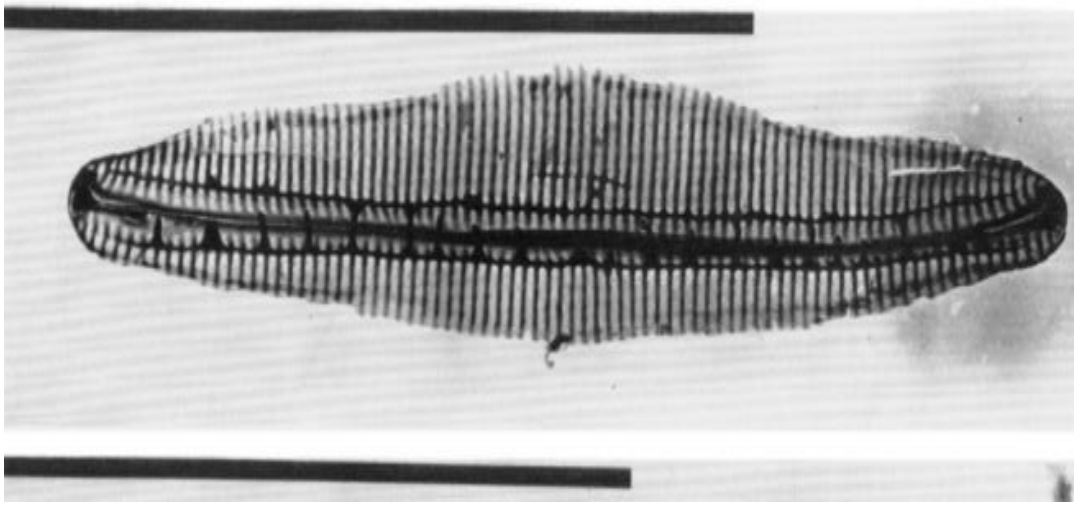

**Figure 4.1 Electron micrographic cell image of *Nitzschia putrida*. Scale bar (black) = 10µm.** Cited from Lewin & Lewin(1967).

entirely on external organic carbon sources for its metabolic needs(Kamikawa et al., 2015).

The evolutionary history of *Nitzschia putrida* is marked by a notable shift from a photosynthetic to a heterotrophic lifestyle. This transition involves a secondary loss of

photosynthesis, a phenomenon observed in various plastid-bearing branches of the eukaryotic tree of life (Kamikawa et al., 2022; Kamikawa et al., 2015). *Nitzschia putrida* has lost more than 50% of its photosynthetic relatives plastid proteins, including essential proteins for light-harvesting antenna, PSI and PSII, cytochrome b6/f complex, and carbon fixing (Kamikawa et al., 2022), but still retains many plastid metabolic pathways typical of photosynthetic diatoms, including the synthesis of ATP, essential amino acids, heme, and riboflavin (Kamikawa et al., 2022).

This transition in metabolic mode has occurred independently multiple times within the genus *Nitzschia*, suggesting that it may have undergone several independent events of photosynthesis loss(Kamikawa et al., 2015). The timing of photosynthesis loss varies among species within the genus, indicating that this phenomenon did not occur uniformly across evolutionary branches (Lewin & Lewin, 1967; Li & Volcani, 1987). The reason why this diatom genus is particularly prone to such major evolutionary transitions remains unclear. While most research on the loss of photosynthesis has focused on parasitic species, such as the red algal parasites adelphoparasites and alloparasites (Freese & Lane, 2017), *Helicosporidium* sp of green algae (de Koning & Keeling, 2006), mixotrophic algae (Janouškovec et al., 2019), and etc. (Hadariová et al., 2018), *N. putrida*, as still a free-living heterotrophic microalga instead of a parasite, provides not only a unique model for investigating the genetic, metabolic, and physiological changes that occurred during the transition from photoautotrophy to heterotrophy but also an ideal model for reverse-engineering photosynthesis using microbial rhodopsin in a heterotrophic eukaryote. Therefore, the establishment of a transformation system allows for more detailed analysis through the direct manipulation of genes and pathways.

The significant ecological and evolutionary interest in diatoms increases the development of molecular tools to advance research in diatom biology and ecology. Since the first successful genetic transformation in the diatom *Cyclotella*

*cryptica* and *Navicula saprophila* by biolistic, this method has rapidly become a standard and most popular technique for various genetic modifications of diatoms (Dunahay et al., 1995). Up to today, several species, including *Thalassiosira pseudonana* (Poulsen et al., 2006), *Phaeodactylum tricornutum* (Apt et al., 1996), *Fragilariopsis cylindrus* (Hopes, 2017), *Pseudo-nitzschia multistriata* and *Pseudo-nitzschia arenysensis* (Sabatino et al., 2015), and *Nitzschia captiva* (Sprecher et al., 2023), have been successfully genetically modified using these methods. Recently, techniques for high-efficient, low-damaging transgene introduction into diatoms through electroporation (Hu & Pan, 2020; Okada et al., 2023; Yin & Hu, 2021) and bacterial conjugation (Karas et al., 2015) have also been applied in diatom transformation system. However, each of these methods has its disadvantages. Biolistic transformation, as described, could cause significant cellular damage, which may affect gene expression and other cellular processes (Gheysen et al., 1987; Godínez-Hernández et al., 2001; Nacry et al., 1998). While for electroporation, carries the risk of DNA damage (Batista Napotnik et al., 2021; Meaking et al., 1995) and can be less effective in cells with thick cell walls, which can hinder delivery efficiency (Azencott et al., 2007). Additionally, the optimisation process for electroporation is more complex than that of biolistic methods. Bacterial conjugation, although has high efficiency, typically results in the lowest yield efficiency (Karas et al., 2015). Given these considerations, biolistic transformation is regarded as a safer and more efficient method and was selected to establish the transformation system for *Nitzschia putrida*.

This chapter focuses on the development of a transformation system for *N. putrida* and using microbial rhodopsin to reverse-engineered this heterotrophic diatom to enable light-driven energy acquisition. Following physiological experiments were tested to analyse the influence of a light-harvesting protein in *N. putrida*. This is the first heterotrophic diatom to be transformed and reverse-engineered to regain the ability of light harvest. This will not only contribute to diatom research but also offer new insights into the implications of diatom diversity and adaptability.

## Method

### Strains and growth conditions

*Nitzschia putrida* (NIES-4239) was collected from the National Institute for Environmental Studies (NIES Collection, Japan). The standard culture medium protocol provided by the NIES Collection was insufficient for the optimal growth of *N. putrida*. Consequently, pre-experiments were conducted to optimise the culture medium receipt.

The finalised growth medium consisted of 16 PSU (practical salinity units) artificial seawater prepared by mixing 20g/L Tropic Marin® artificial sea salt (Germany) with 50% LB broth, containing 5g/L Tryptone, and 5g/L Yeast extraction. Low nutrient 20% LB medium containing 2g/L Tryptone and 2g/L Yeast extraction. This medium was supplemented with f/2 nutrients according to the National Center for Marine Algae and Microbiota (NCMA) protocol (Guillard & Ryther, 1962; Guillard, 1975). For solid media, 1.6% and 0.8 % agar were added before autoclaving. An optional antibiotic mixture could be used to prevent potential bacterial contamination with 50 µg/ml ampicillin, 1 µg/ml gentamycin, 25 µg/ml streptomycin, 1 µg/ml chloramphenicol, and 10 µg/ml ciprofloxacin. All cultures were grown at 20 °C with 200rpm shaker to achieve higher cell concentration (Lewin & Lewin, 1967). Light is not essential for the growth of *N. putrida*.

### Construct for enhanced green fluorescent protein (eGFP), nourseothricin resistance protein (NAT) and xanthorhodopsin (FR1) expression

### Antibiotic sensitivity test

To determine the suitable species and concentration of antibiotic used in selective medium following the microparticle bombardment, two antibiotics, nourseothricin and zeocin, which have been widely used in transformations of model diatoms *T.*

*pseudonana* and *P. tricornutum*, were tested (Karas et al., 2015; Poulsen et al., 2006; Samukawa et al., 2014; Zaslavskaia et al., 2000; Zhang & Hu, 2014). *N. putrida* cells were harvested at the exponential phase and exposed to nourseothricin and zeocin at concentrations of 50, 100, and 150μg/ml in both liquid and solid medium to assess their efficacy. Growth was assessed over a 10-day period.

**Promoter and terminator selection**

| ID | Transcripts per million | Number of reads | Predicted functions |
|---|---|---|---|
| NAA15P02220.m1 | 40,741.12 | 531,595.41 | NADH–ubiquinone reductase complex 1 MLRQ subunit |
| NAA02P08450.m1 | 13,828.98 | 129,286.20 | Small subunit ribosomal protein S28e |
| NAA41P00270.m1 | 12,104.54 | 279,594.59 | Cytochrome c |
| NAA03P04550.m1 | 10,733.23 | 205,861.61 | Ribosomal protein L41 |
| NAA18P02090.m1 | 7100.36 | 127,175.67 | 60S ribosomal protein L37 |
| NAA14P02710.m1 | 6872.14 | 214,966.96 | Ribosomal protein L44e |
| NAA07P03020.m1 | 6236.76 | 19,5091.68 | 60s acidic ribosomal protein |
| NAA42P00920.m1 | 6027.24 | 222,393.81 | Cytochrome c oxidase subunit 6B |
| NAA03P01270.m1 | 5789.20 | 487,003.74 | Acetate transporter |
| NAA07P01730.m1 | 5782.82 | 141,314.63 | 40S ribosomal protein S30 |

**Table 4.2 Ten highest expressed gene under different culture conditions provided by Kamikawa et al. (Deng et al., 2025).**

RNA sequencing data collected from different light treatments were produced by Kamikawa (Kamikawa et al., 2022). To assess the highest heterologous gene expression level, the optimal endogenous promoter and terminator were selected from the upstream and downstream of the highest expression gene (Table 4.1). The 1000bp

coding regions upstream and downstream of the NADH-ubiquinone reductase complex 1 MLRQ subunit protein (NADH) (JGI ID 4914) were selected as the promoter and terminator, respectively. Sequences were then synthesised by Azent (US), with *BpiI* and *BsaI* sites subsequently removed by site-directed mutagenesis (SDM) kit (NEB, UK).

**Codon bias analysis**

Codon bias was analysed by Emboss cusp tool (https://www.bioinformatics.nl/cgi-bin/emboss/cusp) to calculate the usage fraction. The analysis was conducted by comparing the codon usage of *Nitzschia putrida* with the codon usage of the FR1 and eGFP genes. For this comparison, the ten highest expressed *N. putrida* genes, as identified by Kamikawa et al. (2022) were utilised.

**Plasmid construction using Golden Gate cloning**

The construction of plasmids was done using the Golden Gate assembly method

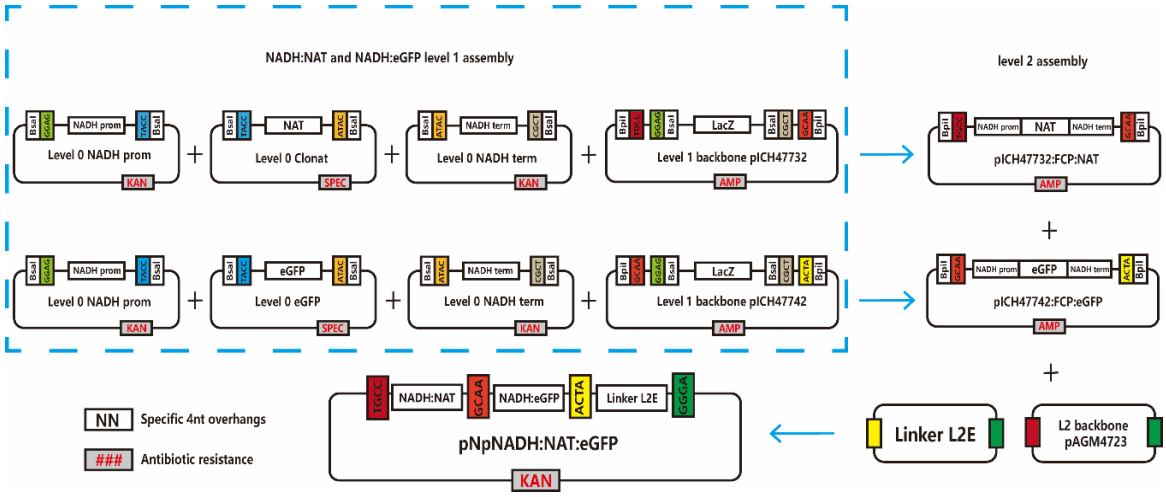


**Figure 4.4 Overview flow chart of the Golden Gate Cloning system for *N. putrida* eGFP and NAT overexpression constructs. This figure was generated as part of my original PhD research.** Level 0 (L0) modules are created by PCR and then cloned into pCR8/GW/TOPO vectors. Key components include the promoter (NADHpr) and terminator (NADHt) of the NADH-ubiquinone reductase complex 1 MLRQ subunit, ampicillin resistance gene (AmpR), kanamycin resistance gene (KanR), and target gene fragment eGFP/FR1 (eGFP). Specific 4nt overhangs are shown in different colors, while the same color indicates the same overhang.

according to the protocol by Weber et al. (2011). With the restriction enzymes of *Bsa*I and *Bbs*I (*Bpi*I) and designed specifical four nucleotide overhangs, Golden Gate Cloning could assemble target DNA fragments into pre-configured module. This method enables a precise ligation of target DNA fragments with scarless assembly. The assembly process has three construct levels from Level 0 (L0), Level 1 (L1), to Level 2 (L2). Individual DNA fragments such as promoter, antibiotic gene, target gene, and terminator. These L0 cassettes were then introduced into the L1 backbones for functional plasmid using *Bsa*I restriction enzyme. Subsequently, the L1 modules are combined within the final L2 backbone, resulting in a fully assembled construct that includes all necessary genetic elements within the *Bbs*I (*Bpi*I) restriction enzyme (Figure 4.2). Golden Gate cloning reactions were optimised from the protocol by Hopes et al. (2017).

To begin the L0 assembly, the *Bsa*I restriction site in the RHO sequence was removed using the Site-Directed Mutagenesis (SDM) kit (NEB, UK) with the following primers: gaacttgcgaaAaccggcagtccg and cccttcgccggtccattcat. The mutation site is indicated by the uppercase letter. Following the mutagenesis, L0 modules were created with specific 4-nucleotide overhangs using a standard PCR process. The primers used for generating these L0 modules are listed in Table 4.2. All PCR-amplified L0 modules were immediately cloned into the pCR8/GW/TOPO vector (ThermoFisher, US). The reaction mixture was prepared by combining 4 µl of PCR product with 1 µl of Salt Solution and 1 µl of TOPO vector, resulting in a total volume of 6 µl. This mixture was incubated at room temperature for 5 minutes. The L0 plasmids were then transformed into NEB 5-alpha Competent *E. coli* (NEB, UK) using the high-efficiency transformation protocol. Specifically, 3µl of the TOPO mixture was added to 25µl of competent *E. coli* cells and incubated on ice for 30 minutes. This was followed by a 30-second heat shock at 42°C, after which the mixture was immediately returned to ice for 5 minutes. Next, 950 µl of room-temperature SOC medium was added, and the tube was incubated at 37°C for 60

minutes with vigorous shaking at 250 rpm or rotation. Finally, an appropriate volume of the transformed cells was spread onto selective LB agar plates and cultured overnight at 37°C. L0 plasmids were extracted using the NEB Monarch Plasmid Miniprep kit (NEB, UK) and using the *Bsa*I enzyme to check the size of the insertion.

Based on the L0 modules, three L1 modules, pICH47732:NADH:NAT, pICH47742:NADH:RHO, and pICH47742:NADH:eGFP, were assembled (Figure 4.3). Each 20µl reaction were mixed with 40 fmol components, 100 units of *Bsa*I restriction enzyme, 100 units of T4 DNA ligase, and 1 x ligation buffer. The reaction

| Target | Sequence |
|---|---|
| RHO F | gcgggtctca***tacc***ATGCTGTGGTCAAAAACAA |
| RHO R | attggtctca***gtat***TTAGAGCAAAGGCGTTTC |
| EGFP F | ggtctca***tacc***ATGGTGAGCAAGGGCGAGG |
| EGFP R | ggtctca***gtat***TTACTTGTACAGCTCGTCC |
| NAT F | caaggtctca***tacc***ATGACCACTCTTGACGACACG |
| NAT R | agtggtctca***gtat***TCAGGGGCAGGGCATGCTC |
| NADH prom F | ggtctca***ggag***CACATAGTGGCGCAGTATCCA |
| NADH prom R | ggtctca***ggta***ATGTTTTTTGTTTTAGAA |
| NADH term F | ggtctca***atac***AGTACAATACAATACAGTCC |
| NADH term R | ggtctca***agcg***GGTATTTTTTCGTAGGAATAAG |

**Table 4.4 PCR primers for creating Golden gate cloning L0 modules.** *Bsa*I sites are shown in underlined. 4nt specific overhangs are shown in italic and bold. Lowercase letters represent extra added sequences, and uppercase letters indicate the part of primer combine with the initial template.

mixtures were incubated at 37°C for 5 hours, followed by 50°C for 5 mins and 80°C

for 10 mins. Following the assembly, 5µl of the reaction were added into 25µl competent *E. coli* and cloned as described above. Cells were selected using a selective medium containing ampicillin, 20µl 40mg/ml X-gal and 7µl 0.1mM IPTG. The correct assembled L1 modules would remove the LacZ gene for blue colony, leading to white colonies. These white *E. coli* colonies were picked up and used for subsequent plasmid extraction.

The extracted L1 plasmids were then verified through double digestion to confirm the presence of the correct inserts. Additionally, the integrity of the L1 module sequences was confirmed by sequencing, performed by Eurofins Genomics (Germany).

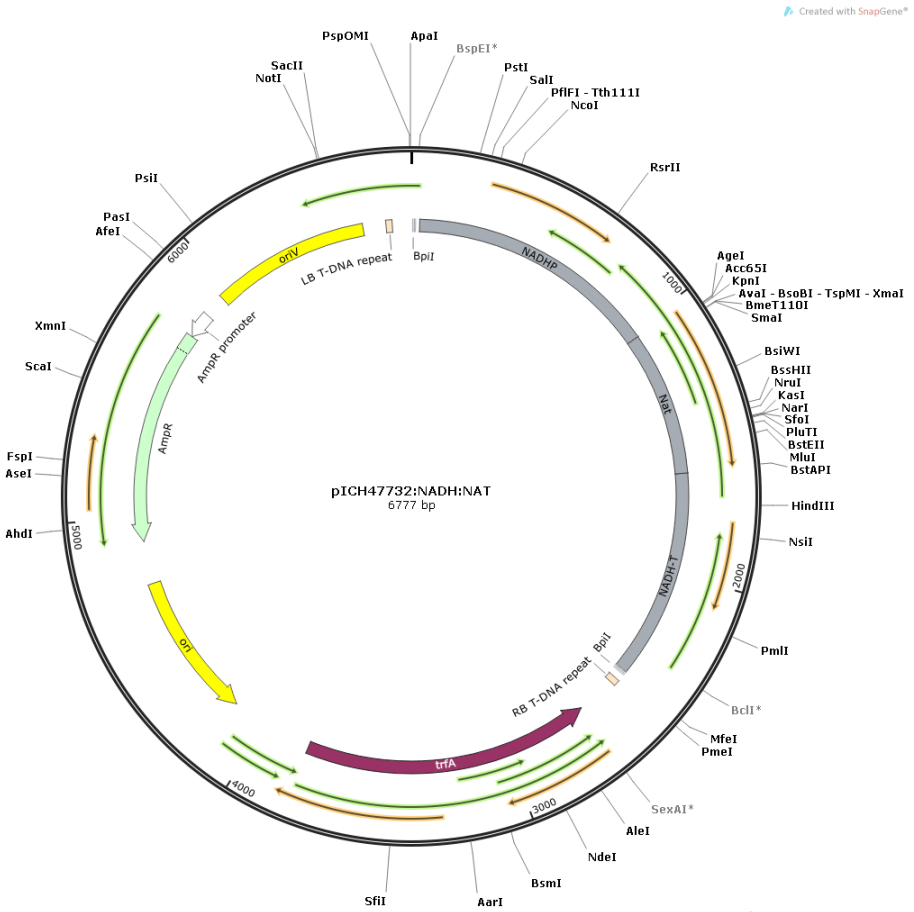
Created with SnapGene®
PspOMI
ApaI
BspEI*
SacII
NotI
PstI
SalI
PflFI - Tth111I
NcoI
RsrII
PsiI
PasI
AfeI
AgeI
Acc65I
KpnI
AvaI - BsoBI - TspMI - XmaI
BmeT110I
SmaI
XmnI
ScaI
BsiWI
BssHII
NruI
KasI
NarI
SfoI
PluTI
BstEII
MluI
BstAPI
FspI
AseI
HindIII
AhdI
NsiI
PmlI
BclI*
MfeI
PmeI
SexAI*
AleI
NdeI
BsmI
SfiI
AarI
pICH47732:NADH:NAT
6777 bp
oriV
LB T-DNA repeat
BpiI
NADHP
Nat
AmpR promoter
AmpR
ori
RB T-DNA repeat
BpiI
NADH-T
trfA
1000
2000
3000
4000
5000
6000

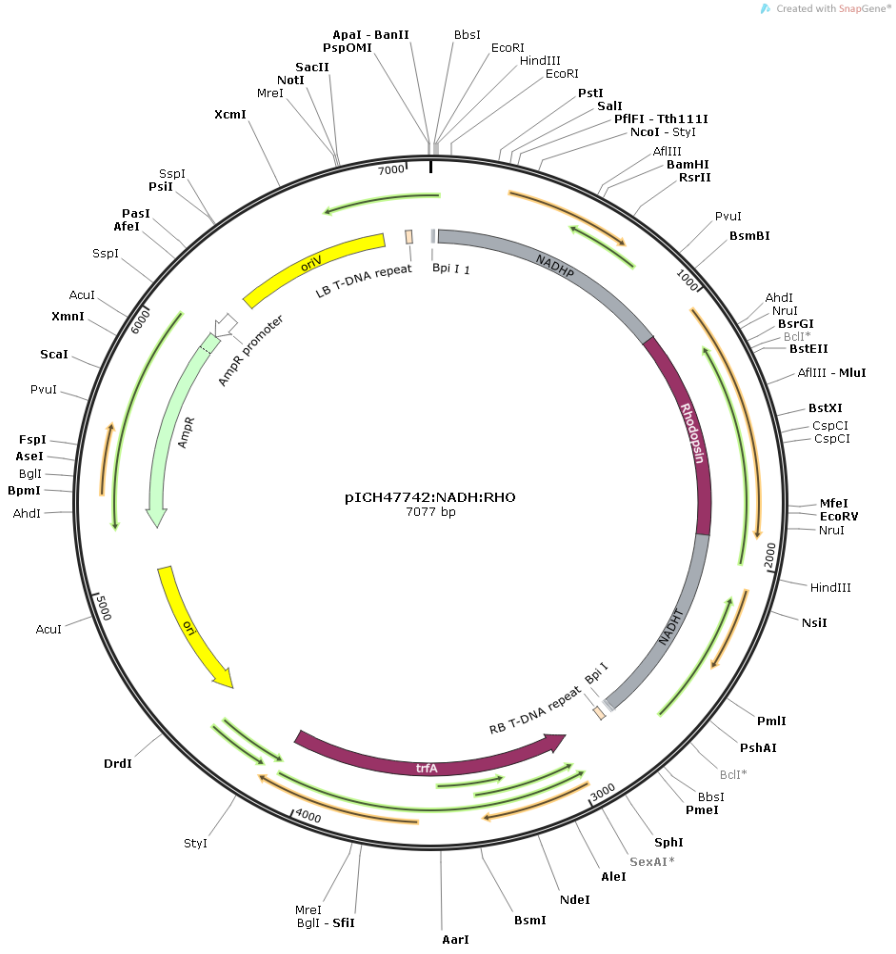
Created with SnapGene®
ApaI - BanII
PspOMI
BbsI
EcoRI
HindIII
EcoRI
SacII
NotI
MreI
PstI
SalI
XcmI
PflFI - Tth111I
NcoI - StyI
AflIII
BamHI
RsrII
7000
SspI
PsiI
PvuI
BsmBI
PasI
AfeI
SspI
oriV
LB T-DNA repeat
Bpi I 1
NADHP
1000
AhdI
NruI
AcuI
BsrGI
BclI*
XmnI
6000
BstEII
ScaI
AflIII - MluI
PvuI
BstXI
CspCI
FspI
CspCI
AseI
BglI
BpmI
AhdI
AmpR promoter
AmpR
Rhodopsin
MfeI
EcoRV
NruI
2000
HindIII
NsiI
5000
AcuI
ori
NADHT
RB T-DNA repeat
Bpi I
PmlI
PshAI
DrdI
trfA
BclI*
3000
BbsI
PmeI
4000
SphI
StyI
SexAI*
AleI
NdeI
MreI
BglI - SfiI
BsmI
AarI
pICH47742:NADH:RHO
7077 bp

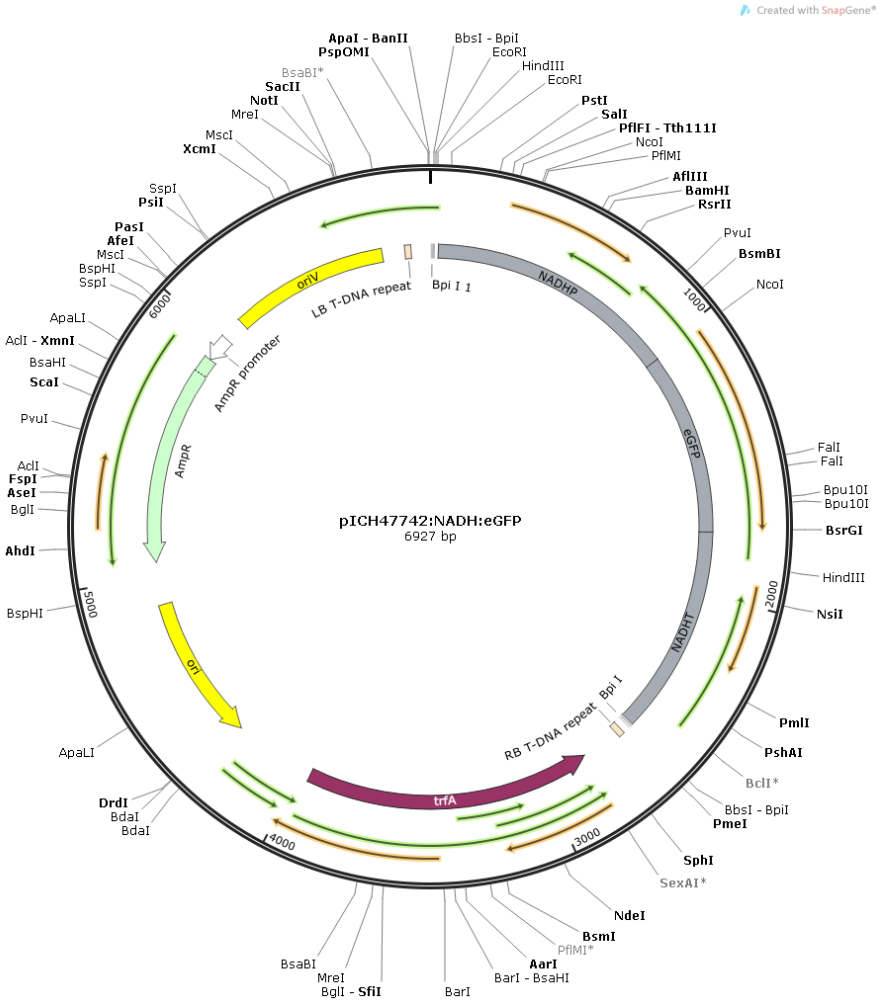


**Figure 4.5 Vector map of three L1 assemblies.** L0 modules were constructed into level 1 backbone pICH47732 and pICH47742.

The verified L1 modules were used to generate L2 plasmids pNpNADH:NAT:eGFP and pNpNADH:NAT:RHO by combining the L1 modules pICH47732:NADH:NAT, pICH47742:NADH:eGFP/ pICH47742:NADH:RHO with the L2E linker piCH41744, assembled into the L2 backbone pAGM4723 (Figure 4.4). For the L2 assembly, the same ligation and transformation steps were followed with *Bpi*I (*Bbs*I) enzyme. Transformed *E. coli* cells were plated on a kanamycin-resistant medium. The correct assembly of L2 constructs disrupted the canthaxanthin biosynthesis gene, resulting in white colonies instead of orange (pink) colonies. Only the white colonies were selected for further analysis, ensuring the accuracy of the L2 plasmids. The plasmids were then checked by at least two different double digestions and sent for whole

plasmid sequencing (Eurofins Genomics, Germany).

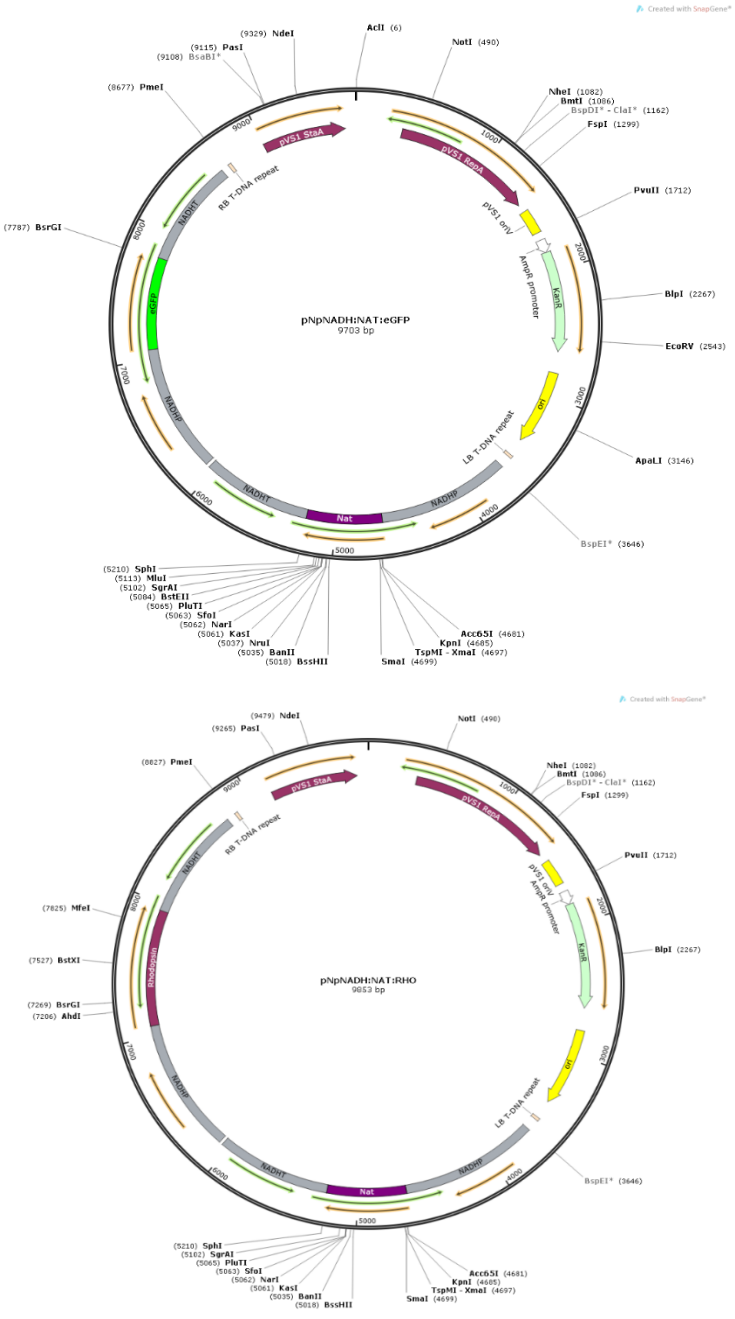


**Figure 4.6 Vector map of two L2 assemblies.** The top construct (pNpNADH:NAT:TeGFP) includes the eGFP reporter gene driven by the NADH promoter, followed by the NAT (nourseothricin resistance) selection marker under control of a separate promoter. The bottom construct (pNpNADH:NAT:RHO) is structurally similar but contains the rhodopsin gene (RHO) instead of eGFP.

**Transforming *Nitzschia putrida***

Transformation of *N. putrida* cells was carried out using the Biolistic PDS-1000/He particle delivery system (BIO-RAD, USA), following the protocols outlined by Poulsen et al., Hopes et al., and Sabatino et al. (Hopes et al., 2016; Poulsen et al., 2006; Sabatino et al., 2015).

To prepare for the transformation, non-selective agar plates were created using half-salinity LB with 1.5% agar, which served as the target surface for particle bombardment. Post-transformation selection was carried out on 0.8% agar f/2 half-salinity LB plates and f/2 half-salinity LB liquid medium containing 100 µg/ml nourseothricin to isolate successfully transformed cells. In parallel, non-selective 0.8% agar plates and liquid medium were prepared as growth controls to ensure the viability of the cells throughout the experiment.

For the particle bombardment, 3 µg of plasmid DNA was coated onto 16 mg of M10 (0.7 µm, Bio-Rad) tungsten particles in the presence of $CaCl_2$ and spermidine. Approximately $5 \times 10^7$ cells in the exponential growth phase were concentrated onto a 0.22 µm Isopore™ polycarbonate membrane filter (MilliporeSigma) via vacuum filtration and then placed on 1.6% agarose plates containing f/2 medium immediately at room temperature. The cells were bombarded using a rupture disc with pressures ranging from 1350 to 1550 psi. The cells were placed at a flight distance of 7 cm from the bombardment device, within a vacuum environment of 25 mmHg. All bombardment procedures were performed in quadruplicate to ensure reproducibility.

Immediately after bombardment, the cells were resuspended in a non-selective culture medium and allowed to recover for 24 hours. Following this recovery period, ten million cells were transferred into a liquid medium containing 100 µg/ml nourseothricin and incubated under optimal culture conditions. Additionally, $5 \times 10^6$ incubated transformed cells were harvested by centrifugation at 1500rpm. The

supernatant was removed and the cell pellet was then resuspended in 100 µL of fresh medium and spread onto 0.8% selective agar plates added with 100 µg/ml NAT to select for successfully transformed cells. Plates and liquids were incubated under standard culture conditions.

Each bombardment was followed by culturing in five liquid mediums and on five solid mediums, along with one positive and one negative control. The positive control consisted of wild-type *N. putrida* in a non-selective medium, while the negative control used the same wild-type in a selective medium. Liquid cultures were incubated under standard conditions until turbidity was observed, indicating cell growth, while solid cultures were monitored until visible colonies formed. Putatively transformed strains were collected after approximately 14 days of incubation.

**Screening**

Once the cell density of the liquid cultures reached approximately $10^6$ cells/ml, cells were harvested for genomic DNA (gDNA) extraction. A 5 ml aliquot of the culture was collected by centrifugation, and the supernatant was carefully removed. The cell pellet was then resuspended in 20µl of lysis buffer, consisting of 10% Triton X-100, 20 mM Tris–HCl (pH 8), and 10 mM EDTA. To ensure complete cell lysis, the suspension was stored at -80°C for 15 minutes, followed by incubation at 95°C for 10 minutes.

For PCR amplification, 2 µl of the lysed DNA was used as a template in a 50 µl reaction system using REDTaq® ReadyMix PCR Reaction Mix™ (Sigma-Aldrich, US). Target gene eGFP, RHO, and NAT were amplified using the following primers:

| Name | Sequence |
|---|---|
| FR271123 F1 | CGTTTGGCCATTCCTTCATATC |

| | |
|---|---|
| Rhodopsin screen R | GAACCGGAGATTCCCATCATAG |
| eGFP screen F | ATGGTGAGCAAGGGCGAG |
| eGFP screen R | TTACTTGTACAGCTCGTCCAT |
| NAT screen F | CTGGATGGGTCCTTCACCAC |
| NAT screen R | TTGACGTTGGTGACCTCCAG |

Amplification was performed with denaturation at 95 °C for 1 min, followed by 35 cycles of 95 °C 30 seconds, 56 °C 30 seconds and 72 °C 1 min; then 72 °C 5 mins. The amplified products were then verified through electrophoresis on a 1% agarose gel, and subsequently were sequenced by Eurofins Genomics (Germany) to confirm the successful integration of the desired sequences. Succussed transformed cell lines were then kept in a selective normal medium with 100 μg/ml NAT, waiting for further sorting.

**Flow cytometry**

To isolate single cell lines from the resistance mixture for culture, fluorescence activated cell sorting was carried out. Before initiating the sorting process, cell suspension was prepared, ensuring that the cells were appropriately filtered by a 10 μm filter and diluted to a concentration of approximately 100,000 cells/ml. The cell sorting was performed using a BD FACSAria II Cell Sorter Brochure (Becton, Dickinson and Company, US). Calibration of the machine was carried out prior to each experiment using BD FACS Accudrop beads and standard calibration beads as per the manufacturer’s instructions to ensure optimal performance and accuracy.

The prepared cell suspension was loaded onto the FACS machine's sample pedestal. Initial data acquisition was conducted to verify that the cell population of interest was correctly gated.

Cells were sorted based on a specific gating strategy tailored to the experiment. The typical gating hierarchy included initial exclusion of doublets using FSC (Forward Scatter) and SSC (Side Scatter) parameters, followed by selection based on fluorescence marker eGFP or just size. Sorting was performed using a 130 µm nozzle at a flow rate of less than 5 to ensure accuracy, leveraging hydrodynamic focusing. Single cells were sorted in Single Cell Mode into the outer left side stream, which was aligned to deposit cells directly into microtiter plates. A stable stream was maintained throughout the process, with regular checks and adjustments to drop delay and stream alignment to ensure precision.

Sorted cells were deposited into individual wells of a 96-well plate preadded with medium and 300 µg/ml nourseothricin. The alignment of the plate was verified prior to sorting to ensure correct deposition in the centre of each well. Post-sort verification was conducted by inspecting the wells to confirm proper cell deposition and checking by a microplate reader with Optical Density (OD) and eGFP fluorescence. Cells were then transferred to 5mL culture bottles for extended culture and verified by inverted fluorescence microscopy and PCR.

**Analysis of gene expression by reverse transcription (RT-PCR)**

To analyse gene expression, 80 ml of *Nitzschia putrida* cells in the exponential growth phase were harvested by centrifugation. Total RNA was initially extracted using the Direct-zol RNA Kit (Zymo, USA), following the manufacturer's protocol. The RNA was then eluted in 30 µl of RNase-free water.

To remove the gDNA contamination, the 30 µl of extracted RNA was transferred into a PCR tube, added with 15 µl DNase I and 5 µl DNA Digestion Buffer (Zymo, USA). The mixture was incubated at 37°C for 60 minutes to ensure the complete digestion of any contaminating DNA. Subsequently, the RNA Clean & Concentrator Kit (Zymo, USA) was used to purify the RNA, following the RNA clean-up protocols provided

by the manufacturer.

For reverse transcription, 0.2 µg of the purified RNA was used to synthesise cDNA using the SuperScript™ IV First-Strand Synthesis System (Thermo Fisher, USA), in accordance with the manufacturer's instructions. The expression of the eGFP and NAT genes were then analysed using specific primer sets through reverse transcription PCR (RT-PCR) as described above. RT-PCR amplification was prepared using a 50 µl reaction volume with REDTaq® ReadyMix PCR Reaction Mix™ (Sigma-Aldrich), following the preparation guidelines. Amplification was performed as screening PCR. The RT-PCR products were run on 1% agarose gels.

**Microscopy**

Cell fluorescence images were captured using an inverted Zeiss Observer 7 microscope equipped with a 63× oil immersion objective (Carl Zeiss AG, Jena). The microscope was configured for multitrack and line acquisition, enabling the simultaneous capture of both brightfield and eGFP fluorescence images. eGFP fluorescence was specifically detected using a 550 nm bandpass filter.

**Phenotyping experiments**

To access the FR1 influence on diatom *N. putrida*, several growth conditions, including dark and light comparison and low carbon source comparison, were carried out. All assessment growth experiments were conducted with 3 µmol $L^{-1}$ retinal. For light experiments, both wildtype *N. putrida* (*NpWT*) and xanthorhodopsin FR1 knocked-in *N. putrida* strain (*NpRHO*) were first treated with two weeks dark treatment to remove the influence of light, then cultured under 50 µmol photons $m^{-2}$ $s^{-1}$ white light and 24-hours daylight (QSL-2101, Biospherical Instruments Inc., USA) with other culture conditions the same as described above. Dark control groups were covered by an aluminium foil to avoid the influence of light. For low-nutrient experiments, *NpWT* and *NpRHO* were cultured in 20%LB treatment conditions. All

treatment groups at least three replicates at initial concentration of approximately 5,000 cells/ml. To estimate the cell fitness, 500µl culture were harvested every 6 to 8 hours to measure the cell density under a microscope with a 10x objective using bright field. ell-specific growth rates (µ) were calculated according to the following equation:

$$\mu = (\ln(Nt2) - \ln(Nt1))/\ \Delta t$$

Where $N_{t1}$ and $N_{t2}$ are the cell density (cells $mL^{-1}$) at sampling times $t_1$ and $t_2$, and $\Delta t$ represents the time between the two measurements (Guillard, 1973). Student t-test was performed to evaluate the significance of the difference. Data were considered statistically significant for p-values $\leq 0.05$.

**Cell viability measurements**

To quantify the viability of cells, a 4',6-diamidino-2-phenylindole (DAPI) was applied to detect the live and dead cell proportion in rhodopsin knock-in and wild-type strains progressed at the stationary phase. Cells were cultured in a standard medium added with retinal for 14 days. 1ml of each population was harvested after well-mixed and added with 1/10 volume of 100 ug/mL DAPI directly to the cultures. Cells were incubated at room temperature for 15 minutes, following mixing thoroughly by gently pipetting the medium up and down. The staining was observed by inverted Zeiss Observer 7 microscope equipped with a 63× oil immersion objective (Carl Zeiss AG, Jena).

**Diatom slicing and immunogold labelling under transmission electron microscope (TEM)**

For TEM, *N. putrida* cells were treated the same as *T. pseudonana*. Cultures of *N. putrida* (wild-type and FR1 knock-in) were centrifuged at 3000 g for 5 minutes, and cell pellets were washed with phosphate-buffered saline (PBS). After resuspension in

1 ml of fixative, cells were fixed at 4°C for 3 hours, followed by three PBS washes. Concentrated cell suspensions were prepared in 10µl PBS, added to 1.5% agar blocks, and sealed with additional hot agar. After cooling, agar blocks (1.5 mm x 1.5 mm) were fixed overnight at 4°C in fixative solution (50 ml 0.2 M PBS, 10 ml 40% paraformaldehyde, 32 ml water, 8 ml 2.5% glutaraldehyde).

The following day, samples were washed in PBS and dehydrated through graded ethanol series (30%-100%). Dehydrated blocks were impregnated with increasing ratios of ethanol to LR resin and left overnight in pure LR resin. Polymerisation occurred under UV light at -20°C for 72-120 hours. Hardened blocks were sectioned to 90-100 nm thickness using an ultramicrotome and transferred to nickel grids.

For immunogold labelling, sections were incubated with primary antibody (1:20 dilution in BAS) overnight at 4°C. Negative controls received only secondary antibodies. After rinsing, sections were incubated with colloidal gold-conjugated secondary antibody for 3 hours at room temperature in the dark. Samples were rinsed and fixed with 2.5% glutaraldehyde, followed by uranium and lead staining for contrast enhancement.

Prepared samples were analysed using an HT-7800 transmission electron microscope (Hitachi, Japan) to determine FR1 subcellular localisation.

**Result**

**Optimise growth conditions of *N. putrida***

The growth conditions for the initial pre-experiment were established based on the protocol described by Kamikawa et al. (2022) and the guidelines provided by the National Institute for Environmental Studies (NIES). *Nitzschia putrida* was cultured in full-salinity artificial seawater supplemented with 1% LB (Luria-Bertani) medium and Aquil* nutrients. The resulting growth curves are presented in Figure 4.5, which

illustrates the effects of two different initial cell densities—labelled as "Dense" and "Less Dense". Contrary to expectations, the growth of *N. putrida* in this experiment displayed significantly lower growth rates and overall yields compared to the results reported by Kamikawa et al. (2022). This discrepancy suggests that differences in nutrient availability or composition, such as carbon sources, oxygen levels, or trace metals, might have played a critical role in influencing growth outcomes.

To investigate whether the concentration of LB medium was the limiting factor in the previous experiment, the LB concentration was increased to 15%. The resulting growth curves are presented in Figure 4.6. Both the growth rate and maximum cell density were significantly higher compared to the first experiment (Figure 4.7), indicating that the lower LB concentration had likely constrained growth. However, even when the LB concentration was further increased to 30%, the maximum cell density and growth rate remained below expected levels.

Subsequent experiments using an air pump to assess the influence of oxygen did not yield significant changes in growth. Additionally, culturing *Nitzschia putrida* in half-salinity Aquil* medium produced results comparable to those obtained with the full-salinity medium, suggesting that salinity was not a limiting factor. Based on these findings, it is hypothesised that the availability of specific nutrients—such as nitrate, phosphate, silicate, and trace metals—might be the key factors that influence the growth observed in these experiments.

Five different nutrient recipes were used to culture the cells to find out the nutrients that limit *N. putrida* growth. Furthermore, since artificial seawater might lack some microelements, sea salt was used to make the medium. The growth curves are shown in Figure 4.8. Based on the result, the synthetic ocean water recipe from NCMA cannot be used to culture the *N. putrida* strain. Culture in f/2 is growing better than the Aquil* medium. Notably, the cells in f/2 N, Si, and P nutrients with Aquil* trace metal media are growing better than the full Aquil* media but worse than the cells in

full f/2 media.

The cultures in half-salinity sea salt based 50%LB full f/2 media are similar to the published result (Kamikawa et al., 2022). Thus, half-salinity sea salt 50%LB f/2 media is considered the suitable medium for culturing *N. putrida* (Figure 4.9).

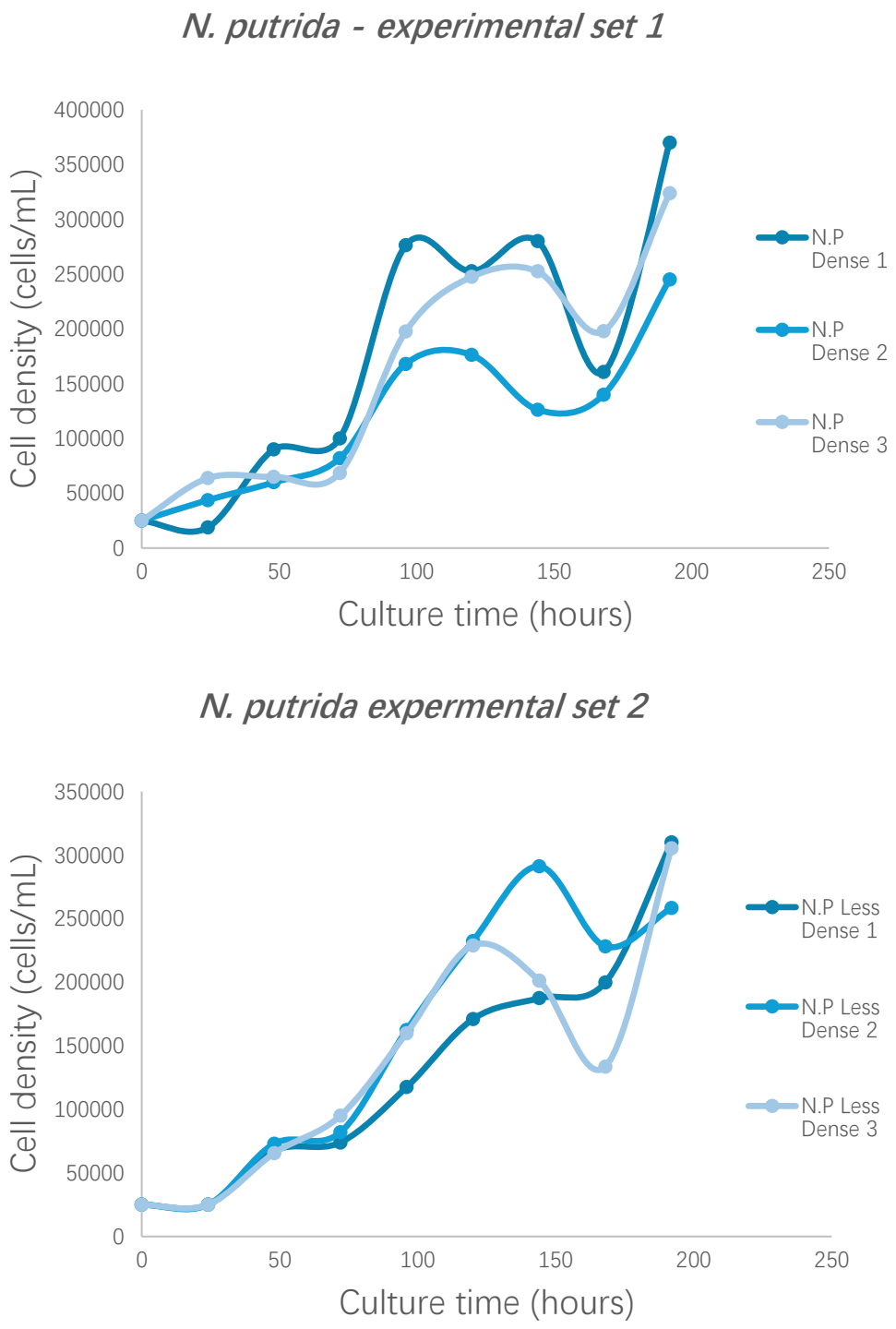


**Figure 4.7 Growth Curves of *Nitzschia putrida* During the Initial Pre-Experiment.** The growth curves represent cell density (cells/mL) over time (hours) for *N. putrida* cultured under two different initial cell concentrations: Dense (25,000 cells/mL) and Less Dense (10,000 cells/mL). Each condition was tested in triplicate. The Y-axis indicates the cell density (cells/mL), and the X-axis represents the culture time (hours).

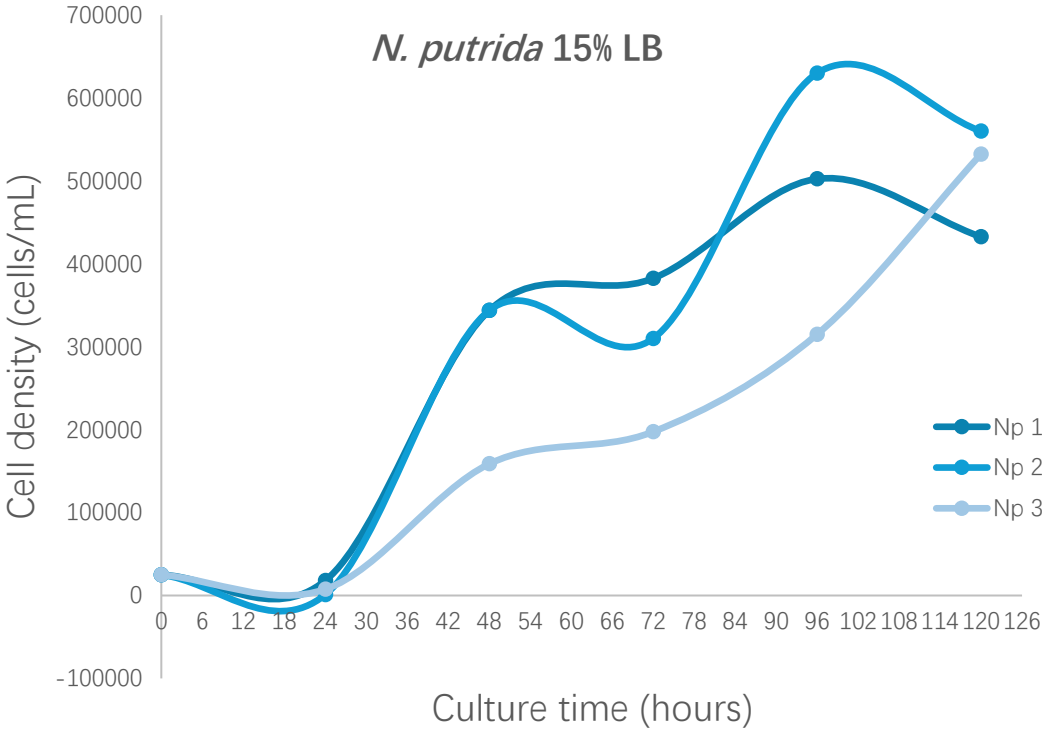


**Figure 4.8 Growth curves of *N. putrida* second in 15% LB medium.** The growth curves depict cell density (cells/mL) over time (hours) for *N. putrida* cultured in a medium containing 15% LB. The Y-axis represents cell density (cells/mL), while the X-axis denotes culture time (hours). The three curves correspond to replicate cultures, illustrating the growth dynamics under the specified condition.

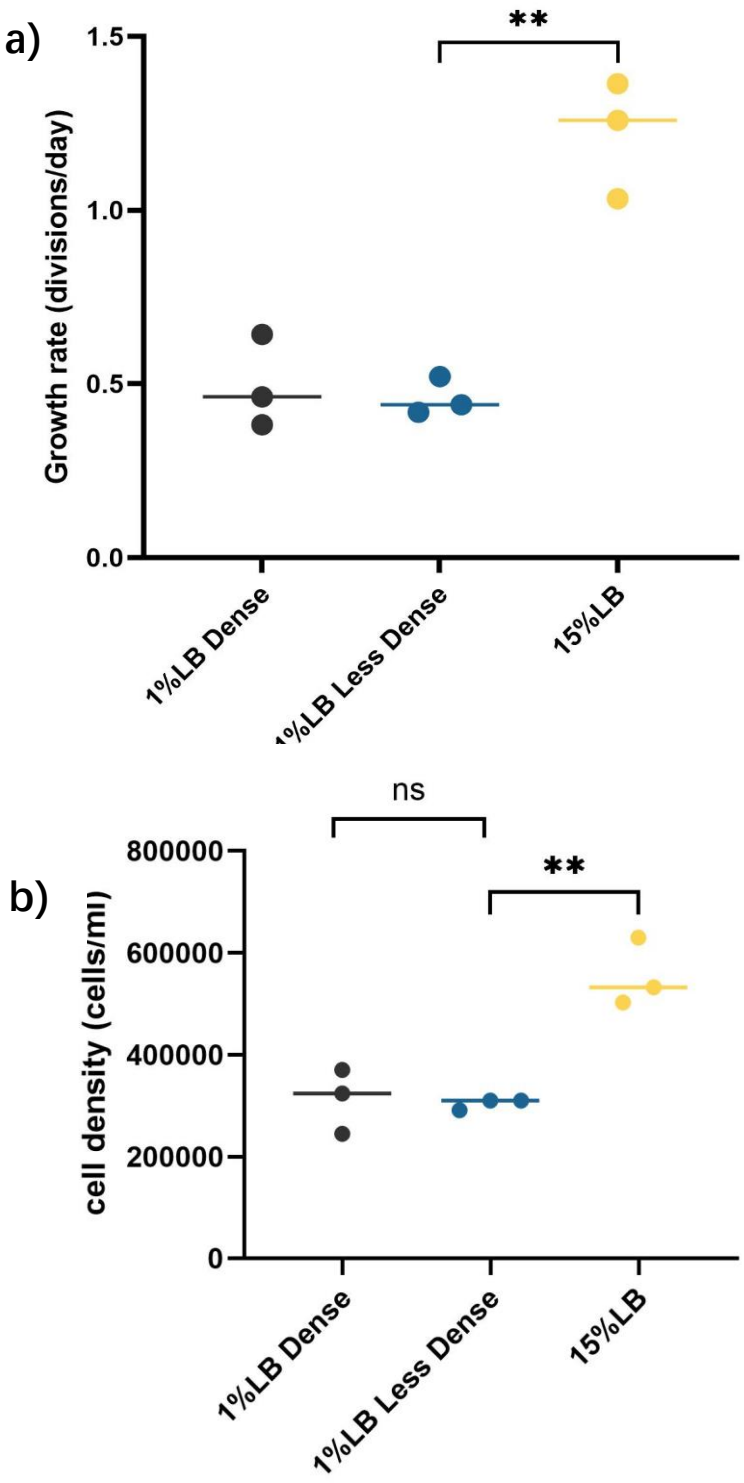


**Figure 4.11 Comparison of Growth Rates (divisions/day) Under Different LB Concentrations.** The graph compares the a) growth rates (divisions/day) and b) the maximum cell density (cells/ml) of *Nitzschia putrida* cultured in different concentrations of LB medium: 1% LB Dense, 1% LB Less Dense, and 15% LB. No significant difference was observed between the 1% LB Dense and 1% LB Less Dense groups. However, a significant increase in growth rate was noted in the 15% LB group, as indicated by the asterisks (**).

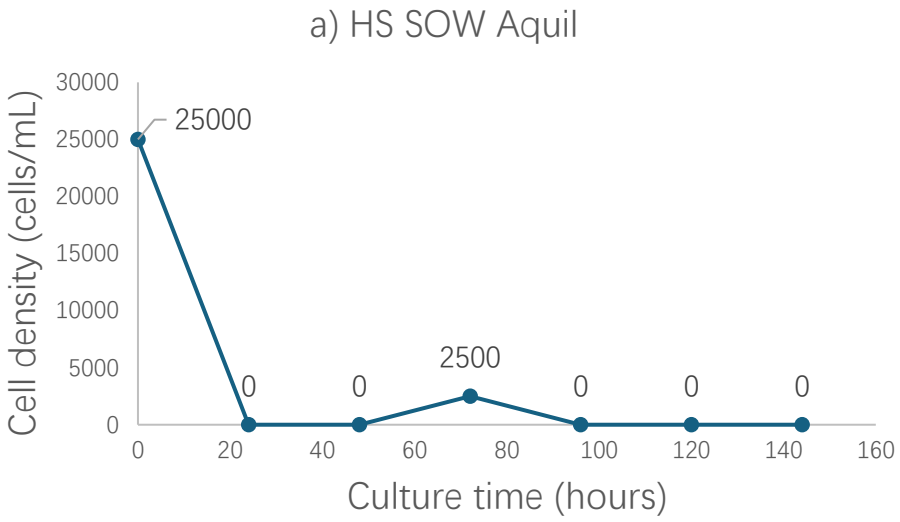
a) HS SOW Aquil
Cell density (cells/mL)
30000
25000
20000
15000
10000
5000
0
25000
0
0
2500
0
0
0
0
20
40
60
80
100
120
140
160
Culture time (hours)

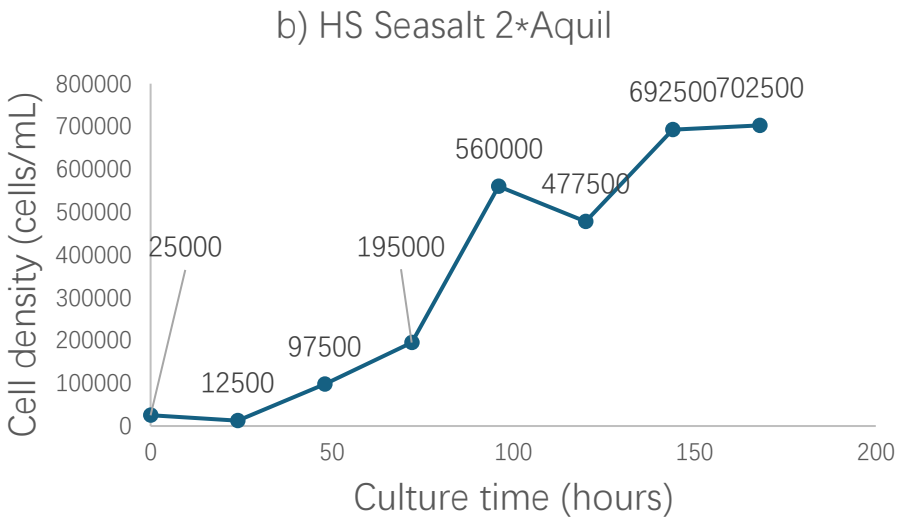
b) HS Seasalt 2*Aquil
Cell density (cells/mL)
800000
700000
600000
500000
400000
300000
200000
100000
0
25000
12500
97500
195000
560000
477500
692500
702500
0
50
100
150
200
Culture time (hours)

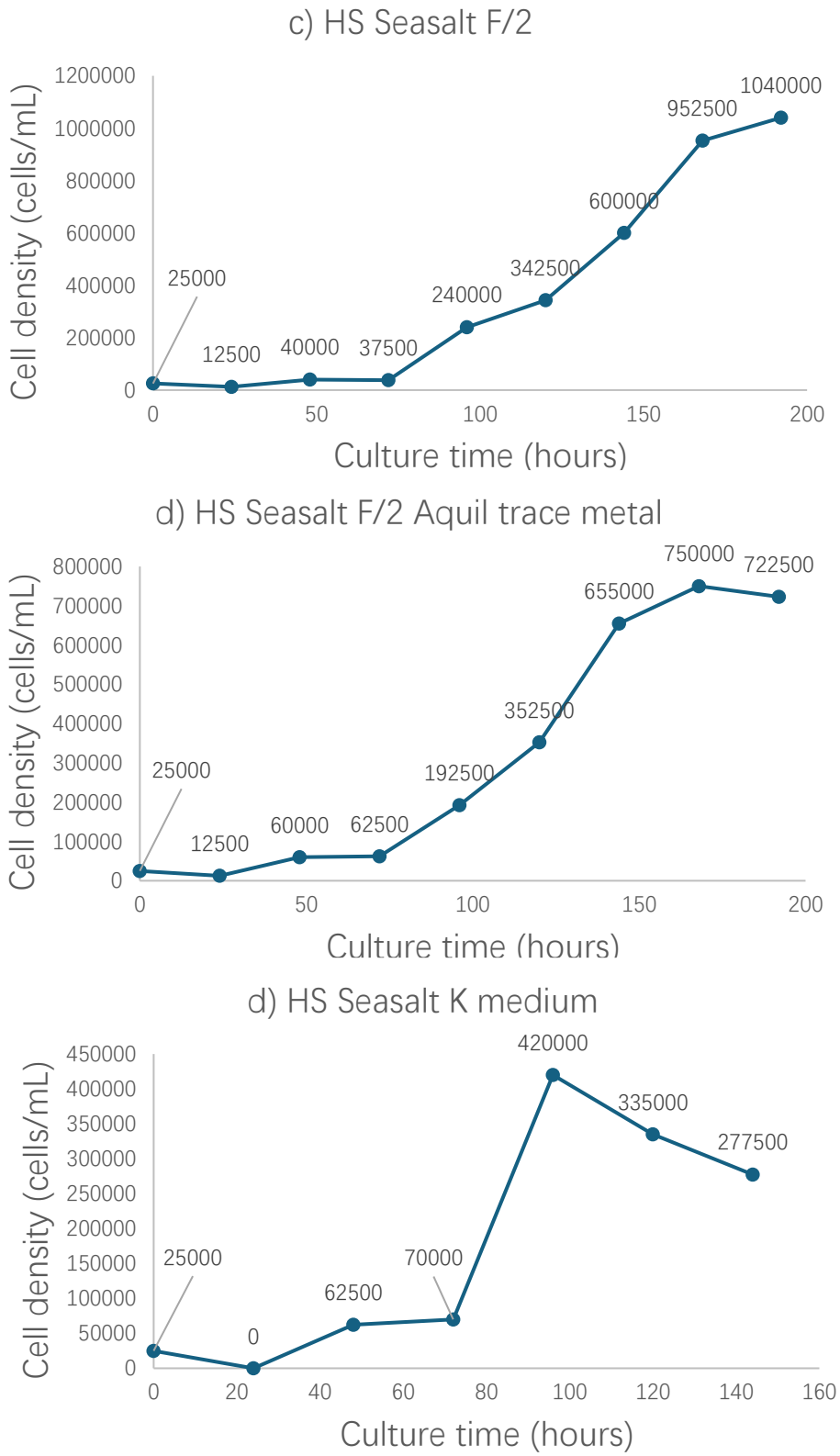


**Figure 4.13 Growth Curves of *Nitzschia putrida* in Different Media**. Growth curves of *Nitzschia putrida* cultured under various media condition containing 50% LBs: (a) Half-salinity Synthetic Ocean Water (SOW) with Aquil* medium, (b) Half-salinity Sea Salt with double Aquil* medium, (c) Half-Salinity Sea Salt with full f/2 medium, (d) Half-Salinity Sea Salt with f/2 N, Si, and P stocks and Aquil* trace metals, and (e) Half-Salinity Sea Salt with K medium. The Y-axis represents cell density (cells/mL), and the X-axis denotes culture time (hours). Cell density of each measurement point were shown.

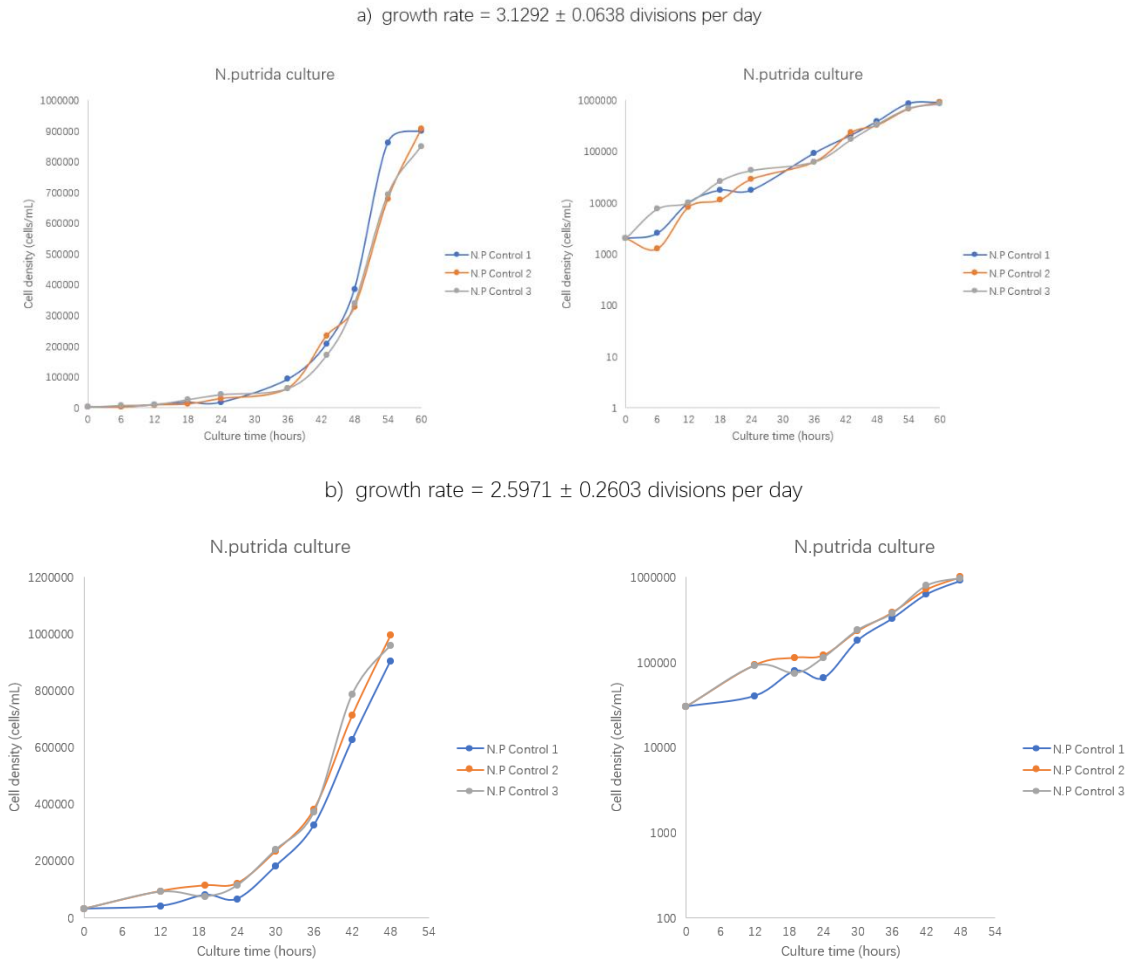


**Figure 4.14 Growth Curves of *Nitzschia putrida* in 50% LB Half-Salinity Sea Salt f/2 Medium with Different Initial Concentrations.** Growth curves of *Nitzschia putrida* cultured in 50% LB half-salinity sea salt f/2 medium with different initial cell concentrations: (a) 30,000 cells/mL and (b) 2,000 cells/mL (n=3). The Y-axis represents cell density (cells/mL), and the X-axis denotes culture time (hours). The Y-axis on the left graphs is shown in a standard linear scale, while the right graphs are displayed on a logarithmic scale to better visualise growth dynamics across a wide range of cell densities.

**Testing antibiotic resistance on plates and liquid medium**

After approximately 10 days of cultivation, most treatment groups—whether on plates or in liquid medium—showed no signs of growth. The medium remained clear, with no colonies or flocculants observed (Table 4.3). In contrast, positive growth controls without any antibiotics displayed a lawn of cells on plates and cell clumping in the liquid medium after just five days (Figure 4.10). These results demonstrate that *N. putrida* is highly sensitive to zeocin, with no growth observed even at low concentrations (Figure 4.11).

In contrast, 100 µg/ml nourseothricin on 100% salinity plates successfully inhibited the growth of wild-type *N. putrida* cells at both low and high cell concentrations while permitting the growth of NAT transformants (Figure 4.10a). This suggests that nourseothricin is a suitable antibiotic for selection in this species. Consequently, the nourseothricin resistance gene was selected as the selective marker for establishing the *N. putrida* transformation system.

| Cells | antibiotics (µg/ml) | | |
|---|---|---|---|
| | 50 | 100 | 150 |
| Nat $10^5$ (liquid) | + | - | - |
| Nat $10^6$ (liquid) | + | - | - |
| Nat 5 x $10^7$ (solid) | + | - | - |
| Zeocin $10^5$ (liquid) | - | - | - |
| Zeocin $10^6$ (liquid) | - | - | - |
| Zeocin 5 x $10^7$ (solid) | - | - | - |

**Table 4.5 Antibiotic sensitivity of *Nitzschia putrida*.** The signs "+" denoting the observation of living cells in flasks after 10 days of selection, and "-" indicating their absence.

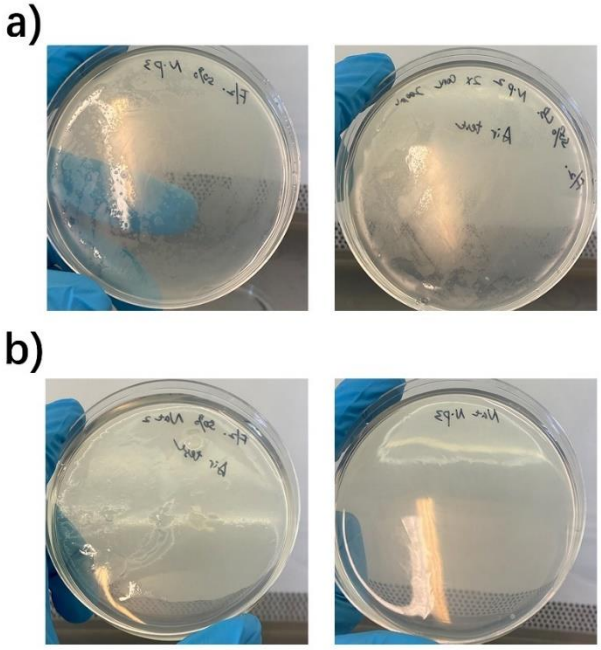


**Figure 4.15 Growth of *Nitzschia putrida* Cells on Selective Plates.** (a) Transformed *N. putrida* cells growing on selective plates. A visible lawn of cells was observed on the surface of the plates. (b) Wild-type *N. putrida* cells on antibiotic-selective plates. No cell growth was observed on the surface of the plates.

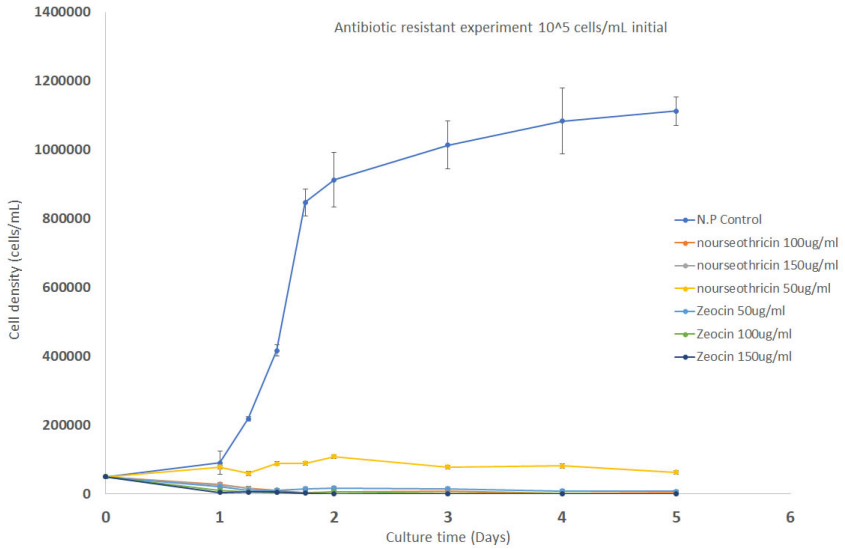


**Figure 4.16 Antibiotic resistance experiments for *Nitzschia putrida* under nourseothricin and zeocin treatment.** The graph demonstrates the growth curves of *N. putrida* under varying concentrations of nourseothricin and zeocin. The Y-axis represents cell density (cells/ml), and the X-axis represents culture time (days). The treatments include control (no antibiotic), nourseothricin at 50µg/ml, 100µg/ml, and 150µg/ml, and zeocin at 50µg/ml, 100µg/ml, and 150µg/ml. The results show significant growth inhibition by zeocin across all concentrations, while 100µg/ml and 150µg/ml nourseothricin could also inhibit the growth of *N. putrida* cells. Error bars show standard deviation.

**Plasmid design and construction**

To ensure the efficient expression of the introduced exogenous genes eGFP, RHO, and NAT in *Nitzschia putrida* cells, I analysed the transcriptome of *N. putrida* and identified several endogenous genes that exhibit high expression across diverse growth conditions. These genes' promoter sequences are likely to be useful for constitutive transgene expression at sufficient levels. Among these highly expressed genes, the gene encoding nicotinamide adenine dinucleotide hydride (NADH)-ubiquinone reductase complex 1, a key component of the mitochondrial respiratory chain, exhibited the highest expression(Almutairi, 2022; Cardol, 2011), indicating that it likely possesses a strong promoter.

In addition to the previously mentioned analyses, a codon bias analysis was conducted to ensure the efficient expression of the foreign genes *eGFP* and xanthorhodopsin *FR1* in *Nitzschia putrida*. Codon usage patterns in the ten highest expressed genes in *N. putrida* were examined and compared to those of the *eGFP* and *FR1* genes. The results, presented in Figure 4.12, reveal that *N. putrida* exhibits a slightly different codon bias compared to the codon usage in *eGFP* and *FR1*.

Despite these differences, most of the codons used by *eGFP* and *FR1* are reasonably well represented in the transcriptomes of other diatoms, such as *Fragilariopsis cylindrus* and *Thalassiosira pseudonana* (Hopes, 2017; Poulsen et al., 2006). This suggests that while there may be some variation in codon preference, the codons employed by eGFP and FR1 are generally compatible with the translational machinery of *N. putrida*.

Although optimising the codon usage to better match *N. putrida*'s codon bias could theoretically enhance the expression efficiency of these genes, the current expression levels are considered sufficiently high to support their intended functions. This conclusion is based on the successful detection of eGFP fluorescence and the

demonstrated impact of FR1 on growth and viability in the engineered strains.

Golden Gate cloning assembly was used to construct all plasmids required for establishing the *N. putrida* transformation system. The reason for choosing Golden Gate cloning is twofold. First, it allows the introduction of multiple gene fragments in a single reaction. By adding unique 4-base overhangs, fragments with matching overhangs can be accurately spliced together while eliminating excess sequences, achieving seamless ligation. Second, the modularity and versatility of the Golden Gate cloning system, with components such as L0 and L1, allow for easy modification and the assembly of new plasmids by simply altering specific fragments.

As shown in Figure 4.2, the initial L1 constructs aimed to combine the promoter, terminator, and gene of interest with the vector backbone. Specifically, the NADH promoter, NAT resistance gene, and NADH terminator were assembled as pICH47732-NAT; the NADH promoter, eGFP gene, and NADH terminator as pICH47742-eGFP; and the NADH promoter, xanthorhodopsin FR1, and NADH terminator as pICH47742-RHO. The vector backbones pICH47732 and pICH47742, used in these constructs, contain the LacZ gene for blue-white screening. Colonies derived from unmodified, uncut templates should appear blue, whereas assembled colonies should be white. The unique palindromic sequences designed into the system minimise the likelihood of vector self-ligation or mismatch. For the three assembled plasmids, pICH47732-NAT, pICH47742-RHO, and pICH47742-eGFP, a total of 36 samples were checked (Figure 4.13), and 35 were correctly assembled according to PCR and sequencing results.

Subsequently, the L2 backbone pAGM4723, which contains a red colour selectable marker (Cred), was used to assemble the completed L1 plasmids. The modular end linker L2E pICH41744 was used to connect the L1 gene fragments with the L2 backbone, resulting in the assembly of pNpNADH:NAT:eGFP and pNpNADH:NAT:RHO. Colonies from unmodified, uncut templates containing the

Cred gene appeared orange-red, while assembled colonies appeared white. Unlike L1 assembly, L2 assembly was prone to some mismatches. Among the assembled plasmids, 28 pNpNADH:NAT:eGFP and seven pNpNADH:NAT:RHO were analysed. The results showed that at least six plasmids were incorrectly assembled, while the sequencing results of the other plasmids matched the expected sequences (Figure 4.14).

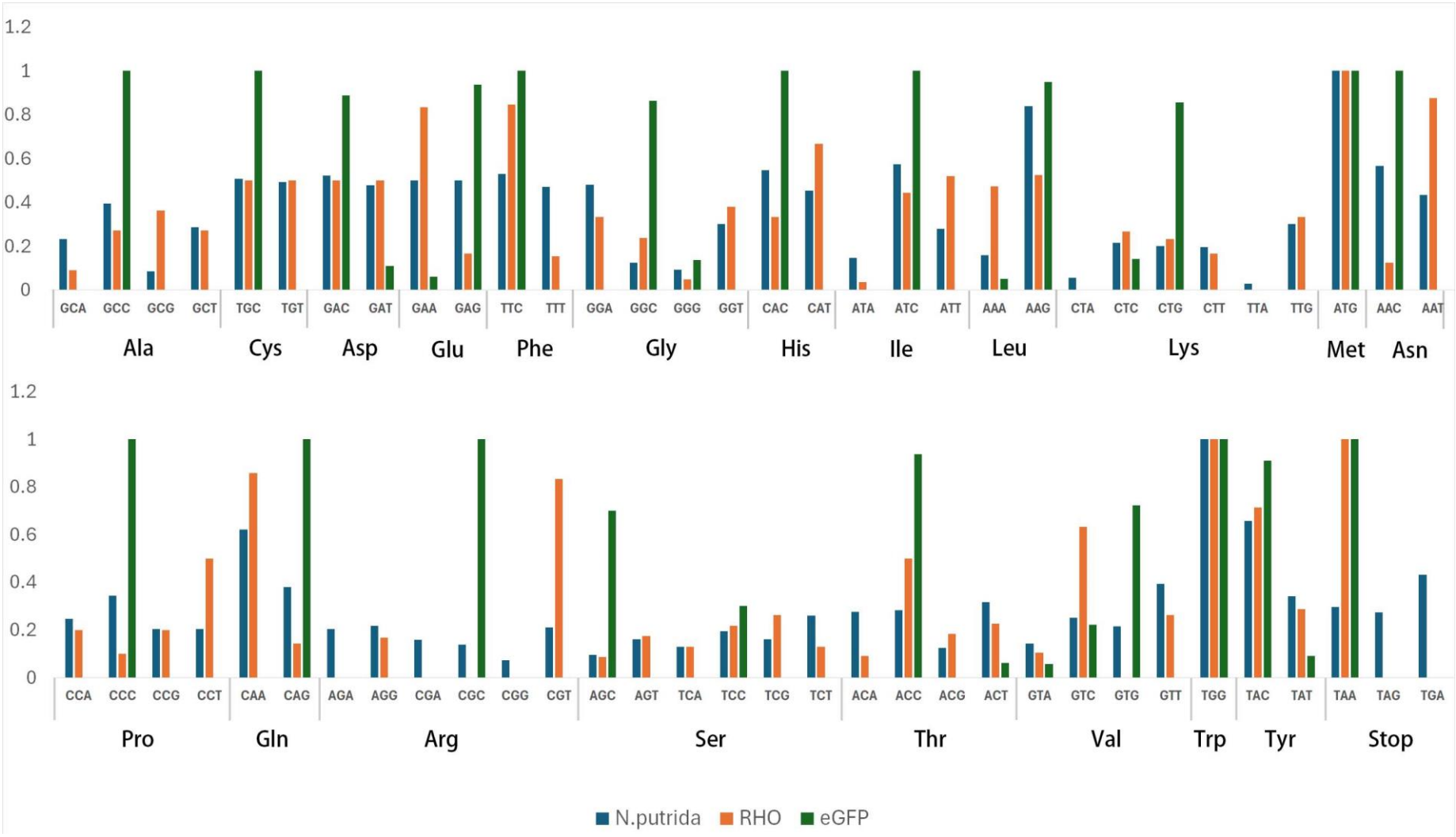


**Figure 4.17 Comparison of codon usage.** This figure compares the codon usage as a fraction of triplets used per amino acid for three different genes: 10 highest expressed gene in *N. putrida* (green), xanthorhodopsin gene (RHO, blue), and enhanced green fluorescent protein gene (eGFP, orange).

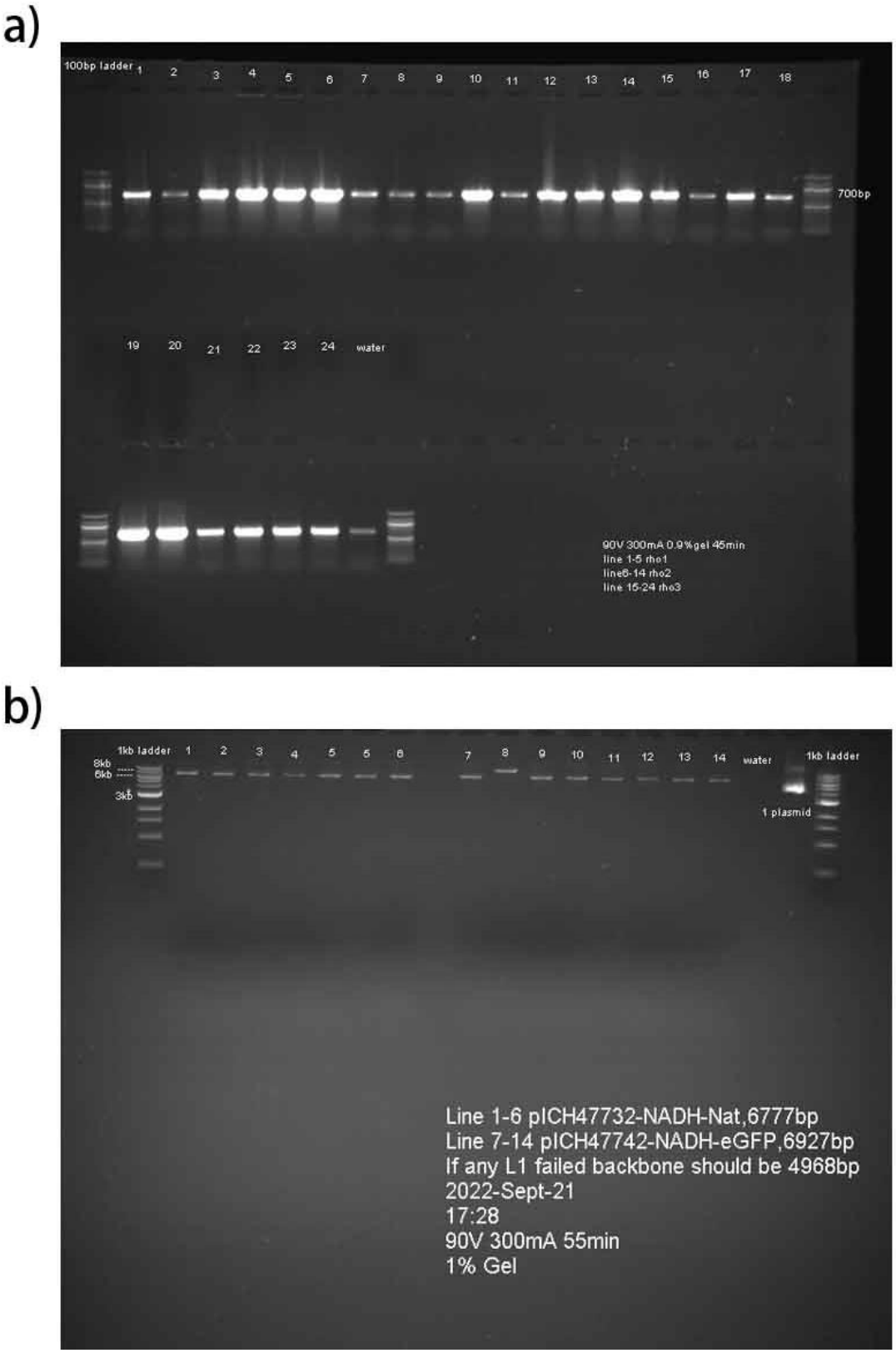


**Figure 4.18 Restriction enzyme digestion analysis of L1 constructs.** (a) Restriction digestion check of pICH47742-RHO, with all products showing the correct length. (b) Lines 1-6 represent pICH47732-NAT, and Lines 7-14 represent pICH47742-eGFP. Notably, Line 8 shows a product of incorrect size, indicating a mispairing, while all other products are of the correct length.

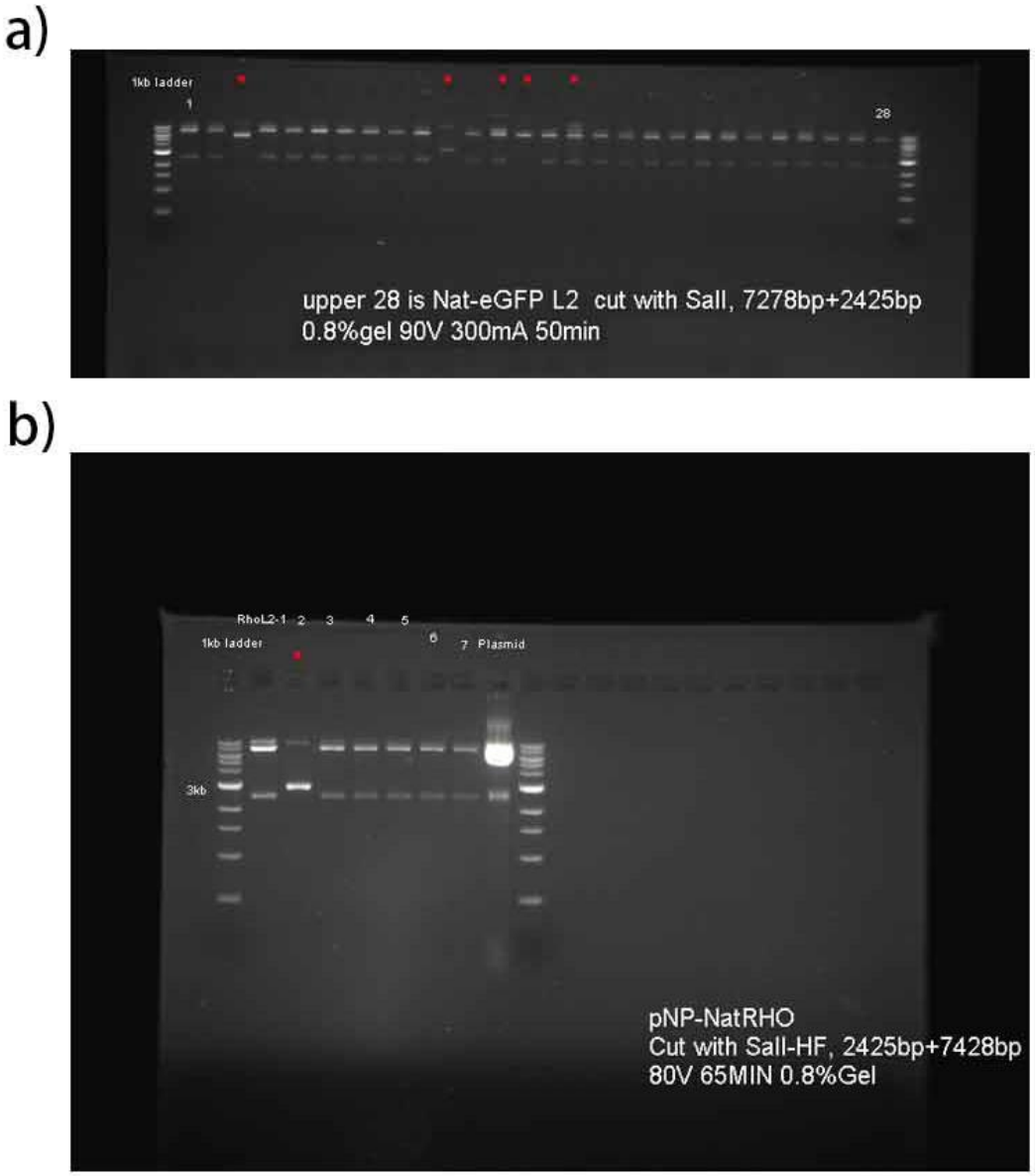


**Figure 4.19 Restriction enzyme digestion analysis of L2 constructs.** (a) Restriction digestion analysis of pNpNADH:NAT:eGFP using *Sal*I-HF. Lane 1 to lane 28 shows 28 individual plasmids cut by restriction enzyme, target length 7278bp and 2425bp. Incorrectly sized products are indicated by red markers. (b) Restriction digestion analysis of pNpNADH:NAT:RHO using *Sal*I-HF. Lane 1 to 7 shows individual plasmids cut by restriction enzyme, target length 2425bp and 7428bp. Incorrectly sized products are indicated by red markers.

**Microparticle bombardment and screening**

After approximately 14 days, the cells were observed under selective growth conditions. These nourseothricin-resistant cells were collected from independent flasks by centrifugation, and the presence of the resistant gene Nat, the reporter gene encoding eGFP, and the rhodopsin gene were confirmed by PCR (Figure 4.15). For the eGFP-overexpressing strain, six *N. putrida* strains exhibiting the nourseothricin resistance phenotype were successfully recovered from six culture flasks. In contrast, four of nine flasks yielded resistant strains under nourseothricin selection for the RHO-overexpressing strain.

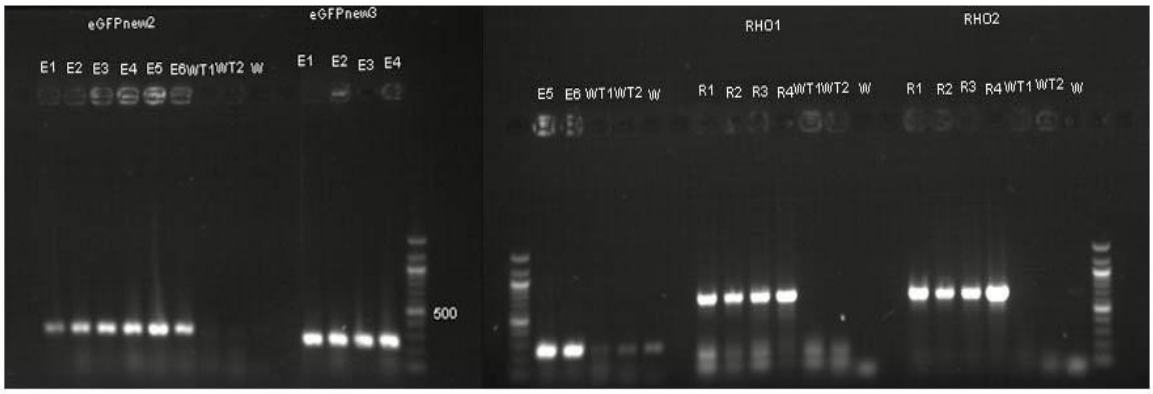


**Figure 4.20 Gel electrophoresis result of transformed *N. putrida* screening PCR result.** The gel electrophoresis results display the PCR screening of transformed *N. putrida* strains. The marker used is a 100 bp ladder. Six NAT-positive strains were analysed following biolistic transformation with a plasmid overexpressing eGFP. Two different sets of primers were tested, targeting products of 263 bp and 255 bp. For the rhodopsin knock-in strains, four NAT-positive strains were tested using the same two primer sets, with the expected product size of 703 bp.

Although the transformation system for *N. putrida* shares many similarities with the microparticle bombardment method used for other diatoms (Hopes et al., 2016; Poulsen et al., 2006; Sabatino et al., 2015), post-bombardment cultivation and selection needed to be adjusted to accommodate this benthic heterotrophic diatom. For instance, I attempted to select resistant strains using agarose plates by spreading 5×106 cells onto selective plates 24 hours after bombardment. Although a lawn of colonies formed (Figure 4.10a), individual colony isolation was not successful. As a

result, liquid medium was chosen for the post-bombardment selection and cultivation of the genetically modified cell lines instead of using solid plates.

However, directly using a liquid medium for selection presented challenges. It prevented the calculation of transformation efficiency. Also, it precluded the isolation of single cell lines, as all recovered flasks contained mixed populations of multiple cell lines. To address this, fluorescence-activated cell sorting (FACS) was employed to isolate single-cell lines. For the eGFP strains, cells expressing fluorescence were isolated and cultured individually in 96-well plates (Figure 4.16). For the RHO knock-in strains, even though no fluorescent signal was present, single cells were still isolated from the population and subjected to further selection for the resistance gene.

To avoid potential fungal or bacterial contamination, a threefold concentration of nourseothricin (30 μg/mL) was used to inhibit contaminants and to perform a secondary selection. The selected single-cell lines were further screened by measuring fluorescence intensity (for eGFP) and optical density (OD), ensuring that only the desired genetically modified strains were propagated. As a result, four eGFP single-cell clones and four rhodopsin single-cell clones were successfully obtained.

To confirm the expression of the integrated genes, RNA was extracted from the RHO and eGFP knock-in strains, and reverse transcription was performed as previously described. The harvested cDNA products were then analysed using reverse transcription PCR (RT-PCR). The RT-PCR results for the RHO and eGFP knock-in strains showed distinct bands at the expected sizes, in contrast to the negative controls and the wild-type (WT) control groups, which showed no bands, as illustrated in Figure 4.17. These results confirm the successful transcription of the RHO and eGFP genes in the respective knock-in strains, validating the transformation and selection processes utilised in this study. Moreover, this outcome demonstrates the effectiveness of the gene editing technique utilised, providing a robust foundation for further

studies and analysis.

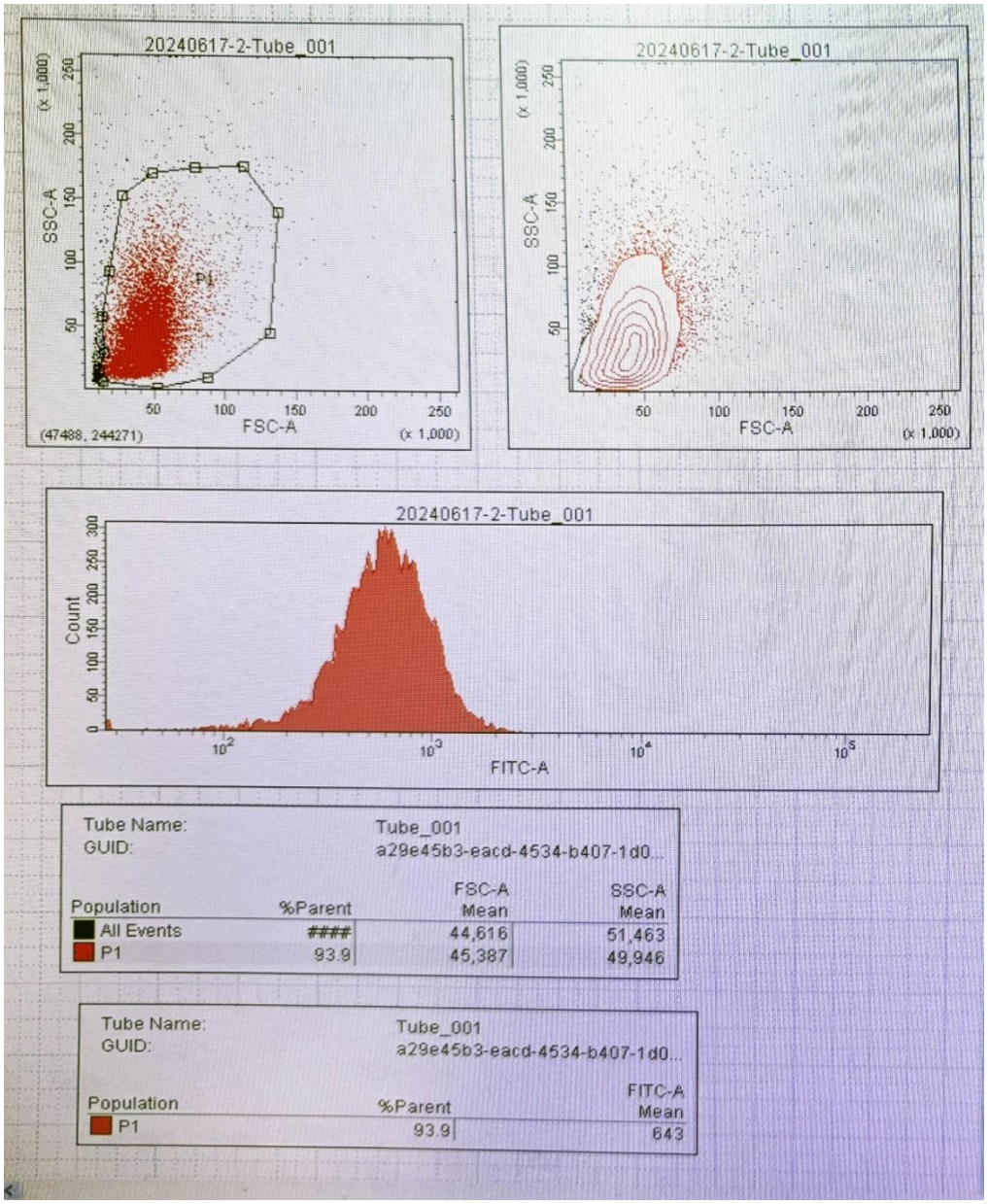


**Figure 4.21 Flow cytometry FACS analysis of *N. putrida* overexpressed strains mixture.** Mixture running by eGFP overexpressed strain. Flow cytometry (FACS) analysis of a mixture of cells from an *N. putrida* strain overexpressing *eGFP*. The plots display the gating strategy used to identify the *eGFP*-positive population. The histogram shows the fluorescence intensity distribution, with 93.9% of the analysed population falling within the gated region (P1), indicating successful expression of *eGFP*. The cells in the selected area P1 were then isolated by single cells. RHO knock-in strains were sorted similarly.

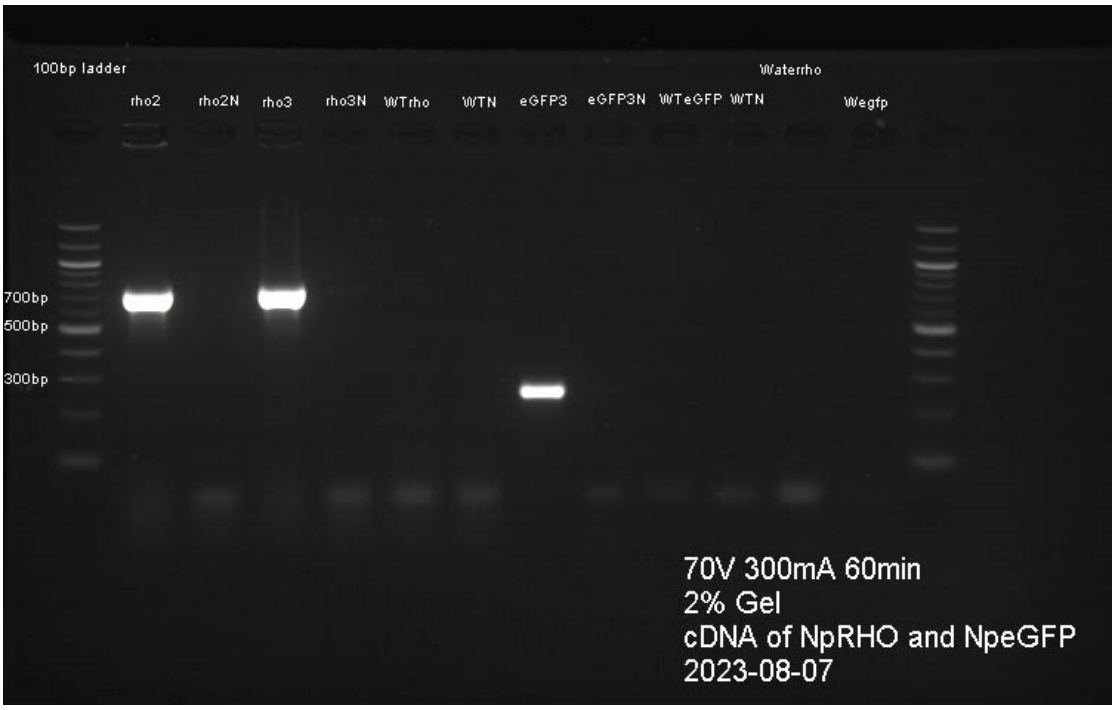


**Figure 4.22 Gel electrophoresis result of RHO and eGFP knock-in *N. putrida* RT-PCR results.** The gel electrophoresis results display the RT-PCR analysis of RHO and eGFP knock-in *N. putrida* strains. The marker used is a 100 bp ladder. Lanes "rho2" and "rho3" represent RT-PCR products from two rhodopsin knock-in strains, while "rho2N" and "rho3N" are the negative controls for cDNA synthesis. Lanes "WTrho" and "WTN" correspond to RT-PCR products from wild-type *N. putrida* using rhodopsin primers and their cDNA synthesis negative control, respectively. Target products length is 703bp. Lane "eGFP3" represents the RT-PCR product from the eGFP knock-in strain, with "eGFP3N" as the negative control for cDNA synthesis. "WTeGFP" corresponds to the RT-PCR product from the wild-type strain amplified using eGFP primers, and "WTN" serves as the negative control for wild-type cDNA synthesis. The "Waterrho" and "Wegfp" lanes are PCR negative controls, where water was used in place of cDNA. Target products length is 263bp.

**Fluorescence microscopy detecting eGFP**

Fluorescence microscopy was employed to detect the expression of eGFP in an overexpressing strain of *N. putrida* using a Zeiss Observer 7 microscope. As shown in Figure 4.18, in the eGFP fluorescence channel, a strong signal was observed, indicating robust expression of the eGFP protein within the cells. This fluorescence signal is distinctly absent in the wild-type (WT) cells, which serve as a negative control, confirming the specificity of the observed fluorescence to the eGFP gene

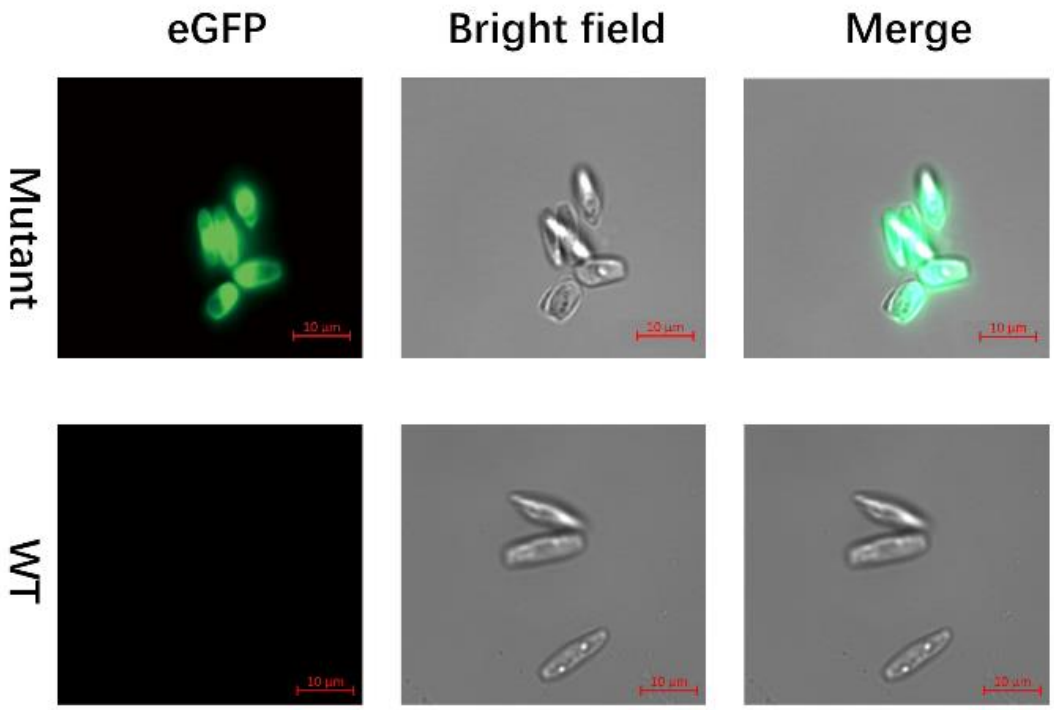


**Figure 4.23 Fluorescence microscopy analysis of eGFP expression in *Nitzschia putrida*.** This figure presents fluorescence microscopy images comparing *Nitzschia putrida* cells overexpressing eGFP (top row) to wild-type (WT) cells (bottom row). The images were captured using a Zeiss Observer 7 microscope. The left column shows the eGFP fluorescence channel, the middle column displays the corresponding bright field images, and the right column provides merged images of the fluorescence and bright field channels.

introduced through transformation.

Most cells in the eGFP transformant cultures exhibited clear and consistent expression of eGFP, as evidenced by the bright fluorescence observed across multiple fields of view. The overlay of the fluorescence and bright field images confirms that the fluorescence is localised within the cells, with no detectable signal in the surrounding medium, ruling out the possibility of extracellular artefacts.

These observations strongly support the successful integration and expression of the eGFP transgene in *N. putrida*. The consistent fluorescence across the population suggests that the transformation method is both effective and reliable, yielding a high proportion of cells expressing the target gene. This result lays a solid foundation for subsequent experiments, where eGFP can be used as a reporter to monitor gene expression, study protein localisation, and analyse cellular processes in real-time within this diatom model.

**Assessing the influence of microbial rhodopsin on *N. putrida***

To evaluate whether the genetic modification process had any impact on the growth characteristics of *Nitzschia putrida*, the growth of the *eGFP*-overexpressing strain with the wild-type (WT) strain under normal cultivation conditions was compared firstly. The experiment was conducted with 20% nutrient concentration under standard culture conditions, and the results are presented in Figure 4.18.

The growth curves (Figure 4.19a) reveal that both the *eGFP* strain and the WT strain followed similar growth trajectories. No significant differences were observed in the maximum cell densities reached by the two strains, indicating that the introduction of the *eGFP* gene did not adversely affect the overall growth capacity of *N. putrida*. Error bars representing the standard deviation across replicates suggest that the results are consistent and reproducible.

Further analysis of the growth rates (Figure 4.19b) showed that the *eGFP* strain and the WT strain had nearly identical growth rates, expressed in divisions per day. Statistical analysis indicated no significant difference between the two groups ($p > 0.05$), confirming that the genetic modification to introduce *eGFP* does not impair the growth performance of *N. putrida*.

These findings demonstrate that the genetic transformation system used to introduce foreign genes into *N. putrida* does not compromise the fitness of the modified strain under the tested conditions.

Subsequently, to assess the influence of microbial rhodopsin on the heterotrophic diatom *N. putrida*, the growth of rhodopsin knock-in strains with WT under reduced nutrient conditions with 20% LB was analysed. The results demonstrated that the rhodopsin knock-in strains exhibited significantly improved growth rates and maximum cell densities compared to the WT strain. This suggests that xanthorhodopsin may confer an advantage by enabling *N. putrida* to utilise light, enhancing its growth and fitness under nutrient-limited conditions (Figure 4.20). However, this significant fitness advantage could potentially be attributed to the cumulative effects of light utilisation over time. To minimise this influence and assess the direct impact of xanthorhodopsin, a two-week pre-dark treatment was applied to the rhodopsin knock-in strains before the growth experiments. Then the growth of wild-type strain, dark-pretreated rhodopsin grown in darkness, and dark-pretreated rhodopsin knock-in strains under full-nutrient conditions. As shown in Figure 4.21, the rhodopsin knock-in strain cultured in darkness after several weeks of dark pretreatment did not show significant differences in growth compared to the WT. However, the rhodopsin knock-in strain that was subjected to dark pretreatment but then cultured under light conditions exhibited a significantly higher growth rate and yield.

These results highlight the impact of microbial rhodopsin on enhancing growth under

illuminated conditions compared to the WT and the diminished growth of the RHO strain in the absence of light. This illustrates the potential photosynthetic advantages conferred by xanthorhodopsin expression, suggesting that microbial rhodopsin may play a key role in optimising energy capture and metabolic efficiency in *N. putrida* when exposed to light.

In addition to the growth experiments, cell viability was assessed after long-term cultivation (14 days). Cells were stained with DAPI, a fluorescent stain that binds strongly to DNA, allowing for the visualisation and quantification of viable cells under a microscope. The comparison focused on cells cultured under light conditions. The results showed that after 14 days of cultivation, most wild-type cells had died, with only 4.62% of the cells remaining viable. In contrast, 54.76% of the FR1 knock-in cells remained viable ($p < 0.0001$) (Figure 4.22). These findings imply that microbial rhodopsin could play an important role in extending the lifespan of *N. putrida* cells under certain environmental conditions, particularly when light is available. The enhanced viability of the FR1 knock-in strain not only supports the idea that microbial rhodopsin contributes to more efficient energy utilisation but also indicates that it could provide a selective advantage in environments where prolonged survival is critical. This could be particularly beneficial in natural habitats where resources fluctuate, and the ability to maintain viability for longer periods could determine competitive success and overall fitness.

In conclusion, the successful genetic modification of *N. putrida* to overexpress microbial rhodopsin has provided valuable insights into the potential benefits of this protein in heterotrophic diatoms. By improving both growth efficiency and cell viability, microbial rhodopsin expression may represent a promising avenue for further research into energy utilisation strategies and could have broader applications in biotechnological processes.

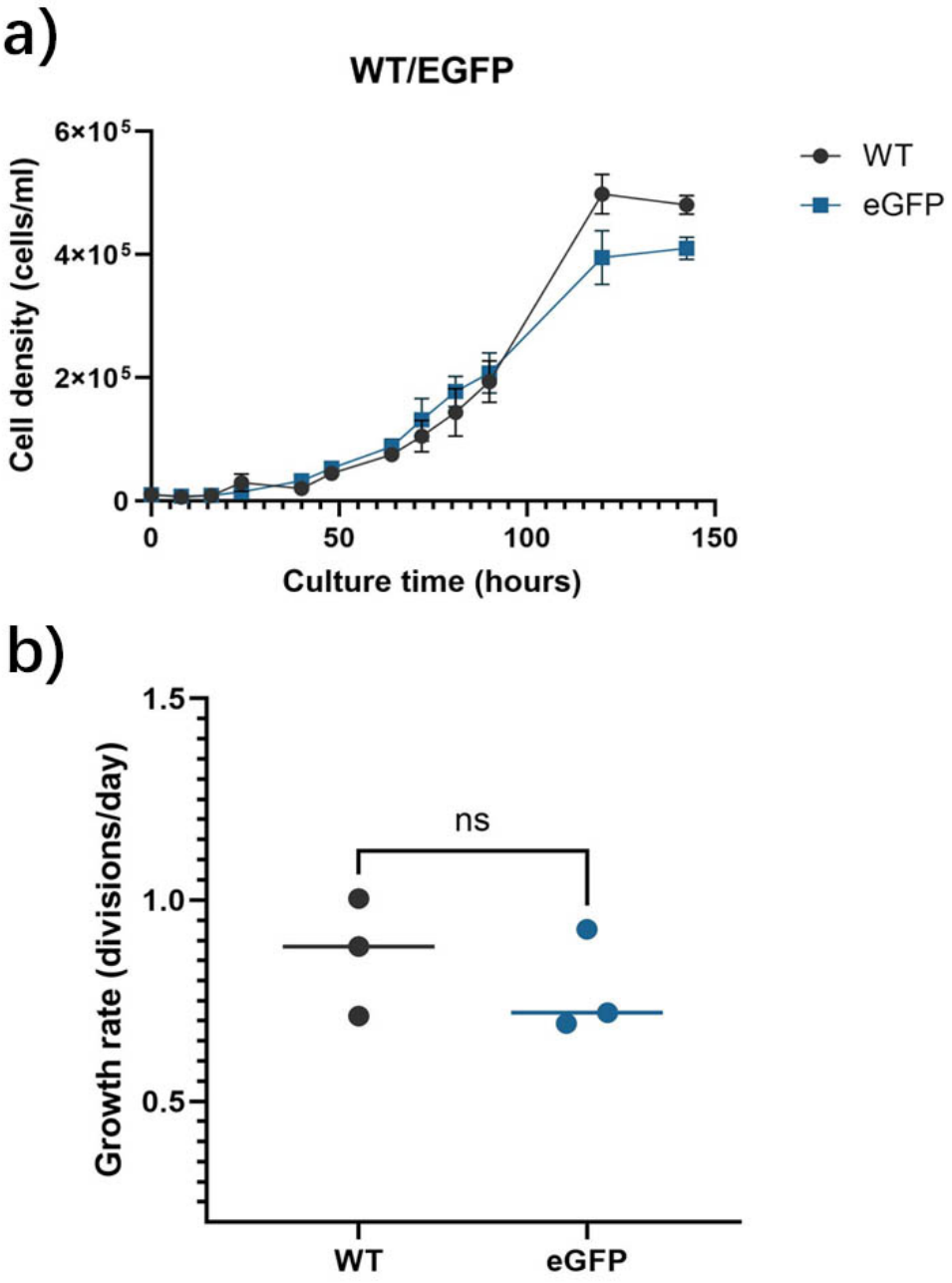


**Figure 4.24 Growth curve of wild-type and eGFP knock-in strains under decreased nutrient medium.** a) This figure demonstrates the cell density (cells/ml) over time (hours) for both the wild-type (WT) and the enhanced green fluorescent protein (eGFP) knock-in strains under conditions of reduced nutrients. The black circles represent the WT strain, and the blue squares denote the eGFP strain. b) This plot compares the growth rates (divisions/day) of the WT and eGFP strains, each represented by individual data points for replicate measurements. The horizontal lines show the average growth rates for each group. The "ns" indicates no significant differences in growth rates between the WT and eGFP strains under these conditions.

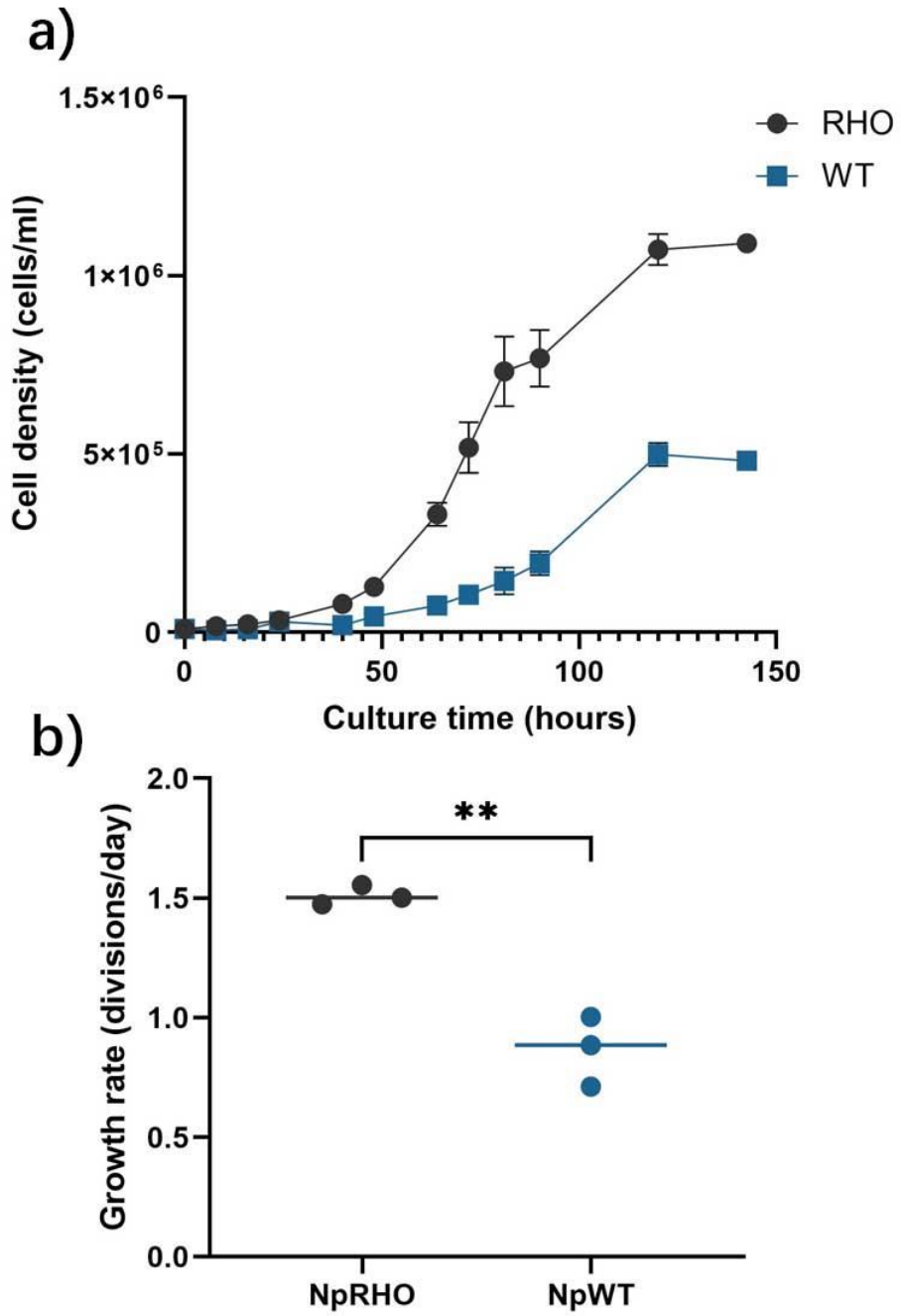


**Figure 4.25 Growth Dynamics of rhodopsin overexpressed and wild-type strains under nutrient-limited conditions.** a) This graph shows the cell density (cells/ml) over time (hours) for both the rhodopsin-overexpressed (RHO) and wild-type (WT) strains under nutrient-limited conditions. The RHO strain, represented by black circles, exhibits a significantly higher growth trajectory compared to the WT strain, shown with blue squares. The data points illustrate a consistent advantage in cell density for the RHO strain throughout the culture period. b) This plot presents the growth rate (divisions/day) for both strains. The RHO strain (*NpRHO*) demonstrates a higher growth rate, significantly outperforming the WT strain (*NpWT*) as indicated by "**" for $p < 0.01$. The individual data points for each replicate are shown, with the line representing the average growth rate for each strain. Error bars show standard deviation.

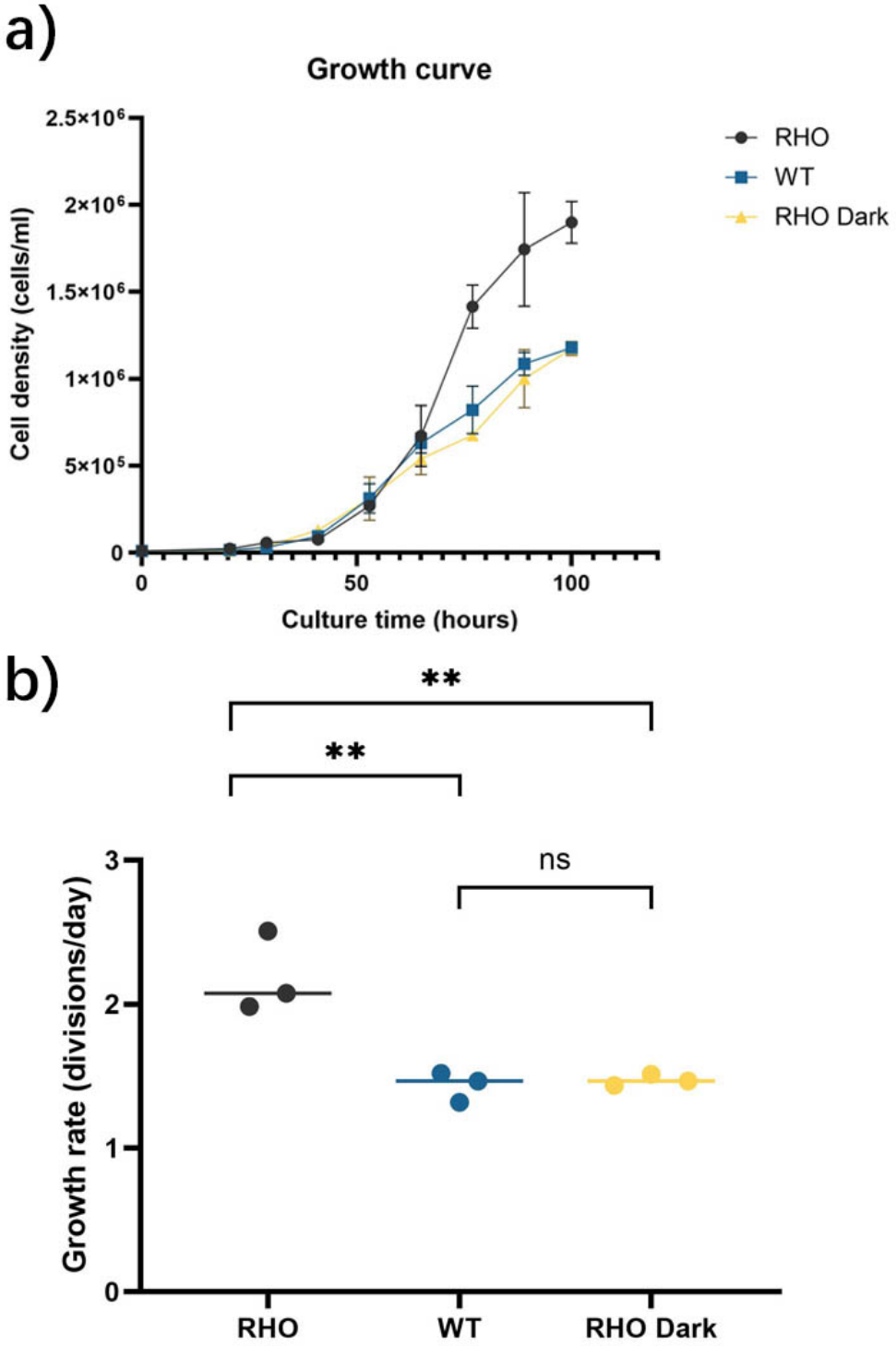


**Figure 4.26 Growth dynamics of rhodopsin-expressing and wild-type strains under different light conditions.** a) This graph presents the cell density (cells/ml) over time (hours) for rhodopsin-expressing (RHO), wild-type (WT), and rhodopsin-expressing in dark conditions (RHO Dark) strains. The RHO strain (black circles) demonstrates superior growth compared to both the WT (blue squares) and RHO Dark (yellow triangles) across the culture period. b) This plot displays the average growth rate (divisions/day) for each strain. The RHO strain shows significantly higher growth rates compared to the WT and RHO Dark, indicated by "**" for $p < 0.01$. The growth rates of WT and RHO Dark do not differ significantly, as denoted by "ns" (not significant). Error bars show standard deviation.

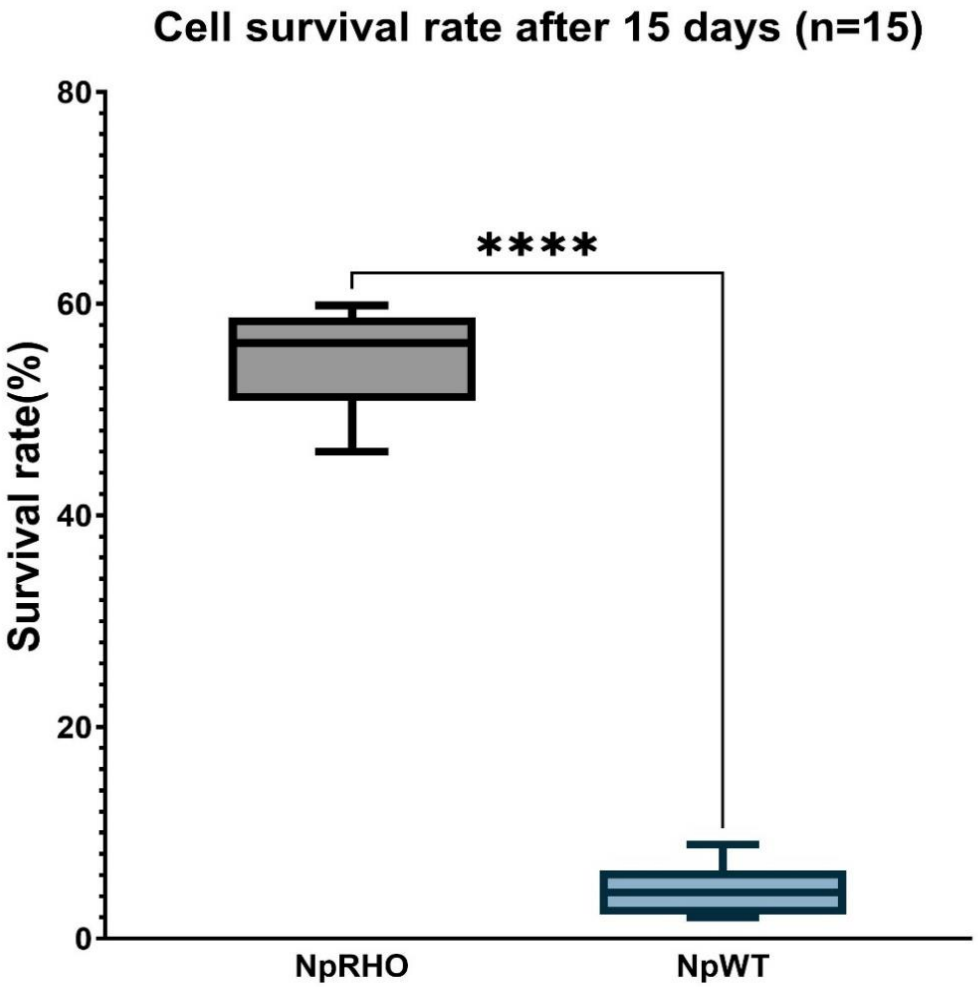


**Figure 4.27 Cell survival rate of rhodopsin-overexpressed and wild-type strains after long-term cultivation.** Plot illustrates the survival rate of cells after 15 days of cultivation for both rhodopsin-overexpressed (*NpRHO*) and wild-type (*NpWT*) strains. The "****" above the comparison indicates an extremely significant difference ($p < 0.0001$) between the survival rates of the two strains. Error bars show standard deviation.

**Immunogold labelling**

To gain insights into the detailed cell structure and subcellular localisation of FR1 in *Nitzschia putrida*, the diatom slicing and immunogold labelling technique, which has been successfully used to study the diatom *Thalassiosira pseudonana in the previous chapter*, was applied to the FR1 knock-in strain of *N. putrida* to reveal the precise localisation of the FR1 protein within the cellular architecture. The results are presented in Figure 4.23.

However, unlike *T. pseudonana*, where clear and distinct cellular compartments allowed for precise localisation of proteins, the cellular structure of *N. putrida* posed significant challenges. Although some localisation points within the cells of *N. putrida* were identified, the overall cell structure did not exhibit the clearly defined and distinct cellular compartments necessary for the accurate determination of the exact location of the FR1 protein. This lack of clear separation in the cellular architecture meant these targets could not be confidently assigned to specific organelles or cellular regions.

Furthermore, when compared to the negative control—where no labelling points were observed—the structural ambiguity of *N. putrida* cells persisted, even though no gold labelling was detected in the control group. This structural indistinctness, coupled with the absence of clear negative control data, made it difficult to draw definitive conclusions about the subcellular localisation of FR1 in N. putrida (Figure 4.24).

Despite these challenges, the presence of localisation points does suggest that FR1 is being expressed and is present within the cells, although the exact role and location of FR1 within the cellular environment of *N. putrida* remain unclear, which requests further investigating with optimised protocol.


a)
x10.0k Zoom-1 HC-1 80.0kV 2023/11/29 10:35
Hitachi TEM system.
1.0µm


b)
x10.0k Zoom-1 HC-1 80.0kV 2023/11/29 10:39
Hitachi TEM system.
1.0µm

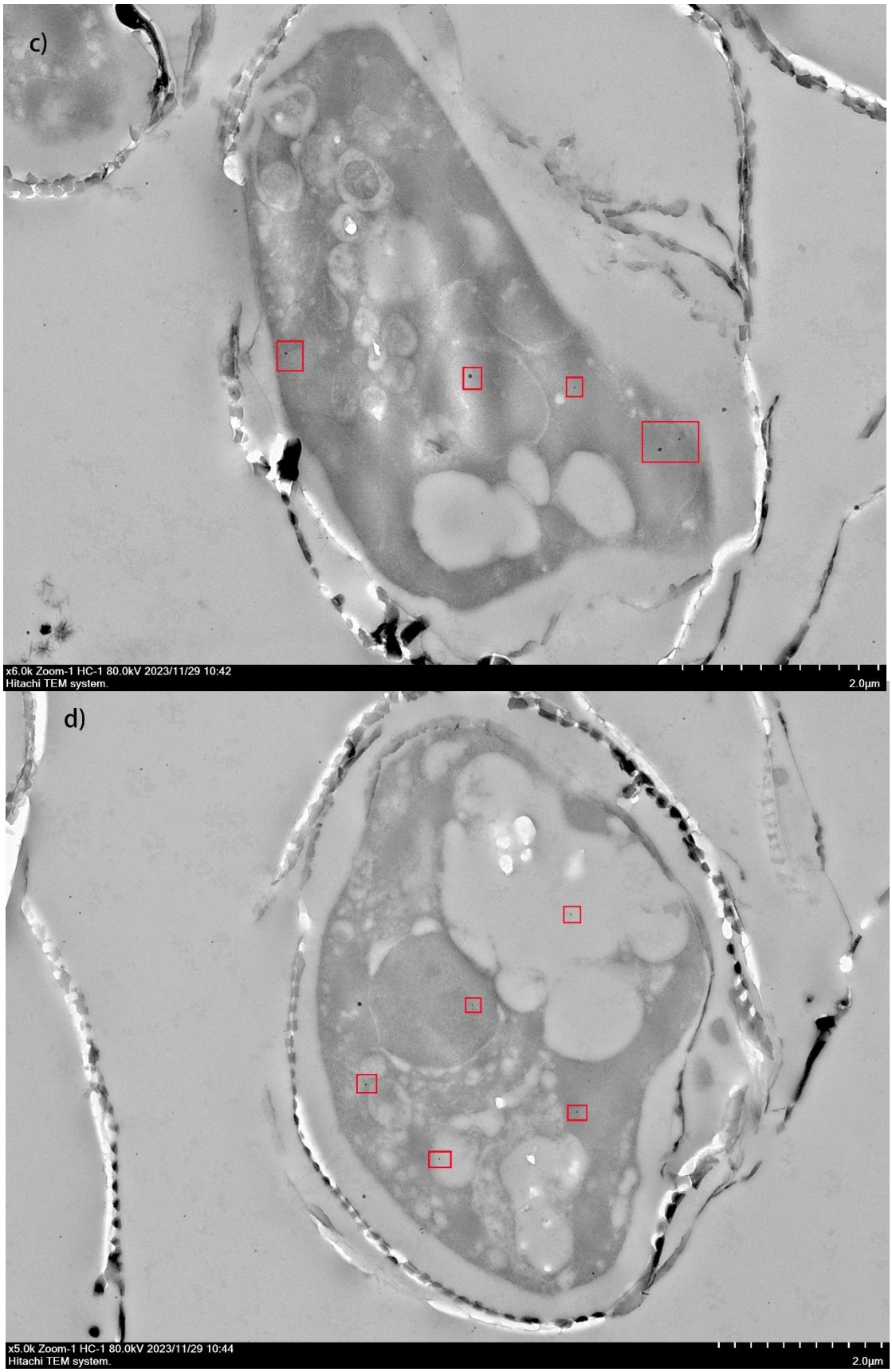


**Figure 4.28 TEM immunogold staining slicing imaging of *N. putrida* rhodopsin knock-in strains.** Each panel from a-d shows a different cell captured at 5000x-10000x magnification. The red boxes highlight specific areas where immunogold labelling points are targeted and visible.

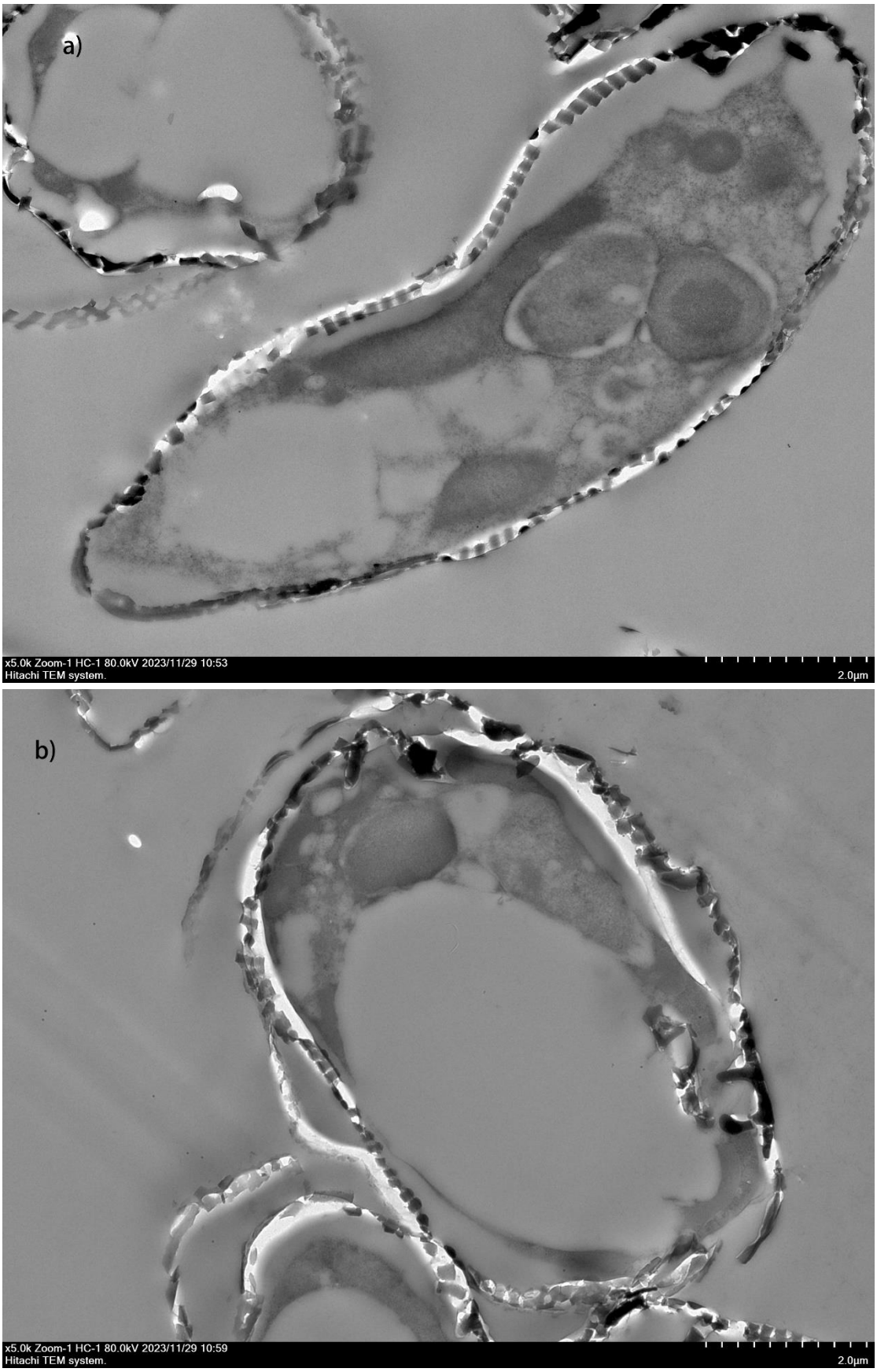


**Figure 4.29 TEM immunogold staining slicing imaging of *T. pseudonana* wild-type (a) and rhodopsin knock-in strain negative control (b). No positive markers were detected in the internal structures of cells in the figure.**

**Discussion**

In this project, I explored the physiological properties of the heterotrophic diatom *Nitzschia putrida*, a species that has undergone secondary loss of photosynthesis. The primary goal was to establish a transformation protocol for *N. putrida* to overexpress microbial rhodopsin and evaluate its growth under various conditions.

Initially, the culture conditions for *N. putrida* were optimised since the cells showed poor growth using the soil extract protocol provided by NIES. The results indicated that, beyond the necessity for a carbon source (LB), *N. putrida* exhibited significantly better growth under f/2 nutrient conditions compared to Aquil* nutrient conditions (Figure 4.8 a-d), as f/2 medium included higher concentrations of most nutrients, especially iron and nitrate. This suggests a sensitivity to nitrogen and iron concentrations, which differ notably between f/2 and Aquil* media. Nitrogen is a fundamental element for life, essential for synthesizing proteins, nucleic acids (DNA and RNA), and other vital biomolecules such as enzymes and some hormones. Both autotrophic and heterotrophic organisms require nitrogen to construct these molecules (Kuypers et al., 2018). Our laboratory data also revealed that increasing nitrogen concentration effectively boosts the maximum yield for both the autotrophic diatom *Thalassiosira pseudonana* and *N. putrida*. Iron, on the other hand, may play a critical role due to *N. putrida*'s habitat in estuarine and nearshore benthic environments (Kamikawa et al., 2022; Lewin & Lewin, 1967). These areas typically have higher iron concentrations, and bottom waters generally contain more iron than surface waters (Su et al., 2015; Zhang et al., 2019). Additionally, the transition to a heterotrophic lifestyle might have further increased the diatom's iron requirements. For instance, oceanic bacteria contain more iron per biomass than phytoplankton (Fourquez et al., 2014; Moreira et al., 2003; Tortell et al., 1996). These factors likely contribute to *N. putrida*'s heightened sensitivity to iron availability, although the detailed reason underlined this phenomenon is still uncleared and requests further

research.

Subsequently, a transformation system using particle bombardment via a biolistic gun was set up to facilitate genetic editing in *N. putrida*. In previously established diatom systems, endogenous fucoxanthin chlorophyll a/c binding protein (fcp) promoters have been commonly used to drive the expression of foreign genes, as demonstrated in species such as *Phaeodactylum tricornutum* (Apt et al., 1996; Falciatore et al., 1999; Zaslavskaia et al., 2000), *Thalassiosira pseudonana* (Belshaw et al., 2023; Hopes et al., 2016; Karas et al., 2015; Poulsen et al., 2006; Strauss et al., 2023), *Fragilariopsis cylindrus*(Hopes, 2017), and *Nitzschia captiva* (Sprecher et al., 2023). However, for *N. putrida*, the absence of highly expressed photosynthetic genes necessitated the identification of alternative promoters. Based on our transcriptome analysis, the promoter and terminator of nicotinamide adenine dinucleotide hydride (NADH)-ubiquinone reductase complex 1 were selected in setting up this transformation system. To the best of my knowledge, this is the first instance of using the NADH as a promoter and terminator in diatoms. The results indicated that this promoter effectively drives the expression of foreign genes as providing nourseothricin resistance and bright eGFP fluorescence. Given its widespread presence as the largest complex in the mitochondrial respiratory chain of plants and animals (Almutairi, 2022; Soole et al., 1992; Walker et al., 1992), , it shows potential as a common endogenous promoter, similar to fcp promoter, to work in other species transformation system. However, further analysis is necessary to determine whether this promoter remains stable under various restrictive conditions. Additionally, promoters from other highly and constitutively expressed genes, such as cytochrome c and ribosomal protein L41, could also potentially function effectively in transforming *N. putrida*.

One of the major challenges during the transformation process was although it could grow on plates, it failed to form individual colonies, instead forming a lawn of cells.

This issue was likely related to its high motility and benthic growth characteristics. In liquid culture, it was observed that when the cell density exceeds $5x10^5$ cells/mL, the cells began to aggregate into flocs. This aggregation made it impossible to isolate single-cell lines by simply picking colonies on agar plates, as was done with other diatoms like *T. pseudonana* and P. *tricornutum*.

To address this challenge, an approach similar to that employed by Sabatino et al. (2015) can be used, where cells are expanded in selective liquid culture directly after transformation and then sorted using fluorescence-activated cell sorting (FACS) to obtain single-cell lines. However, co-transformation is not recommended in this context, as it complicates the selection process. Moreover, the introduction of eGFP during the construction of the FR1 overexpression system was avoided because eGFP could interfere with FR1 expression, making it more difficult to use FACS for cell selection. Given these difficulties, future attempts might consider using microinjection to isolate individual cells, a straightforward and feasible method that could facilitate the selection of cells lacking fluorescent signals (Graf, 2011).

Additionally, the entire transformation system could be further optimised in the future. One possible approach is to test additional antibiotics and selectable markers, which may allow for further genetic modification of cell lines already resistant to a specific antibiotic. Furthermore, introducing antifungal resistance genes could help address the issue of fungal contamination in *N. putrida*'s nutrient-rich culture medium. For example, mutations in the *Candida auris* sterol-methyltransferase gene, ERG6, have been shown to confer high-level resistance to amphotericin B (Rybak et al., 2022).

Moreover, adjusting the parameters of the particle bombardment process, such as flight distance and pressure, could potentially improve the success rate of transformations (Miyagawa et al., 2009; Sprecher et al., 2023). Alternatively, exploring electroporation or multi-pulse electroporation as transformation methods

might yield better results. However, bacterial conjugation poses a challenge, as it is difficult to predict whether bacteria would overgrow in the medium, potentially leading to transformation failure.

This is the first transformation system developed specifically for a heterotrophic diatom, providing a valuable tool for future, more complex, and targeted studies. Such research could include exploring events related to secondary loss of photosynthesis or investigating light-related proteins and their functions. Developing more genetic editing methods, such as CRISPR-Cas, could further allow precise and adaptable gene edits (Jinek et al., 2012).

Building on the established transformation system, the next step involved overexpressing the xanthorhodopsin FR1 from *F. cylindrus* in *N. putrida*. The translation of this gene was successfully verified through reverse transcription PCR, confirming the effective expression of FR1 in the transformed strain. Physiological experiments then revealed intriguing insights into the behaviour of the *N. putrida* rhodopsin overexpressed strain (*NpRHO*). Under light conditions, the *NpRHO* strain exhibited significant growth differences compared to the wild-type *N. putrida* strain (*NpWT*), particularly under carbon-limited conditions, whereas the previous studies have shown no difference in *NpWT* growth between light and dark (Kamikawa et al., 2022). In contrast, no differences were observed between the *NpRHO* and *NpWT* strains in darkness, and it was confirmed that the transformation system itself did not cause these variations. These results underscore the successful reestablishment of a microbial rhodopsin-based light utilisation system in *N. putrida*, facilitated by the introduction of FR1. Interestingly, even under fully nutrient-replete conditions—where neither carbon nor iron limitations were present—the FR1 knock-in strain displayed a significantly higher growth rate and maximum cell density compared to the wild-type strain.

Additionally, long-term cultivation experiments revealed that the *NpRHO* strains

maintained a higher survival rate than the wild-type *NpWT* strains, further indicating that the presence of microbial rhodopsin provides a survival advantage under prolonged growth conditions. This could be particularly valuable for future studies exploring the adaptive mechanisms and evolutionary significance of light-utilizing proteins in diatoms that have transitioned to a heterotrophic lifestyle. These findings not only reaffirm the role of microbial rhodopsin in promoting diatom growth but also highlight the potential of microbial rhodopsin to enhance the metabolic capabilities of heterotrophic diatoms like *N. putrida*, suggesting that the benefits conferred by FR1 might be linked to increased ATP production through light-driven processes rather than enhanced iron absorption or carbon concentrated mechanisms, as iron levels in these conditions were already in excess and the heterotrophic diatom does not use $CO_2$ for photosynthesis (Yoshizawa et al., 2023). This metabolic advantage could involve complex changes, suggesting that future studies should employ RNA-Seq technology to investigate the metabolic alterations in the *NpRHO* strain. Such analysis could help identify specific pathways responsible for the observed growth benefits and improve our understanding of the biosynthetic pathways involved in xanthorhodopsin production in *N. putrida*. Notably, while genes encoding enzymes directly responsible for retinal synthesis, such as BCMO, LCYB, and ZDS, were not identified in *N. putrida* (as shown in Figure 2.4), upstream genes involved in carotenoid syntheses, such as phytoene desaturase (PDS), phytoene synthase (PSY), geranylgeranyl diphosphate (GGPP), isopentenyl diphosphate (IPP), and a gene highly similar to *Fragilariopsis cylindrus* GGPPS (NAA27P00890.m1), were found (Strauss et al., 2023). These genes are involved in the production of ζ-carotene (C40), a precursor in the biosynthesis of carotenoids that can lead to the formation of lutein or retinal (Bertrand, 2010). However, as a heterotrophic diatom, *N. putrida* has lost the genes necessary for lutein synthesis, becoming a colourless diatom (Kamikawa et al., 2022). This loss raises questions about the role of these genes and proteins in the xanthorhodopsin synthesis pathway. *N. putrida* may have entirely lost the downstream

retinal synthesis capability, or it may possess an alternative pathway that allows it to utilise ζ-carotene (C40) to produce retinal (Kamikawa et al., 2022). Future research could explore this possibility by continuously cultivating the *NpRHO* strain long-term to adapt to xanthorhodopsin synthesis and then testing whether it continues to exhibit a growth advantage over the wild type without supplemental retinal. Additionally, RNA-Seq technology, as mentioned, could be employed to search for new metabolic pathways and unannotated genes that might contribute to this process.

Despite the loss of photosynthesis, research by Kamikawa et al. (2022) found that ATPase is still encoded in both the nuclear and plastid genomes of *Nitzschia putrida*. This suggests that *N. putrida* may still retain chloroplasts and thylakoid membranes, raising important questions about whether microbial rhodopsin is produced on thylakoid membranes and what its specific subcellular localisation might be. Understanding the exact localisation of microbial rhodopsin could provide crucial insights into its functional mechanism in *N. putrida*.

To explore this, an attempt was made to use immunogold labelling on cell sections to determine the subcellular localisation of microbial rhodopsin. Unfortunately, *N. putrida* faced several challenges in this process. One major issue was the lack of sufficient labelling points, similar to the problems encountered with *Thalassiosira pseudonana*. Additionally, the cells exhibited severe deformation, which might be attributed not only to the effects of chemical fixation but also to differences in osmotic pressure. Unlike *T. pseudonana*, a marine diatom, *N. putrida* is a freshwater diatom, meaning its intracellular osmotic pressure is lower. This likely made *N. putrida* more susceptible to dehydration during chemical fixation, as evidenced by the complete separation of the cell membrane from the cell wall, indicative of dehydration (Figure 4.23 and Figure 4.24). To address these issues in future optimisations, it will be necessary to adjust the concentrations of solutions such as PBS to match *N. putrida*'s osmotic pressure and prevent cell dehydration. Another

observed challenge was the significant fragmentation of cell walls, possibly due to the high osmotic pressure of the resin used in fixation. This was consistent with the negative control results from wild-type cells, where, in the absence of resin fixation, only plasmolysis was observed, but not wall fragmentation. One potential solution is to use vacuum infiltration of resin-infiltrated specimens to remove air bubbles and reduce deformation or to employ anhydrous freeze-substitution methods for tissue preparation (England et al., 1997).

Another challenge encountered was the unrecognisable internal structure of *N. putrida* cells. Electron microscopy revealed numerous vesicular structures of varying sizes. Some appeared to be vacuoles, while others might be lipid droplets. However, it was difficult to identify the nucleus, mitochondria, and other organelles, making it impossible to pinpoint the exact localisation of the labelling points, which were predominantly found within some vesicular structures. Despite this, some labelling was observed in vacuole-like structures, which could potentially support ATP synthesis—a phenomenon previously observed in *Pseudo-nitzschia subcurvata* (Andrew et al., 2023). Additionally, the presence of microbial rhodopsin in the plastid could help improve the cytoplasmic pH, as intracellular acidification can inhibit metabolism (Wang et al., 2024). This pH regulation could also contribute to the enhanced growth observed in the rhodopsin knock-in strains. Moreover, considering that membrane proteins lacking specific targeting signals are often transported to a mixture of the endoplasmic reticulum (ER) and Golgi apparatus before being directed towards endosomes or vacuoles (Roberts et al., 1992; Teasdale & Jackson, 1996), it is highly possible that FR1 could reposition onto the vacuole membrane if thylakoid membranes are absent in *N. putrida*. However, concrete evidence is needed to support these possibilities. In future studies, it may be necessary to simultaneously label chloroplasts, mitochondria, the nucleus, and other organelles to gain a better understanding of *N. putrida*'s cellular structure and accurately determine the localisation of microbial rhodopsin. This multi-faceted approach could provide deeper

insights into the unique cellular architecture of *N. putrida* and clarify the role of microbial rhodopsin within its cells.

In conclusion, this study successfully established the first transformation system for a heterotrophic diatom, *Nitzschia putrida*, and achieved stable expression of three genes: eGFP, nourseothricin resistance gene, and xanthorhodopsin FR1. The successful overexpression of FR1 in *N. putrida* marks a significant achievement in the genetic engineering project, as it effectively transformed the heterotrophic diatom from a purely heterotrophic organism into a facultative photoheterotroph, enabling it to regain light-harvesting abilities. Under both energy-limited and energy-replete conditions, the *NpRHO* strain demonstrated a distinct growth advantage over the wild-type strain, highlighting the potential of microbial rhodopsin to enhance metabolic efficiency. This advantage suggests that microbial rhodopsin might not only facilitate light-driven ATP production but also contribute to improved cellular processes under various environmental conditions. The ability to exploit light as an energy source likely provides the rhodopsin knock-in *N. putrida* strain with a significant ecological advantage, particularly in fluctuating environments such as estuaries where carbon sources may vary (Cai, 2011). Furthermore, the successful integration and expression of multiple genes in *N. putrida* provide the way for more genetic manipulations in the future, providing bases for setting up more complete genetic editing methods such as CRISPR-Cas9. It also provides the possibility of investigating the evolutionary processes behind the secondary loss and re-acquisition of light-harvesting capabilities in diatoms.

Future studies should aim to figure out the subcellular localisation of microbial rhodopsin in the *NpRHO strain* and the mechanisms under the significant growth advantage provided by xanthorhodopsin FR1. Addressing these questions could help us better understand the role microbial rhodopsin plays in either a diatom or a heterotrophic eukaryote and enhance our ability to engineer microbial rhodopsin into

heterotrophic organisms for various biotechnological applications, such as bioenergy production and carbon sequestration.

# Chapter 5

# Conclusions and future perspectives

This thesis has investigated the role of *Fragilariopsis cylindrus* xanthorhodopsins using the model diatom *Thalassiosira pseudonana* and the heterotrophic diatom *Nitzschia putrida*.

In Chapter 2, it was revealed that *Fragilariopsis cylindrus* expresses two identical microbial rhodopsins, FR1 and FR2, yet these proteins exhibit distinct expression patterns under different environmental conditions. Notably, FR1 was highly responsive to iron availability, suggesting that FR1 plays a critical role in diatom survival under nutrient-limited conditions. The ability of FR1 to function as a light-driven proton pump was demonstrated, highlighting its potential involvement in energy metabolism, particularly when traditional photosynthetic pathways are constrained by environmental factors such as iron scarcity. Furthermore, *in silico* protein alignment indicated that microbial rhodopsins found in diatoms are highly conserved, with key residues suggesting that most of these proteins function as green light-absorbing proton pumps. In addition, a distinct cluster of microbial rhodopsins was identified in diatoms, showing significant divergence from FR1, warranting further investigation into their unique roles and evolutionary significance. The Maximum Likelihood (ML) phylogenetic tree, constructed based on environmental sequence data obtained from FR1 gene searches, revealed that microbial rhodopsins are widely distributed across both prokaryotic and eukaryotic algae, with some evolutionary links between diatom microbial rhodopsins and their prokaryotic counterparts. This suggests the possibility of horizontal gene transfer as a contributing factor to the evolutionary history of microbial rhodopsins in these organisms, facilitating the spread and functional adaptation of these proteins across different taxa.

After exploring the physiological characteristics of FR1, Chapter 3 shifted focus to

the phenotypic analysis of a microbial rhodopsin knock-in strain of *Thalassiosira pseudonana* (*TpRHO*). Under iron-limited conditions, *TpRHO* demonstrated enhanced growth and photosynthetic efficiency compared to the wild-type strain, underscoring the potential role of microbial rhodopsin in improving diatom resilience in nutrient-deprived environments. The enhanced growth and photosynthetic efficiency in *TpRHO* also hint at a broader role for microbial rhodopsin beyond simply compensating for the lack of available iron. By facilitating proton transport, microbial rhodopsin likely assists in maintaining cellular energy production, thus helping diatoms withstand environmental stresses. This adaptive function could be particularly advantageous in the Southern Ocean where iron limitation is prevalent. Additionally, efforts to determine the subcellular localisation of FR1 via immunogold labelling using transmission electron microscopy (TEM) have shown promising preliminary results. These findings suggest that FR1 is likely localised in the thylakoid membrane, supporting the hypothesis that it plays a role in photosynthetic energy conversion. However, further protocol optimisation and additional experiments are required to confirm this localisation with greater certainty and to understand better the precise mechanisms by which microbial rhodopsin contributes to diatom physiology under stress conditions.

Chapter 4 successfully established a transformation system for the heterotrophic diatom *Nitzschia putrida*, enabling the introduction of xanthorhodopsin to geneticengineer the diatom into a photoheterotrophic organism. By overexpressing xanthorhodopsin, *N. putrida* regained the ability to harvest light, allowing it to partially transition from a heterotrophic to a photoheterotrophic lifestyle. Results indicate that *N. putrida* obtained a significant growth advantage, demonstrating the potential of microbial rhodopsin in expanding the metabolic flexibility of diatoms and other marine microorganisms such as dinoflagellates. This finding further supports the hypothesis that microbial rhodopsins enable algae to utilise light as an alternative energy source, providing a crucial energy advantage in nutrient-scarce environments.

By facilitating light-driven proton pumping, xanthorhodopsin appears to support essential cellular processes, allowing heterotrophic algae like *N. putrida* to thrive even when traditional nutrient supplies are limited. Future studies should explore the full implications of rhodopsin-driven metabolic shifts in marine ecosystems and their potential applications in biotechnology.

In conclusion, this research demonstrates that microbial rhodopsins are vital for diatom adaptation in iron-limited oceans, functioning not only as light-driven proton pumps but also contributing to broader metabolic processes that enhance growth and resilience under nutrient stress. These findings advance our understanding of the ecological significance of microbial rhodopsins and suggest potential applications in marine resource management and biotechnology. Further research is needed to explore the precise mechanisms by which microbial rhodopsins support diatom physiology and to investigate their potential utility in addressing environmental challenges. Future research should continue to explore the precise mechanisms by which diatom microbial rhodopsins operate. For example, ATP measurements in live cells, along with solution iron uptake kinetics, could offer valuable insights into the working mechanisms of microbial rhodopsins in eukaryotic algae. However, as noted earlier, these mechanisms might represent a mix of functions.

A key unresolved question concerns the function of FR2, which shares 100% amino acid sequence identity with FR1 but exhibits different expression patterns, remains unclear. The constitutive expression of FR2 indicates that the FR2 plays an important role in diatom physiology. However, whether FR2 performs the same function as FR1 under nutrient replete conditions remains an open question. Its specific role and subcellular localisation are still unknown.

Other proton-pumping rhodopsins recently identified in Antarctic diatom species such as *Pseudo-nitzschia subcurvata* and *Pseudo-nitzschia granii* add to the growing evidence of functional diversity in diatom rhodopsins (Andrew et al., 2023).

Interestingly, unlike the FR1 and FR2 we discovered, both proton-pumping rhodopsins from *Pseudo-nitzschia* diatom localise to the vacuole membrane (Andrew 2023; Yoshizawa 2023). Furthermore, the proton-pumping rhodopsins of *P. subcurvata* and *P. granii* also lack an approximately 30-amino-acid signal peptide at the N-terminus compared to FR1, where they may work alongside vacuole-type ATPases (V-ATPases) or contribute to the carbon concentrating mechanism (Andrew et al., 2023; Strauss et al., 2023; Yoshizawa et al., 2023).

In this context, FR2 may function analogously to these rhodopsins, possibly contributing to intracellular energy management or pH regulation under varying environmental conditions. It now appears that evolution has tested both configurations—rhodopsins with and without transit peptides—in different algal lineages. Minor genetic differences, such as the presence or absence of signal peptides, may redirect rhodopsins to different cellular compartments, thereby fine-tuning their physiological roles.

Despite their distinct localisations, these rhodopsins all share a core light-driven proton-pumping activity that supports ATP synthesis through different routes. Combined with previous results, this suggests that microbial rhodopsin-based light harvesting pathway and chlorophyll-based photosynthesis are functionally distinct yet complementary. These findings collectively highlight the evolutionary plasticity and functional convergence of microbial rhodopsins in diatoms.

Despite successful overexpression of FR1 at the transcript level, the lack of quantitative protein data presents a limitation in interpreting the physiological effects observed in transformed diatom strains. FR1 is membrane-bound protein with pigment, which makes them difficult to extract, solubilise, and detect using standard methods. In the absence of specific antibodies or suitable quantification approaches, it remains unclear whether the elevated mRNA levels resulted in proportionally increased and functional protein.  Relying solely on mRNA or transcript levels can be

misleading, as mRNA abundance often does not linearly translate to functional protein abundance (Liu et al., 2016). Therefore, only by conducting an absolute quantification of FR1 can we correctly interpret its biological phenotype such as quantifying its contribution and efficiency to the energy of diatoms compared to that of chlorophyll. Future studies should consider incorporating protein-level validation, such as absolute label free quantification (Ludwig et al., 2012), proteome ruler based on MS signal of histones (Wiśniewski et al., 2014), and stable isotope labelling with amino acids in cell culture (Ong et al., 2002). These efforts will improve the mechanistic understanding of rhodopsin function and its contribution to cellular energetics under environmental stress. Moreover, environmental sample analyses revealed the presence of microbial rhodopsins in various eukaryotic algae, including diatoms. On one hand, many of these species remain unidentified, highlighting the need for further environmental sampling. On the other hand, another distinct cluster of microbial rhodopsins was identified within diatoms. Whether this cluster shares the same function and mechanism as FR1 is still unknown. Therefore, further research is required to explore the functional roles of these microbial rhodopsins and uncover their potential contributions to diatom physiology and marine ecosystems.

The widespread occurrence of microbial rhodopsins in both eukaryotic phytoplankton and marine bacteria suggests their potential to influence ocean-scale ecological and biogeochemical processes. If, as this study and previous findings indicate, microbial rhodopsins can enhance growth by up to 30%, their contribution to ocean productivity may have been substantially underestimated. This is particularly relevant for diatoms, which are responsible for approximately 20% of global primary production and dominate many iron-limited ocean regions, including the Southern Ocean, Equatorial Pacific, and subarctic North Pacific. Consistent with this, our environmental transcriptomic data show that rhodopsin expression is concentrated in stratified surface waters where dissolved iron levels are low (Fig. 5.1 a–b) (Strauss et al., 2023). While the overall expression of microbial rhodopsins does not correlate significantly

with dissolved iron concentration (Spearman's ρ = –0.03, P = 0.736; Fig. 5.1 c), this may reflect the influence of multiple environmental factors that co-regulate rhodopsin gene expression across diverse taxa. However, when focusing specifically on diatoms, we observed a strong positive correlation between rhodopsin transcript abundance and iron limitation index (Spearman's ρ = 0.43, P = 2.0 × $10^{-4}$; Fig. 5.1 d), particularly in high-latitude, iron-depleted regions such as the Southern Ocean. Additionally, diatom

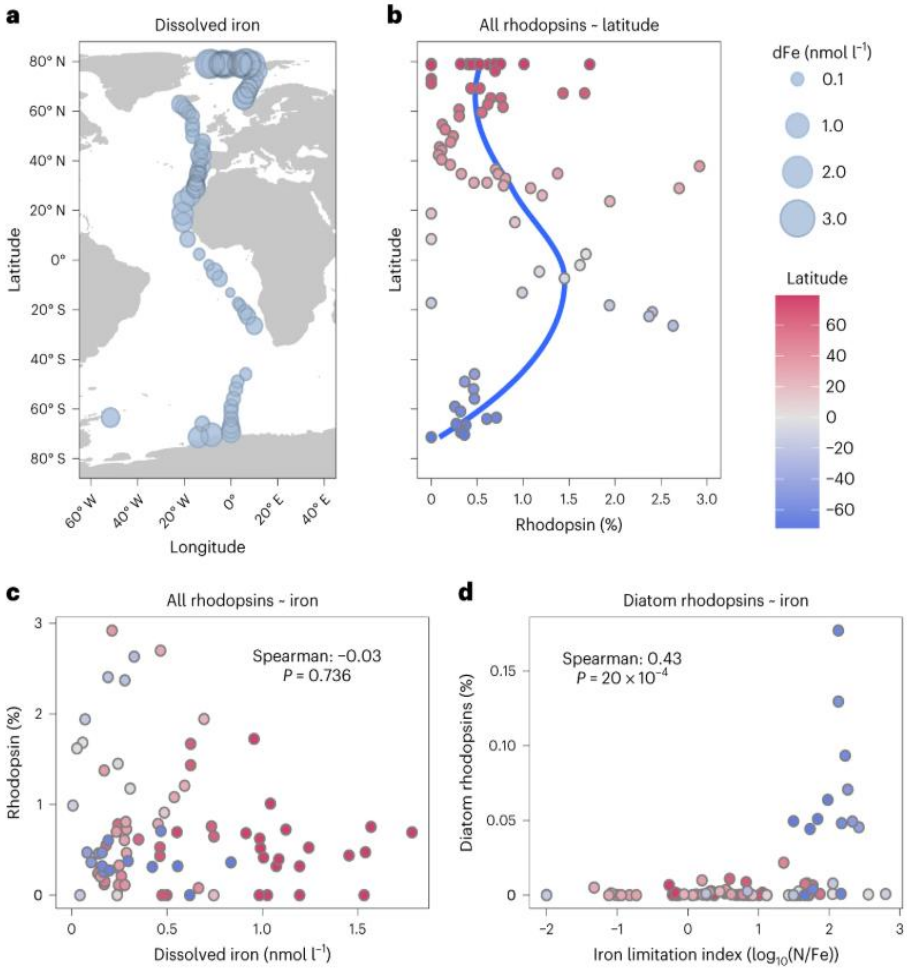


**Figure 5.1 Environmental distribution of rhodopsin transcripts in relation to iron availability.** a) Metatranscriptome sampling stations sized by estimated dissolved iron concentrations. b) Normalized transcript abundances of eukaryotic rhodopsins across latitudes. The blue line indicates the loess-smoothed trend. c) Correlation between total rhodopsin transcript abundance and modelled dissolved iron concentration. d) Correlation between diatom rhodopsin transcript abundance and estimated iron limitation index. P values are from two-tailed t-tests with Benjamini–Hochberg correction. Data and figure from our published paper Strauss et al. (2023)

rhodopsin expression was negatively correlated with dissolved iron ($r(82) = –0.27$, $P = 0.025$), highlighting its potential physiological role in supporting diatom survival and productivity under chronic iron stress—a finding that aligns with earlier observations (Marchetti et al., 2015).

This evidence suggests that rhodopsins may serve as an auxiliary or alternative energy acquisition pathway under conditions where photosynthesis is limited by iron availability. Unlike chlorophyll-based systems, rhodopsins do not require metal cofactors, enabling light energy harvesting even in oligotrophic or low-light conditions. Despite these capabilities, traditional ocean productivity models still focus almost exclusively on chlorophyll-based photosynthesis and nutrient cycling, largely overlooking rhodopsin-mediated energy conversion. Given their widespread distribution across both prokaryotes and eukaryotic phytoplankton, as well as their functional relevance in iron-limited systems, microbial rhodopsins should be considered in next-generation biogeochemical models. Their inclusion will help improve predictions of primary production, carbon export, and ecosystem dynamics—especially in polar and mesopelagic regions, where light and nutrients are scarce and photosynthetic efficiency is inherently constrained.

Regarding the newly established *N. putrida* transformation system, future efforts should aim to develop more versatile transformation tools, such as CRISPR-Cas9, to enable precise gene editing for future studies. This gene-editing technology will allow for more precise manipulation of the genome, enabling researchers to explore gene functions with greater accuracy. As a heterotrophic diatom that has recently lost its photosynthetic capability and possesses a relatively fast growth cycle, *N. putrida* presents potential for future research. It is especially promising as a model for studying various photosynthesis-related genes, providing unique insights into the evolutionary loss of photosynthesis and the functional adaptation of diatoms to heterotrophic lifestyles. Additionally, microscopic observations revealed abundant

lipid accumulation within the cells, indicating that *N. putrida* holds potential for bio-fuel production. This discovery opens up new avenues for investigating the diatom's bioenergy potential, particularly in terms of lipid metabolism and its applications in biotechnology. Further exploration of its lipid production capabilities could contribute to the development of sustainable biofuels, making *N. putrida* not only a valuable model for genetic research but also a promising candidate for industrial applications.

Taken together, while this study has provided molecular and physiological insights into microbial rhodopsin function in diatoms, it also holds implications beyond the cellular level. In summary, this research has provided new insights into the role of microbial rhodopsins in diatoms. As our understanding of these proteins improves, the ecological and biotechnological applications of microbial rhodopsins will become clearer, with the potential to reshape our approach to marine productivity and modelling the role of diatoms under conditions of climate change.

# Reference

Adamian, L., Ouyang, Z., Tseng, Y. Y., & Liang, J. (2006). Evolutionary Patterns of Retinal-Binding Pockets of Type I Rhodopsins and Their Functionst. *Photochemistry and Photobiology*, *82*(6), 1426-1435. https://doi.org/https://doi.org/10.1111/j.1751-1097.2006.tb09795.x

Albelda-Berenguer, M., Monachon, M., & Joseph, E. (2019). Chapter Five - Siderophores: From natural roles to potential applications. In G. M. Gadd & S. Sariaslani (Eds.), *Advances in Applied Microbiology* (Vol. 106, pp. 193-225). Academic Press. https://doi.org/https://doi.org/10.1016/bs.aambs.2018.12.001

Allen, A. E., Laroche, J., Maheswari, U., Lommer, M., Schauer, N., Lopez, P. J., Finazzi, G., Fernie, A. R., & Bowler, C. (2008). Whole-cell response of the pennate diatom Phaeodactylum tricornutum to iron starvation. *Proc Natl Acad Sci U S A*, *105*(30), 10438-10443. https://doi.org/10.1073/pnas.0711370105

Almutairi, Z. M. (2022). Molecular characterization and expression profiling of NADH-ubiquinone reductase Complex 1 MLRQ Subunit in Pennisetum glaucum. *Journal of Plant Biochemistry and Biotechnology*, *31*(2), 361-369. https://doi.org/10.1007/s13562-021-00688-8

Alverson, A. J., Beszteri, B., Julius, M. L., & Theriot, E. C. (2011). The model marine diatom Thalassiosira pseudonana likely descended from a freshwater ancestor in the genus Cyclotella. *BMC Evolutionary Biology*, *11*(1), 125. https://doi.org/10.1186/1471-2148-11-125

Anbar, A. D., & Knoll, A. H. (2002). Proterozoic Ocean Chemistry and Evolution: A Bioinorganic Bridge? *Science*, *297*(5584), 1137-1142. https://doi.org/doi:10.1126/science.1069651

Andrew, S. M., Moreno, C. M., Plumb, K., Hassanzadeh, B., Gomez-Consarnau, L., Smith, S. N., Schofield, O., Yoshizawa, S., Fujiwara, T., Sunda, W. G., Hopkinson, B. M., Septer, A. N., & Marchetti, A. (2023). Widespread use of proton-pumping rhodopsin

in Antarctic phytoplankton. *Proceedings of the National Academy of Sciences*, *120*(39), e2307638120. https://doi.org/doi:10.1073/pnas.2307638120

Apt, K. E., Grossman, A. R., & Kroth-Pancic, P. G. (1996). Stable nuclear transformation of the diatomPhaeodactylum tricornutum. *Molecular and General Genetics MGG*, *252*(5), 572-579. https://doi.org/10.1007/BF02172403

Armbrust, E. V. (2009). The life of diatoms in the world's oceans. *Nature*, *459*(7244), 185-192. https://doi.org/10.1038/nature08057

Armbrust, E. V., Berges, J. A., Bowler, C., Green, B. R., Martinez, D., Putnam, N. H., Zhou, S., Allen, A. E., Apt, K. E., Bechner, M., Brzezinski, M. A., Chaal, B. K., Chiovitti, A., Davis, A. K., Demarest, M. S., Detter, J. C., Glavina, T., Goodstein, D., Hadi, M. Z., . . . Rokhsar, D. S. (2004). The Genome of the Diatom Thalassiosira Pseudonana: Ecology, Evolution, and Metabolism. *Science*, *306*(5693), 79-86. https://doi.org/doi:10.1126/science.1101156

Armbruster, U., Correa Galvis, V., Kunz, H.-H., & Strand, D. D. (2017). The regulation of the chloroplast proton motive force plays a key role for photosynthesis in fluctuating light. *Current Opinion in Plant Biology*, *37*, 56-62. https://doi.org/https://doi.org/10.1016/j.pbi.2017.03.012

Armstrong, R. A., Lee, C., Hedges, J. I., Honjo, S., & Wakeham, S. G. (2001). A new, mechanistic model for organic carbon fluxes in the ocean based on the quantitative association of POC with ballast minerals. *Deep Sea Research Part II: Topical Studies in Oceanography*, *49*(1), 219-236. https://doi.org/https://doi.org/10.1016/S0967-0645(01)00101-1

Arnon, D. I. (1971). The Light Reactions of Photosynthesis. *Proceedings of the National Academy of Sciences*, *68*(11), 2883-2892. https://doi.org/doi:10.1073/pnas.68.11.2883

Årstøl, E., & Hohmann-Marriott, M. F. (2019). Cyanobacterial siderophores—physiology, structure, biosynthesis, and applications. *Marine Drugs*, *17*(5), 281.

Azencott, H. R., Peter, G. F., & Prausnitz, M. R. (2007). Influence of the Cell Wall on Intracellular Delivery to Algal Cells by Electroporation and Sonication. *Ultrasound in*

*Medicine & Biology*, *33*(11), 1805-1817. https://doi.org/https://doi.org/10.1016/j.ultrasmedbio.2007.05.008

Baek, S. H., Jung, S. W., & Shin, K. (2011). Effects of temperature and salinity on growth of Thalassiosira pseudonana (Bacillariophyceae) isolated from ballast water. *Journal of Freshwater Ecology*, *26*(4), 547-552.

Balashov, S. P., Imasheva, E. S., Boichenko, V. A., Antón, J., Wang, J. M., & Lanyi, J. K. (2005). Xanthorhodopsin: A Proton Pump with a Light-Harvesting Carotenoid Antenna. *Science*, *309*(5743), 2061-2064. https://doi.org/doi:10.1126/science.1118046

Bar-Shalom, R., Rozenberg, A., Lahyani, M., Hassanzadeh, B., Sahoo, G., Haber, M., Burgsdorf, I., Tang, X., Squatrito, V., Gomez-Consarnau, L., Béjà, O., & Steindler, L. (2023). Rhodopsin-mediated nutrient uptake by cultivated photoheterotrophic Verrucomicrobiota. *The ISME Journal*, *17*(7), 1063-1073. https://doi.org/10.1038/s41396-023-01412-1

Barrio-Hernandez, I., Yeo, J., Jänes, J., Mirdita, M., Gilchrist, C. L. M., Wein, T., Varadi, M., Velankar, S., Beltrao, P., & Steinegger, M. (2023). Clustering predicted structures at the scale of the known protein universe. *Nature*, *622*(7983), 637-645. https://doi.org/10.1038/s41586-023-06510-w

Basu, S., & Mackey, K. R. M. (2018). Phytoplankton as Key Mediators of the Biological Carbon Pump: Their Responses to a Changing Climate. *Sustainability*, *10*(3), 869. https://www.mdpi.com/2071-1050/10/3/869

Batista Napotnik, T., Polajžer, T., & Miklavčič, D. (2021). Cell death due to electroporation – A review. *Bioelectrochemistry*, *141*, 107871. https://doi.org/https://doi.org/10.1016/j.bioelechem.2021.107871

Bayley, H., Huang, K. S., Radhakrishnan, R., Ross, A. H., Takagaki, Y., & Khorana, H. G. (1981). Site of attachment of retinal in bacteriorhodopsin. *Proceedings of the National Academy of Sciences*, *78*(4), 2225-2229. https://doi.org/doi:10.1073/pnas.78.4.2225

Beer, S., Larsson, C., Poryan, O., & Axelsson, L. (2000). Photosynthetic rates of Ulva (Chlorophyta) measured by pulse amplitude modulated (PAM) fluorometry. *European Journal of Phycology*, *35*(1), 69-74.

Behnke, J., & LaRoche, J. (2020). Iron uptake proteins in algae and the role of Iron Starvation-Induced Proteins (ISIPs). *European Journal of Phycology*, *55*(3), 339-360. https://doi.org/10.1080/09670262.2020.1744039

Behrenfeld, M. J., Halsey, K. H., Boss, E., Karp-Boss, L., Milligan, A. J., & Peers, G. (2021). Thoughts on the evolution and ecological niche of diatoms. *Ecological Monographs*, *91*(3), e01457. https://doi.org/https://doi.org/10.1002/ecm.1457

Behrenfeld, M. J., & Milligan, A. J. (2013). Photophysiological Expressions of Iron Stress in Phytoplankton. *Annual Review of Marine Science*, *5*(Volume 5, 2013), 217-246. https://doi.org/https://doi.org/10.1146/annurev-marine-121211-172356

Béjà, O., Aravind, L., Koonin, E. V., Suzuki, M. T., Hadd, A., Nguyen, L. P., Jovanovich, S. B., Gates, C. M., Feldman, R. A., Spudich, J. L., Spudich, E. N., & DeLong, E. F. (2000). Bacterial Rhodopsin: Evidence for a New Type of Phototrophy in the Sea. *Science*, *289*(5486), 1902-1906. https://doi.org/doi:10.1126/science.289.5486.1902

Béjà, O., Spudich, E. N., Spudich, J. L., Leclerc, M., & DeLong, E. F. (2001). Proteorhodopsin phototrophy in the ocean. *Nature*, *411*(6839), 786-789. https://doi.org/10.1038/35081051

Belshaw, N., Grouneva, I., Aram, L., Gal, A., Hopes, A., & Mock, T. (2023). Efficient gene replacement by CRISPR/Cas-mediated homologous recombination in the model diatom Thalassiosira pseudonana. *New Phytologist*, *238*(1), 438-452. https://doi.org/https://doi.org/10.1111/nph.18587

Bertrand, M. (2010). Carotenoid biosynthesis in diatoms. *Photosynthesis Research*, *106*(1), 89-102. https://doi.org/10.1007/s11120-010-9589-x

Bhattacharjya, R., Marella, T. K., Kumar, M., Kumar, V., & Tiwari, A. (2024). Diatom-assisted aquaculture: Paving the way towards sustainable economy. *Reviews in Aquaculture*, *16*(1), 491-507. https://doi.org/https://doi.org/10.1111/raq.12848

Boukhalfa, H., & Crumbliss, A. L. (2002). Chemical aspects of siderophore mediated iron transport. *Biometals*, *15*(4), 325-339. https://doi.org/10.1023/A:1020218608266

Boyd, P. W., Jickells, T., Law, C. S., Blain, S., Boyle, E. A., Buesseler, K. O., Coale, K. H., Cullen, J. J., de Baar, H. J., Follows, M., Harvey, M., Lancelot, C., Levasseur, M., Owens, N. P., Pollard, R., Rivkin, R. B., Sarmiento, J., Schoemann, V., Smetacek, V., . . . Watson, A. J. (2007). Mesoscale iron enrichment experiments 1993-2005: synthesis and future directions. *Science*, *315*(5812), 612-617. https://doi.org/10.1126/science.1131669

Bressac, M., Guieu, C., Ellwood, M. J., Tagliabue, A., Wagener, T., Laurenceau-Cornec, E. C., Whitby, H., Sarthou, G., & Boyd, P. W. (2019). Resupply of mesopelagic dissolved iron controlled by particulate iron composition. *Nature Geoscience*, *12*(12), 995-1000. https://doi.org/10.1038/s41561-019-0476-6

Brettel, K. (1997). Electron transfer and arrangement of the redox cofactors in photosystem I. *Biochimica et Biophysica Acta (BBA) - Bioenergetics*, *1318*(3), 322-373. https://doi.org/https://doi.org/10.1016/S0005-2728(96)00112-0

Brown, L. S., Gat, Y., Sheves, M., Yamazaki, Y., Maeda, A., Needleman, R., & Lanyi, J. K. (1994). The Retinal Schiff Base-Counterion Complex of Bacteriorhodopsin: Changed Geometry during the Photocycle Is a Cause of Proton Transfer to Aspartate 85. *Biochemistry*, *33*(40), 12001-12011. https://doi.org/10.1021/bi00206a001

Bruland, K. W., Orians, K. J., & Cowen, J. P. (1994). Reactive trace metals in the stratified central North Pacific. *Geochimica et Cosmochimica Acta*, *58*(15), 3171-3182. https://doi.org/https://doi.org/10.1016/0016-7037(94)90044-2

Bryant, D. A., & Frigaard, N.-U. (2006). Prokaryotic photosynthesis and phototrophy illuminated. *Trends in Microbiology*, *14*(11), 488-496. https://doi.org/10.1016/j.tim.2006.09.001

Buesseler, K. O., Andrews, J. E., Pike, S. M., Charette, M. A., Goldson, L. E., Brzezinski, M. A., & Lance, V. P. (2005). Particle export during the Southern Ocean Iron Experiment (SOFeX). *Limnology and Oceanography*, *50*(1), 311-327.

https://doi.org/https://doi.org/10.4319/lo.2005.50.1.0311

Bunt, J. S. (1973). Primary production: Marine ecosystems. *Human Ecology*, *1*(4), 333-345. https://doi.org/10.1007/BF01536730

Cai, W.-J. (2011). Estuarine and Coastal Ocean Carbon Paradox: CO2 Sinks or Sites of Terrestrial Carbon Incineration? *Annual Review of Marine Science*, *3*(Volume 3, 2011), 123-145. https://doi.org/https://doi.org/10.1146/annurev-marine-120709-142723

Capone, D. G., Burns, J. A., Montoya, J. P., Subramaniam, A., Mahaffey, C., Gunderson, T., Michaels, A. F., & Carpenter, E. J. (2005). Nitrogen fixation by Trichodesmium spp.: An important source of new nitrogen to the tropical and subtropical North Atlantic Ocean. *Global Biogeochemical Cycles*, *19*(2). https://doi.org/https://doi.org/10.1029/2004GB002331

Cardol, P. (2011). Mitochondrial NADH:ubiquinone oxidoreductase (complex I) in eukaryotes: A highly conserved subunit composition highlighted by mining of protein databases. *Biochimica et Biophysica Acta (BBA) - Bioenergetics*, *1807*(11), 1390-1397. https://doi.org/https://doi.org/10.1016/j.bbabio.2011.06.015

Cardona, T. (2018). Early Archean origin of heterodimeric Photosystem I. *Heliyon*, *4*(3), e00548. https://doi.org/https://doi.org/10.1016/j.heliyon.2018.e00548

Claustre, H., Legendre, L., Boyd, P. W., & Levy, M. (2021). The Oceans' Biological Carbon Pumps: Framework for a Research Observational Community Approach [Review]. *Frontiers in Marine Science*, *8*. https://doi.org/10.3389/fmars.2021.780052

Cohen, N. R., Gong, W., Moran, D. M., McIlvin, M. R., Saito, M. A., & Marchetti, A. (2018). Transcriptomic and proteomic responses of the oceanic diatom Pseudo-nitzschia granii to iron limitation. *Environmental Microbiology*, *20*(8), 3109-3126. https://doi.org/https://doi.org/10.1111/1462-2920.14386

Cohen, N. R., Mann, E., Stemple, B., Moreno, C. M., Rauschenberg, S., Jacquot, J. E., Sunda, W. G., Twining, B. S., & Marchetti, A. (2018). Iron storage capacities and associated ferritin gene expression among marine diatoms. *Limnology and Oceanography*,

*63*(4), 1677-1691.

Cook, O., & Hildebrand, M. (2016). Enhancing LC-PUFA production in Thalassiosira pseudonana by overexpressing the endogenous fatty acid elongase genes. *Journal of Applied Phycology*, *28*, 897-905.

Curie, C., Alonso, J. M., JEAN, M. L., Ecker, J. R., & Briat, J.-F. (2000). Involvement of NRAMP1 from Arabidopsis thaliana in iron transport. *Biochemical Journal*, *347*(3), 749-755.

Dal-Pizzol, F., Klamt, F., Frota, M. L., Jr., Moraes, L. F., Moreira, J. C., & Benfato, M. S. (2000). Retinol supplementation induces DNA damage and modulates iron turnover in rat Sertoli cells. *Free Radic Res*, *33*(5), 677-687. https://doi.org/10.1080/10715760000301191

Davis, A. K., & Hildebrand, M. (2008). Molecular Processes of Biosilicification in Diatoms. In *Biomineralization* (pp. 255-294). https://doi.org/https://doi.org/10.1002/9780470986325.ch8

Davison, P. A., Tu, W., Xu, J., Della Valle, S., Thompson, I. P., Hunter, C. N., & Huang, W. E. (2022). Engineering a Rhodopsin-Based Photo-Electrosynthetic System in Bacteria for CO2 Fixation. *ACS Synthetic Biology*, *11*(11), 3805-3816. https://doi.org/10.1021/acssynbio.2c00397

de Baar, H. J. W., Boyd, P. W., Coale, K. H., Landry, M. R., Tsuda, A., Assmy, P., Bakker, D. C. E., Bozec, Y., Barber, R. T., Brzezinski, M. A., Buesseler, K. O., Boyé, M., Croot, P. L., Gervais, F., Gorbunov, M. Y., Harrison, P. J., Hiscock, W. T., Laan, P., Lancelot, C., . . . Wong, C.-S. (2005). Synthesis of iron fertilization experiments: From the Iron Age in the Age of Enlightenment. *Journal of Geophysical Research: Oceans*, *110*(C9). https://doi.org/https://doi.org/10.1029/2004JC002601

de Koning, A. P., & Keeling, P. J. (2006). The complete plastid genome sequence of the parasitic green alga Helicosporidium sp. is highly reduced and structured. *BMC biology*, *4*, 1-10.

de la Torre, J. R., Christianson, L. M., Béjà, O., Suzuki, M. T., Karl, D. M., Heidelberg, J., &

DeLong, E. F. (2003). Proteorhodopsin genes are distributed among divergent marine bacterial taxa. *Proceedings of the National Academy of Sciences*, *100*(22), 12830-12835. https://doi.org/doi:10.1073/pnas.2133554100

Deng, L., Li, Y., Tanizawa, Y., Nakamura, Y., Kamikawa, R., Hopes, A., & Mock, T. (2025). A genetic transformation system for the heterotrophic diatom Nitzschia putrida (Bacillariophyceae). *Journal of Phycology*, *n/a*(n/a). https://doi.org/https://doi.org/10.1111/jpy.70070

Dunahay, T. G., Jarvis, E. E., & Roessler, P. G. (1995). GENETIC TRANSFORMATION OF THE DIATOMS CYCLOTELLA CRYPTICA AND NAVICULA SAPROPHILA. *Journal of Phycology*, *31*(6), 1004-1012. https://doi.org/https://doi.org/10.1111/j.0022-3646.1995.01004.x

Eilers, P. H. C., & Peeters, J. C. H. (1988). A model for the relationship between light intensity and the rate of photosynthesis in phytoplankton. *Ecological Modelling*, *42*(3), 199-215. https://doi.org/https://doi.org/10.1016/0304-3800(88)90057-9

England, W. E., Mccully, M. E., & Huang, C. X. (1997). Solvent vapour lock: an extreme case of the problems caused by lignified and suberized cell walls during resin infiltration. *Journal of Microscopy*, *185*(1), 85-93. https://doi.org/https://doi.org/10.1046/j.1365-2818.1997.1360696.x

Facciotti, M. T., Rouhani, S., & Glaeser, R. M. (2004). Crystal structures of bR(D85S) favor a model of bacteriorhodopsin as a hydroxyl-ion pump. *FEBS Letters*, *564*(3), 301-306. https://doi.org/https://doi.org/10.1016/S0014-5793(04)00208-X

Falasco, E., Ector, L., Isaia, M., Wetzel, C. E., Hoffmann, L., & Bona, F. (2014). Diatom flora in subterranean ecosystems: a review. *International Journal of Speleology*, *43*(3), 231-251.

Falciatore, A., Casotti, R., Leblanc, C., Abrescia, C., & Bowler, C. (1999). Transformation of Nonselectable Reporter Genes in Marine Diatoms. *Marine Biotechnology*, *1*(3), 239-251. https://doi.org/10.1007/PL00011773

Falciatore, A., Jaubert, M., Bouly, J.-P., Bailleul, B., & Mock, T. (2019). Diatom Molecular

Research Comes of Age: Model Species for Studying Phytoplankton Biology and Diversity[OPEN]. *The Plant Cell*, *32*(3), 547-572. https://doi.org/10.1105/tpc.19.00158

Falkowski, P. G. (1994). The role of phytoplankton photosynthesis in global biogeochemical cycles. *Photosynth Res*, *39*(3), 235-258. https://doi.org/10.1007/bf00014586

Falkowski, P. G., Katz, M. E., Knoll, A. H., Quigg, A., Raven, J. A., Schofield, O., & Taylor, F. J. R. (2004). The Evolution of Modern Eukaryotic Phytoplankton. *Science*, *305*(5682), 354-360. https://doi.org/doi:10.1126/science.1095964

Feng, S., Jiang, Y., Cai, Z., Zeng, Y., & Zhou, J. (2019). The State of Arts: Sources, Microbial Processes and Ecological Effects of Iron in the Marine Environment [Original Article]. *Advances In Earth Science*, *34*(5), 513-522. https://doi.org/https://doi.org/10.11867/j.issn.1001-8166.2019.05.0513

Field, C. B., Behrenfeld, M. J., Randerson, J. T., & Falkowski, P. (1998). Primary Production of the Biosphere: Integrating Terrestrial and Oceanic Components. *Science*, *281*(5374), 237-240. https://doi.org/doi:10.1126/science.281.5374.237

Fields, P. A., Dong, Y., Meng, X., & Somero, G. N. (2015). Adaptations of protein structure and function to temperature: there is more than one way to 'skin a cat'. *The Journal of Experimental Biology*, *218*(12), 1801-1811.

Firme, G. F., Rue, E. L., Weeks, D. A., Bruland, K. W., & Hutchins, D. A. (2003). Spatial and temporal variability in phytoplankton iron limitation along the California coast and consequences for Si, N, and C biogeochemistry. *Global Biogeochemical Cycles*, *17*(1). https://doi.org/https://doi.org/10.1029/2001GB001824

Fleming, G. R., & Grondelle, R. v. (1994). The Primary Steps of Photosynthesis. *Physics Today*, *47*(2), 48-55. https://doi.org/10.1063/1.881413

Fourquez, M., Devez, A., Schaumann, A., Guéneuguès, A., Jouenne, T., Obernosterer, I., & Blain, S. (2014). Effects of iron limitation on growth and carbon metabolism in oceanic and coastal heterotrophic bacteria. *Limnology and Oceanography*, *59*(2), 349-360. https://doi.org/https://doi.org/10.4319/lo.2014.59.2.0349

Freese, J. M., & Lane, C. E. (2017). Parasitism finds many solutions to the same problems in red algae (Florideophyceae, Rhodophyta). *Molecular and Biochemical Parasitology*, *214*, 105-111. https://doi.org/https://doi.org/10.1016/j.molbiopara.2017.04.006

Fu, W., Shu, Y., Yi, Z., Su, Y., Pan, Y., Zhang, F., & Brynjolfsson, S. (2022). Diatom morphology and adaptation: Current progress and potentials for sustainable development. *Sustainable Horizons*, *2*, 100015. https://doi.org/https://doi.org/10.1016/j.horiz.2022.100015

Galaris, D., Barbouti, A., & Pantopoulos, K. (2019). Iron homeostasis and oxidative stress: An intimate relationship. *Biochimica et Biophysica Acta (BBA) - Molecular Cell Research*, *1866*(12), 118535. https://doi.org/https://doi.org/10.1016/j.bbamcr.2019.118535

Gao, X., Bowler, C., & Kazamia, E. (2021). Iron metabolism strategies in diatoms. *Journal of Experimental Botany*, *72*(6), 2165-2180. https://doi.org/10.1093/jxb/eraa575

Gheysen, G., Montagu, M. V., & Zambryski, P. (1987). Integration of Agrobacterium tumefaciens transfer DNA (T-DNA) involves rearrangements of target plant DNA sequences. *Proceedings of the National Academy of Sciences*, *84*(17), 6169-6173.

Gimeno, A., Zaragozá, R., Vivó-Sesé, I., Viña, J. R., & Miralles, V. J. (2004). Retinol, at concentrations greater than the physiological limit, induces oxidative stress and apoptosis in human dermal fibroblasts. *Exp Dermatol*, *13*(1), 45-54. https://doi.org/10.1111/j.0906-6705.2004.00112.x

Giovannoni, S. J., Bibbs, L., Cho, J.-C., Stapels, M. D., Desiderio, R., Vergin, K. L., Rappé, M. S., Laney, S., Wilhelm, L. J., Tripp, H. J., Mathur, E. J., & Barofsky, D. F. (2005). Proteorhodopsin in the ubiquitous marine bacterium SAR11. *Nature*, *438*(7064), 82-85. https://doi.org/10.1038/nature04032

Gledhill, M., & Buck, K. N. (2012). The organic complexation of iron in the marine environment: a review. *Front Microbiol*, *3*, 69. https://doi.org/10.3389/fmicb.2012.00069

Godínez-Hernández, Y., Anaya-López, J. L., Díaz-Plaza, R., González-Chavira, M., Torres-

Pacheco, I., Rivera-Bustamante, R. F., & Guevara-González, R. G. (2001). Characterization of resistance to pepper huasteco geminivirus in chili peppers from Yucatan, Mexico. *HortScience*, *36*(1), 139-142.

Gómez-Consarnau, L., Akram, N., Lindell, K., Pedersen, A., Neutze, R., Milton, D. L., González, J. M., & Pinhassi, J. (2010). Proteorhodopsin phototrophy promotes survival of marine bacteria during starvation. *PLoS Biol*, *8*(4), e1000358. https://doi.org/10.1371/journal.pbio.1000358

Gómez-Consarnau, L., González, J. M., Coll-Lladó, M., Gourdon, P., Pascher, T., Neutze, R., Pedrós-Alió, C., & Pinhassi, J. (2007). Light stimulates growth of proteorhodopsin-containing marine Flavobacteria. *Nature*, *445*(7124), 210-213. https://doi.org/10.1038/nature05381

Graf, S. (2011). Automated microinjection with integrated cell sorting, immobilization and collection.

Granum, E., Raven, J. A., & Leegood, R. C. (2005). How do marine diatoms fix 10 billion tonnes of inorganic carbon per year? *Canadian Journal of Botany*, *83*(7), 898-908. https://doi.org/10.1139/b05-077

Grigorieff, N., Ceska, T. A., Downing, K. H., Baldwin, J. M., & Henderson, R. (1996). Electron-crystallographic refinement of the structure of bacteriorhodopsin. *J Mol Biol*, *259*(3), 393-421. https://doi.org/10.1006/jmbi.1996.0328

Guillard, R. R., & Ryther, J. H. (1962). Studies of marine planktonic diatoms. I. Cyclotella nana Hustedt, and Detonula confervacea (cleve) Gran. *Can J Microbiol*, *8*, 229-239. https://doi.org/10.1139/m62-029

Guillard, R. R. L. (1973). *Division rates.* (1st ed.). ambridge University Press.

Guillard, R. R. L. (1975). Culture of Phytoplankton for Feeding Marine Invertebrates. In W. L. Smith & M. H. Chanley (Eds.), *Culture of Marine Invertebrate Animals: Proceedings — 1st Conference on Culture of Marine Invertebrate Animals Greenport* (pp. 29-60). Springer US. https://doi.org/10.1007/978-1-4615-8714-9_3

Guo, Z., Zhang, H., & Lin, S. (2014). Light-Promoted Rhodopsin Expression and Starvation

Survival in the Marine Dinoflagellate Oxyrrhis marina. *PLOS ONE*, *9*(12), e114941. https://doi.org/10.1371/journal.pone.0114941

Hadariová, L., Vesteg, M., Hampl, V., & Krajčovič, J. (2018). Reductive evolution of chloroplasts in non-photosynthetic plants, algae and protists. *Current Genetics*, *64*(2), 365-387. https://doi.org/10.1007/s00294-017-0761-0

Hider, R. C., & Kong, X. (2010). Chemistry and biology of siderophores. *Nat Prod Rep*, *27*(5), 637-657. https://doi.org/10.1039/b906679a

Hoff, W. D., Jung, K. H., & Spudich, J. L. (1997). Molecular mechanism of photosignaling by archaeal sensory rhodopsins. *Annu Rev Biophys Biomol Struct*, *26*, 223-258. https://doi.org/10.1146/annurev.biophys.26.1.223

Hoffmann, A., Hildebrandt, V., Heberle, J., & Büldt, G. (1994). Photoactive mitochondria: in vivo transfer of a light-driven proton pump into the inner mitochondrial membrane of Schizosaccharomyces pombe. *Proc Natl Acad Sci U S A*, *91*(20), 9367-9371. https://doi.org/10.1073/pnas.91.20.9367

Hofmann, M., & Schellnhuber, H.-J. (2009). Oceanic acidification affects marine carbon pump and triggers extended marine oxygen holes. *Proceedings of the National Academy of Sciences*, *106*(9), 3017-3022. https://doi.org/doi:10.1073/pnas.0813384106

Höhner, R., Aboukila, A., Kunz, H. H., & Venema, K. (2016). Proton Gradients and Proton-Dependent Transport Processes in the Chloroplast. *Front Plant Sci*, *7*, 218. https://doi.org/10.3389/fpls.2016.00218

Hopes, A. (2017). *Expanding the molecular toolbox in diatoms: developing a transformation system, CRISPR-Cas and Inverse Yeast-1-hybrid* University of East Anglia]. UEA.

Hopes, A., Nekrasov, V., Belshaw, N., Grouneva, I., Kamoun, S., & Mock, T. (2017). Genome Editing in Diatoms Using CRISPR-Cas to Induce Precise Bi-allelic Deletions. *Bio-protocol*, *7*(23), e2625. https://doi.org/10.21769/BioProtoc.2625

Hopes, A., Nekrasov, V., Kamoun, S., & Mock, T. (2016). Editing of the urease gene by CRISPR-Cas in the diatom Thalassiosira pseudonana. *Plant Methods*, *12*(1), 49.

https://doi.org/10.1186/s13007-016-0148-0

Hu, H., & Pan, Y. (2020). Electroporation Transformation Protocol for Phaeodactylum tricornutum. In S. Li, L. Chang, & J. Teissie (Eds.), *Electroporation Protocols: Microorganism, Mammalian System, and Nanodevice* (pp. 163-167). Springer US. https://doi.org/10.1007/978-1-4939-9740-4_17

Hull, P. M. (2017). Emergence of modern marine ecosystems. *Current Biology*, *27*(11), R466-R469. https://doi.org/https://doi.org/10.1016/j.cub.2017.04.041

Hunter, G. A., Al-Karadaghi, S., & Ferreira, G. C. (2011). FERROCHELATASE: THE CONVERGENCE OF THE PORPHYRIN BIOSYNTHESIS AND IRON TRANSPORT PATHWAYS. *J Porphyr Phthalocyanines*, *15*(5-6), 350-356. https://doi.org/10.1142/s108842461100332x

Hutchins, D. A., & Boyd, P. W. (2016). Marine phytoplankton and the changing ocean iron cycle. *Nature Climate Change*, *6*(12), 1072-1079. https://doi.org/10.1038/nclimate3147

Hutchins, D. A., & Bruland, K. W. (1998). Iron-limited diatom growth and Si:N uptake ratios in a coastal upwelling regime. *Nature*, *393*(6685), 561-564. https://doi.org/10.1038/31203

Ifuku, K., Yan, D., Miyahara, M., Inoue-Kashino, N., Yamamoto, Y. Y., & Kashino, Y. (2015). A stable and efficient nuclear transformation system for the diatom Chaetoceros gracilis. *Photosynthesis Research*, *123*(2), 203-211. https://doi.org/10.1007/s11120-014-0048-y

Janouškovec, J., Paskerova, G. G., Miroliubova, T. S., Mikhailov, K. V., Birley, T., Aleoshin, V. V., & Simdyanov, T. G. (2019). Apicomplexan-like parasites are polyphyletic and widely but selectively dependent on cryptic plastid organelles. *eLife*, *8*, e49662. https://doi.org/10.7554/eLife.49662

Jiang, H.-B., Hutchins, D. A., Zhang, H.-R., Feng, Y.-Y., Zhang, R.-F., Sun, W.-W., Ma, W., Bai, Y., Wells, M., He, D., Jiao, N., Wang, Y., & Chai, F. (2024). Complexities of regulating climate by promoting marine primary production with ocean iron

fertilization. *Earth-Science Reviews*, *249*, 104675. https://doi.org/https://doi.org/10.1016/j.earscirev.2024.104675

Jiang, J., Cheong, K. Y., Falkowski, P. G., & Dai, W. (2021). Integrating on-grid immunogold labeling and cryo-electron tomography to reveal photosystem II structure and spatial distribution in thylakoid membranes. *J Struct Biol*, *213*(3), 107746. https://doi.org/10.1016/j.jsb.2021.107746

Jin, X., Gruber, N., Dunne, J. P., Sarmiento, J. L., & Armstrong, R. A. (2006). Diagnosing the contribution of phytoplankton functional groups to the production and export of particulate organic carbon, CaCO3, and opal from global nutrient and alkalinity distributions. *Global Biogeochemical Cycles*, *20*(2). https://doi.org/https://doi.org/10.1029/2005GB002532

Jinek, M., Chylinski, K., Fonfara, I., Hauer, M., Doudna, J. A., & Charpentier, E. (2012). A Programmable Dual-RNA–Guided DNA Endonuclease in Adaptive Bacterial Immunity. *Science*, *337*(6096), 816-821. https://doi.org/doi:10.1126/science.1225829

Johnson, Matthew P. (2016). Photosynthesis. *Essays in Biochemistry*, *60*(3), 255-273. https://doi.org/10.1042/ebc20160016

Jumper, J., Evans, R., Pritzel, A., Green, T., Figurnov, M., Ronneberger, O., Tunyasuvunakool, K., Bates, R., Žídek, A., Potapenko, A., Bridgland, A., Meyer, C., Kohl, S. A. A., Ballard, A. J., Cowie, A., Romera-Paredes, B., Nikolov, S., Jain, R., Adler, J., . . . Hassabis, D. (2021). Highly accurate protein structure prediction with AlphaFold. *Nature*, *596*(7873), 583-589. https://doi.org/10.1038/s41586-021-03819-2

Kamikawa, R., Mochizuki, T., Sakamoto, M., Tanizawa, Y., Nakayama, T., Onuma, R., Cenci, U., Moog, D., Speak, S., Sarkozi, K., Toseland, A., van Oosterhout, C., Oyama, K., Kato, M., Kume, K., Kayama, M., Azuma, T., Ishii, K.-i., Miyashita, H., . . . Nakamura, Y. (2022). Genome evolution of a nonparasitic secondary heterotroph, the diatom Nitzschia putrida. *Science Advances*, *8*(17), eabi5075. https://doi.org/doi:10.1126/sciadv.abi5075

Kamikawa, R., Yubuki, N., Yoshida, M., Taira, M., Nakamura, N., Ishida, K.-i., Leander, B.

S., Miyashita, H., Hashimoto, T., Mayama, S., & Inagaki, Y. (2015). Multiple losses of photosynthesis in itzschia (Bacillariophyceae). *Phycological Research*, *63*(1), 19-28. https://doi.org/https://doi.org/10.1111/pre.12072

Kappler, A., Bryce, C., Mansor, M., Lueder, U., Byrne, J. M., & Swanner, E. D. (2021). An evolving view on biogeochemical cycling of iron. *Nature Reviews Microbiology*, *19*(6), 360-374. https://doi.org/10.1038/s41579-020-00502-7

Karas, B. J., Diner, R. E., Lefebvre, S. C., McQuaid, J., Phillips, A. P. R., Noddings, C. M., Brunson, J. K., Valas, R. E., Deerinck, T. J., Jablanovic, J., Gillard, J. T. F., Beeri, K., Ellisman, M. H., Glass, J. I., Hutchison Iii, C. A., Smith, H. O., Venter, J. C., Allen, A. E., Dupont, C. L., & Weyman, P. D. (2015). Designer diatom episomes delivered by bacterial conjugation. *Nature Communications*, *6*(1), 6925. https://doi.org/10.1038/ncomms7925

Karasuyama, M., Inoue, K., Nakamura, R., Kandori, H., & Takeuchi, I. (2018). Understanding Colour Tuning Rules and Predicting Absorption Wavelengths of Microbial Rhodopsins by Data-Driven Machine-Learning Approach. *Scientific Reports*, *8*(1), 15580. https://doi.org/10.1038/s41598-018-33984-w

Kautsky, H., & Hirsch, A. (1931). Neue versuche zur kohlensäureassimilation. *Naturwissenschaften*, *19*(48), 964-964.

Kazamia, E., Sutak, R., Paz-Yepes, J., Dorrell, R. G., Vieira, F. R. J., Mach, J., Morrissey, J., Leon, S., Lam, F., & Pelletier, E. (2018). Endocytosis-mediated siderophore uptake as a strategy for Fe acquisition in diatoms. *Science Advances*, *4*(5), eaar4536.

Kim, W., Mirdita, M., Karin, E. L., Gilchrist, C., Schweke, H., Söding, J., Levy, E., & Steinegger, M. (2024). Rapid and Sensitive Protein Complex Alignment with Foldseek-Multimer. *bioRxiv*, 2024.2004.2014.589414. https://doi.org/10.1101/2024.04.14.589414

Kirkham, A. R., Richthammer, P., Schmidt, K., Wustmann, M., Maeda, Y., Hedrich, R., Brunner, E., Tanaka, T., van Pée, K.-H., & Falciatore, A. (2017). A role for the cell-wall protein silacidin in cell size of the diatom Thalassiosira pseudonana. *The ISME*

*Journal*, *11*(11), 2452-2464.

Klunder, M. B., Bauch, D., Laan, P., de Baar, H. J. W., van Heuven, S., & Ober, S. (2012). Dissolved iron in the Arctic shelf seas and surface waters of the central Arctic Ocean: Impact of Arctic river water and ice-melt. *Journal of Geophysical Research: Oceans*, *117*(C1). https://doi.org/https://doi.org/10.1029/2011JC007133

Kosman, D. J. (2003). Molecular mechanisms of iron uptake in fungi. *Molecular microbiology*, *47*(5), 1185-1197.

Kraemer, S. M. (2004). Iron oxide dissolution and solubility in the presence of siderophores. *Aquatic Sciences*, *66*(1), 3-18. https://doi.org/10.1007/s00027-003-0690-5

Kramer, J., Özkaya, Ö., & Kümmerli, R. (2020). Bacterial siderophores in community and host interactions. *Nature Reviews Microbiology*, *18*(3), 152-163. https://doi.org/10.1038/s41579-019-0284-4

Kroth, P. (2007). Molecular Biology and the Biotechnological Potential of Diatoms. In R. León, A. Galván, & E. Fernández (Eds.), *Transgenic Microalgae as Green Cell Factories* (pp. 23-33). Springer New York. https://doi.org/10.1007/978-0-387-75532-8_3

Kustka, A. B., Allen, A. E., & Morel, F. M. (2007). Sequence analysis and transcriptional regulation of iron acquisition genes in two marine diatoms 1. *Journal of Phycology*, *43*(4), 715-729.

Kustka, A. B., Sañudo-Wilhelmy, S. A., Carpenter, E. J., Capone, D., Burns, J., & Sunda, W. G. (2003). Iron requirements for dinitrogen- and ammonium-supported growth in cultures of Trichodesmium (IMS 101): Comparison with nitrogen fixation rates and iron: carbon ratios of field populations. *Limnology and Oceanography*, *48*(5), 1869-1884. https://doi.org/https://doi.org/10.4319/lo.2003.48.5.1869

Kuypers, M. M. M., Marchant, H. K., & Kartal, B. (2018). The microbial nitrogen-cycling network. *Nature Reviews Microbiology*, *16*(5), 263-276. https://doi.org/10.1038/nrmicro.2018.9

Lanquar, V., Lelièvre, F., Bolte, S., Hamès, C., Alcon, C., Neumann, D., Vansuyt, G., Curie,

C., Schröder, A., & Krämer, U. (2005). Mobilization of vacuolar iron by AtNRAMP3 and AtNRAMP4 is essential for seed germination on low iron. *The EMBO journal*, *24*(23), 4041-4051.

Lanyi, J. K., & Balashov, S. P. (2008). Xanthorhodopsin: A bacteriorhodopsin-like proton pump with a carotenoid antenna. *Biochimica et Biophysica Acta (BBA) - Bioenergetics*, *1777*(7), 684-688. https://doi.org/https://doi.org/10.1016/j.bbabio.2008.05.005

Lemaitre, N., Planquette, H., Dehairs, F., van der Merwe, P., Bowie, A. R., Trull, T. W., Laurenceau-Cornec, E. C., Davies, D., Bollinger, C., Le Goff, M., Grossteffan, E., & Planchon, F. (2016). Impact of the natural Fe-fertilization on the magnitude, stoichiometry and efficiency of particulate biogenic silica, nitrogen and iron export fluxes. *Deep Sea Research Part I: Oceanographic Research Papers*, *117*, 11-27. https://doi.org/https://doi.org/10.1016/j.dsr.2016.09.002

Letunic, I., & Bork, P. (2024). Interactive Tree of Life (iTOL) v6: recent updates to the phylogenetic tree display and annotation tool. *Nucleic Acids Research*, *52*(W1), W78-W82. https://doi.org/10.1093/nar/gkae268

Lewin, J., & Lewin, R. A. (1967). Culture and Nutrition of Some Apochlorotic Diatoms of the Genus Nitzschia. *Microbiology*, *46*(3), 361-367. https://doi.org/https://doi.org/10.1099/00221287-46-3-361

Li, C.-W., & Volcani, B. E. (1987). Four new apochlorotic diatoms. *British Phycological Journal*, *22*(4), 375-382. https://doi.org/10.1080/00071618700650441

Li, H. Y., Lu, Y., Zheng, J. W., Yang, W. D., & Liu, J. S. (2014). Biochemical and genetic engineering of diatoms for polyunsaturated fatty acid biosynthesis. *Mar Drugs*, *12*(1), 153-166. https://doi.org/10.3390/md12010153

Li, Y., Almassalha, L. M., Chandler, J. E., Zhou, X., Stypula-Cyrus, Y. E., Hujsak, K. A., Roth, E. W., Bleher, R., Subramanian, H., & Szleifer, I. (2017). The effects of chemical fixation on the cellular nanostructure. *Experimental cell research*, *358*(2), 253-259.

Lin, S. (2023). Phosphate limitation and ocean acidification co-shape phytoplankton physiology and community structure. *Nature Communications*, *14*(1), 2699. https://doi.org/10.1038/s41467-023-38381-0

Lin, S., Zhang, H., Zhuang, Y., Tran, B., & Gill, J. (2010). Spliced leader–based metatranscriptomic analyses lead to recognition of hidden genomic features in dinoflagellates. *Proceedings of the National Academy of Sciences*, *107*(46), 20033-20038. https://doi.org/doi:10.1073/pnas.1007246107

Litchman, E., Klausmeier, C. A., Schofield, O. M., & Falkowski, P. G. (2007). The role of functional traits and trade-offs in structuring phytoplankton communities: scaling from cellular to ecosystem level. *Ecology Letters*, *10*(12), 1170-1181. https://doi.org/https://doi.org/10.1111/j.1461-0248.2007.01117.x

Litchman, E., Klausmeier, C. A., & Yoshiyama, K. (2009). Contrasting size evolution in marine and freshwater diatoms. *Proceedings of the National Academy of Sciences*, *106*(8), 2665-2670. https://doi.org/doi:10.1073/pnas.0810891106

Liu, X., & Theil, E. C. (2005). Ferritins: dynamic management of biological iron and oxygen chemistry. *Accounts of chemical research*, *38*(3), 167-175.

Liu, Y., Beyer, A., & Aebersold, R. (2016). On the Dependency of Cellular Protein Levels on mRNA Abundance. *Cell*, *165*(3), 535-550. https://doi.org/https://doi.org/10.1016/j.cell.2016.03.014

Lokstein, H., Renger, G., & Götze, J. P. (2021). Photosynthetic Light-Harvesting (Antenna) Complexes-Structures and Functions. *Molecules*, *26*(11). https://doi.org/10.3390/molecules26113378

Ludwig, C., Claassen, M., Schmidt, A., & Aebersold, R. (2012). Estimation of Absolute Protein Quantities of Unlabeled Samples by Selected Reaction Monitoring Mass Spectrometry*. *Molecular & Cellular Proteomics*, *11*(3), M111.013987. https://doi.org/https://doi.org/10.1074/mcp.M111.013987

Ma, M., Li, H., Wang, C., Li, T., Wang, J., Yuan, H., Yu, L., Wang, J., Li, L., & Lin, S. (2023). A comparative study reveals the relative importance of prokaryotic and eukaryotic

proton pump rhodopsins in a subtropical marginal sea. *ISME communications*, *3*(1), 79.

Maldonado, M. T., & Price, N. M. (1996). Influence of N substrate on Fe requirements of marine centric diatoms. *Marine Ecology Progress Series*, *141*, 161-172. https://www.int-res.com/abstracts/meps/v141/p161-172/

Malviya, S., Scalco, E., Audic, S., Vincent, F., Veluchamy, A., Poulain, J., Wincker, P., Iudicone, D., de Vargas, C., Bittner, L., Zingone, A., & Bowler, C. (2016). Insights into global diatom distribution and diversity in the world's ocean. *Proceedings of the National Academy of Sciences*, *113*(11), E1516-E1525. https://doi.org/doi:10.1073/pnas.1509523113

Man, D., Wang, W., Sabehi, G., Aravind, L., Post, A. F., Massana, R., Spudich, E. N., Spudich, J. L., & Béjà, O. (2003). Diversification and spectral tuning in marine proteorhodopsins. *The EMBO journal*, *22*(8), 1725-1731. https://doi.org/https://doi.org/10.1093/emboj/cdg183

Mann, D. G., & Vanormelingen, P. (2013). An Inordinate Fondness? The Number, Distributions, and Origins of Diatom Species. *Journal of Eukaryotic Microbiology*, *60*(4), 414-420. https://doi.org/https://doi.org/10.1111/jeu.12047

Marañón, E., Cermeño, P., López-Sandoval, D. C., Rodríguez-Ramos, T., Sobrino, C., Huete-Ortega, M., Blanco, J. M., & Rodríguez, J. (2013). Unimodal size scaling of phytoplankton growth and the size dependence of nutrient uptake and use. *Ecology Letters*, *16*(3), 371-379. https://doi.org/https://doi.org/10.1111/ele.12052

Marchetti, A., Catlett, D., Hopkinson, B. M., Ellis, K., & Cassar, N. (2015). Marine diatom proteorhodopsins and their potential role in coping with low iron availability. *The ISME Journal*, *9*(12), 2745-2748. https://doi.org/10.1038/ismej.2015.74

Marchetti, A., & Harrison, P. J. (2007). Coupled changes in the cell morphology and elemental (C, N, and Si) composition of the pennate diatom Pseudo-nitzschia due to iron deficiency. *Limnology and Oceanography*, *52*(5), 2270-2284. https://doi.org/https://doi.org/10.4319/lo.2007.52.5.2270

Marchetti, A., Maldonado, M. T., Lane, E. S., & Harrison, P. J. (2006). Iron requirements of the pennate diatom Pseudo-nitzschia: Comparison of oceanic (high-nitrate, low-chlorophyll waters) and coastal species. *Limnology and Oceanography*, *51*(5), 2092-2101. https://doi.org/https://doi.org/10.4319/lo.2006.51.5.2092

Marchetti, A., Parker, M. S., Moccia, L. P., Lin, E. O., Arrieta, A. L., Ribalet, F., Murphy, M. E., Maldonado, M. T., & Armbrust, E. V. (2009). Ferritin is used for iron storage in bloom-forming marine pennate diatoms. *Nature*, *457*(7228), 467-470.

Marchetti, A., Schruth, D. M., Durkin, C. A., Parker, M. S., Kodner, R. B., Berthiaume, C. T., Morales, R., Allen, A. E., & Armbrust, E. V. (2012). Comparative metatranscriptomics identifies molecular bases for the physiological responses of phytoplankton to varying iron availability. *Proceedings of the National Academy of Sciences*, *109*(6), E317-E325. https://doi.org/doi:10.1073/pnas.1118408109

Martin, J. H. (1990). Glacial-interglacial CO2 change: The Iron Hypothesis. *Paleoceanography*, *5*(1), 1-13. https://doi.org/https://doi.org/10.1029/PA005i001p00001

Martin, J. H., Coale, K. H., Johnson, K. S., Fitzwater, S. E., Gordon, R. M., Tanner, S. J., Hunter, C. N., Elrod, V. A., Nowicki, J. L., Coley, T. L., Barber, R. T., Lindley, S., Watson, A. J., Van Scoy, K., Law, C. S., Liddicoat, M. I., Ling, R., Stanton, T., Stockel, J., . . . Tindale, N. W. (1994). Testing the iron hypothesis in ecosystems of the equatorial Pacific Ocean. *Nature*, *371*(6493), 123-129. https://doi.org/10.1038/371123a0

Martin, J. H., & Fitzwater, S. E. (1988). Iron deficiency limits phytoplankton growth in the north-east Pacific subarctic. *Nature*, *331*(6154), 341-343. https://doi.org/10.1038/331341a0

Martin, J. H., Gordon, R. M., Fitzwater, S., & Broenkow, W. W. (1989). Vertex: phytoplankton/iron studies in the Gulf of Alaska. *Deep Sea Research Part A. Oceanographic Research Papers*, *36*(5), 649-680. https://doi.org/https://doi.org/10.1016/0198-0149(89)90144-1

Martinez, A., Bradley, A. S., Waldbauer, J. R., Summons, R. E., & DeLong, E. F. (2007). Proteorhodopsin photosystem gene expression enables photophosphorylation in a heterologous host. *Proceedings of the National Academy of Sciences*, *104*(13), 5590-5595. https://doi.org/doi:10.1073/pnas.0611470104

Matsuno-Yagi, A., & Mukohata, Y. (1977). Two possible roles of bacteriorhodopsin; a comparative study of strains of Halobacterium halobium differing in pigmentation. *Biochem Biophys Res Commun*, *78*(1), 237-243. https://doi.org/10.1016/0006-291x(77)91245-1

Maxwell, K., & Johnson, G. N. (2000). Chlorophyll fluorescence--a practical guide. *J Exp Bot*, *51*(345), 659-668. https://doi.org/10.1093/jxb/51.345.659

Meaking, W. S., Edgerton, J., Wharton, C. W., & Meldrum, R. A. (1995). Electroporation-induced damage in mammalian cell DNA. *Biochimica et Biophysica Acta (BBA) - Gene Structure and Expression*, *1264*(3), 357-362. https://doi.org/https://doi.org/10.1016/0167-4781(95)00177-8

Melis, A. (1999). Photosystem-II damage and repair cycle in chloroplasts: what modulates the rate of photodamage in vivo? *Trends in Plant Science*, *4*(4), 130-135. https://doi.org/https://doi.org/10.1016/S1360-1385(99)01387-4

Meyerink, S. W., Ellwood, M. J., Maher, W. A., Dean Price, G., & Strzepek, R. F. (2017). Effects of iron limitation on silicon uptake kinetics and elemental stoichiometry in two Southern Ocean diatoms, Eucampia antarctica and Proboscia inermis, and the temperate diatom Thalassiosira pseudonana. *Limnology and Oceanography*, *62*(6), 2445-2462. https://doi.org/https://doi.org/10.1002/lno.10578

Milligan, A. J., & Harrison, P. J. (2000). Effects of non-steady-state iron limitation on nitrogen assimilatory enzymes in the marine diatom thalassiosira weissflogii (BACILLARIOPHYCEAE). *Journal of Phycology*, *36*(1), 78-86. https://doi.org/https://doi.org/10.1046/j.1529-8817.2000.99013.x

Mirkovic, T., Ostroumov, E. E., Anna, J. M., van Grondelle, R., Govindjee, & Scholes, G. D. (2017). Light Absorption and Energy Transfer in the Antenna Complexes of

Photosynthetic Organisms. *Chemical Reviews*, *117*(2), 249-293. https://doi.org/10.1021/acs.chemrev.6b00002

Miyagawa, A., Okami, T., Kira, N., Yamaguchi, H., Ohnishi, K., & Adachi, M. (2009). Research note: High efficiency transformation of the diatom Phaeodactylum tricornutum with a promoter from the diatom Cylindrotheca fusiformis. *Phycological Research*, *57*(2), 142-146. https://doi.org/https://doi.org/10.1111/j.1440-1835.2009.00531.x

Mock T, O. R., Strauss J, McMullan M, Paajanen P, Schmutz J, Salamov A, Sanges R, Toseland A, Ward BJ, Allen AE, Dupont CL, Frickenhaus S, Maumus F, Veluchamy A, Wu T, Barry KW, Falciatore A, Ferrante MI, Fortunato AE, Glöckner G, Gruber A, Hipkin R, Janech MG, Kroth PG, Leese F, Lindquist EA, Lyon BR, Martin J, Mayer C, Parker M, Quesneville H, Raymond JA, Uhlig C, Valas RE, Valentin KU, Worden AZ, Armbrust EV, Clark MD, Bowler C, Green BR, Moulton V, van Oosterhout C, Grigoriev IV. (2008). *JGI-Fragilariopsis cylindrus CCMP 1102*. https://mycocosm.jgi.doe.gov/Fracy1/Fracy1.home.html

Mock, T., Otillar, R. P., Strauss, J., McMullan, M., Paajanen, P., Schmutz, J., Salamov, A., Sanges, R., Toseland, A., & Ward, B. J. (2017). Evolutionary genomics of the cold-adapted diatom Fragilariopsis cylindrus. *Nature*, *541*(7638), 536-540.

Mock, T., Samanta, M. P., Iverson, V., Berthiaume, C., Robison, M., Holtermann, K., Durkin, C., BonDurant, S. S., Richmond, K., Rodesch, M., Kallas, T., Huttlin, E. L., Cerrina, F., Sussman, M. R., & Armbrust, E. V. (2008). Whole-genome expression profiling of the marine diatom Thalassiosira pseudonana identifies genes involved in silicon bioprocesses. *Proceedings of the National Academy of Sciences*, *105*(5), 1579-1584. https://doi.org/10.1073/pnas.0707946105

Mock, T., & Thomas, D. (2008). Microalgae in Polar Regions: Linking Functional Genomics and Physiology with Environmental Conditions. In (pp. 285-312). https://doi.org/10.1007/978-3-540-74335-4_17

Moore, C. M., Mills, M. M., Achterberg, E. P., Geider, R. J., LaRoche, J., Lucas, M. I.,

McDonagh, E. L., Pan, X., Poulton, A. J., Rijkenberg, M. J. A., Suggett, D. J., Ussher, S. J., & Woodward, E. M. S. (2009). Large-scale distribution of Atlantic nitrogen fixation controlled by iron availability. *Nature Geoscience*, *2*(12), 867-871. https://doi.org/10.1038/ngeo667

Moore, C. M., Mills, M. M., Arrigo, K. R., Berman-Frank, I., Bopp, L., Boyd, P. W., Galbraith, E. D., Geider, R. J., Guieu, C., Jaccard, S. L., Jickells, T. D., La Roche, J., Lenton, T. M., Mahowald, N. M., Marañón, E., Marinov, I., Moore, J. K., Nakatsuka, T., Oschlies, A., . . . Ulloa, O. (2013). Processes and patterns of oceanic nutrient limitation. *Nature Geoscience*, *6*(9), 701-710. https://doi.org/10.1038/ngeo1765

Moore, J. K., & Braucher, O. (2008). Sedimentary and mineral dust sources of dissolved iron to the world ocean. *Biogeosciences*, *5*(3), 631-656. https://doi.org/10.5194/bg-5-631-2008

Moore, J. K., Doney, S. C., Glover, D. M., & Fung, I. Y. (2001). Iron cycling and nutrient-limitation patterns in surface waters of the World Ocean. *Deep Sea Research Part II: Topical Studies in Oceanography*, *49*(1), 463-507. https://doi.org/https://doi.org/10.1016/S0967-0645(01)00109-6

Moosburner, M. A., Gholami, P., McCarthy, J. K., Tan, M., Bielinski, V. A., & Allen, A. E. (2020). Multiplexed Knockouts in the Model Diatom Phaeodactylum by Episomal Delivery of a Selectable Cas9 [Methods]. *Frontiers in Microbiology*, *11*. https://doi.org/10.3389/fmicb.2020.00005

Moreira, L. O., Andrade, A. F., Vale, M. D., Souza, S. M., Hirata, R., Jr., Asad, L. M., Asad, N. R., Monteiro-Leal, L. H., Previato, J. O., & Mattos-Guaraldi, A. L. (2003). Effects of iron limitation on adherence and cell surface carbohydrates of Corynebacterium diphtheriae strains. *Appl Environ Microbiol*, *69*(10), 5907-5913. https://doi.org/10.1128/aem.69.10.5907-5913.2003

Mori, M., Hironaga, T., Kajiwara, H., Nakatani, N., Kozaki, D., Itabashi, H., & Tanaka, K. (2011). Use of a polystyrene-divinylbenzene-based weakly acidic cation-exchange resin column and propionic acid as an eluent in ion-exclusion/adsorption

chromatography of aliphatic carboxylic acids and ethanol in food samples. *Anal Sci*, *27*(5), 505. https://doi.org/10.2116/analsci.27.505

Muggli, D. L., Maude, L., & Harrison, P. J. (1996). Effects of iron and nitrogen source on the sinking rate, physiology and metal composition of an oceanic diatom from the subarctic Pacific. *Marine Ecology Progress Series*, *132*, 215-227.

Muhire, B. M., Booker, M. A., & Tolstorukov, M. Y. (2019). Non-neutral evolution of H3.3-encoding genes occurs without alterations in protein sequence. *Scientific Reports*, *9*(1), 8472. https://doi.org/10.1038/s41598-019-44800-4

Murata, M., & Kawanishi, S. (2000). Oxidative DNA Damage by Vitamin A and Its Derivative via Superoxide Generation*. *Journal of Biological Chemistry*, *275*(3), 2003-2008. https://doi.org/https://doi.org/10.1074/jbc.275.3.2003

Murata, N., Takahashi, S., Nishiyama, Y., & Allakhverdiev, S. I. (2007). Photoinhibition of photosystem II under environmental stress. *Biochimica et Biophysica Acta (BBA) - Bioenergetics*, *1767*(6), 414-421. https://doi.org/https://doi.org/10.1016/j.bbabio.2006.11.019

Murik, O., Tirichine, L., Prihoda, J., Thomas, Y., Araújo, W. L., Allen, A. E., Fernie, A. R., & Bowler, C. (2019). Downregulation of mitochondrial alternative oxidase affects chloroplast function, redox status and stress response in a marine diatom. *New Phytologist*, *221*(3), 1303-1316. https://doi.org/https://doi.org/10.1111/nph.15479

Muto, M., Fukuda, Y., Nemoto, M., Yoshino, T., Matsunaga, T., & Tanaka, T. (2013). Establishment of a Genetic Transformation System for the Marine Pennate Diatom Fistulifera sp. Strain JPCC DA0580—A High Triglyceride Producer. *Marine Biotechnology*, *15*(1), 48-55. https://doi.org/10.1007/s10126-012-9457-0

Nacry, P., Camilleri, C., Courtial, B., Caboche, M., & Bouchez, D. (1998). Major chromosomal rearrangements induced by T-DNA transformation in Arabidopsis. *Genetics*, *149*(2), 641-650.

Nakayama, M. (1998). Levels of Major Proteins of Halobacterium halobium During Growth at Different Temperatures. *大阪教育大学紀要 第 III 部門：自然科学*, *47*(1), 83-92.

https://doi.org/10.32287/td00003320

Nolan, T., Hands, R. E., & Bustin, S. A. (2006). Quantification of mRNA using real-time RT-PCR. *Nature Protocols*, *1*(3), 1559-1582. https://doi.org/10.1038/nprot.2006.236

Nuester, J., Vogt, S., & Twining, B. S. (2012). LOCALIZATION OF IRON WITHIN CENTRIC DIATOMS OF THE GENUS THALASSIOSIRA 1. *Journal of Phycology*, *48*(3), 626-634.

Nunn, B. L., Faux, J. F., Hippmann, A. A., Maldonado, M. T., Harvey, H. R., Goodlett, D. R., Boyd, P. W., & Strzepek, R. F. (2013). Diatom Proteomics Reveals Unique Acclimation Strategies to Mitigate Fe Limitation. *PLOS ONE*, *8*(10), e75653. https://doi.org/10.1371/journal.pone.0075653

Oesterhelt, D., & Stoeckenius, W. (1971). Rhodopsin-like protein from the purple membrane of Halobacterium halobium. *Nature new biology*, *233*(39), 149-152.

Oesterhelt, D., & Stoeckenius, W. (1973). Functions of a New Photoreceptor Membrane. *Proceedings of the National Academy of Sciences*, *70*(10), 2853-2857. https://doi.org/doi:10.1073/pnas.70.10.2853

Okada, K., Morimoto, Y., Shiraishi, Y., Tamura, T., Mayama, S., Kadono, T., Adachi, M., Ifuku, K., & Nemoto, M. (2023). Nuclear Transformation of the Marine Pennate Diatom Nitzschia sp. Strain NIES-4635 by Multi-Pulse Electroporation. *Marine Biotechnology*, *25*(6), 1208-1219. https://doi.org/10.1007/s10126-023-10273-w

Ong, S.-E., Blagoev, B., Kratchmarova, I., Kristensen, D. B., Steen, H., Pandey, A., & Mann, M. (2002). Stable Isotope Labeling by Amino Acids in Cell Culture, SILAC, as a Simple and Accurate Approach to Expression Proteomics*. *Molecular & Cellular Proteomics*, *1*(5), 376-386. https://doi.org/https://doi.org/10.1074/mcp.M200025-MCP200

Parkhill, J.-P., Maillet, G., & Cullen, J. J. (2001). FLUORESCENCE-BASED MAXIMAL QUANTUM YIELD FOR PSII AS A DIAGNOSTIC OF NUTRIENT STRESS. *Journal of Phycology*, *37*(4), 517-529. https://doi.org/https://doi.org/10.1046/j.1529-8817.2001.037004517.x

Paytan, A., & McLaughlin, K. (2007). The Oceanic Phosphorus Cycle. *Chemical Reviews*, *107*(2), 563-576. https://doi.org/10.1021/cr0503613

Pechkova, E., Bragazzi, N. L., & Nicolini, C. (2014). Chapter Five - Advances in Nanocrystallography as a Proteomic Tool. In R. Donev (Ed.), *Advances in Protein Chemistry and Structural Biology* (Vol. 95, pp. 163-191). Academic Press. https://doi.org/https://doi.org/10.1016/B978-0-12-800453-1.00005-1

Peers, G., & Price, N. M. (2006). Copper-containing plastocyanin used for electron transport by an oceanic diatom. *Nature*, *441*(7091), 341-344. https://doi.org/10.1038/nature04630

Petersen, J. B. (1928). *The aerial algae of Iceland*. Frimodt.

Pfaffen, S., Bradley, J. M., Abdulqadir, R., Firme, M. R., Moore, G. R., Le Brun, N. E., & Murphy, M. E. (2015). A diatom ferritin optimized for iron oxidation but not iron storage. *Journal of Biological Chemistry*, *290*(47), 28416-28427.

Pichersky, E., Hoffman, N. E., Bernatzky, R., Piechulla, B., Tanksley, S. D., & Cashmore, A. R. (1987). Molecular characterization and genetic mapping of DNA sequences encoding the Type I chlorophyll a/b-binding polypeptide of photosystem I in Lycopersicon esculentum (tomato). *Plant Mol Biol*, *9*(3), 205-216. https://doi.org/10.1007/bf00166457

Pichevin, L. E., Ganeshram, R. S., Geibert, W., Thunell, R., & Hinton, R. (2014). Silica burial enhanced by iron limitation in oceanic upwelling margins. *Nature Geoscience*, *7*(7), 541-546. https://doi.org/10.1038/ngeo2181

Poulíčková, A., Mann, D. G., & Mann, D. G. (2019). Diatom Sexual Reproduction and Life Cycles. In *Diatoms: Fundamentals and Applications* (pp. 245-272). https://doi.org/https://doi.org/10.1002/9781119370741.ch11

Poulsen, N., Chesley, P. M., & Kröger, N. (2006). Molecular genetic manipulation of the diatom Thalassiosira pseudonana (Bacillariophyceae) 1. *Journal of Phycology*, *42*(5), 1059-1065.

Poulsen, N., & Kröger, N. (2023). Thalassiosira pseudonana (Cyclotella nana) (Hustedt)

Hasle et Heimdal (Bacillariophyceae): A genetically tractable model organism for studying diatom biology, including biological silica formation. *Journal of Phycology*, *59*(5), 809-817. https://doi.org/https://doi.org/10.1111/jpy.13362

Price, N. M., Andersen, L. F., & Morel, F. M. M. (1991). Iron and nitrogen nutrition of equatorial Pacific plankton. *Deep Sea Research Part A. Oceanographic Research Papers*, *38*(11), 1361-1378. https://doi.org/https://doi.org/10.1016/0198-0149(91)90011-4

Raven, J. A. (1988). The iron and molybdenum use efficiencies of plant growth with different energy, carbon and nitrogen sources. *New Phytologist*, *109*(3), 279-287. https://doi.org/https://doi.org/10.1111/j.1469-8137.1988.tb04196.x

Raven, J. A. (1990). Predictions of Mn and Fe use efficiencies of phototrophic growth as a function of light availability for growth and of C assimilation pathway. *New Phytologist*, *116*(1), 1-18. https://doi.org/https://doi.org/10.1111/j.1469-8137.1990.tb00505.x

Raven, J. A. (2009). Functional evolution of photochemical energy transformations in oxygen-producing organisms. *Functional Plant Biology*, *36*(6), 505-515. https://doi.org/https://doi.org/10.1071/FP09087

Rijkenberg, M. J. A., Middag, R., Laan, P., Gerringa, L. J. A., van Aken, H. M., Schoemann, V., de Jong, J. T. M., & de Baar, H. J. W. (2014). The Distribution of Dissolved Iron in the West Atlantic Ocean. *PLOS ONE*, *9*(6), e101323. https://doi.org/10.1371/journal.pone.0101323

Roberts, C. J., Nothwehr, S. F., & Stevens, T. H. (1992). Membrane protein sorting in the yeast secretory pathway: evidence that the vacuole may be the default compartment. *The Journal of cell biology*, *119*(1), 69-83.

Roberts, K., Granum, E., Leegood, R. C., & Raven, J. A. (2007). Carbon acquisition by diatoms. *Photosynth Res*, *93*(1-3), 79-88. https://doi.org/10.1007/s11120-007-9172-2

Rue, E. L., & Bruland, K. W. (1995). Complexation of iron(III) by natural organic ligands in the Central North Pacific as determined by a new competitive ligand

equilibration/adsorptive cathodic stripping voltammetric method. *Marine Chemistry*, *50*(1), 117-138. https://doi.org/https://doi.org/10.1016/0304-4203(95)00031-L

Russo, E., Ianora, A., & Carotenuto, Y. (2018). Re-shaping marine plankton communities: effects of diatom oxylipins on copepods and beyond. *Marine Biology*, *166*(1), 9. https://doi.org/10.1007/s00227-018-3456-2

Rybak, J. M., Barker, K. S., Muñoz, J. F., Parker, J. E., Ahmad, S., Mokaddas, E., Abdullah, A., Elhagracy, R. S., Kelly, S. L., Cuomo, C. A., & Rogers, P. D. (2022). In vivo emergence of high-level resistance during treatment reveals the first identified mechanism of amphotericin B resistance in Candida auris. *Clinical Microbiology and Infection*, *28*(6), 838-843. https://doi.org/https://doi.org/10.1016/j.cmi.2021.11.024

Sabatino, V., Russo, M. T., Patil, S., d'Ippolito, G., Fontana, A., & Ferrante, M. I. (2015). Establishment of Genetic Transformation in the Sexually Reproducing Diatoms Pseudo-nitzschia multistriata and Pseudo-nitzschia arenysensis and Inheritance of the Transgene. *Marine Biotechnology*, *17*(4), 452-462. https://doi.org/10.1007/s10126-015-9633-0

Sabehi, G., Massana, R., Bielawski, J. P., Rosenberg, M., Delong, E. F., & Béjà, O. (2003). Novel Proteorhodopsin variants from the Mediterranean and Red Seas. *Environ Microbiol*, *5*(10), 842-849. https://doi.org/10.1046/j.1462-2920.2003.00493.x

Samukawa, M., Shen, C., Hopkinson, B. M., & Matsuda, Y. (2014). Localization of putative carbonic anhydrases in the marine diatom, Thalassiosira pseudonana. *Photosynthesis Research*, *121*(2), 235-249. https://doi.org/10.1007/s11120-014-9967-x

Sanyal, A., Larsson, J., van Wirdum, F., Andrén, T., Moros, M., Lönn, M., & Andrén, E. (2022). Not dead yet: Diatom resting spores can survive in nature for several millennia. *American Journal of Botany*, *109*(1), 67-82. https://doi.org/https://doi.org/10.1002/ajb2.1780

Savio, S., Farrotti, S., Paris, D., Arnaìz, E., Díaz, I., Bolado, S., Muñoz, R., Rodolfo, C., & Congestri, R. (2020). Value-added co-products from biomass of the diatoms Staurosirella pinnata and Phaeodactylum tricornutum. *Algal Research*, *47*, 101830.

https://doi.org/https://doi.org/10.1016/j.algal.2020.101830

Schaum, C.-E., Buckling, A., Smirnoff, N., Studholme, D., & Yvon-Durocher, G. (2018). Environmental fluctuations accelerate molecular evolution of thermal tolerance in a marine diatom. *Nature Communications*, *9*(1), 1719.

Sethi, D., Butler, T. O., Shuhaili, F., & Vaidyanathan, S. (2020). Diatoms for Carbon Sequestration and Bio-Based Manufacturing. *Biology (Basel)*, *9*(8). https://doi.org/10.3390/biology9080217

Sétif, P. (2001). Ferredoxin and flavodoxin reduction by photosystem I. *Biochimica et Biophysica Acta (BBA) - Bioenergetics*, *1507*(1), 161-179. https://doi.org/https://doi.org/10.1016/S0005-2728(01)00205-5

Sharma, N., Simon, D. P., Diaz-Garza, A. M., Fantino, E., Messaabi, A., Meddeb-Mouelhi, F., Germain, H., & Desgagné-Penix, I. (2021). Diatoms Biotechnology: Various Industrial Applications for a Greener Tomorrow [Review]. *Frontiers in Marine Science*, *8*. https://doi.org/10.3389/fmars.2021.636613

Shi, X., Gao, W., Chao, S. H., Zhang, W., & Meldrum, D. R. (2013). Monitoring the single-cell stress response of the diatom Thalassiosira pseudonana by quantitative real-time reverse transcription-PCR. *Appl Environ Microbiol*, *79*(6), 1850-1858. https://doi.org/10.1128/aem.03399-12

Shi, X., Li, L., Guo, C., Lin, X., Li, M., & Lin, S. (2015). Rhodopsin gene expression regulated by the light dark cycle, light spectrum and light intensity in the dinoflagellate Prorocentrum [Original Research]. *Frontiers in Microbiology*, *6*. https://doi.org/10.3389/fmicb.2015.00555

Sikosek, T., & Chan, H. S. (2014). Biophysics of protein evolution and evolutionary protein biophysics. *Journal of The Royal Society Interface*, *11*(100), 20140419. https://doi.org/doi:10.1098/rsif.2014.0419

Simkin, A. J., Kapoor, L., Doss, C. G. P., Hofmann, T. A., Lawson, T., & Ramamoorthy, S. (2022). The role of photosynthesis related pigments in light harvesting, photoprotection and enhancement of photosynthetic yield in planta. *Photosynth Res*,

*152*(1), 23-42. https://doi.org/10.1007/s11120-021-00892-6

Slamovits, C. H., Okamoto, N., Burri, L., James, E. R., & Keeling, P. J. (2011). A bacterial proteorhodopsin proton pump in marine eukaryotes. *Nature Communications*, *2*(1), 183. https://doi.org/10.1038/ncomms1188

Smetacek, V. (1999). Diatoms and the Ocean Carbon Cycle. *Protist*, *150*(1), 25-32. https://doi.org/https://doi.org/10.1016/S1434-4610(99)70006-4

Smetacek, V., Assmy, P., & Henjes, J. (2004). The role of grazing in structuring Southern Ocean pelagic ecosystems and biogeochemical cycles. *Antarctic Science*, *16*(4), 541-558. https://doi.org/10.1017/S0954102004002317

Smetacek, V., Klaas, C., Strass, V. H., Assmy, P., Montresor, M., Cisewski, B., Savoye, N., Webb, A., d'Ovidio, F., Arrieta, J. M., Bathmann, U., Bellerby, R., Berg, G. M., Croot, P., Gonzalez, S., Henjes, J., Herndl, G. J., Hoffmann, L. J., Leach, H., . . . Wolf-Gladrow, D. (2012). Deep carbon export from a Southern Ocean iron-fertilized diatom bloom. *Nature*, *487*(7407), 313-319. https://doi.org/10.1038/nature11229

Soole, K. L., Dry, I. B., & Wiskich, J. T. (1992). Partial Purification and Characterization of Complex I, NADH:Ubiquinone Reductase, from the Inner Membrane of Beetroot Mitochondria 1. *Plant Physiology*, *98*(2), 588-594. https://doi.org/10.1104/pp.98.2.588

Sprecher, B. N., Buck, J. M., Ropella, L. L., Ramsperger, A., Kroth, P. G., & Yamada, N. (2023). Genetic transformation methods for diatom Nitzschia captiva: New tools to better understand dinotom endosymbiosis. *Algal Research*, *72*, 103136. https://doi.org/https://doi.org/10.1016/j.algal.2023.103136

Spudich, J. L., Yang, C. S., Jung, K. H., & Spudich, E. N. (2000). Retinylidene proteins: structures and functions from archaea to humans. *Annu Rev Cell Dev Biol*, *16*, 365-392. https://doi.org/10.1146/annurev.cellbio.16.1.365

Stintzi, A., Barnes, C., Xu, J., & Raymond, K. N. (2000). Microbial iron transport via a siderophore shuttle: a membrane ion transport paradigm. *Proc Natl Acad Sci U S A*, *97*(20), 10691-10696. https://doi.org/10.1073/pnas.200318797

Strauss, J. (2012). *A genomic analysis using RNA-Seq to investigate the adaptation of the psychrophilic diatom Fragilariopsis cylindrus to the polar environment* University of East Anglia].

Strauss, J., Deng, L., Gao, S., Toseland, A., Bachy, C., Zhang, C., Kirkham, A., Hopes, A., Utting, R., Joest, E. F., Tagliabue, A., Löw, C., Worden, A. Z., Nagel, G., & Mock, T. (2023). Plastid-localized xanthorhodopsin increases diatom biomass and ecosystem productivity in iron-limited surface oceans. *Nature Microbiology*, *8*(11), 2050-2066. https://doi.org/10.1038/s41564-023-01498-5

Strzepek, R. F., Boyd, P. W., & Sunda, W. G. (2019). Photosynthetic adaptation to low iron, light, and temperature in Southern Ocean phytoplankton. *Proceedings of the National Academy of Sciences*, *116*, 4388 - 4393.

Strzepek, R. F., & Harrison, P. J. (2004). Photosynthetic architecture differs in coastal and oceanic diatoms. *Nature*, *431*(7009), 689-692. https://doi.org/10.1038/nature02954

Su, H., Yang, R., Zhang, A., & Li, Y. (2015). Dissolved iron distribution and organic complexation in the coastal waters of the East China Sea. *Marine Chemistry*, *173*, 208-221. https://doi.org/https://doi.org/10.1016/j.marchem.2015.03.007

Sugie, K., & Kuma, K. (2008). Resting spore formation in the marine diatom Thalassiosira nordenskioeldii under iron- and nitrogen-limited conditions. *Journal of Plankton Research*, *30*(11), 1245-1255. https://doi.org/10.1093/plankt/fbn080

Sunda, W. G., & Huntsman, S. A. (1995). Iron uptake and growth limitation in oceanic and coastal phytoplankton. *Marine Chemistry*, *50*(1-4), 189-206.

Sunda, W. G., & Huntsman, S. A. (1997). Interrelated influence of iron, light and cell size on marine phytoplankton growth. *Nature*, *390*(6658), 389-392. https://doi.org/10.1038/37093

Sunda, W. G., Price, N. M., & Morel, F. M. M. (2005). Trace metal ion buffers and their use in culture studies.

Sutak, R., Camadro, J.-M., & Lesuisse, E. (2020). Iron Uptake Mechanisms in Marine Phytoplankton [Review]. *Frontiers in Microbiology*, *11*.

https://doi.org/10.3389/fmicb.2020.566691

Tagliabue, A., Bowie, A. R., Boyd, P. W., Buck, K. N., Johnson, K. S., & Saito, M. A. (2017). The integral role of iron in ocean biogeochemistry. *Nature*, *543*(7643), 51-59. https://doi.org/10.1038/nature21058

Teasdale, R. D., & Jackson, M. R. (1996). Signal-mediated sorting of membrane proteins between the endoplasmic reticulum and the golgi apparatus. *Annual review of cell and developmental biology*, *12*(1), 27-54.

Theil, E. C. (1987). Ferritin: structure, gene regulation, and cellular function in animals, plants, and microorganisms. *Annual review of biochemistry*, *56*(1), 289-315.

Todd, A. E., Orengo, C. A., & Thornton, J. M. (2001). Evolution of function in protein superfamilies, from a structural perspective. *Journal of Molecular Biology*, *307*(4), 1113-1143.

Tortell, P. D., Maldonado, M. T., & Price, N. M. (1996). The role of heterotrophic bacteria in iron-limited ocean ecosystems. *Nature*, *383*(6598), 330-332. https://doi.org/10.1038/383330a0

Travella, S., Ross, S. M., Harden, J., Everett, C., Snape, J. W., & Harwood, W. A. (2005). A comparison of transgenic barley lines produced by particle bombardment and Agrobacterium-mediated techniques. *Plant Cell Reports*, *23*(12), 780-789. https://doi.org/10.1007/s00299-004-0892-x

Tréguer, P., Bowler, C., Moriceau, B., Dutkiewicz, S., Gehlen, M., Aumont, O., Bittner, L., Dugdale, R., Finkel, Z., Iudicone, D., Jahn, O., Guidi, L., Lasbleiz, M., Leblanc, K., Levy, M., & Pondaven, P. (2018). Influence of diatom diversity on the ocean biological carbon pump. *Nature Geoscience*, *11*(1), 27-37. https://doi.org/10.1038/s41561-017-0028-x

Trentacoste, E. M., Shrestha, R. P., Smith, S. R., Glé, C., Hartmann, A. C., Hildebrand, M., & Gerwick, W. H. (2013). Metabolic engineering of lipid catabolism increases microalgal lipid accumulation without compromising growth. *Proceedings of the National Academy of Sciences*, *110*(49), 19748-19753.

van Kempen, M., Kim, S. S., Tumescheit, C., Mirdita, M., Lee, J., Gilchrist, C. L. M., Söding, J., & Steinegger, M. (2024). Fast and accurate protein structure search with Foldseek. *Nature Biotechnology*, *42*(2), 243-246. https://doi.org/10.1038/s41587-023-01773-0

Varadi, M., Anyango, S., Deshpande, M., Nair, S., Natassia, C., Yordanova, G., Yuan, D., Stroe, O., Wood, G., Laydon, A., Žídek, A., Green, T., Tunyasuvunakool, K., Petersen, S., Jumper, J., Clancy, E., Green, R., Vora, A., Lutfi, M., . . . Velankar, S. (2021). AlphaFold Protein Structure Database: massively expanding the structural coverage of protein-sequence space with high-accuracy models. *Nucleic Acids Research*, *50*(D1), D439-D444. https://doi.org/10.1093/nar/gkab1061

Varadi, M., Bertoni, D., Magana, P., Paramval, U., Pidruchna, I., Radhakrishnan, M., Tsenkov, M., Nair, S., Mirdita, M., Yeo, J., Kovalevskiy, O., Tunyasuvunakool, K., Laydon, A., Žídek, A., Tomlinson, H., Hariharan, D., Abrahamson, J., Green, T., Jumper, J., . . . Velankar, S. (2023). AlphaFold Protein Structure Database in 2024: providing structure coverage for over 214 million protein sequences. *Nucleic Acids Research*, *52*(D1), D368-D375. https://doi.org/10.1093/nar/gkad1011

Vernet, M. (2009). *Reproduction in Antarctic Diatoms*. Retrieved 24 September 2024 from http://icestories.exploratorium.edu/dispatches/reproduction-in-antarctic-diatoms/index.html

Vernette, C., Lecubin, J., Sánchez, P., Coordinators, T. O., Sunagawa, S., Delmont, T. O., Acinas, S. G., Pelletier, E., Hingamp, P., & Lescot, M. (2022). The Ocean Gene Atlas v2.0: online exploration of the biogeography and phylogeny of plankton genes. *Nucleic Acids Research*, *50*(W1), W516-W526. https://doi.org/10.1093/nar/gkac420

Villar, E., Vannier, T., Vernette, C., Lescot, M., Cuenca, M., Alexandre, A., Bachelerie, P., Rosnet, T., Pelletier, E., Sunagawa, S., & Hingamp, P. (2018). The Ocean Gene Atlas: exploring the biogeography of plankton genes online. *Nucleic Acids Research*, *46*(W1), W289-W295. https://doi.org/10.1093/nar/gky376

Walker, J. E., Arizmendi, J. M., Dupuis, A., Fearnley, I. M., Finel, M., Medd, S. M., Pilkington, S. J., Runswick, M. J., & Skehel, J. M. (1992). Sequences of 20 subunits

of NADH: Ubiquinone oxidoreductase from bovine heart mitochondria: Application of a novel strategy for sequencing proteins using the polymerase chain reaction. *Journal of Molecular Biology*, *226*(4), 1051-1072. https://doi.org/https://doi.org/10.1016/0022-2836(92)91052-Q

Walter, J. M., Greenfield, D., Bustamante, C., & Liphardt, J. (2007). Light-powering Escherichia coli with proteorhodopsin. *Proc Natl Acad Sci U S A*, *104*(7), 2408-2412. https://doi.org/10.1073/pnas.0611035104

Wang, G., Huang, L., Zhuang, S., Han, F., Huang, Q., Hao, M., Lin, G., Chen, L., Shen, B., Li, F., Li, X., Chen, C., Gao, Y., Mock, T., & Liang, J. (2024). Resting cell formation in the marine diatom Thalassiosira pseudonana. *New Phytologist*, *243*(4), 1347-1360. https://doi.org/https://doi.org/10.1111/nph.19646

Wang, T., Sessions, A. O., Lunde, C. S., Rouhani, S., Glaeser, R. M., Duan, Y., & Facciotti, M. T. (2013). Deprotonation of D96 in bacteriorhodopsin opens the proton uptake pathway. *Structure*, *21*(2), 290-297. https://doi.org/10.1016/j.str.2012.12.018

Wang, W.-W., Sineshchekov, O. A., Spudich, E. N., & Spudich, J. L. (2003). Spectroscopic and Photochemical Characterization of a Deep Ocean Proteorhodopsin*. *Journal of Biological Chemistry*, *278*(36), 33985-33991. https://doi.org/https://doi.org/10.1074/jbc.M305716200

Weber, E., Engler, C., Gruetzner, R., Werner, S., & Marillonnet, S. (2011). A Modular Cloning System for Standardized Assembly of Multigene Constructs. *PLOS ONE*, *6*(2), e16765. https://doi.org/10.1371/journal.pone.0016765

Wells, M. L., Price, N. M., & Bruland, K. W. (1995). Iron chemistry in seawater and its relationship to phytoplankton: a workshop report. *Marine Chemistry*, *48*(2), 157-182. https://doi.org/https://doi.org/10.1016/0304-4203(94)00055-I

Wetz, M. S., Hales, B., Chase, Z., Wheeler, P. A., & Whitney, M. M. (2006). Riverine input of macronutrients, iron, and organic matter to the coastal ocean off Oregon, U.S.A., during the winter. *Limnology and Oceanography*, *51*(5), 2221-2231. https://doi.org/https://doi.org/10.4319/lo.2006.51.5.2221

Whittaker, S., Bidle, K. D., Kustka, A. B., & Falkowski, P. G. (2011). Quantification of nitrogenase in Trichodesmium IMS 101: implications for iron limitation of nitrogen fixation in the ocean. *Environmental Microbiology Reports*, *3*(1), 54-58. https://doi.org/https://doi.org/10.1111/j.1758-2229.2010.00187.x

Winkelmann, G. (1992). Structures and functions of fungal siderophores containing hydroxamate and complexone type iron binding ligands. *Mycological Research*, *96*(7), 529-534. https://doi.org/https://doi.org/10.1016/S0953-7562(09)80976-3

Wiśniewski, J. R., Hein, M. Y., Cox, J., & Mann, M. (2014). A "proteomic ruler" for protein copy number and concentration estimation without spike-in standards. *Mol Cell Proteomics*, *13*(12), 3497-3506. https://doi.org/10.1074/mcp.M113.037309

Wolfe-Simon, F., Grzebyk, D., Schofield, O., & Falkowski, P. G. (2005). THE ROLE AND EVOLUTION OF SUPEROXIDE DISMUTASES IN ALGAE1. *Journal of Phycology*, *41*(3), 453-465. https://doi.org/https://doi.org/10.1111/j.1529-8817.2005.00086.x

Wolfe-Simon, F., Starovoytov, V., Reinfelder, J. R., Schofield, O., & Falkowski, P. G. (2006). Localization and Role of Manganese Superoxide Dismutase in a Marine Diatom. *Plant Physiology*, *142*(4), 1701-1709. https://doi.org/10.1104/pp.106.088963

Yamashita, Y., Nishioka, J., Obata, H., & Ogawa, H. (2020). Shelf humic substances as carriers for basin-scale iron transport in the North Pacific. *Scientific Reports*, *10*(1), 4505. https://doi.org/10.1038/s41598-020-61375-7

Yang, J., & Zhang, Y. (2015). I-TASSER server: new development for protein structure and function predictions. *Nucleic Acids Res*, *43*(W1), W174-181. https://doi.org/10.1093/nar/gkv342

Yin, W., & Hu, H. (2021). High-efficiency transformation of a centric diatom Chaetoceros muelleri by electroporation with a variety of selectable markers. *Algal Research*, *55*, 102274. https://doi.org/https://doi.org/10.1016/j.algal.2021.102274

Yool, A., & Tyrrell, T. (2003). Role of diatoms in regulating the ocean's silicon cycle. *Global Biogeochemical Cycles*, *17*(4). https://doi.org/https://doi.org/10.1029/2002GB002018

Yoshizawa, S., Azuma, T., Kojima, K., Inomura, K., Hasegawa, M., Nishimura, Y., Kikuchi, M., Armin, G., Miyashita, H., Ifuku, K., Yamano, T., Marchetti, A., Fukuzawa, H., Sudo, Y., & Kamikawa, R. (2022). Proton-pumping rhodopsins in marine diatoms. *bioRxiv*, 2022.2001.2018.476826. https://doi.org/10.1101/2022.01.18.476826

Yoshizawa, S., Azuma, T., Kojima, K., Inomura, K., Hasegawa, M., Nishimura, Y., Kikuchi, M., Armin, G., Tsukamoto, Y., Miyashita, H., Ifuku, K., Yamano, T., Marchetti, A., Fukuzawa, H., Sudo, Y., & Kamikawa, R. (2023). Light-driven Proton Pumps as a Potential Regulator for Carbon Fixation in Marine Diatoms. *Microbes Environ*, *38*(2). https://doi.org/10.1264/jsme2.ME23015

Yoshizawa, S., Kawanabe, A., Ito, H., Kandori, H., & Kogure, K. (2012). Diversity and functional analysis of proteorhodopsin in marine Flavobacteria. *Environ Microbiol*, *14*(5), 1240-1248. https://doi.org/10.1111/j.1462-2920.2012.02702.x

Zaslavskaia, L. A., Lippmeier, J. C., Kroth, P. G., Grossman, A. R., & Apt, K. E. (2000). Transformation of the diatom Phaeodactylum tricornutum (Bacillariophyceae) with a variety of selectable marker and reporter genes. *Journal of Phycology*, *36*(2), 379-386. https://doi.org/https://doi.org/10.1046/j.1529-8817.2000.99164.x

Zehr, J. P., & Kudela, R. M. (2009). Photosynthesis in the Open Ocean. *Science*, *326*(5955), 945-946. https://doi.org/doi:10.1126/science.1181277

Zehr, J. P., & Ward, B. B. (2002). Nitrogen cycling in the ocean: new perspectives on processes and paradigms. *Appl Environ Microbiol*, *68*(3), 1015-1024. https://doi.org/10.1128/aem.68.3.1015-1024.2002

Zhang, C., Freddolino, P. L., & Zhang, Y. (2017). COFACTOR: improved protein function prediction by combining structure, sequence and protein-protein interaction information. *Nucleic Acids Res*, *45*(W1), W291-w299. https://doi.org/10.1093/nar/gkx366

Zhang, C., & Hu, H. (2014). High-efficiency nuclear transformation of the diatom Phaeodactylum tricornutum by electroporation. *Marine Genomics*, *16*, 63-66. https://doi.org/https://doi.org/10.1016/j.margen.2013.10.003

Zhang, F., Vierock, J., Yizhar, O., Fenno, L. E., Tsunoda, S., Kianianmomeni, A., Prigge, M., Berndt, A., Cushman, J., Polle, J., Magnuson, J., Hegemann, P., & Deisseroth, K. (2011). The Microbial Opsin Family of Optogenetic Tools. *Cell*, *147*(7), 1446-1457. https://doi.org/https://doi.org/10.1016/j.cell.2011.12.004

Zhang, R., Zhu, X., Yang, C., Ye, L., Zhang, G., Ren, J., Wu, Y., Liu, S., Zhang, J., & Zhou, M. (2019). Distribution of dissolved iron in the Pearl River (Zhujiang) Estuary and the northern continental slope of the South China Sea. *Deep Sea Research Part II: Topical Studies in Oceanography*, *167*, 14-24. https://doi.org/https://doi.org/10.1016/j.dsr2.2018.12.006

Zhang, X., Zhu, J., Cai, Z., & Zhou, J. (2022). The Research Advance of Siderophores in Marine Microbes [Research paper]. *Progress in Biochemistry and Biophysics*, *49*(9), 1658-1671. https://doi.org/10.16476/j.pibb.2021.0266

Zhao, P., Gu, W., Huang, A., Wu, S., Liu, C., Huan, L., Gao, S., Xie, X., & Wang, G. (2018). Effect of iron on the growth of Phaeodactylum tricornutum via photosynthesis. *Journal of Phycology*, *54*(1), 34-43. https://doi.org/https://doi.org/10.1111/jpy.12607

Zheng, W., Zhang, C., Li, Y., Pearce, R., Bell, E. W., & Zhang, Y. (2021). Folding non-homologous proteins by coupling deep-learning contact maps with I-TASSER assembly simulations. *Cell Rep Methods*, *1*(3). https://doi.org/10.1016/j.crmeth.2021.100014